Dissertation
submitted to the
Combined Faculties for the Natural Sciences and for Mathematics
of the Ruperto-Carola University of Heidelberg, Germany
for the degree of
Doctor of Natural Sciences

Presented by

Diploma-physicist: Jorge M. Peñarrubia-Garrido
born in: Valencia, Spain

SATELLITE DYNAMICS IN SPIRAL GALAXIES WITH DARK MATTER HALOES

Referees:

Pr. Dr. Andreas Just
Pr. Dr. Joseph W. Fried

Zusammenfassung:

Diese Doktorarbeit analysiert die dynamische Evolution der Satelliten-Galaxien in einer, von einer massiven dunklen Korona (dunkle Materie) umgebenen Spiral-Galaxie. Die Hauptziele sind: (i) die Durchführung einer detaillierten theoretischen Analyse der dynamischen Reibung, d.h. des Prozesses, der die Verschmelzung der Satelliten verursacht und (ii) der Einfluss der Abplattung der dunken Korona auf diesen Prozess sowie deren Konsequenzen für die Beobachtungssatellitdistribution.

Abstract

This study analyses the dynamical evolution of satellite galaxies in spirals embedded in a Dark Matter halo. The main goals of this Thesis have been: (i) The performance of a detailed theoretical analysis of dynamical friction, the main process that leads to satellite merges into the more massive parent galaxies and (ii) the influence that the asphericity of haloes induces on this process and the possible consequences on the observational satellite distribution.

A mis padres, que me lo han dado todo

y siempre me han apoyado.

A Sabine, mi baluarte y mi alegría.

Contents

Chapter 1

General introduction

1.1 Preface

In 1933, the Swiss astronomer Fritz Zwicky suggested the presence of a non-detected large amount of mass in galaxy-clusters in order to explain the discrepancy between the observed velocity dispersion of the galaxies belonging to the Coma cluster and that expected from the virial theorem, where the total mass was estimated from the luminous component. In the past decades, astronomers observe that the content of luminous matter, also called *baryonic mass component*, is too low to account for the gravity of not only galaxy clusters but also of single galaxies and large scale structures in the Universe.

The "missing mass problem" finds a remedy if one assumes that there is a large fraction of mass, whose existence can solely be inferred from its gravitational effects, the so-called **Dark Matter**.

From that year on, a huge number of articles, books, conferences, projects etc., have tried to put light on the nature and properties of the Dark Matter. However, this problem has been around for decades, and there is now consensus that we do not know what the most common material in the Universe is. It is detected only gravitationally, and does not seem to emit or absorb substantial electromagnetic radiation at any known wavelength. The universal average density of Dark Matter determines the ultimate fate of the Universe, and it is clear that the amount and nature of Dark Matter stands as one of the major unsolved puzzles in science.

The aim of this thesis is to make a little step further.

1.2 Standard Big Bang theory and Dark Matter

The most favoured picture of the Universe is based on the Big Bang scenario. So far, this theory has been able to give an explicit explanation for the Cosmic Background Radiation (CBR) and the observations of large scale structures formed by galaxies and clusters of galaxies.

1.2.1 Inflation

The Big Bang theory postulates that the Universe orginally had a point-extension with singular energy density followed by an exponential expansion (*inflationary process*) that gave rise to a flat isotropic Universe (null curvature) nearly homogeneous. Inflation consists of a short period of accelerated superluminal expansion of the early Universe, at the end of which the "standard" description of the Big Bang model is applied.

In general relativity, a spatially homogeneous and isotropic Universe is described by the Friedmann-Lemaitre-Robertson-Walker metric (e.g., Landau & Lifschitz 1989),

$$ds^2 = -dt^2 + a(t)^2 \left[\frac{dr^2}{1 - Kr^2} + r^2 (d\theta^2 + \sin^2 \theta d\varphi^2) \right]$$

where (t, r, θ, φ) are co-moving coordinates, K is the curvature ($K = 0$, $K > 0$ and $K < 0$ imply a flat, close and open Universe, respectively) and $a(t)$ is the scale-factor of the Universe that accounts for its expansion. With this metric, Einstein's equations of general relativity reduce to,

$$\frac{\ddot{a}}{a} = -\frac{4\pi g}{3}(\rho_m + 3P_m) + \frac{\Lambda}{3},$$

$$H^2 \equiv \left(\frac{\dot{a}}{a}\right)^2 = \frac{8\pi G}{3}\rho_m - \frac{K}{a^2} + \frac{\Lambda}{3},$$

where $c = 1$, ρ_m and P_m are, respectively, the energy density and pressure of the matter content of the Universe, which is assumed to be a perfect fluid. H and Λ are the Hubble parameter and the cosmological constant, respectively.

For simplicity, we consider solely the case $K = 0$. Interpreting the presence of Λ as a fluid with energy and pressure $\rho_\Lambda = \Lambda/(8\pi G)$, $P_\Lambda = -\Lambda/(8\pi G)$ (note that negative pressure implies a repulsive force) so that,

$$\frac{\ddot{a}}{a} = -\frac{4\pi G}{3}(\rho + 3P),$$

$$\left(\frac{\dot{a}}{a}\right)^2 = \frac{8\pi G}{3}\rho,$$

where $\rho \equiv \rho_m + \rho_\Lambda$ and $P \equiv P_m + P_\Lambda$.

Inflation is defined as the epoch in the history of the Universe ($t \sim 10^{-34}$ s) when $\ddot{a} > 0$, i.e $P < -\rho/3$.

There are several proposal for inflation. Historically, the prototype has been the exponential expansion corresponding to de Sitter's solution of Einstein's equations ($\rho_m = P_m = 0$),

$$a(t) = a_0 \mathrm{e}^{\mathrm{Ht}},$$

$$H = \left(\frac{\Lambda}{3}\right)^{1/2}.$$

More recently, inflation is obtained by assuming that an early time the energy density of the cosmological fluid was dominated by a scalar field called *inflaton* (ϕ), where $\rho = \dot{\phi}^2/2 + V(\phi)$, $V(\phi)$ and $\dot{\phi}^2/2$ being the potential and kinetic energy of the scalar field. In the regime $V(\phi) \gg \dot{\phi}^2/2$, one can show that the solution of Einstein's equations can be wiritten as,

$$a(t) = a_0 \exp\left[\int H(t)dt\right],$$

where $H^2(t) \simeq 8\pi G V(\phi)/3$. The geometrical de Sitter solution is therefore associated to a quantum field description where $\phi = \phi_0$ with the potential $V = V_0 = \text{const.}$

The exponential growth of the scale factor means that, during the inflation epoch, the perturbation wavelengths inherent to the cosmological fluid soon exceeded the Hubble radius $cH^{-1} \simeq$ const., thus the fluctuation amplitudes were "frozen".

Once the inflation has ended, the Hubble radius increases faster than the scale factor, so that the fluctuations reenter the Hubble radius and structures in the matter and in the radiation background start to grow. The major success of inflation is that it provides the spectrum of perturbations, which can be compared to that the Cosmic Background Radiation.

1.2.2 Dark Matter content in the Universe

Inflation postulates that the Universe is flat and isotropic. From Einstein's equations this requires the density of matter to be $\rho = \rho_{\text{crit}} = 3H^2/(8\pi G)$, i.e $\Omega \equiv 8\pi G\rho/(3H^2) = 1$, which is assumed by the standard cosmology. If the cosmological constant is not zero one has that null curvature implies $\Omega + \Omega_\Lambda = 1$, where $\Omega_\Lambda = \Lambda/(3H^2)$.

Observations at the present day, however, provide a "luminous" (i.e, matter that can be detected from electromagnetic emissions, also called baryonic matter) density around $\Omega_b \simeq 0.0024$ (Fukugita et al. 1998). Therefore, "luminous" matter alone cannot account for the Universe flatness. This problem has found solution by assuming that the "missing mass" is formed by Dark Matter. In the standard cosmology frame $\Omega = \Omega_b + \Omega_m = 1$.
In order to check this hypothesis, researchers usually have followed three independent lines of investigation: (i) calculus of the primordial baryonic abundance at the Universe (assuming that the total amount of matter is constant), (ii) analysis of the CBR fluctuations and (iii) formation of large structures in the Universe.

Big Bang Nucleosynthesis

After the initial adiabatic inflationary process, the Universe starts to cool down. At $t \sim 10^{-4}$ s ($T \simeq 1.2 \times 10^{12}$ K), the formation of particles is in equilibrium, with nucleons $n \longleftrightarrow p$ and leptons $\gamma \longleftrightarrow e^{\pm}$, $\gamma \longleftrightarrow \mu^{\pm}$. These particles interact through electro-weak and gravitational forces.

The standard picture of the matter recombination after this evolutionary phase of the Universe is given by the Big Bang Nucleosynthesis (BBN, see e.g. Carr 1994 for a review). BBN assumes that the primordial abundance of nucleons can be determined by their present observational value and two free-parameters,

$$\eta \equiv \frac{n_b}{n_\gamma} \simeq 2.72 \times 10^{-8} \left(\frac{T}{2.73K} \right)^{-3} \Omega_b h^2,$$

η being the fraction between the number of photons and baryons (strictly speaking nucleons) at a given time and $h = H_0/100$ km s^{-1} kpc, the present Hubble parameter. The second parameter is N_ν, the number of relativistic species.

The proton to neutron ratio at that time plays a very important role in order to compare the primordial with the actual abundance of baryonic elements. It is estimated as $n/p = \exp(-Q/T_{\rm fr})$, where Q is the neutron-proton mass difference, $Q = 1.293$ MeV and $T_{\rm fr} \sim (N_\nu G/G_f^4)^{1/6} \simeq 1$ MeV is the "freeze-out" temperature, resulting from the break of the chemical equilibrium $n \longleftrightarrow p$ as the temperature dropped. The abundance of free neutrons is, thus, directly dependent of N_ν through the value of $T_{\rm fr}$. In the standard cosmology $N_\nu = 3$ and therefore $n/p \simeq 1/6$ at $T \simeq 1$ MeV.

The nucleosynthesis chain begins with the formation of deuterium in the process $p(n,\gamma)$D. The rate of the process is very low until the number of photons with energy higher than the deuterium photo-dissociation falls, which occurs at $T \simeq 0.1$ MeV. Due to the low density of the Universe at that time, only 2-body reactions such as D$(p,\gamma)^3$He, ^{3}He(D,p)^{4}He are important.

Nearly all the surviving neutrons at the beginning of nucleosynthesis end up bound in the most stable isotope of Helium, ^{4}He. Heavier nuclei such as T and ^{7}Be cannot be created due to the strong repulsion between nuclei. The Helium abundance can be obtained from the ratio between neutrons and protons n/p as, ^{4}He/H$= 2(n/p)/(1 + n/p) \simeq 0.25$, whereas the abundance of other elements such as Deuterium and Tritium depends on the value of η.

Once given η and N_ν, BBN theory predicts the universal abundances of D, ^{3}He, ^{4}He and ^{7}Li, which are essentially determined at $t \sim 180$ s. However, their observations can be solely carried out at much later epochs. The main problem in the comparison results as a consequence of the stellar nucleosynthesis and other galaxy chemical processes, which alters the primordial values.

The value of η (and therefore the baryon density Ω_b) is determined from the Cosmic Background Radiation and the measurements of the primordial elements abundances as a function of time (redshift), subsequently extrapolated to null metalicity. Whereas the former provides the value of n_γ fixed by the present CBR temperature, the observed abundances of D, ^{3}He, ^{4}He and ^{7}Li constrain the possible value of η. Since $\Omega_b = 2.65 \times 10^{-13} h^{-2} \eta$, one has that,

$$0.0095 \leq \Omega_b h^2 \leq 0.023.$$

First one must note that $\Omega_b \ll 1$, i.e., baryons cannot close the Universe. Furthermore, the observed luminous matter is $\Omega_{\rm lum} \simeq 0.0024 h^{-1}$, so that $\Omega_b \gg \Omega_{\rm lum}$, which indicates that

most baryons are optically dark. This is consistent with the abundance of baryonic Dark Matter (i.e, bodies, such as Massive Massive Compact Objects "MACHOs" that are formed by baryonic matter but cannot be directly observed, see below), which has been estimated in galaxies as $\Omega_h \simeq 0.011 h^{-1}(R_h/35\mathrm{kpc})$ (Fich & Tremaine 1991), where R_h is the halo radius.
Finally, either if the cosmological parameters are $\Omega = \Omega_m = 1$, $\Omega_\Lambda = 0$ (standard picture CDM), or $\Omega_m \simeq 0.313$, $\Omega_\Lambda \simeq 0.687$ (ΛCDM), as recent observations of the CMB and the large redshift survey (2dFGRS) suggest (Percival et al. 2002), we infer that most matter in the universe takes a non-baryonic form. This result is a key point for the Dark Matter cosmology.

Formation of large structures

The Big Bang theory postulates the formation of galaxies, cluster of galaxies and large structures as a consequence of perturbations in the initial matter density, whose relics can be nowadays observed as fluctuations in the Cosmic Background Radiation.

In this scheme, the growth rate and evolution of perturbations are highly dependent on the matter nature. Since the Universe is more homogeneous on large scales, one expects that these fluctuations follow a power spectrum for which the Fourier amplitude can be described as $|\delta(k)|^2 \propto k$, where k is the wave number. Further, in standard cosmology, it is assumed that the spectrum phases are independent, whereas the amplitudes have a Gaussian distribution about the mean.
At the epoch of radiation domination, perturbations with wavelengths smaller than the horizon grew very slowly. At that time, the Universe was highly homogeneous (and isotropic) as expected from the inflation scenario. As the temperature dropped, the mass density (by hypothesis "cold", i.e., non-relativistic) starts dominating over that of massless particles. The power spectrum $P(k)$ remains proportional to the wave number for wavelengths larger than the horizon radius. However, on scales smaller than the horizon the growth is slower, with a power spectrum asymptotically $P(k) \propto k^{-3}$ as $k \to \infty$ (see Ostriker 1993 for a review).

The main differentiation between baryonic and Dark Matter evolution occurs at this time. Whereas Dark Matter density evolve around the initial over-density points, the baryonic perturbation growth was kept small due to the repulsive electro-magnetic force between the ionized atoms until matter recombines at about $z \sim 10^3$ ($t \sim 180$ s). At this moment, baryons fall into the Dark Matter potential wells that were already formed, evolving to the present "visible" structures.

Due to the delay in the perturbation growth, any model based purely on baryonic matter (i.e., $\Omega_m = 0$ and $\Omega_b = 1$) would need of large amplitudes in the fluctuation spectrum at the recombination time, which is not consistent with the fluctuations observed in the CBR.

The Dark Matter scenario is very successful in order to reproduce the large scale structures (larger than 1 Mpc) in the Universe (Bahcall et al. 1999). However, during last years some observations of matter structure on small scales (few kiloparsecs) may be in conflict with predictions of Dark Matter, which constitutes a topic of discussion nowadays:
(i) The density profile of galaxies in the inner few kiloparsecs appear to be much shallower than predicted by N-body simulations of Dark Matter (Navarro, Frenk & White 1997).
(ii) The central density of Dark Matter haloes is observed to be $\rho_c \simeq 0.02 M_\odot \mathrm{pc}^{-3}$, roughly independent of the halo mass (Firmani et al 2000b), meanwhile CDM (Cold Dark Matter) predicts $\rho_c \simeq 1 M_\odot \mathrm{pc}^{-3}$ in dwarf galaxies, increasing to larger masses (Moore et al. 1999b).
(iii) The number of dwarf galaxies in the Local Group is significantly fewer than predicted by CDM, with the discrepancy growing the higher the numerical resolution is (Moore et al. 1999a, Klypin et al. 1999).
(iv) Observational distribution of satellites around isolated spiral galaxies show that most of them follow polar orbits with respect to the disc plane (Zaritsky & González 1999), whereas the CDM numerical calculations show that the satellite distribution mimics the mass distribution of the DM halo.

The observed discrepancies (i)-(iii) may have a single cause: CDM produces systems with an over-concentration of Dark Matter in the most inner regions. In order to solve the apparent discrepancies between CDM predictions and observations on small scales, a plethora of new alternatives have been suggested. Some of such theories are motivated from particles physics considerations,

Scale/Object	$\Upsilon/\Upsilon_\odot$
Solar neighbourhood	5
Elliptical galaxy cores	$12h$
Satellite galaxies	30
Local Group	100
Group of galaxies	$260h$
Cluster of galaxies	$400h$

Table 1.1: Mass-to-light ratio for different scales and systems. h denotes the normalised Hubble constant (between 0.4 and 1) and $\Upsilon_\odot$ the mass-to-light ratio of the Sun.

though all of them retain the desirable properties of CDM on large scales. For instance, it has been proposed that DM is warm (e.g Colin et al 2000), repulsive (Goodman 2000), fluid (Peebles 2000), self-interacting (Spergel & Steinhardt 2000) among others which, with different degrees of accuracy, solve the problem.

However, the point (iv) remains without explanation. One of the aims of this Thesis is to give an insight on the physical processes that may contribute to the observed anisotropy of the satellite distribution.

1.3 Evidences for Dark Matter

Historically, the most robust evidence for Dark Matter came from the rotation curves of spiral galaxies. Using 21 cm emission, the velocities of clouds of neutral hydrogen can be measured as a function of r, the distance from the centre of the galaxy. In almost all cases, after a rise near $r = 0$, the velocities remain nearly constant out as far as can be measured. By Newton's law for circular motion $GM(r)/r^2 = v^2/r$, this implies that the density drops like r^{-2} at large radius and that the mass at large radii. Once r becomes greater than the extent of the mass, one expects the velocities to drop as $r^{-1/2}$ but, usually, this is not seen, suggesting that the Dark Matter extension around spirals is far beyond the baryonic extension as it is found in clusters of galaxies.

In 1974, Ostriker et al. and Einasto et al. proposed the presence of large amounts of Dark Matter around even isolated galaxies which would reproduce the observed flat rotational curves of galaxies at large distances. The Dark Matter would be located in giant "haloes" extending out to several times the radius of the luminous matter and containing most of the galaxy mass. These haloes also extend around cluster of galaxies, with masses of around $10^{14} - 10^{15} M_\odot$.

There is a great deal of new evidence on Dark Matter in clusters of galaxies, coming from gravitational lensing, from X-ray gas temperatures, and from the motions of cluster member galaxies.

To measure the amount of Dark Matter in a given scale, authors usually determine the value of the *mass-to-light ratio* Υ, defined as the fraction between the mass and luminosity density, providing therefore, the amount of mass that produces the observed luminosity. Evidently, bodies composed mostly by Dark Matter will lead to large values of Υ. In Table 1.1 the values of the mass-to-light ratios are given for different scales and systems (Binney & Tremaine 1987, hereinafter BT). From this Table appears clearly that the more distant the objects are (equivalently to larger scales), the more dominates the Dark Matter over the baryonic component. As we see below, this fact has given occasion for the development of alternative theories that question the Newton's gravity at large scales going, therefore, against the Dark Matter solution for the "missing mass problem".

1.4 Dark Matter candidates

In the standard picture, CDM provides the observed mass distribution on large scales under, solely, two assumptions: (i) Dark Matter particles move on non-relativistic velocities at early ages and

(ii) it interacts only through the gravitational force. There is no shortage of ideas as to what kind of particles have such properties. In fact, the problem is the opposite. Serious candidates have been proposed with masses ranging from 10^{-5} eV = 1.8 10^{-41} kg= 9 $10^{-72} M_\odot$ (axions) up to $10^4 M_\odot$ (black holes). That's a range of masses of over 75 orders of magnitude! It should be clear that no one search technique could be used for all Dark Matter candidates.

Even finding a consistent categorisation scheme is difficult, so that here we merely include the most important suggestions for the Dark Matter components.

1.4.1 Baryonic Dark Matter

The main baryonic candidates are the Massive Compact Halo Object (Macho) class of candidates. These include brown dwarf stars, Jupiters, and $100 M_\odot$ black holes. Brown dwarfs are spheres of H and He with masses below $0.08 M_\odot$, so they never begin nuclear fusion of hydrogen. Jupiters are similar but with masses near $0.001 M_\odot$. Black holes with masses near $100 M_\odot$ could be the remnants of an early generation of stars which were massive enough so that not many heavy elements were dispersed when they underwent their supernova explosions. Other, less popular, baryonic possibilities include fractal or specially placed clouds of molecular hydrogen. The non-baryonic candidates are basically elementary particles which are either not yet discovered or have non-standard properties.

1.4.2 Non-baryonic Dark Matter

Among the non-baryonic candidates there are several classes of particles which are distinguished by how they came to exist in large quantity during the Early Universe, and also how they are most easily detected.

Among the particle Dark Matter candidates an important distinction is whether the particles were created thermally in the Early Universe, or whether they were created non-thermally in a phase transition. Thermal and non-thermal relics have a different relationship between their relic abundance and their properties such as mass and couplings, so the distinction is especially important for Dark Matter detection efforts. For example, the Wimp class of particles can be defined as those particles which are created thermally, while Dark Matter axions come mostly from non-thermal processes.

The largest class is the Weakly Interacting Massive Particle (Wimp) class, which consists of literally hundreds of suggested particles and forms through thermal processes at early stages of the Universe. The most popular of these Wimps is the neutralino from super-symmetry (see Carr 1994 for a review).

Thermal creation occurs early, when the Universe was at very high temperature, thermal equilibrium obtained, and the number density of Wimps (or any other particle species) was roughly equal to the number density of photons. As the Universe cooled the number of Wimps and photons would decrease together as long as the temperature remained higher than the Wimp mass, interacting solely through gravitational force.
The density required by the Cold Dark Matter cosmology (CDM) is $\Omega_{\rm matter} = 1$. Wimp particles would account for this density if the annihilate into ordinary particles through electroweak forces. Therefore, one hypothesis is that any stable particle which annihilates with an electroweak scale cross section is bound to contribute to the Dark Matter of the Universe. It is interesting that theories such as super-symmetry, invented for entirely different reasons, typically predict just such a particle.

Non-thermal relics are also thought to provide the mass density obtained from the CDM model. The best example of a non-thermal particle Dark Matter candidate is the axion. This particle would have null mass at the earliest stage of the Universe. However, when the temperature of the Universe cooled below a few hundred MeV (QCD energy scale), the solution of the QCD Lagrangian predicts a new equilibrium state where the particle has non-null mass. These particles would be observed as a coherent axion field condensate filling the Universe which constitutes the Dark Matter. The relic energy density is thus related to the QCD potential, which in turn is

related to the axion mass, a free parameter of the model. If the axion mass is $m_a \simeq 10^{-5}$ ev, the we obtain $\Omega_{\rm matter} \simeq 1$. Axions could then account for the mass density in the Universe, even if they are so light.

Finally, if the tau and/or muon neutrinos had a mass in the 2 eV to 100 eV range, they could make up all or a portion of the Dark Matter.

1.4.3 Distinction between "cold" and "hot" Dark Matter

A Dark Matter candidate is called "hot" if it was moving at relativistic speeds at the time when galaxies could just start to form (when the horizon first contained about $10^{12} M_\odot$). It is called "cold" if it was moving non-relativistically at that time. This categorisation has important ramifications for structure formation, and there is a chance of determining whether the Dark Matter is hot or cold from studies of galaxy formation. Hot Dark Matter cannot cluster on galaxy scales until it has cooled to non-relativistic speeds, and so gives rise to a considerably different primordial fluctuation spectrum. Of the above candidates only the light neutrinos would be hot, all the others would be cold.

1.5 Non-Newtonian gravity

The Modified Newtonian Dynamics (MOND) has been found as an alternative to solve the "missing mass problem". The basis of this explanation is the suggestion that, although the Newtonian gravity has been successfully checked on the Solar System scale, it breaks down on the scale of galaxies. In particular, the proposal by Milgrom (1983) that the effective law of attraction becomes more like $1/r$ in the limit of low accelerations has been able to reproduce some systematic aspects of this discrepancy between galaxy and groups of galaxies (reviewed by Sanders 1990).

The MOND alternative predicts the precise form of the rotation curve of a spiral galaxy if the observed mass distribution is given and the value of a single universal parameter a_0. Usually, the mass-to-light ratio of the visible disc is used as a free parameter in order to fit rotation curves obtained from the 21-cm emission of the neutral hydrogen.

The simple MOND formula for the gravitational force can be written as

$$\mu(g/a_0)\mathbf{g} = \mathbf{g}_n, \tag{1.1}$$

where $\mathbf{g}_n$ is the Newtonian acceleration and

$$\mu(x) = 1, \quad x \gg 1 \qquad\qquad \mu(x) = x, \quad x \ll 1, \tag{1.2}$$

that can be approached by the analytic function

$$\mu(x) = x(1 + x^2)^{-1/2}, \tag{1.3}$$

It is straightforward to show that rotation curves are asymptotically flat in the low acceleration limit if the mass bounded is finite so that

$$V_c^4 = GMa_0. \tag{1.4}$$

Although Non-Newtonian gravity successfully describes the flat rotation curves of spiral galaxies, there is a large list of physical processes that find no explanation from MOND, such as gravitational lensing, formation of large scale structures in the Universe, tidal disruption of satellites...etc, which makes the Dark Matter scenario the most favoured solution for the "missing mass" problem.

1.6 From satellite dynamics to Dark Matter cosmology

The study of the satellite galaxy dynamics in spiral galaxies may help to determine the Dark Matter nature.

Rotational curves of spiral galaxies show that for $r > 30$ kpc the halo potential dominates over that of the baryonic components (bulge and disc), whereas satellite galaxies can be found at distances as large as 500 kpc from the parent galaxy centre (Zaritsky et al. 1993). Other systems like globular cluster and halo stars are very hard to detect for $r > 50$ kpc. Satellite galaxies, therefore, represent in galaxies the most important indicator in order to investigate the halo potential and also, indirectly, its shape.

Measuring the mass distribution around galaxies provides a critical test for cosmological models. The Dark Matter scenario predicts density profiles scaling as r^{-2} at intermediate scales, which give rise to the observed flat rotation curves, whereas at large distances the mass distribution is steeper $\rho \propto r^{-3}$ (Navarro, Frenk & White 1997). The challenge in comparing theory with observations arises from the difficulty of finding a visible tracer to measure the mass. One of the most commonly used is the neutral hydrogen emission (HI), which is detected well beyond the optical boundary, providing density profiles that go as r^{-2} (e.g Sofue & Rubin 2001). However, HI lines are only detected within $30 - 50$ kpc. X-rays emissions, observed in elliptical galaxies and cluster of galaxies, suffer from a similar limitation in order to give insight of the mass distribution at large distances.

Gravitational lensing provides a more promising method to study the outer parts of galaxies (e.g, Smith et al. 2001 and references therein). Unfortunately, the existing data cannot distinguish between the r^{-2} and r^{-3} profiles in the outer most regions, where the errors are large. Moreover, at such distances, neighbour galaxies can affect the data.

Satellite galaxies represent the most helpful indicator for the mass distribution at large distances. The main disadvantage of this method consist in the large number of satellites necessary to perform good statistics. As a result, observational efforts in this field are somewhat limited (Zaritsky et al. 1993, Zaritsky et al. 1997, McKay et al. 2002). This method constraints the mass distribution in two manners:

First, the velocity distribution of satellites can determine whether the density profile drops at large radii, as the cosmological models predict. Although the singular isothermal sphere is usually employed at large distances as an extrapolation of flat rotation curves, none of the Dark Matter models give rise to such a mass distribution, but all of them predict that $\rho \propto r^{-3}$ in the outer most region of DM systems. This slope does not depend on the mass density, since CDM with $\Omega_{\rm matter} = 1$ as well as ΛCDM with $\Omega_m = 0.3$, $\Omega_\Lambda = 0.7$, have the same slope (Klypin et al. 2001), neither depends it on the Dark Matter nature since hot, cold and self-interacting Dark Matter models make the same prediction (e.g. Spergel & Steinhardt 2000), nor on the halo mass: haloes ranging from galaxy cluster masses to dwarf masses all present $\rho \propto r^{-3}$ for large distances (Navarro, Frenk & White 1997). Only the Modified Newtonian Dynamics (MOND) give rise to a singular isothermal density profile, therefore, with constant velocity dispersion (σ). The studies carried out so far lead to contradictory results. Whereas Zaritsky et al. (1993) and Zaritsky et al. (1997) find that σ does not decline with distance and that it does not correlate with the luminosity of the parent galaxy, McKay et al. (2002) (using a much larger sample of satellites) agree that $\sigma \simeq$ const., though they observe that $\sigma \propto L^{0.5}$, where L is the luminosity of the parent galaxy. Lastly, in a very recent paper, Prada et al. (2003) use the observational data of McKay et al. (2002) and show that σ decreases with distance (obtaining the r^{-3} dependence in the density profile), and that $\sigma \propto L^{0.3-0.5}$. In this case, a new selection criterion gives rise to different results. The results of Prada et al. (2003) go directly against the MOND postulates.

The study of satellite galaxies may also induce constraints on the Dark Matter nature through their distribution with respect to the disc plane. Zaritsky et al. (1993) and Zaritsky & González (1999) show that most of the satellites are found in polar orbits, this anisotropy being stronger the more distant the satellite are from the parent galaxy. There are two possible reasons that explain such a distribution: (i) The phase-space of satellite formation may be limited to volumes where the predominating orbits are polar. (ii) Evolutionary processes may remove those satellites with low and intermediate orbital inclinations, so that nowadays most of satellites are observed following polar orbits.

The currently favoured CDM theory of galaxy formation postulates that the formation of a massive spiral galaxy like our own is a consequence of the hierarchical assembly of sub-galactic dark

haloes, and the subsequent accretion of cooled baryonic gas in a virialized, galaxy-scale dark halo (e.g Peacock 1999). Once galaxies form due to the collapse of matter around over-density peaks in the strongly homogeneous background at the early stages of the Universe, they subsequently interact with each other, forming more massive systems or being destroyed in the assemble process. This is called *hierarchical* galaxy evolution. In this frame, less massive galaxies, such as satellite galaxies, usually merge into the neighbour, more massive, ones (parent galaxies), following a process called *satellite decay*. The main driving mechanism that controls the satellite decay is dynamical friction which, as the name indicates, induces the progressive angular momentum loss that leads to the final merge of both galaxies.

On the another hand, CDM cosmology predicts the formation of highly flattened triaxial haloes, that become nearly oblate due to the disc formation (Dubinsky 1994). From CDM, haloes would follow a Gaussian distribution of aspect ratios, $q_h \equiv c/a > 0$, where c and a are the minor and major axes of an oblate spheroid, of mean $< q_h >= 1/2$ and dispersion equal to 0.15.
These theoretical results have been supported by several observational evidences of halo flattening. Observations of gravitational lensing (Maller et al. 2000; González et al. 1999; Maller et al. 1997; Keeton & Kochanek 1998), galactic disc warps (Binney 1992), X-ray detections (Buote et al. 2002), stellar kinematics (Olling & Merrifield 2000), HI emissions (Olling 1996, Becquaert, Combes & Viallefond 1997), polar ring galaxies (Arnaboldi et al. 1993, Sackett et al. 1994) and precessing dusty discs (Steinman-Cameron, Kormendy & Durisen 1992), give evidences that Dark Matter haloes are **flattened**, with minor to major axis-ratios ranging from 0.2 to 0.9. None of these measures conciliate with spherical haloes.

However, the data outlined above suffer from a strong limitation: they are available for $r < 50$ kpc.

The aim of this document is to give insights on the halo shape from the satellite dynamics investigation. Since satellites are observed as far as 500 kpc from the parent galaxy, this study may also constrain the halo density profile at large radii. Both investigations will provide a hint on the Dark Matter nature.

1.7 Scheme of the investigation

In Fig. 1.1 we show the scheme of our analysis.
From the observational data we construct a galaxy model that describes a spiral galaxy like the Milky Way (Chapter 3). We follow subsequently two lines of investigation:

- **N-body calculations**.Once the galaxy and satellite models are given, we build up the initial systems in equilibrium (Section 2.2) in order to perform N-body calculations to determine the differences that the halo shape (Chapter 7) and the disc and bulge presence (Section 9.3) induce on the satellite dynamics.

- **Semi-analytic calculations**. Observations of satellite galaxies provide a statistical view of the satellite evolution in spiral galaxies. The number of satellites per host galaxy ranges usually from 0 to 5, with the probability p of finding a system with n satellites going as $p = 0.43^n$ (Zaritsky et al. 1993). This implies that host galaxies with small number of satellites are more likely to be observed than those with a large n. In order to produce theoretical data to compare with, one needs to carry out a large number of calculations to cover as much orbital parameter space as possible. Unfortunately, this kind of study is not possible with the present computational capabilities due to the prohibitive CPU-expense. For that reason, we build a semi-analytic code (Chapter 4) that, in a self-consistent way, reproduces the N-body satellite evolution after fixing a free parameter (the Coulomb logarithm), denoted in the scheme as the "comparison" between the semi-analytic and N-body data. The galaxy and satellite models are those employed for the N-body simulations. The semi-analytic code is very simple: it solves the equations of motion of the point-mass satellite within the galaxy potential. Dynamical friction (the force that every body suffers when moving through a background of much lighter particles) is implemented as an external

force. This code also calculates the mass loss induced by tidal forces and rapid encounters with the disc and bulge (*shocks*) which accounts for $M_s(t)$ along the satellite evolution.

The main driving mechanism that controls the progressive satellite decay in spiral galaxies embedded in a more massive Dark Matter halo is dynamical friction. Due to its capital importance, we carry out an exhaustive analysis in Chapter 5 and 6. The key point of this study is based on the differences that the halo shape (more concretely, the halo flattening) may induce on the satellite dynamics through the action of dynamical friction (Chapters 7 and 8). If these differences are strong, one should be able to appreciate them in the observational distribution of satellites (Chapter 10). The question mark in the scheme represents the following question: "do the hierarchical scenario with the present cosmological models, where Dark Matter haloes around spiral galaxies are predicted to be flattened, reproduce the observed satellite distribution?". If yes, this would favour the widely accepted Dark Matter cosmology, otherwise, one should re-examine our actual view of the satellite formation and evolution and, perhaps, even the "missing mass" problem.

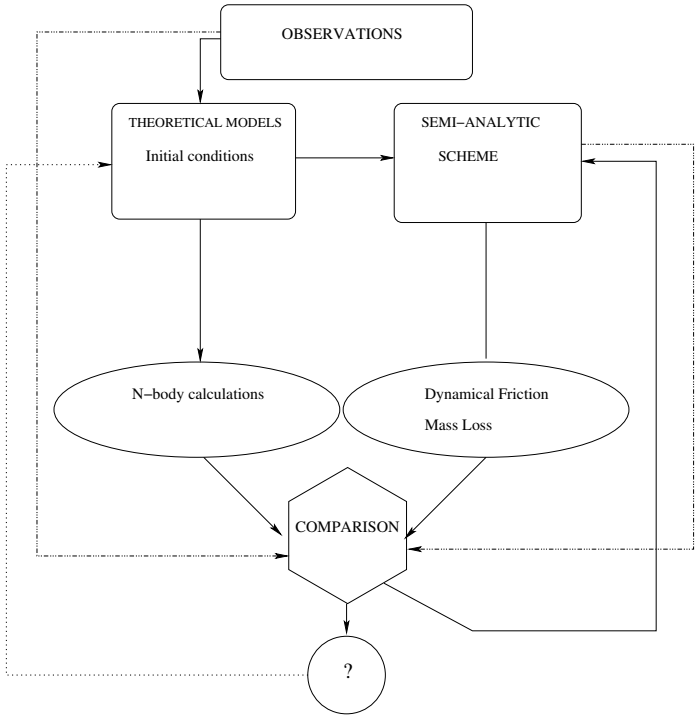

Figure 1.1: Scheme of the investigation carried out.

1.8 The astrophysicists' tool: Numerical codes

Astrophysics has a crucial disadvantage in front of other branches of physics, one cannot play around with several galaxies in a lab in order to investigate processes such collisions, mergers...etc. To solve this problem, researchers construct numerical models that are thought to reproduce what is observed. Subsequently, numerical algorithms based on Newton's laws are used in order to calculate the dynamical evolution of these celestial objects (the use of N-body codes is the most extended, in which systems are formed by a large number of particles solely interacting through the gravitational force). More sophisticated numerical algorithms can also implement gaseous components and stellar evolution.

This is the first approximation. Even if one assumes that these models are reasonably accurate, galaxies are so complex that additional simplifications must be adopted. Here we comment those that our N-body calculations implicitly assume:

- **Collisionless code**. Galaxies are huge, in mass as well as in extension and number of stars (for example, the Milky Way is composed of about 10^{11} stars, with a diameter of about 20 kpc= 4.3×10^9 AU= 6.2×10^{20} m). So far, there is not a numerical algorithm capable to evolve such a number of particles. For example, the galaxy model employed in our numerical calculations is composed of 1.6×10^6 N-body particles. This means that each particle has a mass of around $10^5 M_\odot$. However, if one computes the probability of a collision between two "stars", one will find that the time-scale is longer than one Hubble time. For such a case, the general description of a galaxy can be given by its distribution function, whereas the evolution is calculated by solving the collisionless Boltzman equation (e.g BT). In this case, the galaxy potential is not sensitive to the N-body particle mass. Whereas this equation provides the evolution of the general galaxy properties, it would be non-sense to use a collisionless code to determine the Solar System evolution, since on such small scales, two-body effects are important.

- **Mass of N-body particles**. Galaxies are composed of bodies with masses ranging from $0.1 M_\odot$ (brown dwarfs) to $100 M_\odot$ (black holes) or even larger. N-body algorithms, however, usually evolve systems formed by equal-mass particles (see, as an example, SUPERBOX in Section 2.1), with masses typically $m = 10^5, 10^6 M_\odot$. Although at first look to assume that all particles have the same mass seems a very rough approximation, actually, it is not. The self-potential of a galaxy (which mostly determines the satellite dynamics) is not dependent on the particles masses in a kiloparsec scale. Even black holes with thousands of solar masses in the centre of galaxies change the velocity curve only within one kpc. Again, for such a system the most appropriate is to use a collisionless code, which are not sensitive to the mass spectrum of the N-body galaxy particles.
  Although the galaxy evolution can be accurately described by collisionless algorithms, the satellite-galaxy interaction is a two-body encounter process. In this case, the number of particles, as well as the resolution of the code, shall influence the satellite evolution. This is clearly shown in Section 8.6, where the number of galaxy particles (N) is increased 8 times. We observed that, whereas the overall evolution of the satellite is nearly independent of N, the survival time of the satellite is, however, approximately a 15% reduced. It is important to remark that, despite this result indicates that the time-dependence of processes such satellite decay, mass loss, nutation and precession are sensitive to N, the description of the processes themselves is not.

- **Absence of gas**. Pure N-body algorithms do not include a gaseous component. Although this component plays an important role in models that describe the disc structure (bar formation, spiral arms and dissipation processes), it can be neglected in order to analyse the dynamics of satellite galaxies. The reason is found in the low abundance of gas if compared to the stelar population. The total masses of HI and HII have been derived for hundreds of spiral galaxies, observing that $\mathcal{M}_{\rm gas}/\mathcal{M}_{\rm dyn}$ is around 3×10^{-3} (Sa galaxies) up to 0.1 (Sc galaxies), where $\mathcal{M}_{\rm gas} = \mathcal{M}_{\rm HI} + \mathcal{M}_{\rm HII}$ and $\mathcal{M}_{\rm dyn}$ is the estimation of the galaxy mass (Binney & Merrifield 1998). Since the gas component follows roughly the mass distribution of the stellar disc, the contribution to the satellite dynamics can be neglected for distances larger than a few disc scale-lengths, where the Dark Matter dominates the galaxy potential (as it is observed from the galaxy rotation curves).

- **Stellar evolution**. The properties of stars, such as mass, luminosity and extension change along their evolution, mostly depending on their initial mass and metalicity. Despite of their importance in systems with small number of particles (such as globular and open clusters), stellar evolution processes are usually neglected in galaxy dynamics. As we commented above, the individual properties of stars are not determinant in order to study the galaxy

dynamics, as long as the number of particles in the system leads to a typical time-scale of two-body encounters longer than the Hubble time. In this case, the total mass of the system as well as its mass distribution fully determines the potential of the galaxy. The main advantage of using numerical codes that reproduce the stellar evolution is the possibility to compare the resulting calculations with spectrocopic observations.

1.9 Overview of this Thesis

In this Section we show a brief summary of the contents of each Chapter.

The goal of Chapter 2 is to describe the basis of the collisionless N-body treatment employed to describe the satellite evolution in spiral galaxies. We use a particle-mesh algorithm called SUPERBOX, which provides a high computational velocity even with a large number of particles. Another advantage of this code is that relaxation processes are nearly negligible along the calculations. In the second Section we outline the scheme employed ir order to build up the initial galaxy with N-body particles. This method (Boily, Kroupa & Peñarrubia 2001) was created to construct spiral galaxies in nearly equilibrium with the possibility of implementing the halo flattening as an input parameter. The CPU-time required for the operation is the same as for a galaxy with spherical halo, therefore, improving the efficiency in front of other algorithms, e.g. Hernquist (1991), for which the CPU-expense scales as the square of the particle number.

In Chapter 3 we present the **galaxy and satellite models** employed in our investigation. The galaxy is formed by the disc, the bulge and a Dark Matter halo. Whereas the former are determined by observations of the baryonic structure in the Milky Way, the later is inferred from the rotational curve and X-rays measurements. The satellite model is based on observations of dwarf spheroidal galaxies. The density profiles of each system, the force and the velocity dispersion expressions are outlined in this Chapter, together with the parameters that determine their properties. We also provide here the parameters of SUPERBOX, such as the resolution, grid sizes and time-step since they depend on the galaxy and satellite parameters.

Although SUPERBOX is a high efficient N-body code, an investigation of the satellite distribution in spiral galaxies would require thousands of simulations in order to explore the orbital parameter space of the satellite galaxy, its mass range and the influence of different Dark Matter models on its evolution. We have found a remedy by developing a **self-consistent semi-analytic algorithm** that solves the satellite's equations of motion and mass evolution (Chapter 4). This code consumes 10^4 times less CPU time that SUPERBOX calculations. The basis of the code is simple: assuming that the galaxy does not evolve as a response to the satellite presence, the force acting on the satellite is the sum of the galaxy field (calculated from the density profile) plus two-body encounters with the background particles, the so-called *dynamical friction*. The internal properties of the satellite are then determined by its total amount of mass and mass profile along the orbit. Due to the dependence of the two-body processes on the N-body parameters, such as resolution and number of particles, the semi-analytic algorithm implements two free quantities to be fitted to the N-body data: the disc and halo Coulomb logarithms.

The main driving mechanism that controls the dynamical evolution of our satellite galaxy is **dynamical friction**. Due to its importance, we analyse in detail the theoretical treatment of this process in Chapter 5 and generalise the expressions for flattened systems. We also study the contribution of the first order friction induced by the system inhomogeneity and the dependence of the Coulomb logarithm on the galacto-centre distance.

In Chapter 6 we check the analytic expressions of Chapter 5 by implementing them into our semi-analytic code. The results are compared to the N-body calculations from SUPERBOX. For simplicity, the galaxy model is formed by a **spherical Dark Matter** halo without disc and bulge.

One of the main topic of investigation of this Thesis is the effects that the **halo asphericity** may induce on the satellite dynamics and evolution. The analysis follows two approaches:

- First, in Chapter 7 we carry out numerical N-body calculations covering a wide range of orbital parameters and satellite masses. These simulations include a baryonic component in

the form of a disc and a bulge embedded within a spherical and a flattened Dark Matter halo with the same characteristics, so that a direct comparison can be performed.

- Second, we attempt to reproduce the numerical data with our analytic treatment. In order to separate the disc and bulge effects to those induced by the halo flattening, in Chapter 8 we carry out N-body calculations removing disc and bulge, so that the parent galaxy is formed by a flattened halo. Subsequently, we compare our analytic treatment of anisotropic dynamical friction (implemented in the semi-analytic algorithm) with the resulting N-body calculations. The satellite mass evolution $M_s(t)$ is obtained from the N-body data.
  In Chapter 9, we compare those simulations of Chapter 7 (the galaxy includes the baryonic components) with the self-consistent semi-analytic analysis, which includes the mass loss scheme outlined in Chapter 4. The goal is to check the accuracy of this algorithm in order to describe the satellite dynamics and mass evolution in spiral galaxies for different values of the halo axis-ratio.

The self-consistent semi-analytic code becomes an extremely important tool in order to analyse the evolution of the **satellite distribution** induced by dynamical processes, such as dynamical friction, mass segregation and mass loss, and their dependence on the halo shape and extension. The results have a clear connection to Dark Matter cosmology, since the comparison with observational measurements of satellites will give insights on: (i) the initial satellite distribution, (ii) the halo morphology and (iii) the halo extension, between others. This study is too ambitious to be performed in one Chapter of this Thesis, so that in Chapter 10 we present the preliminary results of this investigation, as well as the most recent observations of the satellite galaxy distribution in spiral galaxies.

Chapter 2

The N-Body Code

2.1 Brief introduction to SUPERBOX

SUPERBOX is a particle mesh code with high resolution sub-grids. The program calculates the accelerations using a high order NGP ('nearest grid point') force calculation scheme based on the second derivatives of the potential. A self-consistent system of several galaxies can be treated by forming sub-grids which follow the motion of each galaxy. The relaxation processes are negligible, even in time scales of a Hubble time.

The main advantage of SUPERBOX is its computational velocity even with a big number of particles (several millions), however the code is highly dependent on the geometry of the system. Whereas the hierarchical tree and direct N-body methods do not suffer from this problem, the particle number has a big limitation and they need a softening to avoid the two-body relaxation effects and meanwhile the direct N-body methods have a dependence of the CPU-time on the number of particles scaling as N_p^2, the mesh-codes have a linear dependence. However, SUPERBOX depends on the number of grid cells (N_{gc}), with the CPU-time going as $N_{gc}\log N_{gc}$. Our calculations are limited to $N_{gc} = 64^3$, which gives the best number for resolution/CPU-time with the present computer resources at the institute.

We shall introduce the theoretical description of the code. For a detailed study on its capabilities and limitations see Fellhauer et al. (2000) and Klessen and Kroupa (1998).

2.1.1 Method

The code develops three calculations at each time-step that can be schemed as follows,
(i) The density at each grid-cell is calculated from the distribution of N-body particles.
(ii) Using the Poisson equation, the potential is found by developing a Fast Fourier Transform (FFT).
(iii) Once the potential at each point is known, a leap-frog scheme is applied to calculate the changes over velocity and position.

Density array

The first step of the code is to calculate from an input file with the position and velocity of each particle the array of mass densities, denoted as $\rho_{i,j,k}$, where (i, j, k) are the Cartesian coordinates of one grid cell. This is done by using a 'particle-in-cell' method, the simplest one being the NGP (Nearest Grid Point) algorithm. Another alternative would be to use a 'Cloud-in-Cell' method. If the number of N-body particles is large this is not necessary, since the spatial density is smoothed enough. Taking all the particles in the same galaxy with the same mass, $m = M_{gal}/N_{p,gal}$, the density in one grid cell is calculated simply by counting the number of particles in that cell.

Our particle 3D-distribution, $n(\vec{x})$, is taken as

$$n(\vec{x}) = \sum_{\alpha} \delta^3(\vec{x} - \vec{x}_\alpha), \tag{2.1}$$

where each particle is considered as a point of position $\vec{x}_\alpha = (x_\alpha, y_\alpha, z_\alpha)$.
As we explained in the introduction, the NGP ('nearest grid point') is used to calculate the force, so our smoothing kernel, $W(\vec{x}, \Delta\vec{x})$, is simply the 3D top-hat function, $\Pi(\xi)$

$$W(\vec{x}, \Delta\vec{x}) = \Pi(\frac{x}{\Delta x})\Pi(\frac{y}{\Delta y})\Pi(\frac{z}{\Delta z}), \tag{2.2}$$

being $\Delta\vec{x} = (\Delta x_\alpha, \Delta y_\alpha, \Delta z_\alpha)$ the vector of smoothing lengths which is given by the resolution selected for our code, and the function $\Pi(\xi)$ defined as

$$\Pi(\xi) = \begin{cases} 0 & \mid \xi \mid > \frac{1}{2} \\ \frac{1}{2} & \mid \xi \mid = \frac{1}{2} \\ 1 & \mid \xi \mid < \frac{1}{2} \end{cases}$$

Therefore the mass density in the grid is

$$\rho(\vec{x}) = mW \circ n = m \int W(\vec{x} - \vec{x}', \Delta\vec{x}) n(\vec{x}') d^3\vec{x}', \tag{2.3}$$

where m is the particle mass and $\circ$ denotes the convolution operator. Because of the finite resolution, the density is smoothed so that each grid cell has a constant density. Mathematically this can be represented by defining a 'mesh sampled functional' $\rho^\dagger(\vec{x})$ in the three dimensional mesh

$$\rho^\dagger(\vec{x}) = \coprod(\vec{x}) \circ \rho(\vec{x}), \tag{2.4}$$

the 3D operator $\coprod(\vec{x})$ being the 'sampling function'

$$\coprod(\vec{x}) = \sum_{i,j,k=0}^{N} \delta(x - x_{i,j,k})\delta(y - y_{i,j,k})\delta(z - z_{i,j,k}), \tag{2.5}$$

where i, j, k are the indices of grid-cells of centre $\vec{x}_{i,j,k} = (x_{i,j,k}, y_{i,j,k}, z_{i,j,k})$.

Potential calculation

Once we know the density array, the potential in each grid cell, $\Phi_{i,j,k}$, is the addition of the potentials at each grid,

$$\Phi_{i,j,k} = G \sum_{a,b,c=0}^{N-1} \rho_{a,b,c} H_{a-i,b-j,c-k}, \tag{2.6}$$

with $i, j, k = 0, 1, \ldots, N-1$, where N denotes the number of cells for dimension, so $N^3 = N_{gc}$, and $H_{i,j,k}$ is a Green's function.

The Poisson equation is much easier to solve in the Fourier space, so making the transformations,

$$\hat{\rho}_{a,b,c} = \sum_{i,j,k=0}^{N-1} \rho_{i,j,k} \exp\Big(-\sqrt{-1}\frac{2\pi}{\mathrm{N}}(\mathrm{ai} + \mathrm{bj} + \mathrm{ck})\Big) \tag{2.7}$$

$$\hat{H}_{a,b,c} = \sum_{i,j,k=0}^{N-1} H_{i,j,k} \exp\Big(-\sqrt{-1}\frac{2\pi}{\mathrm{N}}(\mathrm{ai} + \mathrm{bj} + \mathrm{ck})\Big),$$

where the symmetry is taken by doing $N = 2^K$, being $K > 0$ an integer. Then this two values are multiplied cell by cell, to know the potential we make the inverse Fourier's transformation

$$\Phi_{i,j,k} = \frac{G}{N^3} \sum_{a,b,c=0}^{N-1} \hat{\rho}_{a,b,c} \hat{H}_{a,b,c} \exp\Big(\sqrt{-1}\frac{2\pi}{\mathrm{N}}(\mathrm{ai} + \mathrm{bj} + \mathrm{ck})\Big). \tag{2.8}$$

This is called the Fast Fourier Transform (FFT) method. The selection of the Green's function is in this formulation

$$H_{i,j,k} = \frac{1}{\sqrt{i^2 + j^2 + k^2}} \tag{2.9}$$
$$H_{000} = \frac{4}{3},$$

with $i, j, k = 1, 2, \ldots, N$. The value of H_{000} is arbitrary, since it accounts for the weighting of the particle self-gravity inside a grid-cell. Numerical test show that the best one for low number of particles per cell is $H_{000} = 1$, while for a big number $H_{000} = 4/3$ is selected. The reason is that the first value excludes the effect of the 'self-gravity' of the particles which can leads to non-physical results (if the particle is not in the centre of the cell, it can feel the acceleration of its own gravity, proportional to the distance to the centre). This problem disappears with the second value of H_{000}, but the energy conservation with time is not so accurate.

Lastly, for the exact solution employing the FFT-algorithm we have to double the number of grids ($2N$) and suppose grids with zero density at the edge of the system, by this we have the next symmetry relationships

$$H_{2n-i,j,k} = H_{2n-i,2n-j,k} = H_{2n-i,j,2n-k} = H_{2n-i,2n-j,2n-k} = \tag{2.10}$$
$$= H_{i,2n-j,2n-k} = H_{i,j,2n-k} = H_{i,j,k},$$

This gives the 3D-potential of our isolated system in the area $i, j, k = 0, 1, \ldots, (\mathrm{N}\text{-}1)$. The low-storage algorithm for the FFT in 3D is taken from Hohl (1970).

In each grid cell we have a value of the mass density, which can be obtained from the functional $\rho^\dagger(\vec{x})$ integrating it spatially (by definition of delta function). These values can be represented as $\rho^\dagger_m = \{\rho_{i,j,k}, i, j, k = 0, 1, \ldots, N\}$. Once we know $\rho^\dagger_m$, the grid potentials $\Phi^\dagger_m = \{\Phi_{i,j,k}, i, j, k = 0, 1, \ldots, N\}$ are calculated by doing a FFT, and directly the mesh sampled functional $\Phi^\dagger(\vec{x}) = \coprod(\vec{x})\Phi(\vec{x})$ again by integrating in an arbitrary volume. The function $\Phi(\vec{x})$ is the smoothed gravitational potential.

The leap-frog scheme

Once the potential is known, one can determine the acceleration at each point of the grid-cell, the orbit integration being easily calculated employing the leap-frog scheme.

In order to find the acceleration of each particle, we have to define the one-dimensional difference operator. It gives the spatial gradients in each Cartesian direction, for the x-direction

$$D_x(x, y, z, \Delta x) = \frac{1}{2\Delta x}\Big\{\delta(x + \Delta x) - \delta(x - \Delta x)\Big\}\delta(y)\delta(z). \tag{2.11}$$

To keep clearer the notation,we keep the analysis in one dimension. The x-component acceleration at first order is

$$a^{(1)}_x(x, y, z, \Delta x) = D_x \circ \Phi(\vec{x}) = \frac{\Phi(x + \Delta x, y, z) - \Phi(x - \Delta x, y, z)}{2\Delta x}. \tag{2.12}$$

The mesh sampled acceleration is known by the action of the sample functional, so $a^{\dagger(1)}_x(x, y, z, \Delta x) = \coprod(\vec{x})a^{(1)}_x(x, y, z, \Delta x)$. Again, integrating over an arbitrary volume we can determine the accelerations in each cell centre, obtaining the set $a^{\dagger(1)}_{m,x} = \{a^{(1)}_{x,i,j,k}, i, j, k = 0, 1, \ldots, N\}$ defined as,

$$a^{(1)}_{x,i,j,k} = \frac{\Phi_{i+1,j,k} - \Phi_{i-1,j,k}}{2\Delta x}, \tag{2.13}$$

where the mesh is constructed so that $2\Delta x = x_{i+1,j,k} - x_{i-1,j,k}$. The calculus in x and y directions is analogous.

The resolution (and therefore the energy and angular momentum conservation) is improved by the calculus of the second order accelerations (for instance in the x-direction) from the grid central points $(x_{i,j,k}, y_{i,j,k}, z_{i,j,k}) \equiv (x, y, z)$,

$$a_x^{(2)}(x+dx, y+dy, z+dz) = a_x^{(2)}(x,y,z) + \frac{\partial a_x}{\partial x}(x,y,z)dx + \frac{\partial a_x}{\partial y}(x,y,z)dy + \frac{\partial a_x}{\partial z}(x,y,z)dz + O(d\vec{x}^2), \tag{2.14}$$

where we have defined the offset to the centre of the grid

$$\begin{aligned} dx &= x - x_{i,j,k} < \frac{\Delta x}{2} \\ dy &= y - y_{i,j,k} < \frac{\Delta y}{2} \\ dz &= z - z_{i,j,k} < \frac{\Delta z}{2}. \end{aligned} \tag{2.15}$$

At this point, one has to remain in mind the difference between the mesh spacing $\Delta\vec{x}$ and the quantities $d\vec{x}$, the first are given by the resolution of the code, meanwhile the second are defined in each grid cell in order to a better computation of the acceleration. In fact, this freedom on the choice of the values of $d\vec{x}$ will be used to calculate the acceleration inside the grid cell. This scheme avoids the discontinuities present on the force calculation.

In the new scheme the resolution is not as important as the one defined before because the goodness of the force calculation depends directly on $d\vec{x}$ (which is related to the mesh spacing $\Delta\vec{x}$ in the sense that larger mesh spacing implies larger interpolation ranges and, therefore, poorer calculation). If we take $d\vec{x}$ as the distances of the particles to the centre of the grid cell, then the error of the acceleration is approximately $< dx^2 + dy^2 + dz^2 >$, i.e the squared averaged distance of all the cell particles to the cell centre, whereas in the old scheme the error is the mesh spacing $\Delta\vec{x}$.

Following the development of our scheme, the next step is to calculate the accelerations in terms of the grid potential. For that we can approach the divergences as differences at first order

$$\begin{aligned} a_x^{(2)}(x,y,z,\Delta x) &= \frac{\partial\Phi}{\partial x}(x,y,z,\Delta x) \equiv D_x\Phi \\ \frac{\partial a_x}{\partial x}(\vec{x},\Delta\vec{x}) &= \frac{\partial^2\Phi}{\partial x^2}(\vec{x},\Delta\vec{x}) \equiv D_{xx}\Phi \\ \frac{\partial a_x}{\partial y}(\vec{x},\Delta\vec{x}) &= \frac{\partial^2\Phi}{\partial x\partial y}(\vec{x},\Delta\vec{x}) \equiv D_{xy}\Phi \\ \frac{\partial a_x}{\partial z}(\vec{x},\Delta\vec{x}) &= \frac{\partial^2\Phi}{\partial x\partial z}(\vec{x},\Delta\vec{x}) \equiv D_{xz}\Phi. \end{aligned} \tag{2.16}$$

The values of the acceleration in each grid cell, for that we only have to use the mesh sampled operator to know the sampled acceleration $a_x^{\dagger(2)} = \coprod(\vec{x})a_x^{(2)}$, and then integrate this function over an arbitrary volume to obtain a set of acceleration values $a_{m,x}^{\dagger(2)} = \{a_{x,i,j,k}^{(2)}, i,j,k = 0,1,\ldots,N\}$ defined as

$$\begin{aligned} a_{i,j,k,x}^{(2)}(d\vec{x}) = &\frac{\Phi_{i+1,j,k} - \Phi_{i-1,j,k}}{2\Delta} + \frac{\Phi_{i+1,j,k} + \Phi_{i-1,j,k} - 2\Phi_{i,j,k}}{(\Delta x)^2}dx \\ &+ \frac{\Phi_{i+1,j+1,k} - \Phi_{i-1,j+1,k} + \Phi_{i-1,j-1,k} - \Phi_{i+1,j-1,k}}{4\Delta x\Delta y}dy \\ &+ \frac{\Phi_{i+1,j,k+1} - \Phi_{i-1,j,k+1} + \Phi_{i-1,j,k-1} - \Phi_{i+1,j,k-1}}{4\Delta x\Delta z}dz. \end{aligned} \tag{2.17}$$

The treatment in y and z directions is analogous.
Once we know the acceleration for each particle one has to integrate the motion equation in time.

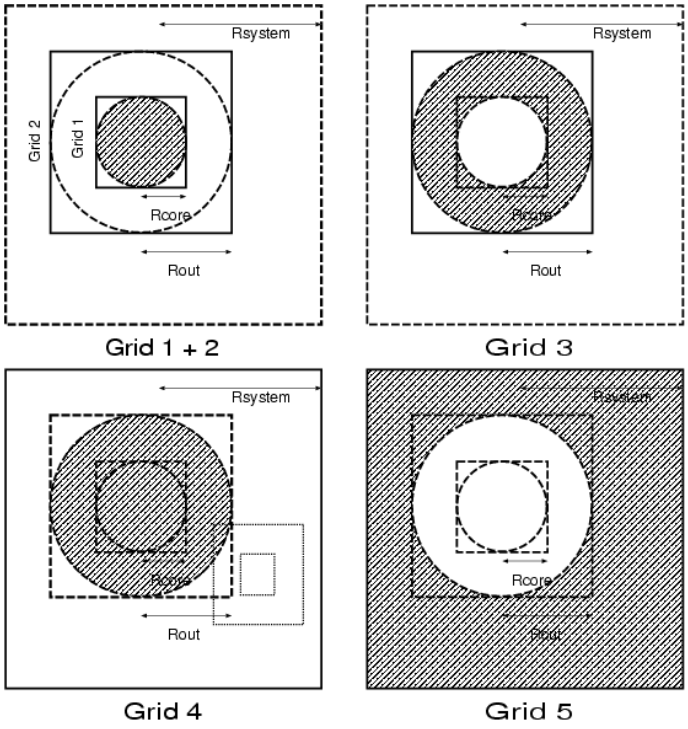

Figure 2.1: The five grids in SUPERBOX. Solid lines denote the particular grid. The particles are counted in the shaded areas. In the grid 4 we plot an hypothetical grid for a second galaxy

This is done in the simplest way, following the so called 'leap-frog scheme'. To give an example, we can imagine the l-particle in the position x with velocity in the x-direction which feels an acceleration the x-component, then the integration of its orbit in the time step $n+1$ is

$$v_{x,l}^{n+1/2} = v_{x,l}^{n-1/2} + a_{x,l}^{n}\Delta t \tag{2.18}$$

$$x_{l}^{n+1} = x_{l}^{n} + v_{x,l}^{n+1/2}\Delta t, \tag{2.19}$$

where Δt is the time step. As we can see, in the leap-frog scheme the position and accelerations are calculated in each n time step , while the velocities are interpolated between two time steps. This kind of time integration is very sensible in the choice of Δt so we have to be careful in taking this value small enough to get a good conservation of energy and momentum. Generally the time step is compared with the 'crossing time' of the system (t_{cross}), taking $\Delta t \sim 0.02 t_{cross}$.

2.1.2 The grids

SUPERBOX is structured in the following way: For each galaxy there are 5 grids with 3 different resolution, so that the potential felt by one particle is the sum of the potentials calculated in each grid. The grid structure is plotted in Fig. 2.1. These scheme allows us to resolve zones where a big concentration of particles is present, for instance the core of a galaxy or globular cluster, by using poorer resolution where we don not need it.

The grids are as follows:

- Grid 1 gives the highest resolution. In our simulations this grid covers 3 scale lengths of our exponential disc. As we can see i the figure, its length is $2R_{\rm core}$. All the particles with $r \leq R_{\rm core}$ produce the potential of this most inner grid.

- Grid 2 has an intermediate resolution. Its length is $2R_{\rm out}$, but the particles which are used to compute the density, and therefore the potential, are also the particles stored in grid 1.

- Grid 3 has just the same size and resolution as grid 2, but here we store the particles with $R_{\rm core} \leq r \leq R_{\rm out}$.
- Grid 4. contains the whole system. All the particles with $r \leq R_{\rm out}$ are included. This grid has the lowest resolution.
- Grid 5 stores the particles that scape from the system ,i.e $r \leq R_{\rm out}$. This grid has the same resolution and size as the grid 4.

All the grids have the same number of cells per dimension, N. However we need four grids to give the boundary condition $\rho = 0$ necessary for the Fourier transformations, so in fact there are $N - 4$ active cells per dimension in each grid.

Since the potential is additive, we can combine the different grid potentials for each particle depending on its position:

$$\Phi(r) = [\theta(R_{\rm core} - r)\Phi_1 + \theta(r - R_{\rm core})\Phi_2 + \Phi_3]\theta(R_{\rm out} - r) + \theta(r - R_{\rm out})\Phi_4 + \Phi_5, \qquad (2.20)$$

where $\theta(\xi) = 1$ for $\xi > 0$ and $\theta(\xi) = 0$ otherwise. The suffix of $\Phi_i, i = 1, \ldots, 5$ denotes the grid in which the potential is calculated. In this context this means that

- Particles with $r \leq R_{\rm core}$ feel the potentials form the grids 1,3 and 5 in order to calculate the acceleration.
- Particles in the range $R_{\rm core} \leq r \leq R_{\rm out}$ feel the potential from grids 2,3 and 5.
- Finally, the acceleration of the particles with $r > R_{\rm out}$ is calculated from the potential of the grids 4 and 5.
- Particles with $r > R_{\rm system}$ are removed.

We should note that, the gain of resolution in zones with high density also entails the presence of the discontinuities at the grid boundaries. This problem is usually avoided by selecting the grid sizes corresponding to points of low density gradient.

2.2 Building up the initial conditions

[1]The scheme used to construct the initial galaxy model follows that proposed by Hernquist (1993). This method builds up the different subsystems which form the galaxy (namely, the disc bulge and halo) so that the out-coming galaxy is formed in nearly dynamical equilibrium. Obviously, this approach have the advantage over the Barnes' (1988) of a resulting system closer to the sought equilibrium.

In practice, the Hernquist's scheme has been shown to be a powerful method when embedding the disc in a galaxy where the components have spherical morphology. However, if the purpose is to construct a spiral galaxy with axi-symmetric haloes (or bulges), the CPU-time required for the operation increases up to prohibitive times, scaling as N^2, where N is the number of N-body particles, mainly due to the computation of the velocity dispersions in the three-directions.

A possible solution has been found by Boily, Kroupa & Peñarrubia (2001). This method approximates the equilibrium state, which one would obtain from the integration of the Boltzmann equations in axi-symmetric systems, by transforming the spherical solution into two dimensions. For such a purpose, we use the potential iso-contours, the multi-component galaxy being constructed by perturbing the velocity field of the individual component, with its subsequent adaptation to the background potential (axi-symmetric). The time required is, therefore, as for the spherical system.

In this Section, we present briefly the basis of this scheme (for a detailed discussion together with the analysis of the stability of the resulting systems see Boily,Kroupa & Peñarrubia 2001).

[1] *Section based on:* Boily, Kroupa & Peñarrubia (2001)

2.2.1 Method

The basic steps of the method consists in building an oblate system from a transformations of the spherical symmetric equilibria. The key point is that, if we consider as given the mass profile of the galaxy, it is then sufficient to construct the velocity field to match the gravity. So that, we perform the following steps:
(i) Given the desired spatial anisotropy $e^2 = 1 - c^2/a^2$, where a, c are the major and minor axis lengths, respectively, we carry out the homologous transformation $(R, z) \rightarrow (R', z') = (R, z \cdot \sqrt{1-e^2})$.
(ii) The velocity anisotropy e_v is calculated from e and the galaxy potential. As in (i) a homologous transformation is performed, additionally we impose the virial condition so that the transformed system is nearly in equilibrium.

The velocity anisotropy. Homogeneous system

Let's consider a homogeneous ellipsoid with ellipticity. The potential of the homogeneous and oblate system can be calculated as sum of similar shells (BT), giving for the axisymmetric case

$$\Phi(\vec{x}_{int}) = -\pi G\rho[I(e)a^2 - A_R(e)R^2 - A_z(e)z^2], \tag{2.21}$$

where

$$\begin{aligned} I(e) &= 2\frac{\sqrt{1-e^2}}{e}\text{arcsin(e)} \\ A_R(e) &= \frac{\sqrt{1-e^2}}{e^2}\left[\frac{\text{arcsin(e)}}{e} - \sqrt{1-e^2}\right] \\ A_z(e) &= 2\frac{\sqrt{1-e^2}}{e^2}\left[\frac{1}{\sqrt{1-e^2}} - \frac{\text{arcsin(e)}}{e}\right]. \end{aligned} \tag{2.22}$$

These values remain constant in the inner part of the homogeneous oblate and accomplish that $A_z \geq A_R$.

The equations of motion of a single star within a given potential are

$$\ddot{x}_i = \nabla_i \Phi. \tag{2.23}$$

The velocity anisotropy of the star, e_v, can be connected to the galaxy potential by averaging the squared velocity components in the vertical and planar directions (defined from the potential axi-symmetry plane) over one orbit so that

$$\frac{< v_z^2 >}{< v_R^2 >} = \frac{A_z < z^2 >}{A_R < R^2 >} = \frac{A_z}{A_R}(1-e^2) \equiv 1 - e_v^2, \tag{2.24}$$

whereas for homogeneous systems the potential anisotropy e_Φ can be calculated analytically from the iso-contour lines

$$e_\Phi^2 = 1 - \left[\frac{z^2}{R^2}\right]_\Phi^2 = 1 - \frac{A_R}{A_z}. \tag{2.25}$$

Combining these last two equations, one finds that the anisotropy of the velocity ellipsoid is

$$e_v = \left[\frac{e^2 - e_\Phi^2}{1 - e_\Phi^2}\right]^{1/2}. \tag{2.26}$$

Therefore, since the three ellipticities satisfy $e_\Phi < e_v < e$, the velocity ellipsoid is never as flat as the mass distribution that gives rise to it.

The velocity anisotropy. Inhomogeneous system

The applications of this equation is actually limited since the galaxies are formed by peak density profiles. In this case, the potential does not usually have an analytic form. However, if we assume that most of the mass for such systems is concentrated in the inner regions, one can expand the resulting potential in harmonic series, this approximation being valid when the orbit avoids the inner part of the galaxy. This expansion can be written as (Goldstein 1980)

$$\Phi(r,\theta) = -\frac{GM_0}{r} + \frac{GM_0}{2r^3}(I_z - I_R)P_2(\cos\theta) + \mathcal{O}\left(\frac{a}{r}\right)^4, \tag{2.27}$$

where $\tan\theta = z/R$, $P_n(x)$ is a Legendre polynomial and M_0 the mass within r. The value a denotes the major axis of the ellipsoid. The quantities I_i denote the eigen-components of the inertia tensor per unit mass, defined as

$$I_i \equiv \int \rho(r)(r^2 - x_i^2)d^3r.$$

Supposing that $e = \text{const}$, the moments of inertia are constant. Thus for $r >> a > c$ the quadrupole, and therefore e_Φ, tends to zero as a/r^3, the velocity anisotropy approaches to $e_v = e$.

A realistic mass distribution in equilibria will have a value of e_v between a homogeneous and point mass distributions. From the potential expansion, the interpolated value between these two possibilities is chosen as

$$e_v^2 = e_\Phi^2 + (e^2 - e_\Phi^2)\sqrt{1 - \frac{< r^2 >}{r_g^2}}, \tag{2.28}$$

where e_Φ is numerically calculated from the potential iso-contours. This approximation has been shown by Boily, Kroupa & Peñarrubia (2001) to yield to adequate equilibria. This condition assurances that the velocity ellipticity is the same for all the particles with equal binding energy, so that if the "star" is located at some radius r (in spherical coordinates), the value $< r^2 >$ denotes the averaged squared radius inside the volume $4\pi r_g^3/3$, where r_g is defined,

$$r_g = \frac{GM}{-W},$$

M being the mass enclosed within r and,

$$W = 2\pi \int_0^r \rho(x)\Phi(x)x^2 dx,$$

is the *binding energy* at r.

We should note that the interpolated function of e_v yields to velocity ellipsoids that accomplish,

$$e_v \simeq e,$$

for a large set of density profiles.

The spherical symmetric velocity distribution

If the velocity distribution is isotropic, the velocity ellipsoid accomplishes that $\overline{v_r^2} = \overline{v_\phi^2} = \overline{v_\theta^2}$. From the Jeans equations in spherical coordinates (BT, eq. 4-27)

$$\overline{v_r^2} = \frac{1}{\rho(r)}\int_r^\infty \rho(r)\frac{d\Phi}{dr}dr = \frac{1}{\rho(r)}\int_r^\infty \rho(r)\frac{GM(r)}{r^2}dr, \tag{2.29}$$

Φ being the potential and $M(r)$ the total mass inside r. Assuming isotropy, the velocity components are subsequently converted to Cartesian coordinates.

We assume that the velocity distribution can be locally described by a Maxwellian form

$$F(\mathbf{v}) = \left(\frac{1}{2\pi\overline{v_r^2}}\right)^{3/2} \exp\left(\frac{-v^2}{2\overline{v_r^2}}\right) \exp\left(\frac{v_{\rm esc}^2}{2\overline{v_r^2}}\right), \tag{2.30}$$

where v is the velocity of one halo particle and $\overline{v_r^2}$ is the one-dimensional velocity dispersion in the radial direction (using the same notation as BT). In practice all bound particles have velocities below the local escape velocity $v_{\rm esc} \equiv \sqrt{-2\Phi(r)}$, which effectively sets an upper limit for v in eq. (2.30). This condition needs from a proper renormalisation, which is done by imposing,

$$\overline{v^2} = 3\sigma(r)^2,$$

where σ is the one-dimensional velocity dispersion at r and $\sigma^2 = \overline{v_r^2}$ for non-rotating systems.

From spheres to axi-symmetry

Given the spherical morphologies of the mass distribution and the potential, one can perform an homologous transformation

$$(R, z) \rightarrow (R', z') \text{ where } R' = R,\ z' = z\sqrt{1-e^2}. \tag{2.31}$$

Once the spherical system is transformed into a axi-symmetric one, we make use of the virial theorem to find the modification of the velocity field, which tellx us that the potential energy of the star after the coordinate transformation should be invested in kinetic energy, thus, for each particle

$$T_i = E_i - \Phi(r_i) \rightarrow T_i' = T_i + \frac{\Phi(r_i) - \Phi_{\rm obl}(R_i, z_i)}{2}, \tag{2.32}$$

where the subfix "obl" denotes the potential of the ellipsoidal system.

The velocity transformation of the particle i that satisfies the virial condition and follows eq. (2.28) is

$$\mathbf{v}_i' = \left[\frac{2T_i'}{2T_i - v_z^2 e_v^2}\right]^{1/2} \times (v_x, v_y, v_z\sqrt{1-e_v^2}), \tag{2.33}$$

the quantities $< r^2 >$ and r_g calculated prior the transformation (2.31).

It is evident that this transformation scales linearly with the number of particles, whereas the Hernquist schemed has a CPU dependence scaling as N^2. The resulting systems were found to yield to adequate equilibria for a large set of models and parameters even for highly flattened systems.

This new method allows us to construct galaxy models with number of particles as high as $N = 1.4\ 10^6, 1.2\ 10^7$ for the high resolution investigation of satellite decay in flattened haloes.

2.2.2 Setting the galaxy in equilibrium

The galaxy system is constructed near the equilibrium state. However, due to the different force resolutions existing between the build-in code and SUPERBOX, before injecting the satellite the system shall be evolved for a few dynamical times until it settles in equilibrium. If the resolution is not too poor, the resulting density profile must nearly trace the initial one.

In Fig. 2.2 we plot the comparison of the analytic density profile of the model H1 (see Chapter 6) and the numerical outputs from our code before and after integrating the galaxy one dynamical time[2]. The results show a contraction of the inner shells and the respective expansion of the outer

[2] The system is considered in equilibrium when the Lagrange radii (defined as the radius at which the spherically enclosed mass amounts to 10, 20..90 % of the total mass) show small evolution.

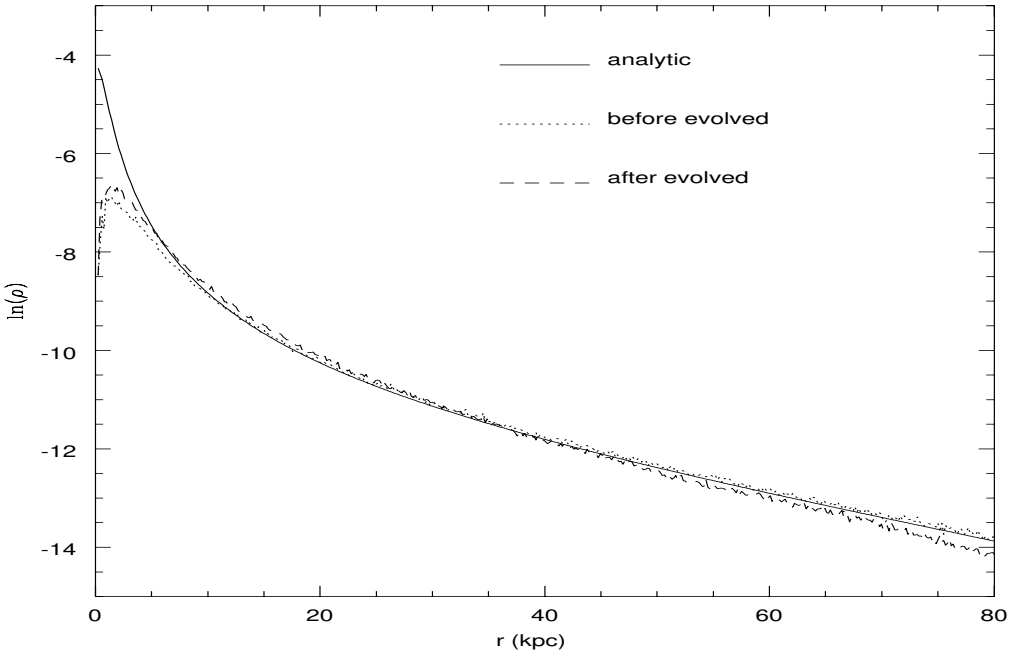

Figure 2.2: Comparison between the density profile after and before integrating it one dynamical time. The solid curve represent the analytic profile. We use the galaxy model H1 (see Chapter 6).

ones which, in any case, is not higher than 5%. More worrying is the lack of resolution at the most inner part of the galaxy ($r < 5$ kpc), which may induce an underestimation of dynamical friction at late-times of the satellite orbit.

Once that the galaxy and satellite systems are virialized, the satellite is injected with an initial velocity and position which determines the orbital parameters.

2.3 Satellite mass loss

The action of tidal forces induce a satellite mass loss along its evolution. The satellite mass plays an important role in order to determine the ultimate face of its evolution and survival. The scheme employed is widely used by several authors to describe the satellite mass evolution (see e.g., Velázquez & White (1999), hereinafter VW, Klessen & Kroupa 1998).

The mass remaining bound to the satellite, $M_s(t)$, is known by computing the potential energy $\Phi_i < 0$ of each satellite particle presumed bound to the satellite, and its kinetic energy (T_i) in the satellite frame. Following PKB, particles with $E_i = m_s T_i + m_s(\Phi_i + \Phi_{\rm ext}) > 0$ are labelled unbound, where m_s is the mass of one satellite particle and the potentials

$$\Phi_i = -\sum_{i \neq j} \frac{G m_s}{\sqrt{|r_i - r_j|^2 + \epsilon^2}} \qquad (2.34)$$
$$\Phi_{\rm ext} = |\Phi_g(r_s)|,$$

the softening being $\epsilon = 0.1 = 0.35$ kpc, which is the resolution of the inner grid focused on the satellite centre-of-density r_s, and Φ_g the galaxy potential at this point, where the tidal contribution is neglected. All the particles of the satellite are thus assumed to feel the same external potential, which is an useful and sufficiently accurate approximation, taking into account that most of the bound particles are located very close to this point.

Particles with $E_i > 0$ are removed and the procedure repeated until only negative energy particles are left.

The mass is calculated each $\Delta t = 0.312$ Gyr, so that the semi-analytic code interpolates the value for intermediate points at each time-step. The error is of the order of $\Delta M(t)/\Delta t$, going linearly with the mass loss. This means that the interpolation might introduce not negligible differences at times where the mass loss is significant (i.e late times of the satellite evolution).

Chapter 3

Galaxy and satellite models. SUPERBOX parameters

Along our studies we compare the results from the semi-analytic code to those found from the N-body computations of Peñarrubia, Kroupa & Boily (2001), hereinafter PKB. The models employed to describe the galaxy mass distribution are, therefore, the same. A subset of our spherical models are similar to the models of VW, which facilitates an inter-comparison of different numerical treatments.
In this Chapter we provide the density profile of the galaxy and satellite models employed in our investigation as well as the analytic expressions of gravitational force and velocity dispersion that correspond to each mass profile.

The N-body parameters are summarised in last Section. Due to the strong dependence of these parameters on the galaxy and satellite models, we decide to outline them here and not in Chapter 2.

3.1 Parent galaxy model

The galaxy is composed by disc, bulge and a Dark Matter halo. The total contribution of the galaxy field to the force experienced by the satellite is

$$\mathbf{F}_g = \mathbf{F}_d + \mathbf{F}_b + \mathbf{F}_h.$$

3.1.1 Dark Matter Halo (DMH)

We use a flattened non-singular isothermal profile to describe the Dark Matter Halo. Although, in principle, the exact profile of the DMH remains unknown, the observational rotational curves imply that the haloes can be described by isothermal systems. For simplicity, following the scheme developed by Hernquist (1993), the mass profile of the halo is taken as

$$\begin{aligned}\rho_h(R,z) &= \frac{M_h\alpha}{2\pi^{3/2}r_{\rm cut}}\exp\Big[-\frac{1}{r_{\rm cut}^2}\big(R^2+\frac{z^2}{1-e^2}\big)\Big] \\ &\quad\times\frac{1}{R^2+z^2/(1-e^2)+\gamma^2} \\ &\equiv \frac{M_h\alpha}{2\pi^{3/2}r_{\rm cut}}\exp\Big[-\frac{m_0^2}{r_{\rm cut}^2}\Big]\frac{1}{m_0^2+\gamma^2},\end{aligned} \tag{3.1}$$

where

$$m_0^2 = R^2+\frac{z^2}{1-e^2}, \tag{3.2}$$

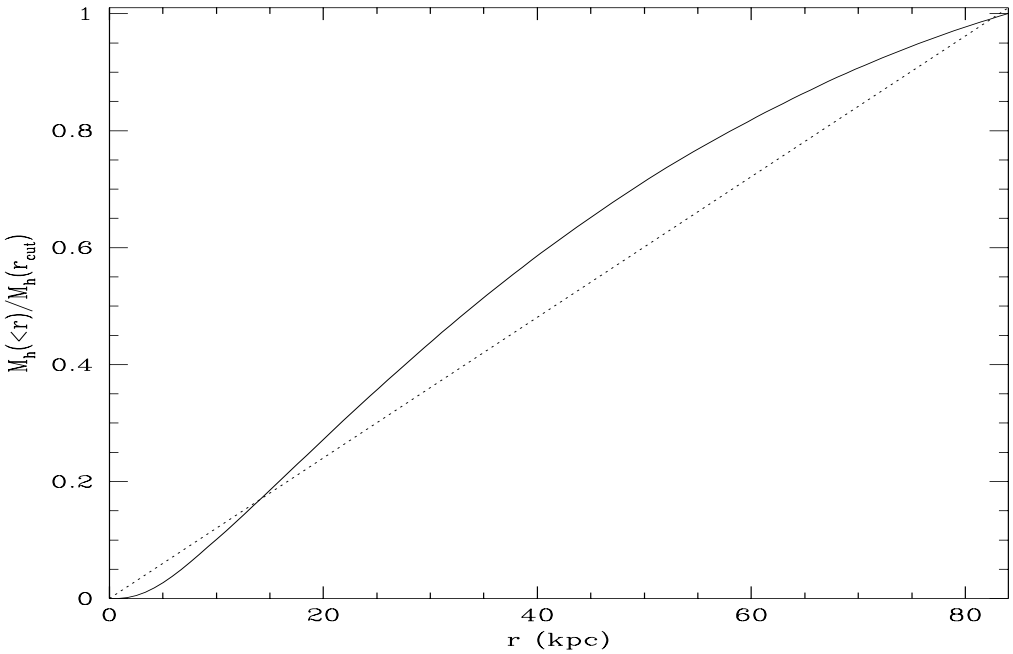

Figure 3.1: Mass distribution of the halo model H1. The dotted line represents the corresponding profile of a singular isothermal sphere with the same mass at $r_{\rm cut}$.

and M_h being the DMH mass, $r_{\rm cut}$ the cut-off radius, $e^2 = 1 - q_h^2$ the eccentricity, q_h the halo axis-ratio and γ its core-radius. The normalisation constant α can be simplified,

$$\alpha \equiv \{1 - \sqrt{\pi}\beta \exp(\beta^2)[1 - \mathrm{erf}(\beta)]\}^{-1} = 1 + \sqrt{\pi}\beta + (\pi - 2)\beta^2 + O(\beta^3), \tag{3.3}$$

where $\beta = \gamma / r_{\rm cut} \simeq 1/24$ in our calculations. For $\beta = 1/24$ we find $\alpha \simeq 1.076 \rightarrow 1$ already and hence thereafter we set $\alpha = 1$ in our analysis.

This density profile leads to the mass distribution plotted in Fig. 3.1, where we make use of the halo parameters of the model H1 (see Table 3.1).

The force from this density distribution is derived following Chandrasekhar (1960)

$$\begin{aligned} F_{h,i} &= -2\pi M_s G x_i \int_0^\infty \frac{du}{(1+u)^2(1+e^2+u)^{1/2}} \rho_h[m^2(u)] \\ F_{h,z} &= -2\pi M_s G z \int_0^\infty \frac{du}{(1+u)(1+e^2+u)^{3/2}} \rho_h[m^2(u)], \end{aligned} \tag{3.4}$$

where $x_i = x, y$ and,

$$m^2(u) = \frac{R^2}{1+u} + \frac{z^2}{1-e^2+u}. \tag{3.5}$$

The velocity distribution of this system can be described by a Gaussian with velocity dispersions calculated from the Jeans equations (see e.g BT) and the mass distribution (3.1). In a system with axi-symmetry, the velocity dispersion ellipsoid has two components (σ_R, σ_z), i.e the parallel and perpendicular velocity dispersions with respect to the plane of axi-symmetry, respectively.

The solutions of the Jeans equations with spherical symmetry are obtained by means of the method proposed by Boily, Kroupa & Peñarrubia (2001). The 1D velocity dispersion is calculated

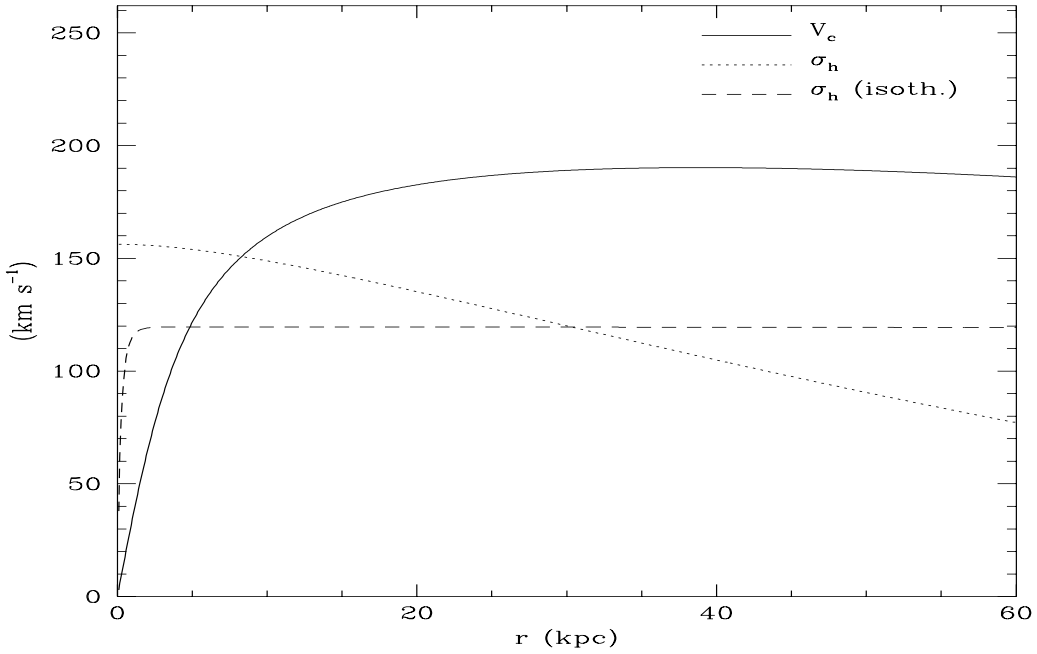

Figure 3.2: Circular velocity and velocity dispersion curves of our halo H1. It is also plotted the velocity dispersion for a singular isothermal sphere of the same enclosed mass at $r_{\rm cut}$.

for a spherical system as

$$\sigma^2 = -\frac{1}{\rho_h}\int \rho_h(r')\frac{d\Phi_h(r')}{dr'}dr' \tag{3.6}$$
$$= \frac{r^2+\gamma^2}{\exp(-r^2/r_{\rm cut}^2)}\int_r^\infty \frac{\exp(-r'^2/r_{\rm cut}^2)}{r'^2+\gamma^2}\frac{GM_h(r')}{r'^2}dr',$$

The profile of such a function is plotted in Fig. 3.2 for the parameters corresponding to the halo model H1, together with the circular velocity curve. We also include the velocity dispersion for a singular isothermal sphere with the same mass at the cut-off radius.

The perpendicular and parallel components are, respectively

$$\sigma_R = \sigma \tag{3.7}$$
$$\sigma_z = \sigma\sqrt{1-e_v^2},$$

the velocity anisotropy $e_v^2 = 1 - q_v^2$ being calculated as

$$e_v^2(r) = e_\Phi^2 + (e^2 - e_\Phi^2)\sqrt{1 - \frac{< r^2 >}{r^2}}, \tag{3.8}$$

where e_Φ, e are the potential and mass eccentricity at r, respectively, and $< r^2 >$ is the mass-weighted average of r^2 inside the volume $4\pi r^3/3$. This method was found to yield systems with adequate numerical equilibria (see Boily, Kroupa & Peñarrubia 2001 for a detailed explanation). We note that for a singular isothermal system formed by ellipsoids of constant eccentricity, one can readily check that $< r^2 >= r^2$, therefore, having that $e_v = e_\Phi = e$. In our case, the density profile is not singular but $\gamma/r_{\rm cut} = 1/24$, so that $< r^2 > \simeq r^2$, as it is shown in Boily, Kroupa & Peñarrubia (2001).

3.1.2 Disc

Observations of the Milky Way and other spiral galaxies suggest that the disc can be reproduced by a exponential density profile in the axi-symmetry direction (Freeman 1970) and isothermal sheets in the vertical direction (Bahcall & Soneira 1980, Spitzer 1942), therefore, the disc mass distribution being

$$\rho_d(R,z) = \frac{M_d}{4\pi R_d^2 z_0}\exp(-\mathrm{R}/\mathrm{R_d})\mathrm{sech}^2(\mathrm{z}/\mathrm{z_0}), \tag{3.9}$$

M_d being the disc mass, z_0 the vertical thickness and R_d the exponential scale length in the radial direction. The mass profile decays exponentially with R and is composed of isothermal sheets along the vertical direction. Velocities are assumed to have a Gaußian distribution. The square of the radial velocity dispersion is taken to be proportional to the surface density (see Lewis & Freeman 1989), $\overline{v_R^2} \propto \Sigma(R) = \Sigma(0)\exp(-\mathrm{R}/\mathrm{R_d})$, where the constant of proportionality is determined by fixing Toomre's Q-parameter at the Solar radius. Following VW, we select $Q_\odot = Q(R_\odot) = 1.5$. The vertical component of the velocity ellipsoid is $\overline{v_z^2} = \pi G\Sigma(R)z_0$ in agreement with an isothermal sheet (Spitzer 1942). The azimuthal component is obtained from the epicyclic approximation $\sigma_\phi^2 = \overline{v_R^2}\kappa^2/(4\Omega^2)$ (e.g. BT).

Since, (i) the mass of the disc is $\approx 7\%$ of the halo and (ii) the anisotropy of the disc potential can be neglected at distances where the satellite orbits, we calculate it simply as

$$\mathbf{F}_d = -\frac{GM_d(r'<r)\mathbf{r}}{r^3}. \tag{3.10}$$

Note that this equation neglects the potential quadrupole, which is an accurate approximation in the range of distances where the satellite moves, since eq. (2.27) shows that this term goes as $1/r^3$. In practice, the potential quadrupole can induce significant effects if the satellite is located at $r \leq R_d$. However, we stop our calculations at that point.

To compute the disc velocities, we have made use of the epicycle approximation (BT) where

$$V_{c,d}^2 = R^2\Omega^2(R) = R\left(\frac{\partial\Phi_g}{\partial R}\right)_{z=0}, \tag{3.11}$$

$\Omega(R)$ being the circular frequency and $\Phi_g = \Phi_d + \Phi_h + \Phi_b$ the galaxy potential. The disc potential is

$$\Phi_d = -\frac{GM_d(r'<r)}{r}, \tag{3.12}$$

and the velocity dispersions for our disc model

$$\begin{aligned}\sigma_{d,R}^2(R) &= \sigma_{d,R}^2(0)\exp(-R/R_d) \\ \sigma_{d,z}^2(R) &= \pi G\Sigma(R)z_0 \\ \sigma_{d,\phi}^2(R) &= \sigma_{d,R}^2\kappa^2/(4\Omega^2),\end{aligned} \tag{3.13}$$

where $\kappa^2 = \partial^2\Phi_d/\partial R^2 - 3\Omega^2$ is the epicycle frequency. Along our calculi, we approximate $\sigma_d \approx \sigma_{d,\phi}$, with $\sigma_R(0) = 100$ km/s (Lewis & Freeman 1989).

We have to note that, differently to TB, we have chosen to fix our disc parameters as those at $t = 0$, i.e, without evolution. In this way, we avoid a parameter dependence on the disc evolution which, in fact, is extremely complicated and goes further our study.

3.1.3 Bulge

For the bulge we adopt the spherical Hernquist profile (Hernquist 1990)

$$\rho_b = \frac{M_b}{2\pi}\frac{a}{r(r+a)^3}, \tag{3.14}$$

where M_b is the bulge mass and a the spherical scale length. This analytical profile fits the de Vaucouleurs law (de Vaucouleurs 1948).

The force induced by the bulge being

$$\mathbf{F}_b = -\frac{GM_b}{(r+a)^2}\mathbf{e}_r, \tag{3.15}$$

where $\mathbf{e}_r$ is the unity vector in the radial direction.

The velocity dispersion, as obtained from the Jeans equations, follows the expression (Hernquist 1990)

$$\sigma_b^2 \equiv \bar{v_r^2} = \frac{GM_b}{12a}\left\{\frac{12r(r+a)^3}{a^4}\ln\left(\frac{r+a}{r}\right) - \right. \tag{3.16}$$
$$\left.\frac{r}{r+a}\left[25+52\frac{r}{a}+42\left(\frac{r}{a}\right)^2+12\left(\frac{r}{a}\right)^3\right]\right\}.$$

3.1.4 Galaxy parameters

Our system of units is such that $M_d = R_d = 1$ and $G = 1$. According to Bahcall, Smith & Soneira (1982), $M_d = 5.6 \times 10^{10} M_\odot$ and $R_d = 3.5$ kpc for the Milky Way which we adopt as a typical primary galaxy model, so that time and velocity units are, respectively, 1.3×10^7 yr and $262\,\mathrm{kms}^{-1}$. The half-mass radius of the disc is located at $R_{0.5} \sim 1.7R_d = 5.95$ kpc, with a rotation period of 13 time units.

For our N-body investigations we make use of 6 different galaxy models, which can be separated in two groups: Models G (from "galaxy") and models H (from "halo"). Whereas the former include disc, bulge and halo as outlined above, in the later we consider the galaxy as a pure halo by removing the disc and bulge components. Therefore our notation implies Gn = disc + bulge + Hn, where $n = 1, ..., 5$.

In Table 3.1 we present the galaxy parameters used in the N-body and semi-analytic calculations (note that the "number of particles" is only useful for N-body simulations).

3.1.5 Remarks

As VW point out, there are some caveats to keep in mind concerning the above models: (i) The DMHs are possibly too small in mass and extension. Zaritsky & White (1994) show, by studying satellite orbits in the Local Group and external galaxies, that DMH limits may extend beyond 200 kpc with masses over $2 \times 10^{12}\mathrm{M}_\odot$. However, as VW comment, the velocity curves of our DMHs G1 and G2 are consistent with the largest velocities observed for stars in the solar neighbourhood (Carney & Lathman 1987), and they are possibly massive enough to give realistic velocities of satellites on eccentric orbits. (ii) The DMHs may be too concentrated. Persic, Salucci & Stel (1996) argue for a DMH core radius of $\gamma = (1 \to 2) \times R_{\rm opt}$, $R_{\rm opt} = 3.2\,R_d$, where R_d is the disc scale-length. However the DMH parameters were selected to avoid bar formation in the disc. We observed that a less concentrated DMH or bulge allows a stable disc to form a bar after few satellite passages. With our γ, the presence of a bar is avoided at least until the destruction of the satellite.

3.2 Satellite model

Following PKB and VW, we select King models (King 1966) with concentration $c = \log(rt/rc) = 0.8$, where r_c and r_t are the core and "tidal" radii, respectively. Central potential and concentration are related, any of them parametrising the model, so that $c = 0.8 \to \Psi(0) = 5\sigma^2$, where σ is the one-dimensional velocity dispersion.

For comparison between our semi-analytical code and N-body simulations it is necessary to include the satellite mass loss which, of course, depends on the satellite profile. The King profiles

	Symbol	Value(ph.u)	Value (m.u)
Disc	N_d	100000	
	M_d	$5.60 \times 10^{10}\mathrm{M}_\odot$	1.00
	R_d	3.50 kpc	1.00
	z_0	1.40 kpc	0.40
	$Q_\odot$	1.50	1.50
	$R_\odot$	8.50 kpc	2.43
Bulge	N_b	33328	
	M_b	$1.87 \times 10^{10}\mathrm{M}_\odot$	1/3
	a	0.53 kpc	0.15
DMH (H1) (spherical)	N_h	1400000	
	M_h	$7.84 \times 10^{11}\mathrm{M}_\odot$	14.00
	γ	3.50 kpc	1.00
	q_h	1.00	1.00
	r_{cut}	84.00 kpc	24.00
DMH (H2) (oblate)	N_h	1400000	
	M_h	$7.84 \times 10^{11}\mathrm{M}_\odot$	14.00
	q_h	0.60	0.60
	γ_a	3.80 kpc	1.10
	γ_c	2.28 kpc	0.65
	r_{cut}	84.00 kpc	24.00
DMH (H3) (spherical)	N_h	1400000	
	M_h	$7.84 \times 10^{11}\mathrm{M}_\odot$	14.00
	γ	3.50 kpc	1.00
	q_h	1.00	1.00
	r_{cut}	133.00 kpc	38.00
DMH (H4) (oblate)	N_h	1400000	
	M_h	$7.84 \times 10^{11}\mathrm{M}_\odot$	14.00
	q_h	0.60	0.60
	γ_a	3.80 kpc	1.10
	γ_c	2.28 kpc	0.65
	r_{cut}	133.00 kpc	38.00
DMH (H5) (oblate)	N_h	11200000	
	M_h	$7.84 \times 10^{11}\mathrm{M}_\odot$	14.00
	q_h	0.60	0.60
	γ_a	3.80 kpc	1.10
	γ_c	2.28 kpc	0.65
	r_{cut}	84.00 kpc	24.00

Table 3.1: Primary galaxy models. Oblate models have an aspect ratio $q_h = 0.6$. The units are such that Ph.u. means 'physical units', and m.u. 'model units'.

are obtained by solving numerically the Poisson's equations with spherical symmetry in the satellite frame (BT)

$$\rho_s(\Psi) = \rho_1 \left[e^{\Psi/\sigma^2} \mathrm{erf}\left(\frac{\sqrt{\Psi}}{\sigma}\right) - \sqrt{\frac{4\Psi}{\pi\sigma^2}}\left(1 + \frac{2\Psi}{3\sigma^2}\right)\right], \tag{3.17}$$

$$\frac{d}{dr}\left(r^2 \frac{d\Psi}{dr}\right) = -4\pi G \rho_s(\Psi) r^2,$$

from which $M_s(r)$ is calculated.

In the lower panel of Fig. 4.3 we plot the mass profile of a King satellite of concentration $c = 0.8$ used along the numerical and semi-analytic calculations. Note that most of the mass is within $r < 4r_c$.

In our semi-analytic calculations, the satellite is considered a point-mass, so that its motion within the galaxy potential does not depend on the satellite profile. This approximation is accurate enough whenever the satellite core radius is larger than its distance to the galaxy centre. If this condition is not accomplished, we consider that it has merged into the parent galaxy.
We suppose that the satellite remains spherical, with its internal properties changing over time. The satellite structure is fully specified each time step by its profile, tidal and core radius, mass, and the amount of heating it has experienced. The satellite is considered as disrupted if the mass is smaller than 10% of its initial mass.

3.2.1 Satellite parameters

The satellite concentration and "tidal radius" are selected originally from N-body criteria: it must be accomplished that all satellite particles are bound at $t = 0$. This condition is provided by the density contrast, $\rho_s(r_t)/\overline{\rho_g}(r_a) \sim 3$, at the minimum apo-centric distance where we initially locate the satellites ($r_a = 55$ kpc), $\overline{\rho_g}(r)$ being the averaged density of the galaxy (same procedure as VW). Tables for the numerical rendition of the corresponding King profiles can found in BT or in the original paper of King (1966). Table 3.2 summarises the parameters, while Fig. 3.3 plots rotational curves. Note that we use the same M_s, r_c and "r_t" despite placing the satellites at different apo-galactica $r_a \geq 55$ kpc, which increases the true tidal radius of the satellite, though the stability condition at $t = 0$ is still well-accomplished. We do this rather than using different r_c or r_t in order to study the same satellites on different orbits.

We note that our satellites are much more massive than the Milky Way dSph satellites which have $M_s \sim 10^8\, M_\odot$, but our adopted values are typical for the satellites that enter distant samples such as used by Holmberg (1969) and Zaritsky & González (1999).

3.3 SUPERBOX parameters

The selection of the numerical parameters depends on the galaxy and satellite models. The criteria are chosen in order to maximise the N-body code efficiency, i.e, reducing numerical errors and the CPU-expense.

We use SUPERBOX (Fellhauer et al. 2000) to evolve the galaxy-satellite system. SUPERBOX is a highly efficient particle mesh-code based on a leap-frog scheme, and has been already implemented in an extensive study of satellite disruption by Kroupa (1997) and Klessen & Kroupa (1998). For more details see Chapter 2.

The N-body simulations carried out implement the following parameters:
Our integration time step is 0.39 Myr which is about 1/25th the dynamical time of satellite S2. We have three resolution zones, each with 64^3 grid-cells: (i) The inner grid covers out to 3 radial disc scale-lengths, which contains ≈ 90 % of the disc mass, providing a resolution of 350 pc per grid-cell. (ii) The middle grid covers the whole galaxy, with an extension of 24 disc scale-lengths (84 kpc) for the models G1 and G2, giving a resolution of 2.8 kpc per grid-cell. The satellite always orbits within this grid except when it reaches the disc, avoiding cross-border effects (see

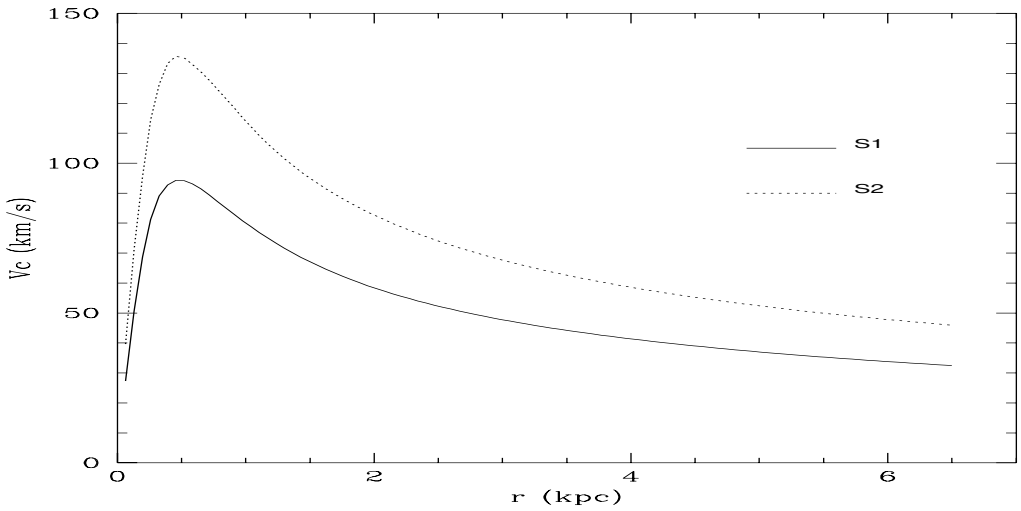

Figure 3.3: Rotational curve of the satellite models S1 and S2 (see Table 3.2 for the characteristics of each one).

Fellhauer et al. 2000). For the models G3 and G4, the middle grid extends to 141 kpc and has a resolution of 4.7 kpc per grid-cell. The orbits of the satellites are located within this zone. (iii) The outermost grid extends to 348 kpc and contains the local universe, at a resolution of 11.6 Kpc.

As for the satellite grid-structure, the resolutions are 816 pc per grid-cell for the inner grid that extends to 24.48 kpc, 1.2 kpc per grid-cell for the middle grid which extends to 36 kpc, and 11.6 kpc per grid-cell for the outermost grid that covers the local universe. Only the inner and middle grids move along with the satellites, remaining positioned on their centre-of-density locations. The outer grid is identical for primary galaxy and satellite.

Klessen & Kroupa (1998) compared calculations performed with SUPERBOX with direct-integration N-body calculations and found good agreement. Specifically, they verified that varying the grid resolution by factors of a few did not lead to unstable satellite models. The stability of the satellite models does not depend strongly on the values adopted here. Furthermore, based on the comparison with the direct-integration method, the heating introduced by two-body effects prove entirely negligible for the model satellites we consider. The selection of grid parameters ensures the conservation of energy and angular momentum for satellites in isolation over times as long as our calculations to a high degree. Conservation of total energy and angular momentum is better than 1% for all the models.

The disc is poorly resolved in the z–direction and we do not study its evolution in any detail. We verified that the disc parameters do not evolve for galaxies in isolation (no satellites). Since SUPERBOX is a mesh code, a poor z-resolution for the disc is expected due to the limited number of grids. This provokes the disc modelled here to be unrealistically thick, however it does provide a quadrupolar (non-spherical) potential of the appropriate magnitude. A mesh code has the advantage that it does not introduce self-heating since it does not calculate two-body interactions, which would have been significant in the disc given the finite number of particles used (see the discussion in VW).

One of the main advantages of SUPERBOX, however, is that the effects on the satellite dynamics due to two-body interactions are drastically reduced by the low mass of the halo particles (see Steinmetz & White 1997). Furthermore the disc heating by halo particles is minimised since each component particle masses are in a one-to-one ratio.

	Symbol	Value(ph.u)	Value (m.u)
S1	N_s	40000	
	M_s	$5.60 \times 10^9 \mathrm{M}_\odot$	0.10
	$\Psi(0)/\sigma_0^2$	5.00	5.00
	r_c	1.00 kpc	0.29
	r_t	6.31 kpc	1.80
	c	0.80	0.80
	$< r >$	1.64 kpc	0.47
	σ_0	$52.00 \mathrm{kms}^{-1}$	0.20
S2	N_s	40000	
	M_s	$1.12 \times 10^{10} \mathrm{M}_\odot$	0.20
	$\Psi(0)/\sigma_0^2$	5.00	5.00
	r_c	1.00 kpc	0.29
	r_t	6.31 kpc	1.80
	c	0.80	0.80
	$< r >$	1.64 kpc	0.47
	σ_0	$74.00 \mathrm{kms}^{-1}$	0.28

Table 3.2: Satellite models. $\Psi(0) = \Phi(r_t) - \Phi(0)$, $\Phi(0)$ being the central potential and $\Phi(r_t)$ the potential at the tidal radius (following BT notation); σ_0 is the velocity dispersion at the centre, and $< r >$ the average radius of the satellite.

Lastly, we note that the N-body parameters outlined in this Section remain unchanged in all our investigations.

Chapter 4

The semi-analytic code

In this Chapter we briefly present the code used to solve the satellite dynamics within different physical systems. Our algorithm simplifies the processes that influence the satellite dynamics along the orbit, by separating them into different analytical approaches: (i) The parent galaxy force given in Chapter 3, (ii) dynamical friction and (iii) satellite mass loss. This scheme is similar to that employed by Taylor & Babul (2001) (hereinafter TB) and it is shown to give accurate results.

Data from high resolution codes give important insights on the physical processes occurring along the satellite orbit. However, due to the complexity of the satellite-galaxy interaction it is hard to quantify, sometimes even distinguish, the mechanisms that determine the satellite properties. To solve this limitation a huge parameter space must be explored, the parameters being carefully selected so that some process is thought to dominate ever the others in order to decouple them. Unfortunately, the main disadvantage of the numerical codes is that they are extremely expensive computationally, forcing a reduction of the parameter range. Moreover, the satellite dynamics and evolution may be influenced by numerical quantities, such as number of particles and resolution.

A complementary approach to the study of the satellite evolution has been found in the semi-analytic methods. These codes are extremely fast (for example, the calculations carried out by Peñarrubia, Kroupa & Boily 2001, hereinafter PKB summarised in Chapter 7, take over 10^4 longer than those with the semi-analytic approach outlined in this Chapter), and the control over the processes to study is total, so that they are useful to determine the relative importance of each galaxy component on the satellite evolution. The semi-analytic schemes also suffer from strong limitations, (i) not all physical processes can be included and (ii) of course, they are high dependent on the theories employed, although, this also gives occasion for checking the accuracy of the theoretical approaches on reproducing the numerical data (e.g the theoretical investigation of dynamical friction in spherical and flattened systems, Chapters 6 and 8, respectively).

The semi-analytic scheme is similar to the one of TB. However, we must note that, whereas they calculate the mass loss from gravitational shocks by computing the tidal forces acting on the satellite galaxy, we introduce the analytic estimations of Gnedin & Ostriker (1999) based on their N-body simulations to account for the disc shocks and those of Gnedin & Ostriker (1997) for the bulge shocks. The formulæ given by these authors avoid the overestimation of tidal heating observed by TB in low eccentric satellites by analysing in detail the re-distribution of energy after the shock as a function of the time-scale of the encounter (see for more details Section 4.3).

The semi-analytic code that we present in this Chapter has two free parameters to be calibrated from the numerical data: The disc and halo Coulomb logarithms.

4.1 The integration of the equations of motion

The algorithm employed to solve the differential equations

$$\mathbf{a} = \frac{d^2\mathbf{x}}{dt^2} = \mathbf{F}_g + \mathbf{F}_{\rm df},$$

where $\mathbf{F}_g$ is the force from the galaxy system (see Chapter 3), and $\mathbf{F}_{\rm df}$ that due to the dynamical friction (see Chapter 5), is based on the Bulirsch-Stoer method (for a complete description see Press et al. 1986).
This method gives high-accurate solutions with minimal computational effort. It is based on an adaptative step-size scheme, being ideal therefore for systems with non-smooth potentials, as may be the case for satellites following high eccentric orbits.

The forces made by each galaxy component, namely the disc, bulge and halo, on the satellite are outlined in Chapter 3 for convenience.

This subroutine uses two free parameters: (i) The desired precision for the solutions $\mathbf{x}(t)$, which is called EPS. This number controls the error of the integration at each time step. Subsequent errors are slightly cumulative, thus the numerical solution slowly deviates from the theoretical one as the number of time steps increases. (ii) The initial value of the time step, denoted as $h_{\rm try}$. Contrary to non-adaptative codes, for instance a Runge-Kutta algorithm, in the Bulirsch-Stoer scheme numerical errors are nearly independent of the initial time step selection.
However, the CPU time of the integration does depend on it. If one selects an extremely large $h_{\rm try}$, the algorithm must make more iterations in order to achieve the desired precision, whenever a extremely small $h_{\rm try}$ mishandles the power of the interpolation scheme, leading to a total number of time steps unnecessarily large. A $h_{\rm try} \sim 1/r(t=0)$ (in model units) takes a good advantage of the code capability.
In each step $[t, t+h_{\rm try}]$, the Burlirsch-Stoer algorithm interpolates the solution using a prefixed analytical function, dividing the interval h_{try} in smaller steps until the difference $x_i(t+h_{\rm try}) - x_i(t) < {\rm EPS} h_{\rm try} dx_i/dt$, therefore the smoother the potential is the lower the number of subdivisions should be.

To check the precision of our algorithm, we test it with the well known Keplerian potential, $\Phi = GM/r$, comparing the results to the analytical solutions for EPS=10^{-5} (full line),10^{-6} (dotted line). In the upper-left panel of Fig. 4.1, we plot the evolution of the distance $r(t)$ from the numerical integration to the Kepler solution $r_t(t)$, the time given in dynamical time units. If we give the same physical values to M and r as in the following sections, we obtain a time-scale range of the order of one Hubble time. The difference between both is about 10^{-4}, being constant along the integration as expected. Analogously, the difference of eccentricities shown in the upper-right panel ($e[t=0] = 0.75$) is also of the same order, both with slight sensitivity on the value of EPS. In the lower left and right panels, we plot the angular momentum and energy conservation, being respectively of the order of 10^{-8} and 10^{-7}.
In Fig. 4.2 equivalent comparisons are done for more circular orbits ($e[t=0] = 0.64$). A notable improvement is found in the eccentricity evolution as well as in the energy-angular momentum conservation, noting the error in $r(t)$ remains fairly the same. From these results, we deduce that the accuracy of the code is sensitive, although within tolerable limits, to the potential gradients, being higher the smaller the initial eccentricity is.

Once being proved the high accuracy of the solutions, we fix the free parameters as, $h_{\rm try} = 0.1$ and EPS= 10^{-5} along our calculations.

4.2 Dynamical friction force

As Chandrasekhar (1943) showed, a body travelling within a background of much lighter particles will experience a force opposed to its sense of motion due to the formation of a density wake. This "drag-force" causes the angular momentum and energy loss of the satellite, the so-called

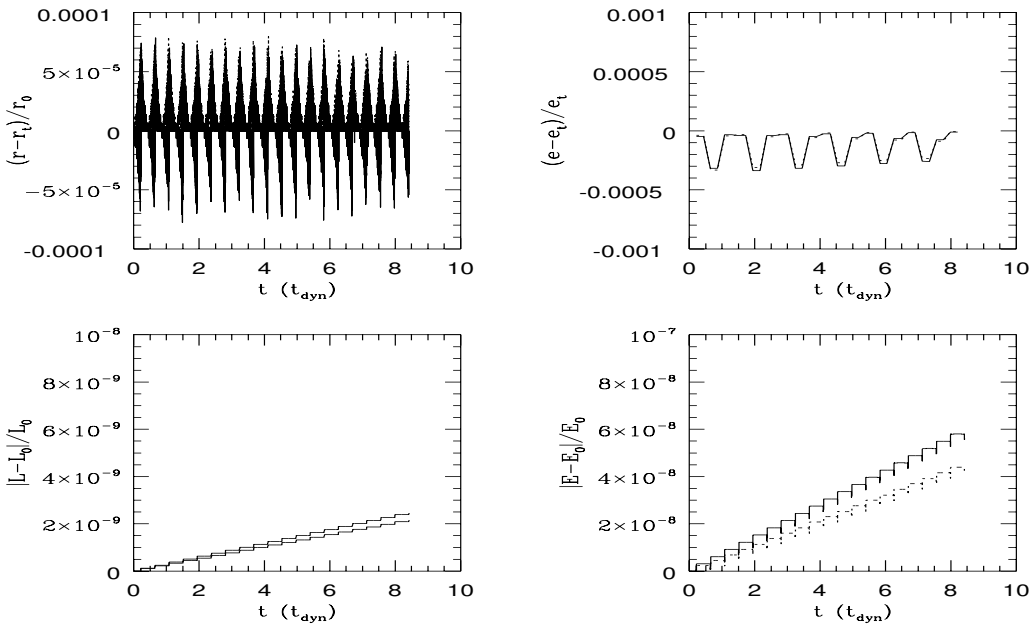

Figure 4.1: Comparison between the numerical and analytical solutions of an orbit in the Kepler potential for the distance (upper-left) and the orbital eccentricity (upper-right), together with the energy (lower-right) and angular momentum (lower-left) conservation. EPS is fixed to 10^{-5} (full lines) and 10^{-6} (dotted lines). The time is given in dynamical times and the initial eccentricity is $e(t=0) = 0.75$.

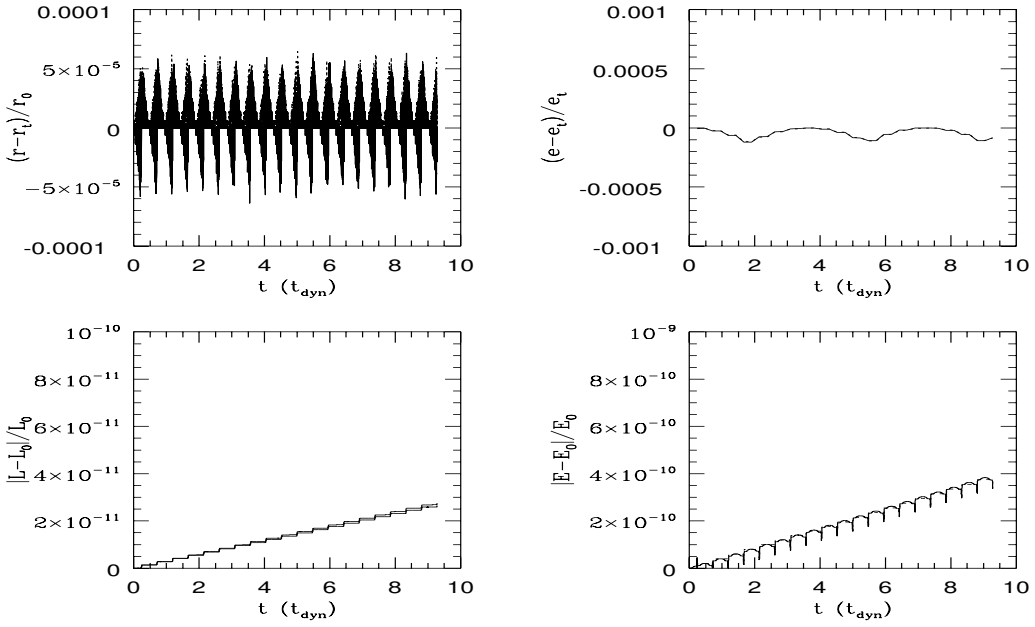

Figure 4.2: As Fig. 4.1 for $e(t=0) = 0.64$.

dynamical friction. If this body is a satellite orbiting around a spiral galaxy, the decreasing energy and angular momentum causes the satellite sinking into inner zones of the galaxy potential.

Recent studies of Hashimoto, Funato & Makino (2002) have shown that a varying Coulomb logarithm may fit better in the inner part of the galaxy, where Chandrasekhar's expressions crash due to the steep potential gradient. We have investigated this possibility in Chapter 6 and compared to the usual dynamical friction (i.e, that with constant Coulomb factor). For simplicity, we outline the friction equations in this Chapter, whereas here we merely describe the case in which the Coulomb logarithm does not depend on the satellite position.

Our galaxy model is divided into three subsystems: halo, disc and bulge, each of them exerting a drag force over the satellite. Along our study, we have chosen to neglect the bulge dynamical friction. The analytic expressions that describe the density profile and velocity dispersion of each galaxy component are outlined in Chapter 3 for convenience.

4.2.1 Halo dynamical friction

As commented above, the Chandrasekhar's expressions for dynamical friction cannot explain some effects observed in N-body calculations of satellite decay within flattened haloes (PKB). We carry out a detailed study on the dynamical friction scheme in Chapter 5, whereas here we give the expressions implemented in the semi-analytic code.

We use Binney's formulæ for dynamical friction which describe the satellite decay in systems with an anisotropic velocity distribution, recovering Chandrasekhar's expression if the velocity distribution is isotropic. In Cartesian coordinates Binney's equations become

$$F_{\mathrm{df,h,i}} = -\frac{\sqrt{2\pi}\rho_h(\mathbf{r})G^2M_s^2\sqrt{1-e_v^2}\ln\Lambda_h}{\sigma_R^2\sigma_z}B_R v_i \qquad (4.1)$$

$$F_{\mathrm{df,h,z}} = -\frac{\sqrt{2\pi}\rho_h(\mathbf{r})G^2M_s^2\sqrt{1-e_v^2}\ln\Lambda_h}{\sigma_R^2\sigma_z}B_z v_z,$$

where $i = x, y$ and (σ_R, σ_z) is the velocity dispersion ellipsoid in cylindrical coordinates with local eccentricity $e_v^2 = 1-(\sigma_z/\sigma_R)^2$. We denote $\ln\Lambda_h$ as the Coulomb logarithm of the halo and

$$B_R = \int_0^\infty dq \frac{\exp(-\frac{\mathrm{v_R^2}/2\sigma_\mathrm{R}^2}{1+\mathrm{q}} - \frac{\mathrm{v_z^2}/2\sigma_\mathrm{R}^2}{1-\mathrm{e_v^2}+\mathrm{q}})}{(1+q)^2(1-e_v^2+q)^{1/2}}$$

$$B_z = \int_0^\infty dq \frac{\exp(-\frac{\mathrm{v_R^2}/2\sigma_\mathrm{R}^2}{1+\mathrm{q}} - \frac{\mathrm{v_z^2}/2\sigma_\mathrm{R}^2}{1-\mathrm{e_v^2}+\mathrm{q}})}{(1+q)(1-e_v^2+q)^{3/2}}.$$

As Binney shows, the mass M_s will suffer a decrease of its orbital plane inclination whenever $B_z > B_R$ (oblate halo). If the orbit is either coplanar or polar, the inclination remains constant since, respectively, either the perpendicular or the planar component of v is zero. One can easily check that this expression reproduces Chandrasekhar's when $e_v = 0$.

$$\mathbf{F}_{\mathrm{ch}} = -4\pi G M_s^2 \rho_h(R,z)\ln\Lambda\big[\mathrm{erf}(X) - \frac{2X}{\sqrt{\pi}}e^{-X^2}\big]\frac{\mathbf{v}_s}{v_s^3}, \qquad (4.2)$$

where $X = |\mathbf{v}_s|/\sqrt{2}\sigma$.

The derivation of Binney assumes that a massive point particle moves through an infinite medium of much lighter particles with anisotropic Maxwellian velocity distribution (in our case $\sigma_z/\sigma_R < 1$). The inclusion of the Coulomb logarithm is made to avoid the divergence of the calculus when one integrates over the impact parameter in an infinite medium (Chandrasekhar 1943). In principle, this parameter can be expressed as $\Lambda = b_{\max}/b_{\min}$, where $b_{\max}$ and $b_{\min}$ are the maximum and minimum impact parameters respectively. As Binney points out, the value of

Λ depends on the velocity of the satellite, though this dependence may be considered as negligible for most of the values of the orbital parameters (for more details see Chapters 5 and 6).

Several studies of satellite decay have shown that Chandrasekhar's dynamical friction is accurate enough if the Coulomb logarithm remains as a free parameter to fit to the N-body data (e.g. van den Bosch et al. 1999, Colpi et al. 1999, VW) since it also depends on the code and the number of particles employed. For instance, Prugniel & Combes (1992) and Whade & Donner (1996) find that dynamical friction is artificially increased due to numerical noise if the particle number is small. Similar differences were also noted in the computations by Klessen & Kroupa (1998) of satellite harassment using different codes.

The Coulomb logarithm is also sensitive to the satellite extension. BT suggest that the formula derived for the case where the satellite is a point-mass will only slightly overestimate the drag experienced by an extended body, therefore we do not include the correction since it has to be fixed from numerical calculations.

4.2.2 Disc dynamical friction

Following TB, we use Chadrasekhar's formula to reproduce the dynamical friction exerted by the disc

$$\mathbf{F}_{\rm df,d} = -4\pi G M_s^2 \rho_d(< v_{\rm rel}) \ln\Lambda_d \frac{\mathbf{v}_{\rm rel}}{|\mathbf{v}_{\rm rel}|^3}, \tag{4.3}$$

$\mathbf{v}_{\rm rel} = \mathbf{v} - \mathbf{V}_{\rm c,d}$ being the relative velocity between the satellite and the disc rotation, where we have neglected the velocity dispersion contribution, $\ln\Lambda_d$ is the Coulomb logarithm of the disc and

$$\rho_d(< v_{\rm rel}) = \rho_d(r)\big[{\rm erf}(X_d) - \frac{2X_d}{\sqrt{\pi}} e^{-X_d^2}\big],$$

where $X_d = |\mathbf{v}_{\rm rel}|/\sqrt{2}\sigma_d$.

The presence of the factor $1/v_{\rm rel}^2$ in the eq.(4.3) implies that the disc dynamical friction shall not be negligible compared to the one of the halo when the satellite orbit is nearly coplanar (low orbital inclination) and prograde. In this case, for a circular orbit $v_{\rm rel} \sim \sigma_{d,\phi}$.

As TB, we smooth the disc density in the vertical direction by doubling the value of z_0 to avoid errors in calculating dynamical friction for coplanar satellites, where the z-component of the potential has steep changes over small scales.

4.3 Analytic treatment of satellite mass loss

The satellite dynamics is highly dependent on the ratio of the satellite to the galaxy mass, mostly through dynamical friction, therefore, it is necessary to implement some analytical scheme able to reproduce the satellite mass evolution along the orbit. In this Section, we introduce the two methods employed along our calculations.

Satellites experience mass loss whenever the external potential is stronger than the binding energy of its components. This material becomes unbound and can subsequently escape from the satellite. Depending on the variation rate of the external potential, we can distinguish between two regimes: (i) Tidal mass loss, when the potential changes slowly and (ii) tidal heating, for rapid variations.

Tidal mass stripping

In the first regime, the amount of bound mass is determined by the tidal radius (King 1962), which is defined for a spherically symmetric satellite as the distance to the satellite centre where the satellite and the galaxy force cancel out. If the satellite follows a circular orbit the system can

be considered as static in a rotational frame, and one can estimate the tidal radius as (King 1962, BT)

$$R_t \approx \left(\frac{GM_s}{\omega^2 - d^2\Phi/dr^2} \right)^{1/3}, \tag{4.4}$$

where ω is the angular velocity of the satellite and Φ the potential of the main system.

This estimate is valid when: (i) The satellite mass is much smaller than the one of the parent galaxy and (ii) R_t is small compared to the satellite distance to the galaxy centre. Even under these conditions, the mass within R_t is not exactly equal to the bound mass, since there may be particles that have (small) positive energy and stay in transient orbits within the satellite (e.g. BT).

If the satellite follows a non-circular orbit one can still use eq. (4.4) to calculate the instantaneous tidal radius, now ω being the instantaneous angular velocity. For these kind of orbits, the mass loss occurs nearby the peri-galacticon where the force gradient is maximum (e.g, PKB, Piatek & Pryor 1995). In our calculi, the transient orbits are assumed as of second order compared to the total amount of mass stripped out by the peri-galacticon passages, so that the time these particles need to escape is considered much shorter than the orbital period.

Whereas eq. (4.4) is quite accurate in accounting for the mass loss of satellites in coplanar orbits, tidal shocks will dominate the mass loss process of satellites following orbits inclined with respect to the disc plane.

Tidal heating

Satellites travelling through regions where the external potential changes rapidly suffer tidal shocks. This process can be described as perturbations with a given frequency that add energy to the satellite particles. The shocks will occur near the galaxy centre, where the disc and bulge induce a steep force gradient.

As a result of the shock, Gnedin & Ostriker (1999) (herinafter GO) show that the satellite is contracted, with following expansions and re-contractions until it reaches a final state of equilibrium, in which the binding energy is smaller than originally and the satellite has expanded. This non-equilibrium phase lasts for their models around 20 satellite dynamical times.

The study of tidal shocks is far beyond our purpose. We mainly follow the method of GO in order to calculate the energy gained from disc shocks, whereas for the bulge we use the analytical expressions of Gnedin & Ostriker (1997).

1) Disc shocks.

Using the harmonic approximation, the first and second order terms of the averaged energy change per unit mass of stars with positions $\mathbf{r} = (x, y, z)$ and velocities $\mathbf{v}$ with respect to the satellite centre due to disc shocks are given by Spitzer (1987) and Kundić & Ostriker (1995), respectively

$$\begin{aligned} \langle \Delta E \rangle_d &\equiv \frac{1}{2} \langle (\Delta v)^2 \rangle = \frac{2 g_m^2 r^2}{3 V_z^2} A_1(x) \\ \langle \Delta E^2 \rangle_d &\equiv \langle (v \Delta v)^2 \rangle = \frac{4 g_m^2 r^2 v^2(r)(1+\chi_d)}{9 V_z^2} A_2(x), \end{aligned} \tag{4.5}$$

where g_m is the maximum vertical acceleration produced by the disc, V_z is the vertical component of the satellite velocity and v is the root mean squared velocity of the satellite. The factor χ_d denotes the disc two-point correlation function, which depends on (r, v) and takes a value of -0.3 from the GO calculus.

The energy injection of the shock is distributed to each satellite star depending on its orbital parameters. The functions $A_1(x)$ and $A_2(x)$ are called *adiabatic corrections* and account for the

energy distribution within the satellite after the shock. There are several approximations to the adiabatic corrections: (i) Spitzer (1987) simplifies the satellite as a set of 1D harmonic oscillators which absorb energy resonantly to the vertical orbital frequency of the satellite. (ii) The Linear theory of Weinberg (1994) assumes the stars as a 3D non-linear oscillators. This allows a wider set of frequencies that may enter in resonance with the satellite motion. As a result, Weinberg shows that the Spitzer's calculation underestimates the energy absorption in the inner part of the satellite. (iii) Along our study, we use the results of GO who, comparing the Weinberg's expressions with N-body simulations, find the following adiabatic corrections

$$\begin{aligned} A_1(x) &= (1+x^2)^{-\gamma_1} \\ A_2(x) &= (1+x^2)^{-\gamma_2}, \end{aligned} \tag{4.6}$$

where $x \equiv t_{\rm d,sh}/t_{orb}(r)$, i.e, the ratio between the shock duration and the satellite orbital period at a given radius

$$t_{\rm d,sh} = \frac{Z}{V_z}$$

$$t_{\rm orb}(r) = 2\pi \frac{r}{v(r)}.$$

As it is deduced from the last definitions, the value of A tends to zero as x tends to infinity, whereas it approaches asymptotically to one for $x \to 0$. The adiabatic corrections therefore have small values in the inner part of the satellite, where the frequencies of the stars are much higher than the satellite frequency, this is the so-called adiabatic zone, tending to one in the outer most region of the satellite.

Whereas Weinberg (1994) predicts $\gamma_1 = \gamma_2 = 3/2$, independently of $t_{\rm sh}$, GO show that these exponents do depend on the shock duration, i.e, on the satellite orbital parameters. They calculate the value of the exponents from the best fit to N-body calculations. The results are shown in their Table 2, obtaining that (γ_1, γ_2) take values from (2.5,3) for rapid shocks ($t_{\rm d,sh} \leq t_{\rm orb}(r_h)$, r_c being the satellite half mass radius) to (1.5,1.75) for slow shocks ($t_{\rm d,sh} \sim 4t_{\rm orb}(r_h)$).

2) Bulge shocks.

The energy gain from a bulge shock is deduced by Gnedin & Ostriker (1997) by calculating the tidal field of a extended system at the peri-centre

$$\begin{aligned} \langle \Delta E \rangle_b &= \frac{4}{3}\left(\frac{GM_b}{V_p R_p^2}\right)^2 r^2 \lambda(R_p) A_1(x_b) \\ \langle \Delta E^2 \rangle_b &= \frac{8}{9}\left(\frac{GM_b}{V_p R_p^2}\right)^2 r^2 v^2 (1+\chi_b) \lambda(R_p) A_2(x_b), \end{aligned} \tag{4.7}$$

where R_p, V_p are the distance and the velocity of the satellite at that point and $\lambda(R_p)$ defined as,

$$\lambda(R_p) = \frac{1}{2}\left[(3J_0 - J_1 - I_0)^2 + (2I_0 - I_1 - 3J_0 + J_1)^2 + I_0^2\right],$$

where,

$$I_0(R_p) \equiv \int_1^\infty m_b(R_p y) \frac{dy}{y^2(y^2-1)^{1/2}}$$

$$I_1(R_p) \equiv \int_1^\infty m_b'(R_p y) \frac{dy}{y^2(y^2-1)^{1/2}}$$

$$J_0(R_p) \equiv \int_1^\infty m_b(R_p y) \frac{dy}{y^4(y^2-1)^{1/2}}$$
$$J_1(R_p) \equiv \int_1^\infty m_b'(R_p y) \frac{dy}{y^4(y^2-1)^{1/2}},$$

$m_b(R) \equiv Mb(R)/M_b$ being the normalised mass distribution at radius R and $m_b'(R) \equiv d\ln m_b(R)/d\ln R$. For a Hernquist bulge we fit $\chi_b = -0.4$.

In the numerical calculations of GO the satellite is described by a King model of concentration $c = 0.86$, very similar to the model we use ($c = 0.8$), which allows us to implement their results in the semi-analytic scheme. Eq. (4.5) and (4.7) can be rewritten as

$$\langle \Delta E \rangle = \langle \Delta E \rangle_{t_{\rm sh}=0} \left[1 + \frac{t_{\rm sh} v(r)}{2\pi r} \right]^{-\gamma_1}$$

$$\langle \Delta E^2 \rangle = \frac{2}{3} r^2 v^2(r)(1+\chi) \langle \Delta E \rangle_{t_{\rm sh}=0} \left[1 + \frac{t_{\rm sh} v(r)}{2\pi r} \right]^{-\gamma_2},$$

where $< \Delta E >_{t_{\rm sh}=0}$ is the energy change during a shock of infinitesimal duration and $t_{\rm sh}$ the shock time-scale. The exponents of the adiabatic corrections γ_1, γ_2 are those outlined above.

Our treatment of mass loss distinguishes from that of TB in two points: (i) The re-distribution of energy within the satellite depends on the position of the star through the adiabatic correction term, which reduces the shock effects in the inner zone of the satellite and (ii) the adiabatic exponent depends on the shock regime, whereas TB fix $\gamma = 2.5$, assuming most of the heating induced by rapid shocks.

In Fig. 4.3 we show the radial profile of the energy gain (upper panel) and shell expansion (lower panel, from eq.[4.8]) after a shock of one time-step duration. The disc is the main contributor to the shock, the energy injection from the bulge being around three orders of magnitude smaller. As we commented, the adiabatic corrections prevent from energy enhance at the inner part of the satellite (approximately $r < 5r_c$), tending monotonically to one as we go farther out. The small gain of energy at the inner part leads to a negligible expansion of the shells, so that the mass profile within this zone can be approximated as that of the King model before the shock.

One must consider that tidal forces interact with the satellite continuously along its orbit. Following GO, we assume a Gaussian-shape evolution for the time evolution of the tidal interaction, which is centred at the time (t_0) when the tidal force experiences a maximum and its dispersion is equal to the shock time-scale. As GO we define the function

$$I^2_{\rm imp} \equiv \frac{1}{3\pi} \left(\frac{\Delta t}{t_{\rm sh}} \right)^2 \exp\left[-\frac{(t-t_0)^2}{t^2_{\rm sh}} \right],$$

which multiplies the energy changes of equations (4.5) and (4.7). The approximation has been shown to be accurate in order to reproduce the tidal effects along the satellite orbit. We note that the expression has been normalised so that it recovers the same total energy change as the impulsive shock $t_{\rm sh} \to 0$.

Our code is constructed so that the energy gained after each time-step accumulates (the energy injected in the satellite grows monotonically in time, since for each tidal shock the averaged $\Delta E > 0$) meanwhile the satellite profile remains unchanged. Despite that after the first shock the satellite is not a King model any more, from the work of PKB, Piatek & Pryor (1995) and GO, we can assert that this is fully consistent as long as the satellite energy is not dramatically increased, i.e, for early and middle times. As Fig. 4.3 shows, the inner part of the satellite is barely changed after a shock, whereas the outer part receives most of the energy. The particles of this region are, either because of the subsequent reduction of binding energy or by the tidal radius evolution, stripped out. If a non-mixing shells is assumed, the inner part of the satellite can be considered to follow the initial King profile for most part of its evolution.

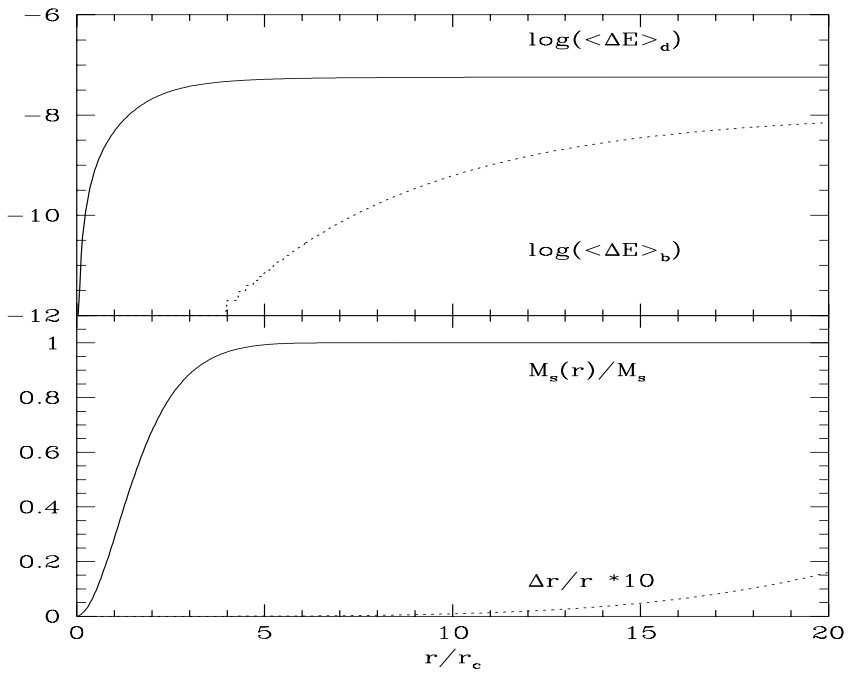

Figure 4.3: Upper panel: Energy gain (in model units) after a disc and bulge shock of duration Δt as a function of the satellite radius. The calculus corresponds to the first peri-centre passage of the model G1S145 (see Chapter 7). Lower panel: Mass shell expansion. Due to its small value we multiply the values of $\Delta r/r$ by a factor 10. It is also plotted the mass profile for comparison.

Fig. 4.4 illustrates the shock interactions along the orbit G1S145 (see Chapter 8). In the upper panel we plot the energy addition at each time, whereas the lower panel show the cumulative energy along the orbit (we assume that the energy change from tidal shocks accomplishes $E[t + \Delta t] = E[t] + \Delta E$, i.e., it accumulates). The main contribution comes from the disc-satellite interactions, approximately two orders of magnitude higher than those with the bulge. As expected, shocks occur at the peri-galacticon passages, where the disc and bulge tidal forces reach their respective maximums.
This figure also shows that shocks are high efficient when the satellite velocity and $t_{\rm shock}$ decrease. Meanwhile the first produces stronger tides on the satellite particles, the second enhances the wideness of the Gaussian, leading to larger interactions.

To determine the changes experienced by the satellite after the energy injection, we assume that the ulterior mass distribution does not involve shell crossing. Under this condition, a change of energy $E \to E + \Delta E$ result in an expansion of the satellite

$$\Delta r = \frac{\Delta E r^2}{G M_s(r)}, \tag{4.8}$$

so that the mass distribution (3.17) after the tidal shock is $M_s(r') = M(r + \Delta r) = M(r)$. As this equation suggests, some material will be expanded out of the tidal radius which, therefore, will enhance the satellite mass loss. As we assumed for the energy function, the shell radii expand monotonically in time after each tidal shock.

As TB comment, this technique suffers from some limitations: (i) The assumption of virial equilibrium between the satellite shocks. Numerical calculations (e.g, PKB, Piatek & Pryor 1995) show that this approximation is accurate only in the inner parts of the satellite, where the velocity dispersion results nearly constant after the shock, whereas the outer parts are subsequently re-virialized. (ii) To approximate $\Delta E r^2$ as a quantity independent of radius (null shell crossing) is strictly true only for the outer parts of the satellite. The heating experienced by the inner regions

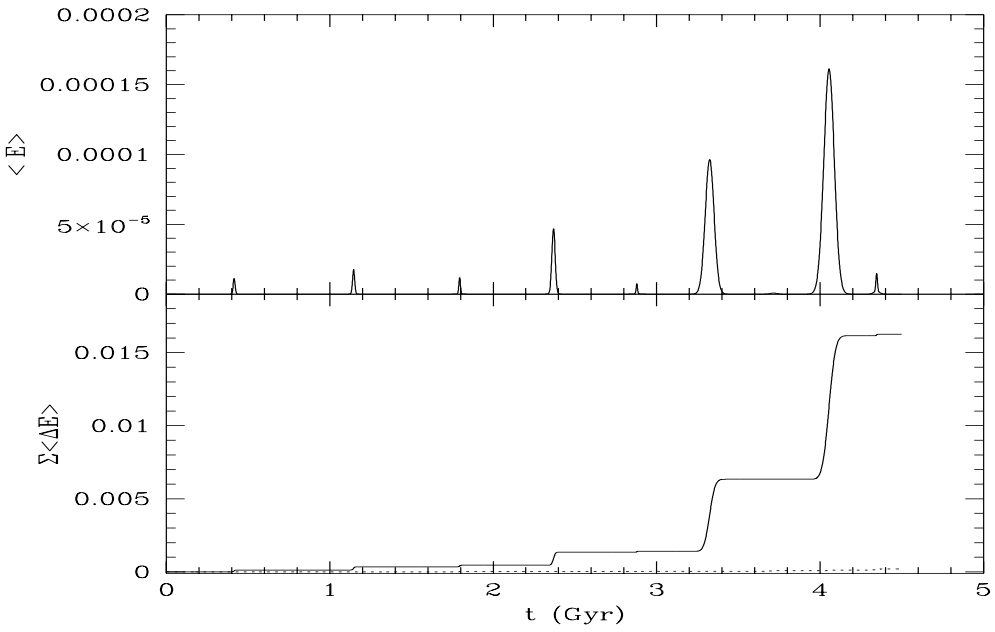

Figure 4.4: Upper panel: Energy addition (without adiabatic corrections) along the orbit G1S145. The values are in model units $G = M_d = Rd = 1$, see Chapter 3. Lower panel: Total cumulative energy along the orbit.

is over-estimated by a factor that depends on the mass profile and is larger the more concentrated the satellite is. (iii) The mass loss scheme does not account for the angular momentum of the escaping particles, which may induce changes on the satellite orbit.

The implementation of the satellite mass evolution in our semi-analytic code give rise to a self-consistent description of the satellite dynamics in spiral galaxies that will be employed in Chapters 9 and 10.

The analytical expressions of mass loss inevitably introduces errors on the value of M_s that may depend on the satellite orbital parameters. One of the main topics of this work is the comparison between different analysis of dynamical friction, for which a high accuracy in the value of the satellite mass is necessary. For that reason, in such studies we use the numerical curve of M_s along the orbit integrated by the semi-analytical code (see Section 2.3).

4.4 Calculus of the Energy and angular momentum

Axisymmetric systems have three constant of motion: the energy, the component of the angular momentum perpendicular to the axi-symmetry plane (that we denote as L_z) and a third value with no analytical representation. The total angular momentum $L^2 = L_R^2 + L_z^2$ is, however, not constant along the satellite orbit (see e.g BT), but has periodic variations that correspond to a precession of the orbital plane around the z-axis and a nutation of the angular momentum vector.

Since the dynamical friction force is directed contrary to the satellite velocity, it acts by decreasing the angular momentum and energy of the satellite which induces a monotonic sink into the inner regions of the halo potential.

We calculate the energy and angular momentum of the satellite as follows,

$$E = \frac{1}{2}\mathbf{v}^2 + \Phi_g(\mathbf{r}) \tag{4.9}$$
$$L_z = \left(\mathbf{r} \times \mathbf{v}\right)_z = xv_x - yv_z,$$

employing Cartesian coordinates along our calculi

$$(\mathbf{r}, \mathbf{v}) = (x, y, z), (v_x, v_y, v_z).$$

Whereas the disc and bulge potentials are simply calculated as,

$$\Phi_i = \frac{GM_i(r' < r)}{r}$$

the subindex $i = d, b$ and $M(r' < r)$ being the mass enclosed within the radius r, the halo potential needs a more complicated calculus.

The potential of the halo considered as a heterogeneous ellipsoid with density of the form (3.1). At an internal point (R, z) it can be calculated from Chandrasekhar (1960) as

$$\Phi_h(R, z) = -q_h \frac{GM_h\alpha}{2\sqrt{\pi}r_{\rm cut}} \int_0^\infty \frac{\Psi[m^2(u)]}{(1+u)(q_h^2+u)^{1/2}} du, \tag{4.10}$$

where $\Psi(m^2)$ is defined as

$$\Psi(m^2) = \frac{1}{a^2} \int_{a^2}^{m^2} \rho_h(m'^2) dm'^2, \tag{4.11}$$

and $m^2(u)$ as in (3.5) and a can be interpreted as the size of the halo in which the satellite is embedded, which is chosen to be $a = r_{\rm cut}$.

The angular momentum is directly calculated from the position and velocity $(\mathbf{r}, \mathbf{v})$ at each time step. We should note that, due to the nature of the semi-analytical code, it is not included the effects that the mass loss introduces on the angular momentum evolution, which may be not negligible in orbits with strong variations of the galaxy potential, for instance, in low eccentric orbits.

Remark

We also use this scheme to calculate the energy and angular momentum evolution from the N-body data given by SUPERBOX.

Whereas the kinetic energy is directly calculated from the numerical output, the value of the potential is derived by making use of eq. (4.10). In doing this, we assume that,
(i) N-body haloes follow perfectly the distribution function given in the eq. (3.1) neglecting, therefore, the evolution subsequent to the implementation of the system in SUPERBOX. This was proved by the numerical test of Boily, Kroupa & Peñarrubia (2001) to be an accurate approximation as far as the satellite remains in the inner part of the halo (where around the 80 per cent of the mass is included). (ii) We also neglect the change in the distribution due to the self response of the system to the satellite presence. (iii) We do not take into account the motion of the halo centre-of-mass due to the satellite orbit, which is of the order of M_s/M_g, where r is the satellite initial radius. This approximation causes the presence of periodic oscillations in the angular momentum and in the energy curves as we show in following Chapters.

Chapter 5

Dynamical friction theory

5.1 Introduction. Mathematical tools

A gravitating body moving through a background of lighter particles suffers from a drag fore due to the interaction with its own induced wake. For collisionless systems the classical Chandrasekhar expression (Chandrasekhar 1943), based on the perturbation theory, has been shown to be useful in determining the orbital decay of clusters and satellites around spherical backgrounds, such as elliptical galaxies (e.g Lin & Tremaine 1983, Cora, Muzzio & Vergne 1997 and references therein). Although this formula was inferred for uniform backgrounds, it is often applied to inhomogeneous systems by making use of the local approximation and neglecting the first and higher orders of dynamical friction. There are still open issues, for which the effects of Chandrasekhar expression on the satellite dynamics are not clear. For instance, several authors claim (e.g Colpi, Mayer & Governato 1999, Cora, Muzzio & Vergne 1997) that this treatment of dynamical friction leads to a circularisation of the orbit that is not present on the numerics, whereas van de Bosch et al. (1999), making a statistical survey of satellite eccentricities, do not observe such an effect.

Recently, there have been applied other perturbation schemes in other to give a description of the friction from the global interaction satellite-galaxy. For example, the Theory of Linear Response (TLR) has been successful in describing the decay of satellites in spherical systems (Colpi, Mayer & Governato 1999, Nelson & Tremaine 1999). This method infers analytically the collective response of the background to the satellite motion (the satellite is considered as a perturbation) and calculates the gravitational force of the perturbed particles (wake) on the satellite. Despite the completeness of the method, it suffers from different limitations: (i) This scheme assumes a spherical symmetric background. The develop of the scheme to other symmetries would be very complicate, (ii) the dynamical friction force is a result of a time integral that preserves the actual dynamics of the satellite and the dynamics of the galaxy bodies. One can readily see the numerical complications that in practice this fact includes: to calculate dynamical friction at a given position (with a given velocity) it is necessary to know all the previous positions along which the satellite moved.

Another scheme to describe the drag force experienced by satellites orbiting around spherical systems has been carried out by Sánchez-Salcedo & Brandenburg (1999, 2001). The investigation was done for a gaseous background with an inhomogeneous density profile. The results are given in terms of the local response of the galaxy to the satellite perturbation, finding that (i) the decay time is independent of the initial eccentricity, (ii) the Coulomb factor $\Lambda = b_{\max}/b_{\min}$ (where, $b_{\max}$ and $b_{\min}$ are the maximum and minimum impact parameters, respectively) varies linearly with the satellite galacto-centre distance, (iii) besides the friction force directed against the satellite motion (the so-called "drag force") it appears a perpendicular component of the order of the parallel one. It is however unclear how to interpret the results for a stellar system, although it seems obvious that the perpendicular component may be not negligible, playing a important role in accounting for the change over the satellite orbital eccentricity.

We have based our investigation of dynamical friction on the perturbation theory, following the method of Chandrasekhar and, *a posteriori* Binney (1977). The aim is to develop the first order term of dynamical friction and infer the effects that it may induce on the satellite dynamics. We also clarify the approximations employed when using Chandrasekhar's and Binney's formulæ and the limits inherent to them. Along our study, we analyse the effects of the velocity dependence of the Coulomb factor and show its importance in order to calculate the first order term. Recently, Hashimoto, Funato & Makino (2002) have shown that a linearly dependent Coulomb factor fits better to the numerical calculations in pure stellar galaxies (as it has been found in gaseous systems). In this Chapter we apply the perturbation theory and the local approximation to find a function $\Lambda(r)$ that agrees with the our analytical scheme. In subsequent Chapters we investigate, first, the degree of improvement of this assumption in fitting the numerical results and, second, the differences that it yields on the satellite dynamics.

5.1.1 Analytical method

In this Section the basis of the method we follow is explained, together with the approximations employed and the conditions under which can be applied.

The perturbation theory

A massive body travelling through a medium of much lighter particles experiences encounters that can be treated like two-body collisions; higher order encounters like three-, four-body collisions are negligible.

The perturbation theory assumes that the final change over the satellite properties is the sum of small alterations as a result from individual (independent) two-body encounters.
Therefore, the condition under this theory can be employed is

$$m/M_s << 1,$$

where m is the mass of a background particle and M_s the mass of the heavy body.

Let's assume that the massive body moves through a medium with distribution function $f(\mathbf{r}, \mathbf{v})$. The perturbation theory assures that, if Δv is the change over the velocity of M_s after a two-body collision, the total change at a given time is

$$\int\int \Delta v d\nu f(\mathbf{r}, \mathbf{v}) d^3r d^3v,$$

where the integration is over a given volume of the impact parameter phase-space and ν is a function that depends on the relative velocity between the massive body and the background particles (as we shall see, this function is linear if assuming straight line encounters).

The straight line approximation

The change over the velocities of two particles that collide can be described in isolation, as the motion of a reduced particle with mass $\mu = mM_s/(m + M_s)$ in a Keplerian potential $\Phi = -(m + M_s)/r$, where r is the relative distance between both particles (see e.g BT, Section 7.1), which is equivalent to the absence of an external potential during the encounter. Defining $t = 0$ as the minimum relative distance and (x, z) as the coordinates of the particle m relative to the body M_s, we have that the extrapolation to $t \to \infty$ results to an evolution of the relative velocity $V \to V_0$, and $z \to b_0$, where z is component perpendicular to $\mathbf{V}_0$. The value b_0 is the so-called *impact parameter*.

It is evident that if the medium is inhomogeneous, it appears an external potential during the two-body encounter that varies the dynamics and, therefore, the final change over the massive body velocity. The possible dependence of dynamical friction on the system inhomogeneity is still unclear and beyond our study. However, it is necessary to clarify the approximation that one

usually assumes when applying Chandrasekhar's formula for non-homogeneous systems, which is called the *straight line approximation*.

To determine the accuracy of this approximation, one must first calculate the exact collision equations in such a medium.

The orbit of two particles that move in a medium with a given density profile and collide can be inferred from the equations

$$\begin{aligned}\frac{d^2\mathbf{R}_m}{dt^2} &= \mathbf{F}_g(\mathbf{R}_m) - \frac{GM}{r^2}\mathbf{e}_r \\ \frac{d^2\mathbf{R}_M}{dt^2} &= \mathbf{F}_g(\mathbf{R}_M) - \frac{Gm}{r^2}\mathbf{e}_r,\end{aligned} \tag{5.1}$$

where $\mathbf{R}$ denotes the distance to the galaxy centre, r the relative distance between both particles, with unit vector $\mathbf{e}_r$, and $\mathbf{F}_g$ being the galaxy force.

These equations represent actually the *reduced three body problem* in a fixed potential, with no analytical solution. To go deeper into the problem, we must simplify our equations by making some assumptions.

The first one is to calculate the effect of the galaxy potential as a tidal interaction, by expanding the force as

$$\begin{aligned}\mathbf{F}_g(\mathbf{R}_m) &= \mathbf{F}_g(\mathbf{R}_{cm}) + \nabla\mathbf{F}_g\big|_{cm}\mathbf{r}_m + ... + \mathcal{O}\left(\frac{r_m}{R_{cm}}\right) \\ \mathbf{F}_g(\mathbf{R}_M) &= \mathbf{F}_g(\mathbf{R}_{cm}) + \nabla\mathbf{F}_g\big|_{cm}\mathbf{r}_M + ... + \mathcal{O}\left(\frac{r_M}{R_{cm}}\right),\end{aligned} \tag{5.2}$$

where we define the vectors

$$\mathbf{R} = \mathbf{R}_{cm} + \mathbf{r},$$

and $\mathbf{R}_{cm}$ being the centre-of-mass of the pair M, m, i.e,

$$\mathbf{R}_{cm} \equiv \frac{M\mathbf{R}_M + m\mathbf{R}_m}{M+m}.$$

The potential of a spherically-symmetric system Φ_g is

$$\Phi_g = -\frac{GM_g(R)}{R} - 4\pi G\int_R^\infty \rho(r')r'dr', \tag{5.3}$$

which produces a tidal force per unit mass

$$\mathbf{F}_{\rm tid} \equiv \nabla\mathbf{F}_g\big|_{cm}\cdot\mathbf{r} = -\left.\frac{\partial^2\Phi_g}{\partial\mathbf{R}\partial\mathbf{R}}\right|_{cm}\cdot\mathbf{r} = \frac{GM_0}{R_{cm}^3}\big[(3\mu-\mu')(\mathbf{n}\cdot\mathbf{r})\mathbf{n} - \mu\mathbf{r}\big], \tag{5.4}$$

where M_0 is the total mass of the galaxy, $\mu(R)$ the normalised mass profile and $\mu'(R)$ a function defined as

$$\begin{aligned}\mu &= \frac{M_g(R)}{M_0} \\ \mu' &= \frac{d\mu(R)}{d\ln R},\end{aligned} \tag{5.5}$$

and $\mathbf{n}$ is the unitary vector directed to the centre-of-mass of the pair $\mathbf{n} \equiv \mathbf{R}_{cm}/R_{cm}$.

At order (r/R_{cm}) eq.(5.2) becomes therefore

$$\begin{aligned}\frac{d^2\mathbf{R}_m}{dt^2} &= \mathbf{F}_g(\mathbf{R}_{cm}) + \nabla\mathbf{F}_g\big|_{cm}\mathbf{r}_m - \frac{GM}{r^2}\mathbf{e}_r \\ \frac{d^2\mathbf{R}_M}{dt^2} &= \mathbf{F}_g(\mathbf{R}_{cm}) + \nabla\mathbf{F}_g\big|_{cm}\mathbf{r}_M - \frac{Gm}{r^2}\mathbf{e}_r.\end{aligned} \tag{5.6}$$

The relative motion of the two particles with respect to the centre-of-mass is from last equation and eq.(5.4),

$$\frac{d^2\mathbf{r}}{dt^2} = \frac{GM_0}{R_{cm}^3} r\big[(3\mu - \mu')(\mathbf{n}\cdot\mathbf{e}_r)\mathbf{n} - \mu\mathbf{e}_r\big] - \frac{G(M+m)}{r^2}\mathbf{e}_r, \tag{5.7}$$

defining the relative vector,

$$\mathbf{r} = \mathbf{r}_m - \mathbf{r}_M = r\mathbf{e}_r.$$

Therefore, in the tidal approximation the three-body problem is simplified. Of course, this approximation is only valid in the range $r/R_{cm} << 1$. We can see that the force is not radial but has a component parallel to the galacto-centre vector $\mathbf{n}$ which, as a matter of fact, implies that the tidal force makes the angular momentum not to be constant along the interaction. Equivalent to the motion in an axis-symmetric system we have that the component L_z =const, with the z-axis perpendicular to $\mathbf{e}_r$.

The evolution of the relative distance in such a potential is given by the equations (BT, Section 3.2),

$$\begin{aligned} \ddot{r} &= -\frac{GM_0}{R_{cm}^3} r\mu - \frac{G(M+m)}{r^2} \\ \ddot{z} &= \frac{GM_0}{R_{cm}^3} r(3\mu - \mu')\cos\theta, \end{aligned} \tag{5.8}$$

where $\cos\theta = \mathbf{n}\cdot\mathbf{e}_r$.

These equations represent the first step in order to exactly determine the effects of the galaxy potential on the description of the two-body encounter. However, due to the complexity of such a subject, we decided to postpone it for a further work.

The meaning of the "straight line approximation" in inhomogeneous systems is now clear, since this is just to assume that the tidal force can be neglected in front of the two-body force along the whole interaction, i.e

$$\frac{G(M+m)}{r^2} >> \frac{GM_0}{R_{cm}^3} r.$$

For purposes that we see below, it is convenient to define the scale parameter

$$l_{\rm tid} = \left[\frac{(M+m)}{M_0||(3\mu-\mu')(\mathbf{n}\cdot\mathbf{e}_r)\mathbf{n} - \mu\mathbf{e}_r||}\right]^{1/3} R_{cm}, \tag{5.9}$$

so that the validity of the approximations holds for $r << l_{\rm tid}$, equivalently to the anterior condition. We note, that $l_{\rm tid} \to \infty$ for systems with constant force, such as an infinite homogeneous medium.

The local approximation

Contrary to the analytical treatments of dynamical friction that suppose the satellite as a perturbation of the background, our scheme analyses directly the perturbation of the system particles on the satellite motion. In this work frame, the properties of these particles are given locally, which means that, so to say, the satellite "does not remember its orbit", i.e, the dynamical friction is independent of the previous interaction along its motion. This approximation assumes that the background remains unchanged despite of the satellite presence, having therefore a constant distribution function.

In practice, this allows us to treat the global properties of the systems locally by expanding the spatial distribution function $n(\mathbf{r})$ as

$$n(\mathbf{r}) = n(\mathbf{r}_M) + \nabla n\big|_{\mathbf{r}_M}(\mathbf{r}-\mathbf{r}_M) + \mathcal{O}\left(\frac{r-r_M}{r}\right)^2, \tag{5.10}$$

if the distribution function takes the form $F(\mathbf{r},\mathbf{v}) = n(\mathbf{r})f(\mathbf{v})$, where the spatial dependence of the distribution function in velocity space is neglected by means of the local approximation.

One can see that this approximation is only valid if (i) the satellite does not alter dramatically the distribution function of the system and (ii) the distribution function accomplishes that at $\mathbf{r}$

$$r - r_M << \left.\frac{n}{\nabla n}\right|_{r_M 0} \equiv l,$$

where l is density scale-length.

For following calculations, it is useful to define the density gradient vector,

$$\hat{\mathbf{n}} = \frac{\nabla n(r_M)}{||\nabla n(r_M)||}. \tag{5.11}$$

5.2 Dynamical friction in inhomogeneous systems

We make use of the perturbation theory in order to determine the change over the satellite velocity due to encounters with field particles. This scheme is a fair approximation since galaxies have a huge particle number with much lower mass than that of the satellite, which we consider as a rigid body. Interactions satellite-background particle are treated as two-body collisions, neglecting the case of higher number of encounters occurring at once due to its scarce probability.

Consider first that the mass M travels through a background of infinite number of particles of mass m. The system is not homogeneous but has a distribution function $f(\mathbf{x}, \mathbf{v}_m)$. We are interested in the study of dynamical friction in systems with an axi-symmetric distribution function, which is assumed to be Gaussian in the velocity space

$$\begin{aligned} f(\mathbf{x}, \mathbf{v}_m) &\equiv n(\mathbf{x}) f(\mathbf{v}_m) \\ f(\mathbf{v}_m) &\equiv \frac{1}{(2\pi)^{3/2}} \frac{\exp[-(v_R^2/2\sigma_R^2 + v_z^2/2\sigma_z^2)]}{\sigma_R^2 \sigma_z}, \end{aligned} \tag{5.12}$$

where (σ_R, σ_z) are the components of the velocity distribution spheroid oriented to the axi-symmetry plane and accomplishing that $\sigma_R > \sigma_z$. These both quantities are constant, being related by the definition of eccentricity $e_v^2 \equiv 1 - \sigma_z^2/\sigma_R^2$. The results obtained for such a distribution can be extrapolated to spherical symmetric systems in the limit $e_v = 0$.

By means of the straight line approximation, the change of velocities experienced by a particle of mass M, moving with velocity $\mathbf{v}_M$, due to a encounter with a much lighter particle of mass m with velocity $\mathbf{v}_m$ is (BT, eqs. 7-10)

$$\begin{aligned} |\Delta \mathbf{v}_{M\perp}| &= \frac{2mbV_0^3}{G(M+m)^2} \left[1 + \frac{b^2 V_0^4}{G^2(M+m)^2}\right]^{-1} \\ |\Delta \mathbf{v}_{M\parallel}| &= \frac{2mV_0}{M+m} \left[1 + \frac{b^2 V_0^4}{G^2(M+m)^2}\right]^{-1}, \end{aligned} \tag{5.13}$$

where $\mathbf{V}_0 = \mathbf{V}(t = -\infty)$, $\mathbf{V} = \mathbf{v}_m - \mathbf{v}_M$ being the relative velocity between both particles,and b their impact parameter. The notation assumes the perpendicular and parallel values of $\Delta \mathbf{v}_M$ with respect to the vector $\mathbf{V}_0$. We define

$$a(V_0) = \frac{G(M+m)}{V_0^2},$$

to simplify the notation. We note that this quantity has distance dimension and corresponds to the impact parameter with 90° deflection..

5.2.1 Encounter rate and mean-filed correction

Following Binney's calculus, we shall define a coordinate system such the z-axis is parallel to the relative velocity $\mathbf{V}_0$ and the x-axis parallel to the unity vector $\hat{\mathbf{x}} \equiv [(\mathbf{V}_0 \times \nabla n) \times \mathbf{V}_0]/\|(\mathbf{V}_0 \times \nabla n) \times \mathbf{V}_0\|$. Let θ be the angle between $\mathbf{V}_0$ and ∇n.

In this frame the rate at which M encounters "stars" that have velocities in the velocity-space element $d^3\mathbf{v}_m$ and impact-parameters between $\mathbf{b}$ and $\mathbf{b} + \mathbf{db}$ is

$$d\nu = bdb \cdot d\phi \cdot V_0 \cdot f(r, \mathbf{v}_m) d^3\mathbf{V}_0 \equiv dA \cdot V_0 \cdot f(r, \mathbf{v}_m) d^3\mathbf{V}_0, \tag{5.14}$$

where $dA = bdbd\phi$ is the element of area in the plane with normal vector $\mathbf{V}_0$. The fact that the distribution function remains constant along the relative velocity direction, with the rate of encounters being proportional to V_0, is a direct consequence of the straight line approximation. Had the presence of the main field produced by the inhomogeneous density profile taken into account, the centre-of-mass of the two-body systems would be accelerated, leading to a time-dependent encounter rate (see Section 5.2). Even if employing the straight line approximation, it is necessary to subtract the mean-field force that appears when integrating along the $\mathbf{V}_0$ direction due to the inhomogeneity of the spatial distribution function. Denoting the mean-field force within the interval $z, z + dz$ as $dF_{\rm mf}$ we have by symmetry that

$$\begin{aligned} d\mathbf{F}_{\rm mf} &= \frac{Gmf(r, \mathbf{v}_m) dA dz d^3\mathbf{V}_0}{b^2 + z^2}(\mathbf{b}, \mathbf{z}) \\ \mathbf{F}_{\rm mf} &= Gmf(r, \mathbf{v}_m) d^3\mathbf{V}_0 dA \int_{-\infty}^{\infty} \frac{(\mathbf{b}, \mathbf{z})}{b^2 + z^2} dz \\ &= 2Gmf(r, \mathbf{v}_m) dA d^3\mathbf{V}_0 \frac{\mathbf{b}}{b^2}, \end{aligned} \tag{5.15}$$

the only term that survives is that parallel to the impact parameter vector. The main-field contribution, therefore, shall be removed when integrating over the perpendicular change of the satellite velocity.

5.2.2 Integration over impact parameters

The contribution to the force is due to the particle flow across the plane $(\mathbf{r} \times \mathbf{V}_0) = 0$ in the element of area dA (see Fig 5.1). The coordinates in the plane are $\mathbf{x} = (x, y, 0)$.

The integration over b is carried out in the interval (b_0, b_1), b_0, b_1 being the minimum and maximum impact parameters, respectively. The physical meaning of these two quantities is up to now an open topic of discussion.

Usually, if the satellite is a point-mass, b_0 is interpreted as the impact parameter for which the angle deflection is $\pi/2$, whereas it is estimated as $b_0 \simeq r_h$ for an extended body, where r_h is the half-mass radius.

The concept of maximum impact parameter is even harder to discern. Initially it was used to avoid the divergence of the spatial integration of eqs. (5.13), relating its concrete value to the mass extension of the system. Due to the dependence of the satellite dynamics on the parameters of the numerical calculations (such as the particle number, resolution ...etc), the value of b_1 is fitted to the resulting curves. Recently, Hashimoto, Funato & Makino (2002) have claimed the possibility of a maximum impact parameters that linearly depend on the satellite galacto-centre distance, observing a quantitative improvement of the fit to the numerical results.

For completeness, the value of b_1 must agree with the diverse approximations employed along our study.

(i) The local approximation. The integration over b cannot be extended to distances larger than $n(\mathbf{r})/\nabla n(\mathbf{r})$, for which this approximation loses its validity, thus

$$b_1 \leq \frac{n(\mathbf{r})}{\nabla n(\mathbf{r})} \equiv l,$$

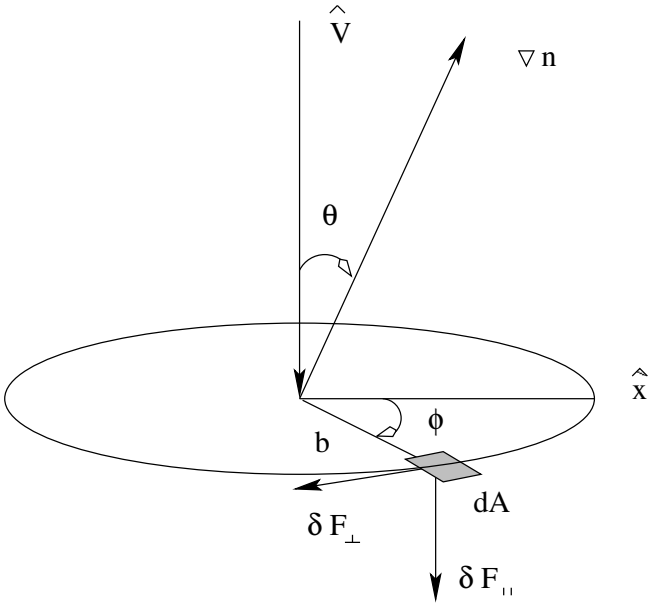

Figure 5.1: Coordinate system used along our calculi.

(ii) The straight line approximation and the perturbation theory. These both schemes imply that the collision time ($\tau_{\rm col} \equiv 2b/V_0$) must be shorter than the local dynamical time ($\tau_{\rm dyn} \equiv l/v_M$). In this case, since the encounter occurs in a short time, the line straight approximation simplifies the approach of the particle m to the particle M as a straight line, and the perturbation theory can be employed since the velocity change of M is small. This condition can be written as

$$\tau_{\rm col} = \frac{2b}{V_0} << \tau_{\rm dyn} = \frac{l}{v_M}.$$

Combining (i) and (ii) one finds that, according with our scheme, the maximum impact parameter is

$$b_1 = l \cdot \min\left[1, \frac{V_0}{2v_M}\right],$$

which can be approximated by the function

$$b_1^2 \simeq b_0^2 + Q^2 l^2 \frac{V_0^2}{4v_M^2 + V_0^2}, \tag{5.16}$$

guaranteeing $b_1 > b_0\ \forall V_0$. The factor Q is introduced *ad hoc* to fit to the numerical data.

Integration at order 0

For comparison, we include the calculus of dynamical friction at order 0 of the spatial distribution expansion around the satellite position $\mathbf{r}_M$, which corresponds to Chandrasekhar's formula. The integration over the perpendicular velocity change is zero by symmetry, so that at this order only the parallel component contributes to the friction force. From eq. (5.13)

$$\begin{aligned}\mathbf{F}^{(0)} &= \int d^3V_0 n(r_M) f(\mathbf{v}_m) \frac{2Gm}{a(V_0)} \frac{\mathbf{V}_0}{V_0^2} \int_{b_0}^{b_1} db \frac{b}{1 + b^2/a^2(V_0)} \int_0^{2\pi} d\phi \\ &= 4\pi G^2 m(M+m) n(r_M) \int d^3V_0 \frac{\mathbf{V}_0}{V_0^2} f(\mathbf{v}_m) \ln\Lambda,\end{aligned} \tag{5.17}$$

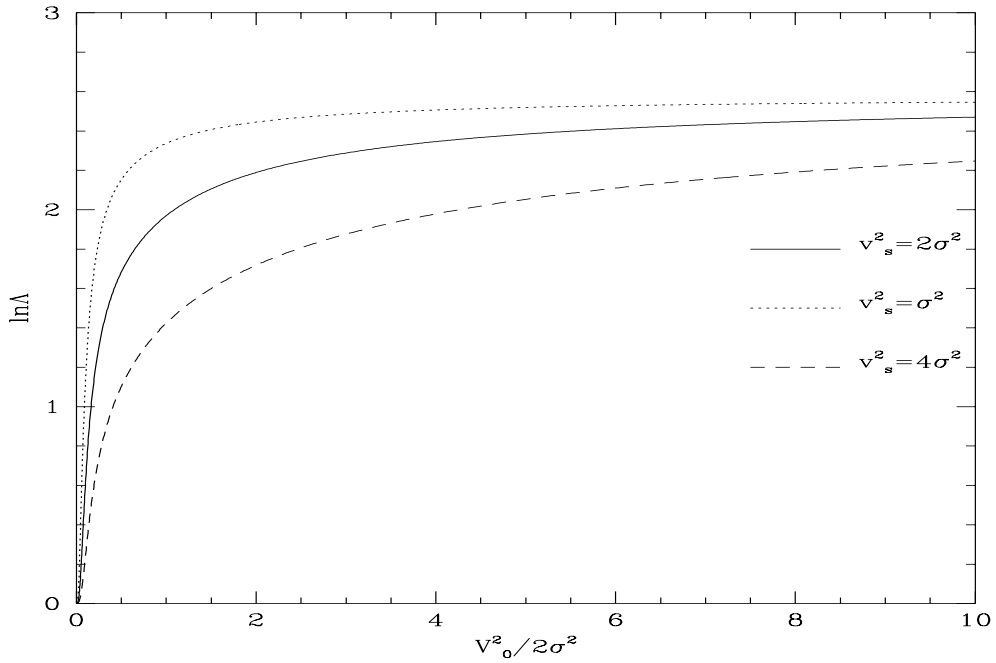

Figure 5.2: Coulomb logarithm as a function of V_0. We use a singular isothermal model for the galaxy density profile and a mass ratio of $M/M_g = 0.01$, where $M_s = 0.1$.

where

$$\Lambda \equiv \left[\frac{1 + b_1^2/a^2(V_0)}{1 + b_0^2/a^2(V_0)}\right]^{1/2} \tag{5.18}$$

is the so-called 'Coulomb factor'. In the literature, one usually finds that $\Lambda = b_1/b_0 = \text{const} \gg 1$, neglecting, therefore, its velocity dependence (i.e, assuming $a(V_0) = a(V_0 = \sigma)$. To illustrate the order of accuracy of this assumption, in Fig. 5.2 we plot the resulting Coulomb logarithm of inserting eq. (5.16) into (5.18), denoted as $\ln\Lambda(v_s, V_0)$, for three different values of the satellite velocity. As we can see, it approaches asymptotically to a given value as the relative velocity increases, whereas it tends to zero for $V_0 \to 0$, which represents a natural cut-off for dynamical friction at low relative velocities. It interesting to note that, in the regime of high satellite velocities, the variability of $\ln\Lambda$ increases.
The approximation of choosing a constant Coulomb factor, whose value describes the satellite decay in numerical calculations, can be interpreted as the average over a certain range of satellite velocities, for which the Coulomb logarithm within $v_M \pm \sigma$ is considered constant (note that, since the velocity distribution is Gaussian, the maximum contribution to the friction force comes from those background particles with $V_0 = v_M$).

Integration at 1st order

After integrating over $d\phi$ one can readily check that the only term surviving is that parallel to $\mathbf{b}$, which corresponds to the perpendicular component of the velocity change. After correcting the mean-field effects of eq. (5.15) one has

$$\Delta\mathbf{v}_{M\perp} d\nu - \mathbf{F}_{\rm mf} = -2Gm\nabla n(\mathbf{r}) \frac{f(\mathbf{v}_m)}{V_0} \frac{\mathbf{b}}{b^2} \left[1 + \frac{b^2}{a^2(V_0)}\right]^{-1} dA d^3V_0,$$

which, after the integration over the impact parameters, leads to the force

$$\begin{aligned}\mathbf{F}^{(1)} &= -2Gmn(r_M)\int d^3V_0 f(\mathbf{v}_m)\int_{b_0}^{b_1}\frac{db}{b^2}\left[1+\frac{b^2}{a^2(V_0)}\right]^{-1} \\ &\qquad\times\int_0^{2\pi}\mathbf{b}(\cos\phi,\sin\phi)\frac{\nabla n(r_M)}{n(r_M)} \\ &= -\frac{2\pi Gmn(r_M)}{l}\sin\theta\int d^3V_0 f(\mathbf{v}_m)a^2(V_0)\ln\Lambda\cdot\hat{\mathbf{x}},\end{aligned} \tag{5.19}$$

where $\hat{\mathbf{x}}$ is a vector perpendicular to $\mathbf{V}_0$, $\ln\Lambda$ the Coulomb logarithm defined in eq. (5.18) and θ the angle between ∇n and $\hat{\mathbf{V}}_0$.

5.2.3 Integration over velocity space

The equations for the parallel and perpendicular terms of dynamical friction are integrated for systems with velocity distributions presented in eq. (5.12).

Integration at order 0

The integration at order 0 is given in Binney (1977). For completeness, we reproduce the calculus.

Assuming that the Coulomb logarithm is constant, one has that from eq. (5.17) the integration over velocity is actually equivalent to the force integration of the "mass distribution" $f(\mathbf{v}_m)$, [1]

$$\int d^3v_m\frac{\mathbf{V}_0}{V_0^2}f(\mathbf{v}_m)\ln\Lambda = \langle\ln\Lambda\rangle\frac{d}{d\mathbf{v}_M}\int d^3v_m\frac{f(\mathbf{v}_m)}{V_0}, \tag{5.20}$$

where $\langle\ln\Lambda\rangle$ is the averaged Coulomb logarithm.

Rewriting the distribution function (5.12) in elliptical coordinates one has

$$f(m^2) = \frac{1}{(2\pi)^{3/2}}\frac{\exp[-m^2]}{\sigma_R^2\sigma_z}, \tag{5.21}$$

where

$$m^2 = \frac{v_R^2}{2\sigma_R^2}+\frac{v_z^2}{2\sigma_z^2}.$$

The velocity distribution is therefore formed by equivalent homeomoids with constant axis-ratio, which allows us to use the scheme found by Chandrasekhar (1960) to derive the "potential" for such a distribution $f(\mathbf{v}_m) = f(m^2)$ at the "point" $\mathbf{v}_M$. The integrals $I_i = \nabla_i V$ can be written,

$$I_i = \int d^3v_m\frac{V_{0,i}}{V_0^2}f(\mathbf{v}_m) = \frac{d}{dv_{i,M}}\int d^3v_m\frac{f(m^2)}{V_0}.$$

Be a shell of "mass" $dM = 4\pi\sigma_R^2\sigma_z f(m^2)m^2dm$. Since the "potential" V inside a shell is constant one has that $V(\mathbf{v}_M) = V(0)$, therefore

$$dV = \frac{GdM}{4\pi\sigma_R^2\sigma_z}\int\frac{d^3v_m}{V_0} = \frac{GdM}{4\pi\sigma_R^2\sigma_z}\int\frac{d^3v_m}{v_m} = \frac{GdM}{8\pi\sigma_R^2\sigma_z}\int_S v_m^2dw,$$

where w is the solid angle integrated over the surface S.

In spherical coordinates (v_m,θ,ϕ) the modulus can be written as

$$\frac{1}{v_m^2} = \frac{\cos^2\theta}{\sigma_z^2}+\frac{\sin^2\theta}{\sigma_R^2},$$

[1] Since by definition $\mathbf{V}_0 = \mathbf{v}_m - \mathbf{v}_M$, the integration over the velocity space is independent of the infinitesimal we select, this means, the calculus is equivalent either integrating over d^3v_m or over d^3V_0.

inserting this equation and integrating over ϕ

$$dV = \frac{dM}{2}\sigma_z \int_0^{\pi/2} \frac{\sec^2\theta \sin\theta d\theta}{(\sigma_R^2 + \sigma_z^2 \tan^2\theta)^{1/2}(\sigma_z^2 + \sigma_R^2 \tan^2\theta)^{1/2}}$$

$$= \pi dM \int_0^\infty \frac{du}{(\sigma_R^2 + u)(\sigma_z^2 + u)^{1/2}},$$

where $u = \sigma_z^2 \tan^2\theta$. Integrating over dm from $m = 1$ to $m(u)$ one has that

$$I_i = \frac{d}{dv_{i,M}} \int d^3V_0 \frac{f(m^2)}{V_0} \tag{5.22}$$

$$= 2\pi\sigma_R^2\sigma_z \frac{d}{dv_{i,M}} \int_0^\infty \frac{du}{(\sigma_R^2 + u)(\sigma_z^2 + u)^{1/2}} \int_1^{m^2} f(m^2)dm^2$$

$$= -\pi \int_0^\infty \frac{dq}{\Delta(q, e_v)} f(m^2) \frac{2v_i}{\sigma_i^2/\sigma_R + q},$$

where the subindex $i = (R, z)$ and

$$\Delta(q, e_v) = (1+q)\sqrt{1 - e_v^2 + q}, \qquad q = \frac{u}{2\sigma_R^2}$$

$$m^2(u) = \frac{v_R^2}{2\sigma_R^2 + u} + \frac{v_z^2}{2\sigma_z^2 + u}.$$

Inserting the value of I_i into eq. (5.17) one finds

$$F_i^{(0)} = -\frac{\sqrt{2\pi}\rho_h(\mathbf{r})G^2M_s^2\sqrt{1-e_v^2}\langle \ln\Lambda\rangle}{\sigma_R^2\sigma_z} B_i v_i. \tag{5.23}$$

The values of B_i are in cylindrical coordinates,

$$B_R = \int_0^\infty \frac{dq}{(1+q)^2(1-e_v^2+q)^{1/2}} \exp\left(-\frac{\mathrm{v_R^2/2\sigma_R^2}}{1+\mathrm{q}} - \frac{\mathrm{v_z^2/2\sigma_R^2}}{1-\mathrm{e_v^2+q}} \right)$$

$$B_z = \int_0^\infty \frac{dq}{(1+q)(1-e_v^2+q)^{3/2}} \exp\left(-\frac{\mathrm{v_R^2/2\sigma_R^2}}{1+\mathrm{q}} - \frac{\mathrm{v_z^2/2\sigma_R^2}}{1-\mathrm{e_v^2+q}} \right).$$

As Binney shows, the mass M_s will suffer a decrease of its orbital plane inclination whenever $B_z > B_R$ (oblate halo). If the orbit is either coplanar or polar, the inclination remains constant since, respectively, either the perpendicular or the planar component of v is zero. One can easily check that this expression reproduces Chandrasekhar's when $e_v = 0$.

The reduction of the velocity integration into the potential scheme is, unfortunately, not possible for non-constant Coulomb factors, due to the dependence on $\mathbf{V}_0$ rather that on $\mathbf{v}_m$. In this case, the "density" $f(\mathbf{v}_m)\ln[\Lambda(V_0)]$ can not be expressed as a function of m^2, which makes the potential not to be constant in the inner part of a shell, the integrations being more complicate.

The simplest calculation is for a coordinate system oriented in the velocity space, where the z-axis is parallel to the velocity $\mathbf{v}_M$. Defining the vector (n_x, n_y, n_z) as parallel to the velocity dispersion ellipsoid, we have that $\mu' = \cos\theta' = \mathbf{n}_z \cdot \hat{\mathbf{v}}_m$, $\mu = \hat{\mathbf{v}}_M \cdot \hat{\mathbf{V}}_0$ and $\mu_M = \mathbf{n}_z \cdot \hat{\mathbf{v}}_M$, which accomplishes $\hat{\mathbf{v}}_m \cdot \mathbf{n}_z = \cos\theta' = \cos(\theta + \theta_M)$

$$v_m^2 = V_0^2 + v_M^2 + 2v_m v_M \cos\theta \tag{5.24}$$

$$f(\mathbf{v}_m) = \frac{1}{(2\pi)^{3/2}\sigma_R^2\sigma_z} \exp\left[-\frac{v_m^2}{2\sigma_R^2}\left(1 - \cos^2\theta' + \frac{\cos^2\theta'}{1-e_v^2}\right)\right]$$

$$= \frac{1}{(2\pi)^{3/2}\sigma_R^2\sigma_z} \exp\left(-\frac{v_m^2}{2\sigma_R^2}\right) \exp\left(-\epsilon_v \frac{v_m^2}{2\sigma_R^2}\cos^2\theta'\right),$$

where $\epsilon_v = 1/(1-e_v^2) - 1$ and, therefore, with null value if the system has isotropic velocity distribution.

Substituting the definition of v_m and θ' one finds the "simple" form of the distribution function in this coordinate system

$$f(V_0,\theta,v_M,\theta_M) = \frac{1}{(2\pi)^{3/2}\sigma_R^2\sigma_z}\exp(-X^2-W^2)\exp(-u\cos\theta) \tag{5.25}$$
$$\exp[-\epsilon_v(X^2+W^2)\cos^2(\theta+\theta_M)]\exp[-\epsilon_v u\cos\theta\cos^2(\theta+\theta_M)],$$

where $W = V_0/\sqrt{2}\sigma$, $X = v_M/\sqrt{2}\sigma$ and $u = 2WX$.

The integrals are,

$$I = \int d^3V_0 \frac{\mathbf{V}_0}{V_0^2} f(\mathbf{v}_m)\ln\Lambda(V_0)$$

$$= \int dV_0 \sin\theta d\theta d\phi \mathbf{V}_0 f(V_0,\theta,v_M,\theta_M)\ln\Lambda(V_0),$$

where it has been used that $d^3V_0 = V_0^2 dV_0 \sin\theta d\theta d\phi$. The integration over ϕ is trivial, leading to,

$$I = 2\pi \mathbf{v}_M \int_0^\infty dV_0 V_0 \ln\Lambda(V_0)\int_{-\pi/2}^{\pi/2} d\theta \sin\theta f(V_0,\theta,v_M,\theta_M). \tag{5.26}$$

The presence of θ_M in the integral accounts for the result of Binney, who obtains an anisotropic friction due to the inequality $B_z > B_R$ in eq. (5.23). This effect vanishes if neither the Coulomb logarithm nor the distribution function depend on θ as it is the case of systems with spherical symmetry. The integration over θ is not analytical if the distribution function is that of eq. (5.25).

In Appendix B we develop the integrals for the isotropic case, showing that the solution recovers Chandrasekhar's equations if the Coulomb logarithm is constant. If $\ln\Lambda$ is written in the form of eqs. (5.16) and (5.18), the integration of eq. (5.26) with $e_v = 0$ leads to

$$F^{(0)} = \frac{2\pi G^2 mn(r_M)(M+m)^2}{\sigma^2}\int_0^\infty dW \ln\Lambda g(W) \tag{5.27}$$
$$\equiv K_{\rm ch}\int_0^\infty dW \ln\Lambda g(W),$$

where

$$g(W) = \frac{2}{\sqrt{\pi}}\frac{\exp(-W^2-X^2)}{WX}\left[\cosh(2WX) - \frac{\sinh(2WX)}{2WX}\right] \tag{5.28}$$

$$\Lambda^2 = 1 + \frac{Q^2 l^2}{a^2(X)+b_0^2}\frac{X^2}{4X^2+W^2}. \tag{5.29}$$

In Fig. 5.3 we plot the dependence of the zero order dynamical friction on the satellite velocity. We use an isothermal halo to calculate the galaxy parameters due to its simplicity, which accomplishes that M/M_g is inversely proportional to the galactro-centre distance. We note that the variation of $\ln\Lambda$ is independent of the model by means of the local approximation. The fitting factor $Q = 1$. The Chandrasekhar formula is plotted for the case $\langle\ln\Lambda\rangle = 1.5$ (dashed line).
The force tends to zero for small and large velocities whereas the maximum is located around the circular velocity $v_M = \sqrt{2}\sigma$ ($X = 1$). The figure shows a decrease of the friction at small distances due to the presence of the factor l in the Coulomb logarithm. This distance dependence is not present in Chandrasekhar's formula, so that we expect strong differences in the decay curves depending on which formula we use. In the case of fixing l to some value, a proper selection of Q (or equivalently $\ln\Lambda$) will produce similar results in the orbital evolution, concluding that, the dependence of Λ on the relative velocity introduces small variations on the resulting force.

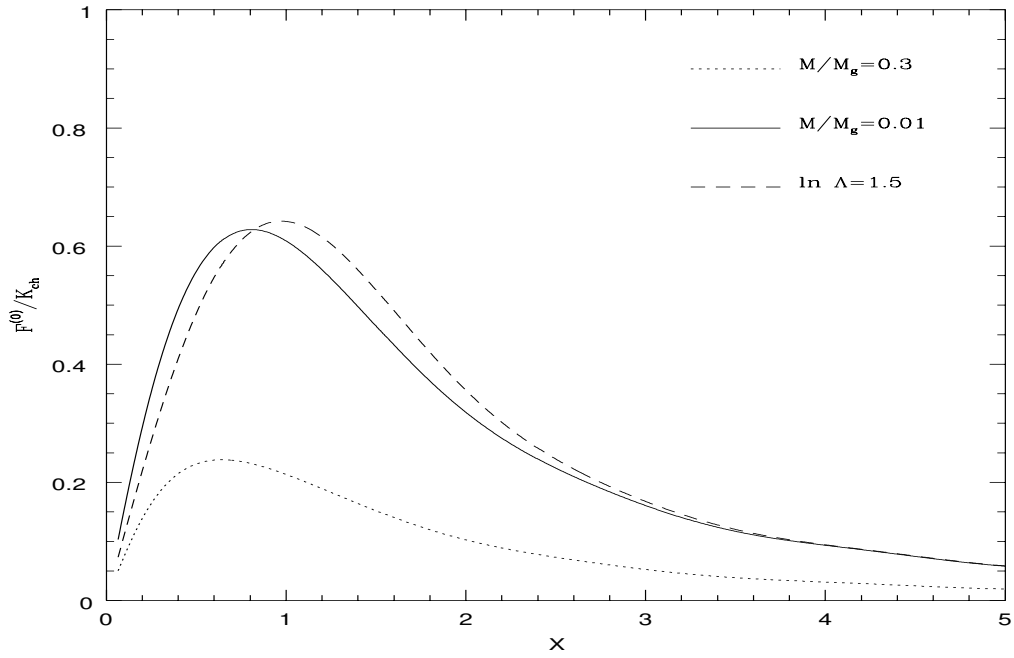

Figure 5.3: Zeroth order dynamical friction as a function of the satellite velocity and the satellite mass ratio. The Chandrasekhar friction is plotted for $\langle \ln \Lambda \rangle = 1.5$ (dashed line).

Integration at first order

The integration over velocities of the first order friction is done in a similar manner. We note that the unit vector perpendicular to the relative velocity was defined as

$$\hat{\mathbf{x}} = \frac{\hat{\mathbf{n}} - (\hat{\mathbf{n}} \cdot \hat{\mathbf{V}}_0) \cdot \hat{\mathbf{V}}_0}{||\hat{\mathbf{n}} - (\hat{\mathbf{n}} \cdot \hat{\mathbf{V}}_0) \cdot \hat{\mathbf{V}}_0||},$$

where the have made use of the freedom in the selection of ϕ.

Selecting the same coordinate system as that of the integration at order zero, we have that

$$\int_0^{2\pi} \mathbf{x} d\phi = \pi(1 + \cos^2\theta)\hat{\mathbf{e}}_\perp + 2\pi \sin^2\theta \hat{\mathbf{v}}_M,$$

where

$$\hat{\mathbf{e}}_\perp = \frac{\hat{\mathbf{n}} - (\hat{\mathbf{n}} \cdot \hat{\mathbf{v}}_M) \cdot \hat{\mathbf{v}}_M}{||\hat{\mathbf{n}} - (\hat{\mathbf{n}} \cdot \hat{\mathbf{v}}_M) \cdot \hat{\mathbf{v}}_M||}$$

is an unit vector perpendicular to the satellite velocity. We denote hereinafter "parallel" and "perpendicular" as referring to the satellite velocity vector. From eq. (5.20) the integrals are

$$I_\parallel = 2\pi \int_0^\infty dV_0 \ln(V_0) \int_{-\pi/2}^{\pi/2} d\theta \sin^3\theta \frac{f(V_0, \theta, v_M, \theta_M)}{V_0^2} \tag{5.30}$$

$$I_\perp = \pi \int_0^\infty dV_0 \ln(V_0) \int_{-\pi/2}^{\pi/2} d\theta \sin\theta(1 + \cos^2\theta) \frac{f(V_0, \theta, v_M, \theta_M)}{V_0^2}.$$

The integration over θ is only analytic for systems with isotropic distribution. The result is given, as for the zero order integration, in Appendix B being

$$F_\parallel^{(1)} = -\frac{1}{2} \frac{G(M+m)}{4\sigma^2 l} \cos\Psi K_{\rm ch} \int_0^\infty dW \ln\Lambda(W) \frac{2g(W)}{W^3 X} \hat{\mathbf{v}}_M \tag{5.31}$$

$$F_\perp^{(1)} = -\frac{1}{2} \frac{G(M+m)}{4\sigma^2 l} \sin\Psi K_{\rm ch} \int_0^\infty dW \ln\Lambda(W) \frac{2h(W) - g(W)}{W^3 X} \hat{\mathbf{e}}_\perp,$$

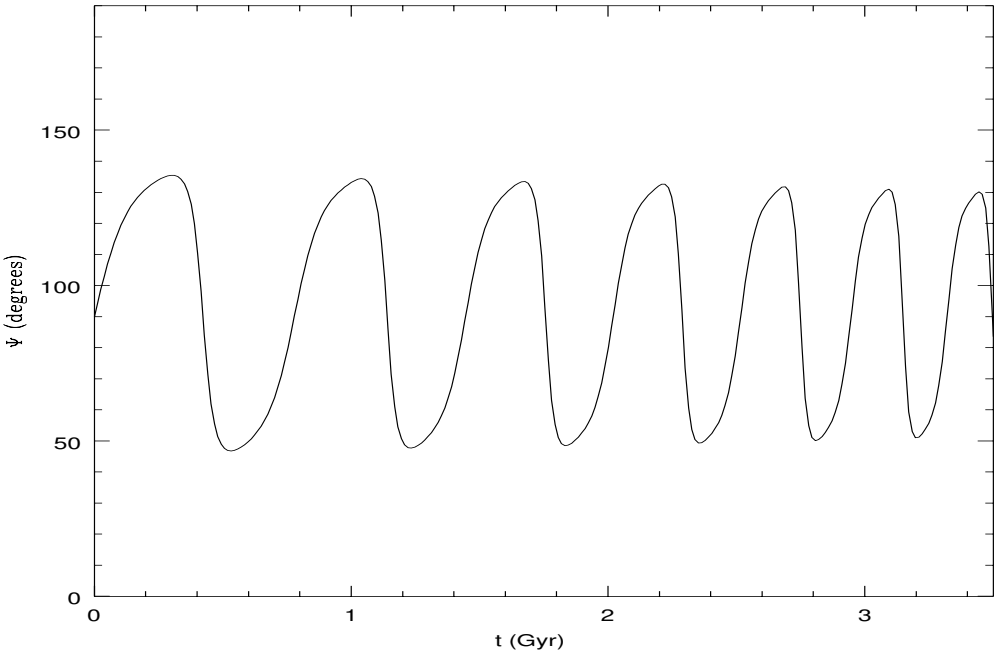

Figure 5.4: Evolution of Ψ along the orbit H1S130a.

where Ψ is defined as $\cos\Psi = \hat{\mathbf{n}} \cdot \hat{\mathbf{v}}_M$ and the function

$$h(W) = \frac{2}{\sqrt{\pi}} \exp(-W^2 - X^2)\sinh(2WX). \tag{5.32}$$

As Binney found, the first order dynamical friction diverges as the relative velocity tends to zero if the Coulomb logarithm is constant. However, taking into account the velocity dependence this divergence disappears, what avoids implementing a lower cut-off on V_0.

The first order term has been divided into two vectorial components with respect to the satellite velocity, where the magnitude of of them depends on the orientation of the orbit. Going to the extreme cases one has that, (i) circular orbits lead to the banishment of the parallel term ($\cos\Psi = 0$) whereas the perpendicular term can be considered a small correction to the main field of the galaxy expecting, therefore, no substantial effects on the orbital shape, (ii) for radial orbits the term surviving is the parallel one. In this case, the first order friction acts as a correction to the zeroth order. In Fig. 5.4we plot the typical evolution of Ψ for a satellite following an orbit with $e = (r_a - r_p)(r_p + r_a)^{-1} = 0.5$, where r_a, r_p are apo and peri-centre, respectively (this orbit corresponds to the model H1S130a, see Chapter 6). The direction between $F^{(0)}$ and $F^{(1)}$ varies within a range of 40^o, whereas $\Psi = \pi/2$ corresponds to the apo and peri-centre passages.

In Fig. 5.5 we show the amplitude of the first order friction compared to the zeroth order. The main difference between is that, whereas $F^{(0)}$ tends to zero for small satellite velocities, the first order has a non-zero value for $X = 0$, which causes the radio to diverge in this limit. The ratio decays quickly with increasing velocities since this term is proportional to $1/v_M^4$ (meanwhile $F^{(0)} \propto 1/v_M^2$). We also observe no strong differences between the amplitude of the first order components.

It is interesting to remark the smaller dependence of $F^{(1)}$ on the mass ratio (i.e galacto-centre distance) as compared to the zeroth order term. This is due to the presence of the factor $l = r_M/2$ in the denominator. This fact accounts for the increase of the first order friction as the satellite goes to inner regions of the system and *viceversa* when it moves outwards. However, the Coulomb logarithm has the opposite dependence on the satellite distance, which reduces the final decrease of $F^{(1)}$ for increasing radii.

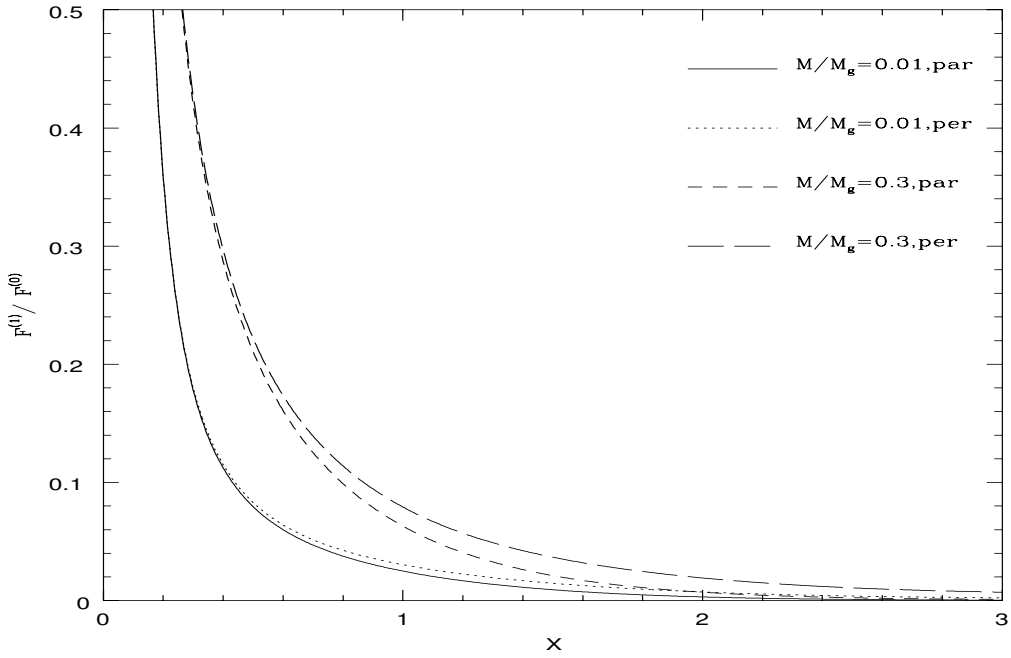

Figure 5.5: Ratio of the components of the first order dynamical friction and the zeroth order for different velocities and mass ratios.

After analysing the amplitude and direction of the first order force, we expect small changes over the satellite orbit if this term is included, which will be studied in detail in Chapter 6 by comparison with numerical calculations. If this is the case, and the new term can be neglected we consider not necessary a further study in systems with anisotropic velocity distribution.

Chapter 6

Dynamical friction in spherical systems

6.1 Introduction

In Chapter 5 we have presented the different approaches to dynamical friction obtained by means of the perturbation theory. Here, we attempt to determine the degree of accuracy of each of them in order to reproduce the dynamical friction effects in systems with spherical symmetry and density profile $\rho(r)$.

The additional use of the local approximation allows the separation between the effects of the parallel and perpendicular components of the velocity change, with respect to the relative velocity of the encounter which, after integrating over the impact parameters, correspond to the zeroth ($F^{[0]}$) and first ($F^{[1]}$) order of dynamical friction, respectively. The integration over the spatial part of the impact parameter space introduces in both orders a new function $\ln\Lambda$, the so-called Coulomb logarithm. Following the local approximation, we have shown in Section 5.2 that it depends on V_0, v_s, l, the relative velocity, the satellite velocity and the scale length $l = \left|\rho/\nabla\rho\right|$, respectively. After integrating over the velocity part of the impact parameter space d^3V_0, the Coulomb logarithm accomplishes that $\Lambda = \Lambda(v_s, l)$.

Our investigation covers the following studies,

- Case 1: **Standard dynamical friction: calculus at zeroth order with constant Coulomb logarithm**.
  Authors have usually employed this approximation to calibrate the semi-analytic codes by fitting the data to the numerical results. Following this scheme, the Coulomb logarithm is considered as a free parameter, where the dependence on the density profile, the satellite velocity and the relative velocity are neglected, by the fact that the logarithm varies slowly in the range of l, v_s along a typical orbit and that the integration over dV_0 is mainly weighted by values of V_0 where the Coulomb logarithm is practically independent of the relative velocity. Along the orbit, the approximation of Λ independent of l and v_s is equivalent to consider the average over these two factors. From eq. (5.17)

  $$\langle \ln\Lambda \rangle = \frac{1}{T}\int_C dt \frac{\int d^3V_0 \mathbf{V}_0/V_0^2 f(\mathbf{v}_m)\ln\Lambda(l, v_s, V_0)}{\int d^3V_0 \mathbf{V}_0/V_0^2 f(\mathbf{v}_m)}, \tag{6.1}$$

  where C denotes the satellite orbit and T the period. The distribution function in the velocity space is $f(\mathbf{v}_m)$ and $\mathbf{V}_0$ the relative velocity of the two-body encounter. If the Coulomb logarithm is fitted to a set of orbits, this average extends to a sum over these orbits.

- Case 2a: **Dynamical friction at zeroth order with** $\Lambda = \Lambda(v_s, V_0)$.
  Instead of using a constant parameter $\langle \ln\Lambda \rangle$, in Chapter 5 is presented a Coulomb factor that

explicitely gives the function $\Lambda = \Lambda(v_s, V_0, l)$ (see eq. 5.28), which is developed in order to introduce the diverse limits that the perturbation theory and the local approximation induce when integrating over the impact parameter space. Despite that this expression depends on the galacto-centre distance through the typical distance l, we also carry out calculations where l is fixed to the initial value $\left|\rho/\nabla\rho\right|_{r_0}$, where r_0 is the initial distance, in order to compare explicitely the effects of the velocity dependence (v_s) in the Coulomb logarithm. The fitting procedure that we present below leads to the value of χ that better fits to the numerical data, which is equivalent to the average over l. One expects this average to be more accurate the more circular the orbit is, since the range of variation of v_s is smaller.

- case 3a: **Dynamical friction at zero order with** $\Lambda = \Lambda(v_s, V_0, l)$.
  The value of l is calculated at each point and introduced in the Coulomb logarithm in order to integrate over d^3V_0. In a recent paper Hashimoto, Funato & Makino (2002) carry out N-body simulations in order to analyse the effects of the linear dependence of the Coulomb factor on the galacto-centre distance, finding that the semi-analytical orbit fits better to the numerical one if $\Lambda = r_s/1.4\epsilon$, where ϵ is the softening scale-length of the N-body code, interpreted as the minimum impact parameter. Moreover, since dynamical friction is reduced at the peri-galacticon passages, the excessive orbit circularisation suffered by the satellite if using Chandrasekhar's formula with constant $\langle \ln \Lambda \rangle$ is reduced. Unfortunately, they only use one orbital model, so that it is unclear whether this approach of dynamical friction also produces accurate fits for a set of orbits with different eccentricities. It is important to remark that they treat the satellite as a point-mass, which can be approximated as a Plummer sphere with core radius equal to the smoothing-length of the numerical code. The role played by the satellite mass loss in determining the orbital dynamics is ambiguous if a comparison between our results and those of Hashimoto, Funato & Makino (2002) is performed since, as we show below, the general behaviour of the radial evolution clearly shows strong differences.

- Case 4b and 5b: **Dynamical friction at first order**.
  We include the first order terms of dynamical friction, which arise from the system inhomogeneity, in order to investigate the effects on the satellite orbit. We do not include the analysis for $\ln\Lambda$ =const since this approach leads to a divergent solution of $F^{(1)}$ when integrating over dV_0. Binney (1977) found a possible solution by including *ad hoc* a lower cut-off for small relative velocities, which should be treated as a free-parameter. To avoid the presence of this term, this study is carried out using a the Coulomb logarithm defined in the eq. (5.28) for the two averages of Λ corresponding to the cases 2 and 3.

We employ the galaxy model presented in Chapter 3 for this analysis. We carry out a set of numerical calculations, where the initial system is builded following the scheme presented in Section 2.2. and evolved by SUPERBOX. Subsequently, the semi-analytic code of Chapter 4 is used to fit this data with the different theoretical analysis. The satellite mass evolution is calculated from the numerical data (see Section 4.3) and introduced as an external input in the semi-analytic code to avoid the possible discrepancies induced by the theoretical mass loss scheme. Even though, the treatment of the satellite as a point-mass neglects effects such the change of angular momentum due to an anisotropic mass loss and those arising from the galaxy potential acting on the tidal arms, which may alter the satellite orbit whenever the mass change becomes important.

6.2 Numerical calculations

6.2.1 Galaxy and satellite parameters

The selection of the satellite and galaxy parameters used along our study is outline in Chapter 3.

We analyse dynamical friction in the spherical halo H1. This will permit the analyse of the disc and bulge effects on the satellite dynamics in a following Chapter.

The values of the galaxy and satellite (S1 model) parameters can be found in the Tables 3.1 and 3.2, respectively.

6.2.2 N-body parameters

The numerical simulations were carried out by using the particle mesh-code SUPERBOX (see Chapter 2) to evolve the galaxy-satellite system.

The system used was exactly that of PKB, with the difference that we remove the disc and bulge components. In this paper a detailed description of the system and the grid structure is presented, whereas here we merely summarise the most important orbital parameters.

Our integration time step is 0.39 Myr which is about 1/25th the dynamical time of the satellite. We have three resolution zones, each with 64^3 grid-cells: (i) The inner grid covers out to 3 radial disc scale-lengths, providing a resolution of 350 pc per grid-cell. (ii) The middle grid covers the whole galaxy, with an extension of 24 disc scale-lengths (84 kpc), giving a resolution of 2.8 kpc per grid-cell. The satellite always orbits within this grid except when it reaches the disc, avoiding cross-border effects (see Fellhauer et al. 2000). (iii) The outermost grid extends to 348 kpc and contains the local universe, at a resolution of 11.6 Kpc.

As for the satellite grid-structure, the resolutions are 816 pc per grid-cell for the inner grid that extends to 24.48 kpc, and 1.2 kpc per grid-cell for the middle grid which extends to 36 kpc. Only the inner and middle grids move along with the satellites, remaining positioned on their centre-of-density locations. The outer grid is identical for primary galaxy and satellite.

6.2.3 Orbital parameters

We carry out a set of calculations varying the parameters of the satellite that remark the differences between the different analytical treatments, when applying both of them to the decay of a satellite within a spherical halo. By symmetry, the initial orbital inclination is irrelevant to the satellite dynamics. For the analysis of Chandrasekhar's expression using diverse Coulomb logarithms we concentrate our study on the satellite's initial orbital eccentricity, defined as $e = (r_a - r_p)/(r_a + r_p)$, where r_a, r_p are the apo and peri-galacticon, respectively, since other orbital and satellite parameters are not changed. With this definition, $e = 0$ implies circular orbits and $e = 1$ radial orbits.

The eccentricity evolution may be an indicator of the accuracy of the analytical expressions and may also determine whether it is necessary to include additionally the perpendicular term of dynamical friction. The study of the effects of this term should cover a wider range of satellite masses, since the specific friction at first order goes as $F^{(1)} \propto M_s^2$ whereas $F^{(0)} \propto M_s$. However, this goes beyond our aim, since the purpose of this study is merely the qualitative analysis of the first term effects and not a detailed parameter survey.

The system galaxy-satellite is constructed as follows: Before injecting the satellite into the primary galaxy we allow the galaxy and satellite to settle into a stationary state by integrating the isolated systems for a few dynamical times with SUPERBOX (as in Kroupa 1997). Examples of the stationarity of multi-component galaxies are given in Boily, Kroupa & Peñarrubia (2001). The satellite is then placed at apo-galacticon with a velocity determined by the circular velocity at the initial distance and the desired eccentricity.

The parameters of the numerical experiments are listed in Table 6.1. We denote our numerical experiments as H1+S1+character, which means that the parent galaxy and the satellite are described by the models H1 and S1, respectively, whereas the character defines the initial orbital eccentricity.

6.3 The fitting procedure

The analytical expressions presented in Chapter 5 have two free parameters once the orbit and the satellite model are fixed, namely, the averaged Coulomb logarithm $\langle \ln \Lambda \rangle$ and the fitting factor Q.

Name	Gal. model	Sat. model	e	r_p [kpc]	r_a [kpc]
H1S1a	H1	S1	0.5	18.0	55.0
H1S1c	H1	S1	0.0	55.0	55.0
H1S1d	H1	S1	0.7	8.5	55.0
H1S1e	H1	S1	0.3	27.5	55.0
H1S1f	H1	S1	0.6	12.3	55.0
H1S1g	H1	S1	0.8	5.3	55.0

Table 6.1: The numerical experiments. The peri- and apo-galactica are r_p and r_a, respectively, and $e = (r_a - r_p)/(r_a + r_p)$ is the orbital ellipticity .

Authors usually fit by eye these two values to numerical data, the semi-analytic orbit approaching as much as possible to the numerical one, so that the overall orbital evolution is reproduced. This procedure can actually be considered as the "calibration" of the semi-analytic code, which must be done carefully if a detailed inter-comparison between different schemes of dynamical friction is desired. For that reason we present in what follows a method to describe the accuracy of the semi-analytic scheme.

We propose the parameter χ to measure the degree of exactitude of the fit, where

$$\chi^2 = \frac{1}{k}\sum_{i=1}^{k}\left[(x_i - x_{i,n})^2 + (y_i - y_{i,n})^2 + (z_i - z_{i,n})^2 + \sigma^2(r_0)(t_i - t_{i,n})^2\right],, \tag{6.2}$$

(x, y, z) being the Cartesian components of the position at the peri and apo-galactica and t the time at which the satellite passes by these points. The subindex n denotes the numerical values and $\sigma(r_0)$ the velocity dispersion at the initial galacto-centre distance. The sum is over a given number of orbits k.

We note that this selection of the fit accuracy may be weighted by the fit at the apo-galacticon points $\Delta r_i/|r_i|$ and $\Delta t/t$ instead of the absolute values. However, this has been proved to smooth the dependence of χ on the Coulomb logarithm and Q, making harder the selection of these free parameters.

The definition of the fitting factor accounts for the divergence of the numerical and semi-analytical satellite position vector and also the possibility that the curves of both radial evolutions become out-of-phase in time. By definition, χ is equivalent to the discrepancy between the numerical and semi-analytical position evolution per unit orbit. The selection of the maximum and minimum galacto-centre distances for comparison permits a direct control over the orbital eccentricity evolution, although the measure of χ can be extended to the other points without loss of generality.

The value of k depends on the objectives of the study. For instance, if the aim is to find the best calibration for long times, as it may be to reproduce the satellite decay in spiral galaxies, the number of orbits should cover most of the orbit evolution. In this Chapter, however, we pretend to clarify the effects of the first order of dynamical friction. Due to its small magnitude, these effects are expected to be at least comparable to those induced by the mass loss and other physical processes, such the galaxy feed-back. For that reason, we limit our fit to the first satellite orbits, namely, $k = 2, 3$, for which we expect the first order of dynamical friction to dominate over the other secondary processes (we note that for $k = 2, 3$ the mass loss is always smaller than 10% even for radial orbits). In some cases, however, the differences that the analytical models generate are too small to differentiate the orbits, being forced to enhance the value of k.

6.4 Dynamical friction analysis

The aim of this Section is to answer two questions: (i) which of the five approaches presented above produce the best fit to the numerical data and, therefore, comes closer to the best description of

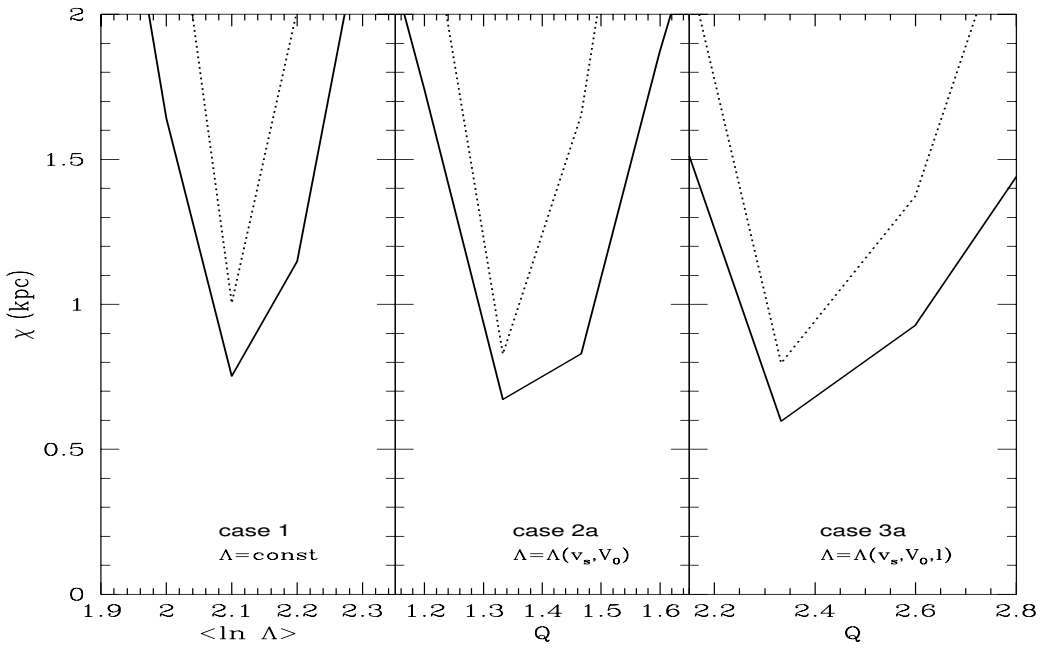

Figure 6.1: χ values as a function of the free parameters $\ln\Lambda$ and Q for the satellite orbit H1S130a. We plot the result of the approaches denoted as case 1, 2 and 3 presented above. The measure of χ is done for two number of orbits, $k = 3, 4$ (solid and dotted lines respectively). The x-axis measures the $\ln\Lambda$ for the case of constant Coulomb logarithm, whereas for the other cases the functional parameter is Q.

dynamical friction in spherical systems, and (ii) which are the differences that each approach introduce on the satellite orbit evolution, putting especial emphasis on the problem of the orbit circularisation.

6.4.1 Comparison between the different approaches

We make use of the fitting factor χ to fix the free parameters $\langle\ln\Lambda\rangle$ and Q. Associated with each fit is the error per unit orbit, defined as the fitting factor of the best fit, which allows the determination of the quality of each dynamical friction approach in order to describe the numerical data.

Fitting a given simulation

First, we develop the fitting analysis for a given numerical calculation. In Fig. 6.1, we plot the function $\chi = \chi(\langle\ln\Lambda\rangle)$ and $\chi = \chi(Q)$ for the model H1S130a, which we suppose to be a representative case. Evidently, the best fit corresponds to the minimum of each curve. The calculus was done for $k = 3, 4$ since $k = 2$ produce barely differences between the different analytical approaches.

Contrary to the results of Taylor & Babul (2001), the fit accuracy is very sensitive to the selection of the Coulomb logarithm, since the fitting parameter χ shows strong discrepancies for small variations of $\langle\ln\Lambda\rangle$. This behaviour changes if the free parameter is inside the Coulomb logarithm and not the Coulomb logarithm itself. In this case, the shallower dependence of $\ln\Lambda$ on Q makes harder the selection of the best fit (note that $d\ln\Lambda = 1/\Lambda \cdot d\Lambda/dQ \cdot dQ \leq dQ$).

The results schemed in Table 6.2 shows a similar degree of accuracy independently of how the Coulomb logarithm is averaged. This is actually not surprising since:

Case	Order	k	$\langle \ln \Lambda \rangle$	$Q_{\min}$	$\chi_{\min}$(kpc)
1 lnΛ=const	zero	3	2.1		0.7
	zero	4	2.1		1.0
2a $\Lambda = \Lambda(v_s, V_0)$	zero	3		1.3	0.8
	zero	4		1.3	1.0
3a $\Lambda = \Lambda(v_s, V_0, l)$	zero	3		2.3	0.6
	zero	4		2.3	0.8

Table 6.2: Results of the fitting procedure applied to the numerical calculation H2S130a for each of the five approaches of dynamical friction. The second column, denoted as "order" represent the order of the force expansion, so that "zero" means dynamical friction treated at zero order and "first" at first order.

(i) As several authors have shown, a constant Coulomb logarithm has shown to be a good approximation in order to reproduce dynamical friction in spherical systems. The reason can be found in the shallow dependence of a logarithmic function on its variable (for the model H1S130a, the value of $v_s^2/2\sigma^2$ lies within the range $[0.7, 1.5]$). Taking into account that the largest contribution of the background particles to dynamical friction is from those with $V_0 \simeq v_s$, one can readily check in Fig. 5.2 shows that the value of the Coulomb logarithm is approximately 2.1, which corresponds to the averaged value along the orbit.
(ii) The dependence of the Coulomb logarithm on the relative velocity V_0 leads to small differences. This can be explained by the main weight of the velocities $V_0/\sqrt{2}\sigma \sim 1$ in the integral over dV_0 where, for this range of satellite velocities, the Coulomb logarithm can be considered constant.
(iii) Lastly, the inclusion of the typical distance $l \equiv \rho/\nabla\rho$ improves the accuracy of the fit in around 40%. This will be discussed in detail in following sections.
We note that the value of $Q_{\min}$ is larger than in the case 2a, so that dynamical friction at the peri-galactica is of similar magnitude in both approximations.

The different analysis of dynamical friction produce discrepancies to the numerical data that barely increase if the average is done for an additional orbit ($k = 4$), which indicates that the value of free parameters that lead to $\chi_{\min}$ may also produce the best for the rest of the orbit. This is analysed in following sections.

The best fit produces discrepancies of around $\chi_{\min} = 1$ kpc per unit orbit which, for the model H1S130a, represents differences in the orbital eccentricity of $de/e \simeq 3\%$ and of the order of 4 per cent in the radial amplitude. It is unclear whether these small discrepancies are purely due to our treatment of dynamical friction or, however, are produced by other physical processes such the system feedback and mass loss or, however, by numerical reasons, such the code resolution, the time-step selection...etc. Nevertheless, new implementations of the semi-analytic code in order to decrease χ is beyond our purposes.

Fitting a set of simulations

We expect higher discrepancies between the numerical data and the different semi-analytical approaches since the range of variation of the orbital parameters enhances the larger the number of simulations to fit. For instance, nearly circular orbits accomplish that $l, v_s \simeq$const along their evolution, which makes $\Lambda = \Lambda(v_s, V_0)$ and $\Lambda = \Lambda(v_s, V_0, l)$ to be similar to the averaged Coulomb logarithm $\langle \ln \Lambda \rangle$, contrary to high eccentric orbits, which suffer dramatic changes of both l and v_s.

The dependence of the fit on the initial eccentricity is plotted in Fig. 6.2 for the models H2s130a, H2s130g and H2S130c[1] . For the three treatments of the Coulomb logarithm, the free parameters that produce the best fit vary as a function of the initial eccentricity. In the range of eccentricities $[0, 0.8]$ this variation is $\langle \ln \Lambda \rangle \in (1.9, 2.2)$ and $Q \in (1.5, 2.2)$, $Q \in (3.2, 4.3)$ for the cases 2a and 3a

[1] The comparison between numerical and semi-analytic data is usually done at the peri and apo-centres in order to calculate χ. In the case of circular orbits this calculus is carried out each 0.5 Gyr, approximately the period of the H1S1a orbit.

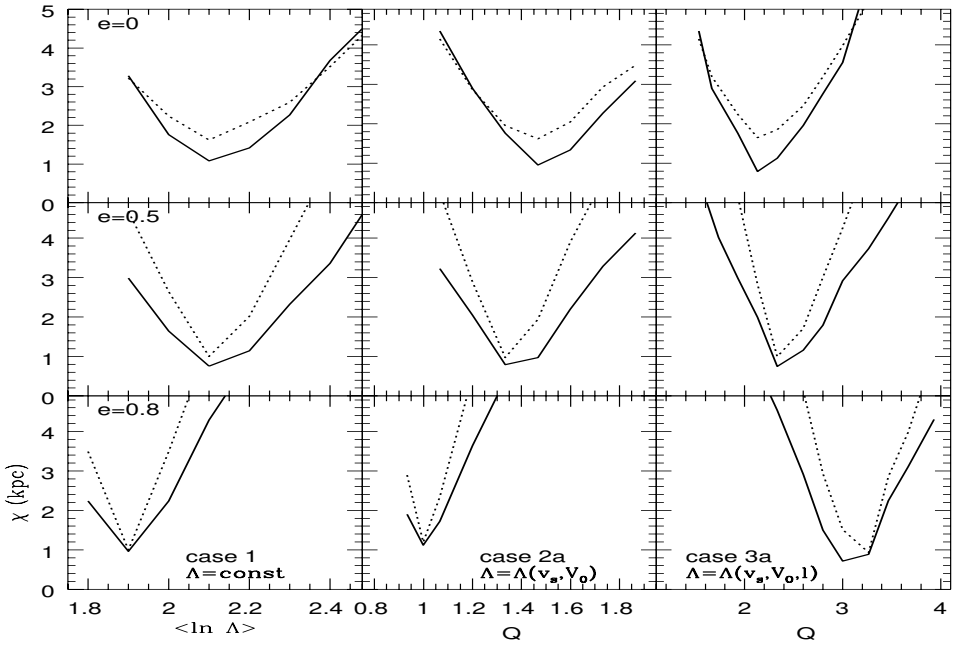

Figure 6.2: Fit of the models H2S130c, H2s130a, H2s130g. Solid and dotted lines denote calculi of χ for $k = 3, 4$, respectively.

which represents approximately a 15, 35 and 30 per cent of variation, respectively.

In Fig. 6.3 we plot the fitting parameters after averaging eq. (6.2) over the numerical calculations presented in Table 6.1. As expected, the different averages of the Coulomb logarithm produce different degrees of accuracy if the range of orbital parameters suffer strong variations. From this plot we deduce that,
(i) the approximation of constant Coulomb logarithm leads to discrepancies of around 1.8 kpc for $k = 3$ to 2.9 kpc for $k = 4$ indicating a poorer accuracy whenever the number of orbits increases. It is remarkable that the best fit corresponds to $\langle \ln \Lambda \rangle = 2.1$ as for the simulation H2S130a, which implies that this average does not strongly depend on the orbital eccentricity as shown in Fig. 6.2.
(ii) the assumption $\Lambda = \Lambda(v_s, V_0)$ produces a similar accuracy also with similar dependence on the number of orbits. All seems to indicate that the addition of the relative velocity dependence to the Coulomb logarithm scarcely changes the force obtained if Λ is constant.
(iii) a inter-comparison between the different approaches to the Coulomb logarithm shows that the fitting factor of eq. (6.2) produces the smallest discrepancy when the variable l is not averaged but has the form $l = \rho/\nabla\rho$. In this case, $\chi_{\rm min}$ is minimum for the first 3,4 orbits. The small dependence on k may indicate that it is also the best analytic approach for the rest of the orbit, although this will be analysed in a following Section.

The calculus of $\chi_{\rm min}$ when dynamical friction is calculated at first order leads to negligible differences for the case 2b as well as for 3b, suggesting a poor contribution of this term in order to alter the satellite orbit.

These results fully agree to those of Hashimoto, Funato & Makino (2002). They find that the best fit to the satellite decay of a point-mass satellite within a singular isothermal halo is achieved if the Coulomb factor takes the form $\Lambda = r_s/1.4\epsilon_s$, where ϵ_s is the softening length of the satellite particle, rather than if it is considered constant. Inserting the orbital and galaxy parameters into eq. (5.28), and assuming that the biggest contribution to dynamical friction is from those particles with $V_0 = X$ one has

$$\Lambda^2 = 1 + \frac{Q^2 l^2}{a^2(V_0) + b_0^2} \frac{X^2}{4X^2 + W^2} \simeq \frac{Q^2 l^2}{5 b_0^2}.$$

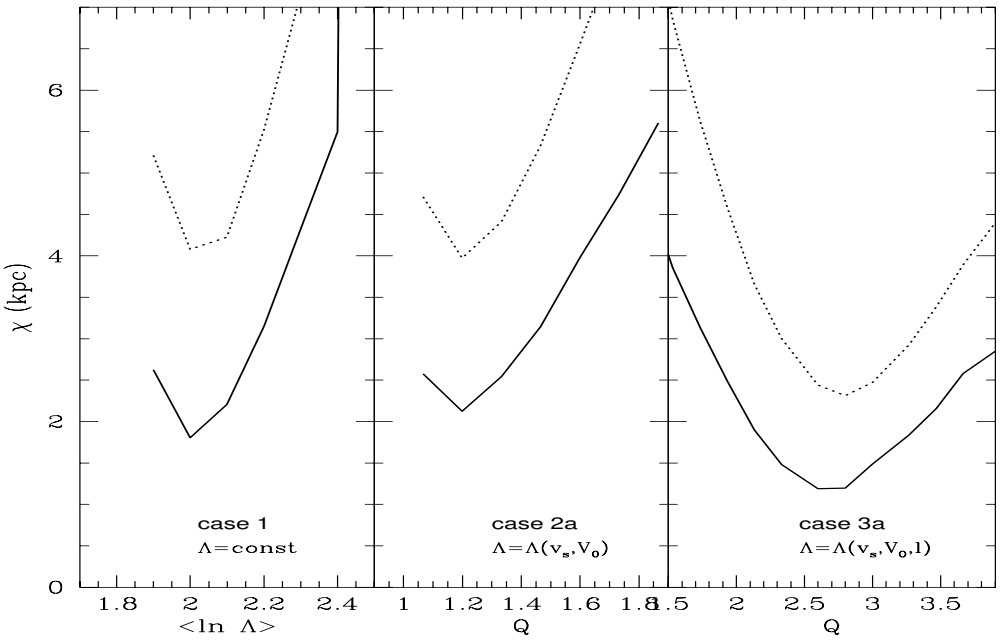

Figure 6.3: Same as Fig. 6.1 but the parameter χ as result of the average over the numerical calculations of Table 6.1.

The approximation holds for most of the two-body encounters along the orbit, which is equivalent to the assumption that one usually finds in the literature $\Lambda = b_{\max}/b_{\min}$ where the velocity dependence of $b_{\max}$, $X^2/(4W^2 + X^2)$, is removed. Taking into account that, as last figures show, dynamical friction is maximum at $X = v_s/\sqrt{2}\sigma = 1$, then $\Lambda \simeq Q r_s/(2b_0\sqrt{5}) \simeq r_s/(1.35b_0)$, which nearly reproduces the value of Hashimoto, Funato & Makino (2002).

6.4.2 Orbital evolution. The Coulomb logarithm.

We employ the model H2S130a to compare the orbit evolution of the different theoretical approaches to the Coulomb logarithm. The comparison is done for the zeroth order of dynamical friction, whereas the first order is studied below. The free parameters $\langle \ln \Lambda \rangle$ and Q are those of Table 6.2.

The differences that the three approaches (cases 1, 2a and 3a) produce on the integration over relative velocities are plotted in Fig. 6.4. We have employed a singular isothermal sphere to reproduce our halo. As a result of applying the local approximation, the selection of ρ only accounts for the value of $K_{\rm ch}$. The use of the singular isothermal sphere simplifies the selection of the satellite distance and the galaxy velocity dispersion, so that once the satellite and galaxy mass are known at a give point the fraction $M/M_g \propto 1/r_s$ and $\sigma = M_g/(4\pi/3r_s^3) = \text{const}$ are easily calculated for the rest of distances.

If the dependence of the Coulomb factor on the radial distance is included, a strong variations of the integral between the apo-centre (approximately $M/M_g = 0.01$) and the peri-centre ($M/M_g = 0.03$) is observed, this last being smaller. If the Coulomb logarithm is considered constant, the integration has values similar to the case of $\Lambda = \Lambda(V_0, v_s)$, proving that the dependence of the Coulomb factor on the relative velocity leads to small changes on the friction force. Since these resulting curves lie within the apo-centre and peri-centre forces, the case 1 and 2 can be contemplate as an average of the case 3a over the radial distance along this orbit.

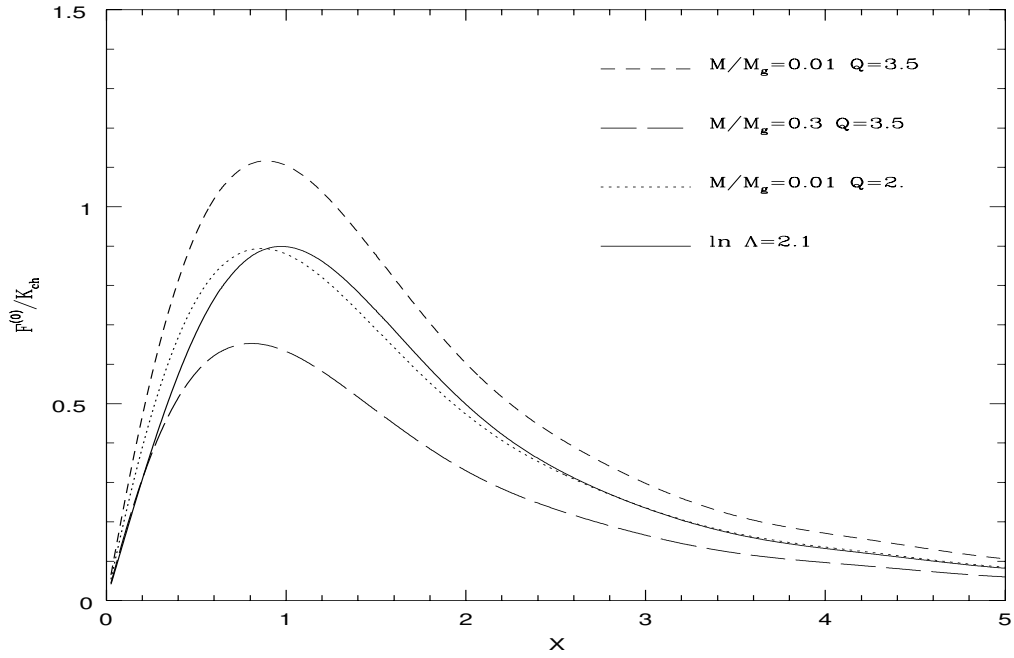

Figure 6.4: Dynamical friction normalised to quantity $K_{\rm ch} = 2\pi G^2 M_s \rho_h(r_s)/\sigma^2$, using the three different analytical approaches to the Coulomb factor. The halo is modelled by a singular isothermal sphere, so that the mass ratio is inversely proportional to the galacto-centre distance. We note that the satellite velocity varies for the model H2s130a within the range $X \in [0.7, 1.5]$.

The distance evolution

For a better understanding of the fitting results, we must analyse the effects that each analytic treatment of the Coulomb logarithm introduces in the satellite orbit evolution. Due to the small differences between the case 1 and 2, for simplicity, we decide to concentrate the study on the cases 1 and 3.

In Fig. 6.5 is plotted the satellite decay of the numerical calculation (dotted line), and that reproduced by the semi-analytical code supposing Λ =const (full line, case 1) and $\Lambda = \Lambda(v_s, V_0, l)$ (dashed line, case 3a). The values of $\langle \ln \Lambda \rangle$ and Q are those schemed in Table 6.2.
One can distinguish between two epochs in the radius evolution, for which the dynamical friction schemes reproduce with different degree of accuracy the numerical data.
Along the first orbits, the case 1 and 3 produce similar fit to the numerical result, reflected in Fig. 6.1, where $\chi_{\rm min}$ for the case 3a is smaller than for the case 1.
This behaviour suffers a radical change at late times of the orbit. The numerical evolution of the galacto-centre distance shows a strong decrease of the apo and peri-galacticon distances for $k > 7$, which can not be reproduced by none of the Coulomb factors that we employ. The approximation of constant Coulomb logarithm comes closer to the time-scale of the decay, however, the small rate of peri-galacticon reduction leads to the so-called "orbital circularisation", a strong decrease of the orbital eccentricity. The process of circularisation will be commented explicitely below.

We must note that these results do not come into contradiction to those found by Hashimoto, Funato & Makino (2002). They carry out a numerical calculation in order to study the effects of having $\Lambda \propto r_s$ in comparison with $\langle \ln \Lambda \rangle$=const, which corresponds to our case 3a and 1, respectively. Differently to our study, the numerical calculations were carried out using a point-mass satellite, which avoids the mass loss effects, meanwhile the satellite extension can be assumed as the smoothing length of the numerical code. They find that $\Lambda \propto r_s$ produces better fits along most of the orbit than the typical approximation of constant Coulomb logarithm. However, in

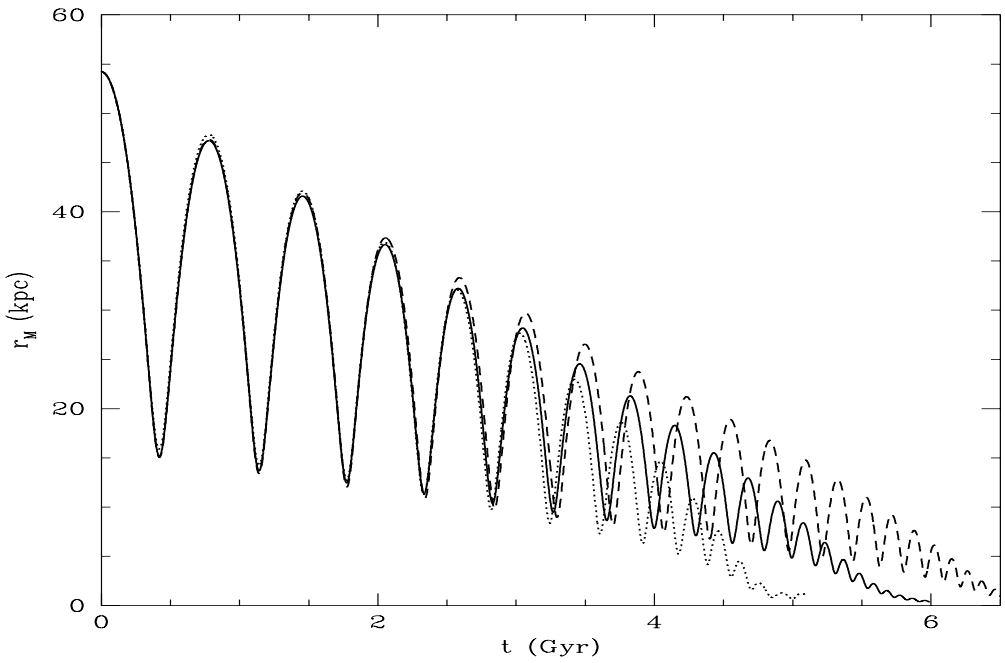

Figure 6.5: Galacto-centre distance evolution for the analytical treatments 1 (solid line) and 3 (dashed line) compared to the numerical one (dotted line, corresponding to the model H2S130a).

their numerical experiments the strong decrease of radial distance is not visible at late orbital times so that the decay time-scale is also well reproduced.

The main difference between the system employed along this study and that of Hashimoto, Funato & Makino (2002) is the satellite model. Although the causes of the rapid decay at late-times are unclear, it may be likely caused by some physical process related to the satellite mass loss, since it is at these times when most of the mass is stripped away due to the galaxy tidal forces. This should be studied in detail although, due to its complexity, it goes further our work.

The energy and angular momentum evolution

In spherical potentials the orbit of the satellite is fully determined by two constant of motion, the energy and the angular momentum vector. Dynamical friction causes a progressive decrease of this last, which leads to the satellite sink into the inner regions of the galaxy, this process is called "satellite decay". As a consequence, the absolute value of the energy increases. It is interesting to analyse the evolution of the constant of motion along the orbit to analyse the differences that the different approaches of dynamical friction induces on the decay process. In Fig. 6.6 we plot in the upper and middle panels the energy and angular evolution for the case 1 (solid line) and 3a (dashed line) for the orbit H1S130a. Both variables are normalised to the initial value. The energy evolution clearly shows that dynamical friction alters the orbit mainly at the peri-centres passages. The enhancement of $|E|$ at those points is equivalent to the subsequent decrease of the apo-galacticon distances, i.e the satellite decay. The stronger increase of energy by the peri-galacticon passages can be understood by a simple calculus. With $\dot{E} = v_M \dot{v}_{\rm df}$, where $\dot{v}_{\rm df}$ is the velocity change due to the drag force and $\dot{L} = L\dot{v}_{\rm df}/v_M$ one has that

$$\frac{\dot{E}}{\dot{L}} = \frac{v_M^2}{L}, \tag{6.3}$$

which holds along the whole orbit, independently of the eccentricity. The smooth decrease of angular momentum implies a large enhancement of $\dot{E}$ at the peri-galactica, since the satellite velocity is maximum at those points (see Fig. 6.7, dashed line).

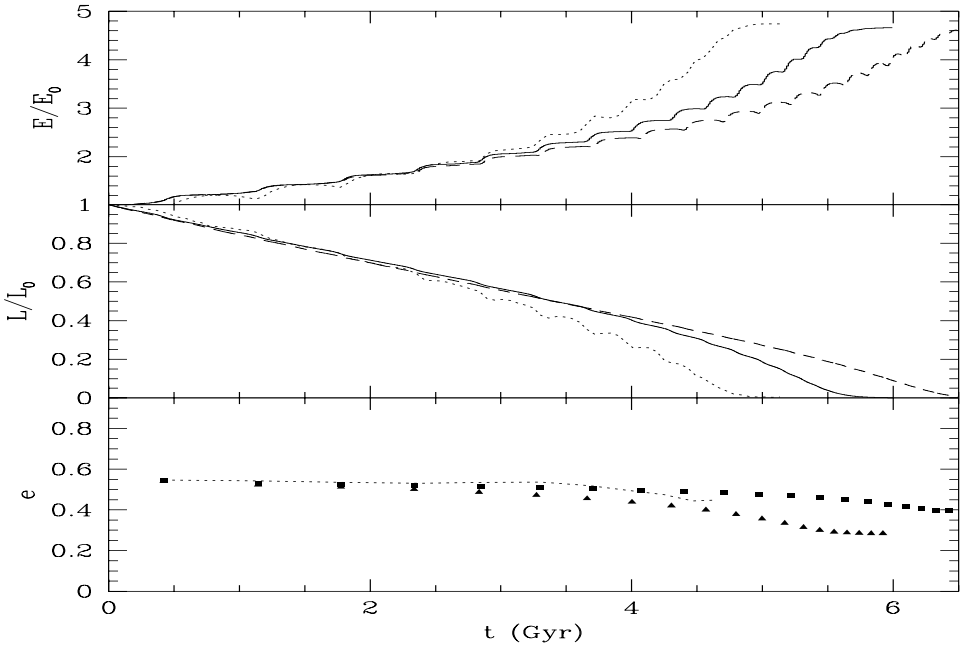

Figure 6.6: Secular evolution of specific energy, angular momentum and orbital eccentricity. We plot the analytical treatments 1 (solid line) and 3a (dashed line) compared to the numerical curve (dotted line, corresponding to the model H2S130a). The eccentricity is defined as $e = (r_a - r_p)/(r_a + r_p)$, where r_a, r_p are the apo and peri-galacticon distances, respectively. Triangles correspond to constant Coulomb logarithm whereas we use squares for the case $\Lambda = \Lambda(l)$, case 3a.

The comparison between the analytic approaches leads to the same results as those obtained from the radius evolution shown in Fig. 6.5.

The eccentricity evolution

It is well known that dynamical friction with constant Coulomb logarithm leads to rates of orbit circularisations not present in the numerical calculations. As Fig. 6.5 shows, the large circularisation, i.e eccentricity decrease, is equivalent to a progressive apo-galacticon decline and nearly constant peri-galacticon distances.

In Fig. 6.6 we compare the evolution of the orbital eccentricity calculated for the cases 1 and 3 to that of the numerical experiment H2s130a. The results show, as expected, that the assumption of $\langle \ln \Lambda \rangle$ =const induces a decline of e from early times on, suffering high rate of eccentricity decrease for $k > 6$ similar to that of the numerical calculus. This circularisation is remarkably reduced if $\Lambda = \Lambda(l)$.

One can readily check that, with our definition of eccentricity

$$\dot{e} = \frac{\dot{r}_a(1-e) - \dot{r}_p(1+e)}{r_a + r_p}, \tag{6.4}$$

therefore, the condition of constant eccentricity along the orbit evolution is $\dot{e} = 0$,

$$\dot{r}_a = \dot{r}_p \frac{1+e}{1-e}, \tag{6.5}$$

where $(1+e)/(1-e) \geq 1$, i.e, if the eccentricity is constant, the apo-galacticon distance decreases faster than the peri-galacticon one. The circularisation implies that the reduction of r_a is accelerated, as one can see in Fig. 6.5 for the standard case (solid line).

We conclude that none of the analytical approaches fit accurately the numerical eccentricity evolution, although the overall decrease is well reproduced if $\Lambda = \Lambda(l)$. The numerical eccentricity is nearly constant for $k < 6$ suffering a strong decline until the satellite sinks to the galacto-centre. This behaviour contrast to that of point-mass satellites (which suffer barely circularisation) and may be due to the mass loss, since the reduction of the mass is maximum at the late times of the evolution.

6.4.3 Dynamical friction at first order

The fitting procedure carried out to fix the free parameters has shown that the first order dynamical friction barely alters the results. To understand the reasons, we analyse the differences that this term introduces on the satellite orbit evolution. We use $Q = 2.8$, that corresponds to the best over the set of numerical calculations.

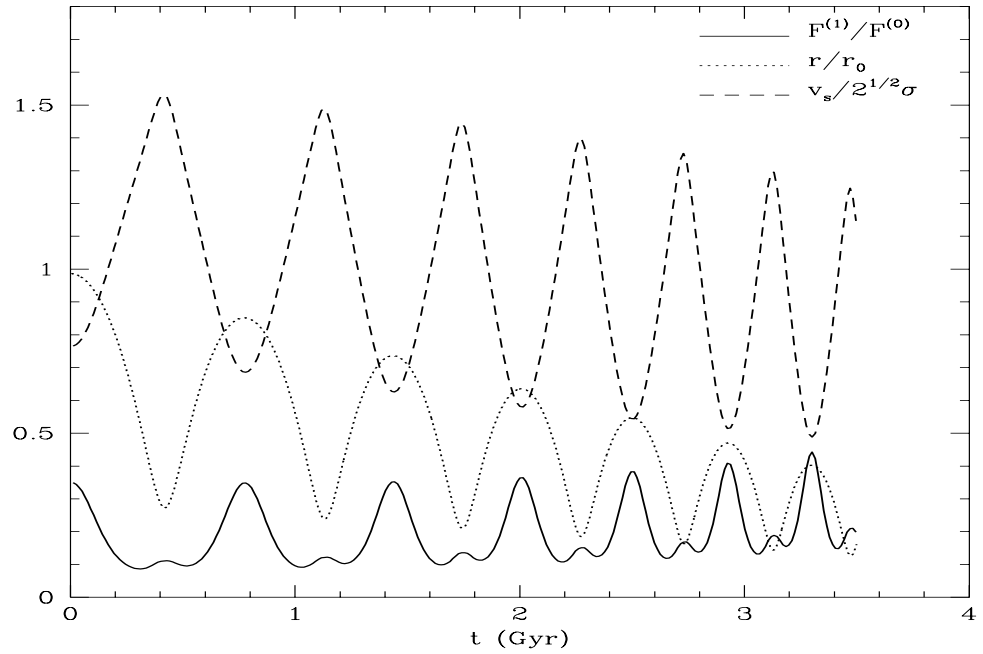

Figure 6.7: Ratio evolution of the first to zeroth order term of dynamical friction for the model H2S130a (solid line). We also plot the normalised distance (dotted line) and velocity of the satellite (dashed line) along the orbit evolution. It is assumed $\Lambda = \Lambda(l)$.

In Fig. 6.7 we plot the ratio $F^{(1)}/F^{(0)}$ along the satellite orbit H2S130a assuming that $\Lambda = \Lambda(l)$. For a better analysis, it is also plotted the evolution of the normalised galacto-centre distance and satellite velocity.
As expected, the first order contribution is maximum at the apo-galactica and minium at the peri-galactica. The relative maximums are due to the change of sign of $\cos\Psi$ (see Chapter 5). The ratio diverges as the satellite sinks to the galacto-centre due to the $1/l$ proportionality in the first order friction.

The differences on the radius and position evolution that the first order adds are plotted in Fig. 6.8. The plot indicates that the first order force barely introduces changes over the satellite orbit, the main effect being a slight shift of the orbit to larger radii which leads to a secular prolongation of the orbital period over large times.

The small contribution of this term can be understood by analysing its direction and magnitude along the orbit evolution. The first order friction at the peri-gacticon is parallel to the mean field force, this means that this term acts like a correction to F_g, the galaxy force, which accomplishes

$F^{(1)}/F_g \ll F^{(1)}/F^{(0)}$ expecting, therefore, small effects where the orbit is supposed to experience most of the variation (Piatek & Pryor 1995). Between the peri and apo-galactica, the direction of $F^{(1)}$ with respect to the zeroth order forms an angle $\psi \in (\pi/4, \pi/2)$ for the model H2s130a, therefore, the correction parallel being of the order of 10% along the major part of the orbit which, as Fig. 6.8 shows, leads to small effects.

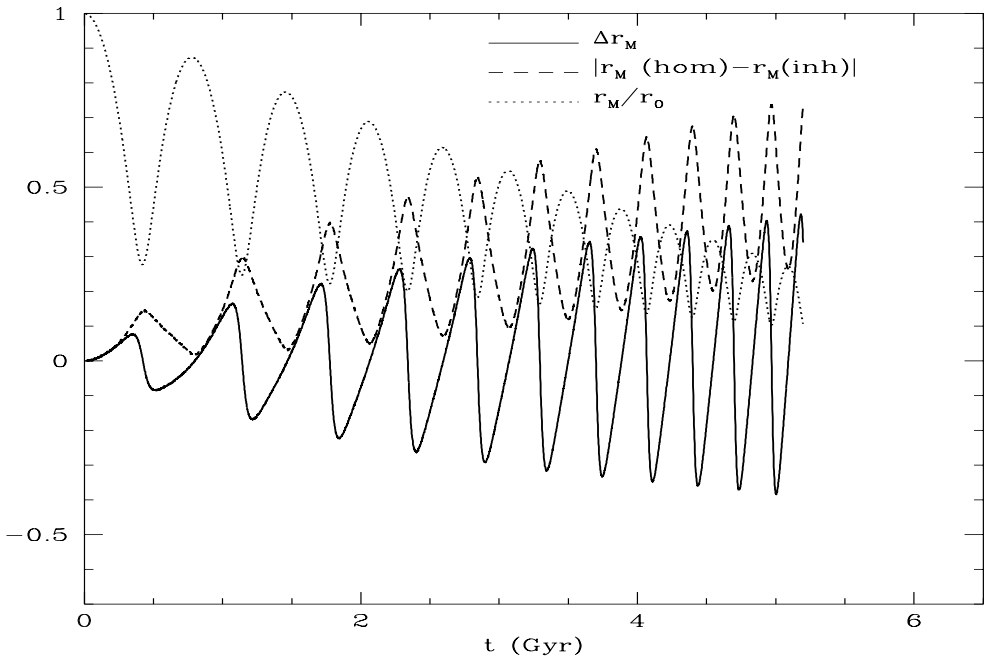

Figure 6.8: Effects of the addition of the first order friction term on the radius evolution. Since the effects are small we show the radial distance difference Δr_M (solid line) and the difference in the position $|\mathbf{r}_{M,\mathrm{hom}} - \mathbf{r}_{M,\mathrm{inh}}|$ (dashed line), both measured in kpc. We also plot the satellite distance evolution normalised to its initial value r_M/r_0 (dotted line).

The explicit evolution of the vectorial component of $F^{(1)}$ is plotted in Fig. 6.9. Meanwhile the perpendicular component (with respect to $\mathbf{v}_s$) is directed to the inner part of the galaxy along the whole orbit (the unit vector is defined as $\mathbf{e}_\perp = \{\hat{\mathbf{n}} - [\hat{\mathbf{v}}_s \circ \hat{\mathbf{n}}] \circ \hat{\mathbf{v}}_s\}/||\hat{\mathbf{n}} - [\hat{\mathbf{v}}_s \circ \hat{\mathbf{n}}] \circ \hat{\mathbf{v}}_s||$, where $\hat{\mathbf{n}}$ is the density gradient vector), the parallel one can be direct ($\Psi > \pi/2$) or opposite ($\Psi < \pi/2$) aligned to the velocity vector. In the first case, $\Psi > \pi/2$, the zeroth order friction becomes lower by the action of the parallel component of $F^{(1)}$ whereas, if $\Psi < \pi/2$, the zeroth order increases, leading to positive values of ΔE. The perpendicular component of $F^{(1)}$ barely contributes to the satellite torque torque since, despite this term is maximum by the peri-galacticon passages, the direction is nearly parallel to the position vector and, therefore, perpendicular to the velocity vector which leads to negligible drag forces.

6.5 Conclusions

We have found that the best fit to the numerical data for the first orbits of the satellite evolution is achieved if $\Lambda \propto r_s$, in clear agreement with the results of Hashimoto, Funato & Makino (2002). However, if the satellite is modelled as a system compound by several thousand of N-body particles, this treatment of the Coulomb logarithm leads to an underestimation of dynamical friction at late times of the satellite orbit, contrary to what is observed for point-mass satellites. We think that this difference in the decay process may be connected to the reduction of angular momentum and energy due to an anisotropic mass loss, since it occurs at times similar to the beginning of the

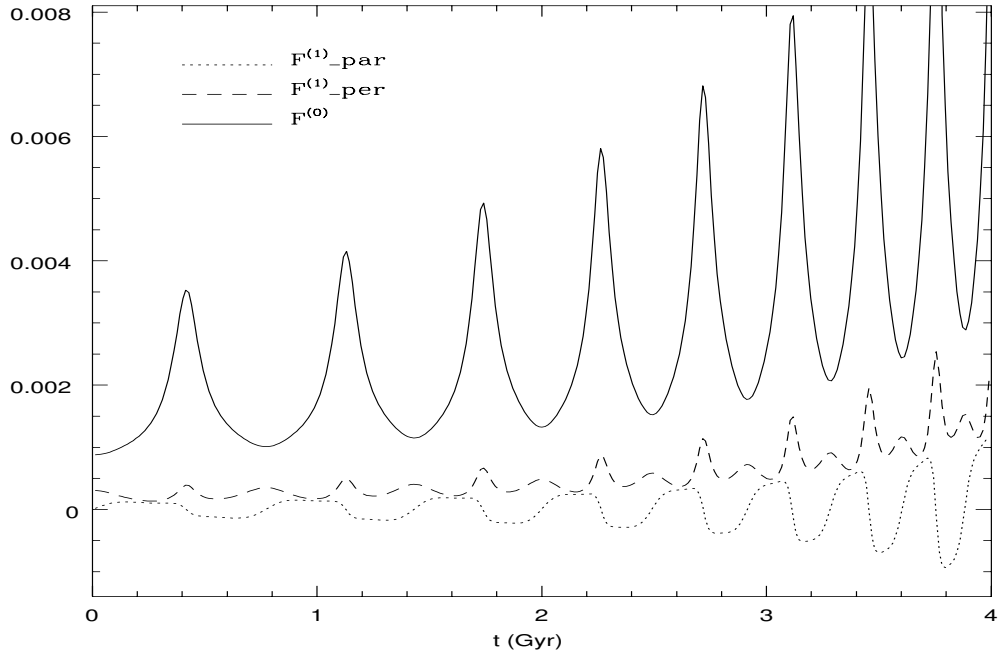

Figure 6.9: Dynamical friction components. The zeroth order is normalised to the satellite velocity as well as the parallel component of the first order term, whereas the perpendicular one is normalised to the galactro-centre distance. The values are in model units.

rapid sink. This hypothesis should be studied in detail, which goes further our purposes.

The assumption of constant Coulomb logarithm, widely used by several authors, produces a good agreement with the numerical experiments in order to describe the time-scales of the decay, but not in tracing accurately the orbit itself.

The differences introduced on the satellite dynamics by the dependence of Λ on the relative velocity can be neglected.

The first order friction also leads to a negligible influence on the satellite dynamics due to its low magnitude. Moreover, the direction the peri-galacticon, parallel to mean force, also contributes to the low efficiency of this term in order to change the satellite orbit.

Chapter 7

Satellite decay in flattened haloes

7.1 Abstract

[1]We carry out a set of self-consistent N-body calculations to compare the decay rates of satellite dwarf galaxies orbiting a disc galaxy embedded in a Dark Matter halo (DMH). We consider both spherical and oblate axisymmetric DMHs of aspect ratio $q_h = 0.6$. The satellites are given different initial orbital inclinations, orbital periods and mass. The live flattened DMHs with embedded discs and bulges are set-up using a new fast algorithm, MaGalie (Boily, Kroupa & Peñarrubia 2001).

We find that the range of survival times of satellites within a flattened DMH becomes $\sim 100\%$ larger than the same satellites within a spherical DMH. In the oblate DMH, satellites on polar orbits have the longest survival time, whereas satellites on coplanar prograde orbits are destroyed most rapidly. The orbital plane of a satellite tilts as a result of anisotropic dynamical friction, causing the satellite's orbit to align with the plane of symmetry of the DMH. Polar orbits are not subjected to alignment. Therefore the decay of a satellites in an axisymmetric DMH may provide a natural explanation for the observed lack of satellites within $0 - 30^\circ$ of their host galaxy's disc (Holmberg 1969; Zaritsky & González 1999).

The computations furthermore indicate that the evolution of the orbital eccentricity e is highly dependent of its initial value $e(t = 0)$ and the DMH's shape.

7.2 Galaxy and satellite models. Orbital parameters

The host and satellite galaxy models used for our calculations are outlined in Chapter 3. In Fig. 7.1 we plot plot the rotational curves for the model G1.

We carry out a set of calculations varying the parameters of the satellite and the primary galaxy that influence the satellite–primary galaxy interaction. These parameters are: (i) the initial orbital inclination (i), defined as the angle between the initial angular momentum vector of the satellite and the initial angular momentum of the disc, (ii) the satellite's mass, (iii) the satellite's apo-galactic distance, (iv) its orbital eccentricity, and (v) the DMHs ellipticity, $1 - q_h$.

Before injecting the satellite into the primary galaxy we allow the galaxy and satellite to settle into a stationary state by integrating the isolated systems for a few dynamical times with Superbox (as in Kroupa 1997). Examples of the stationarity of multi-component galaxies are given in BKP. The satellite is then placed at apo-galacticon with a velocity that determines the value of the orbital eccentricity by multiplying the circular velocity by $0 \leq \xi \leq 1$. We note that the orbit of the satellites are rosettes. The parameters of the numerical experiments are listed in Table 7.1.

[1] *Chapter based on:* Peñarrubia J., Kroupa P. & Boily C.M., 2001, MNRAS, 333, 779

Name	Gal. model	Sat. model	i_i	e	r_p [kpc]	r_a [kpc]
G1S100	G1	S1	0°	0.5	18	55
G1S1180	G1	S1	180°	0.5	18	55
G1S145	G1	S1	45°	0.5	18	55
G1S1135	G1	S1	135°	0.5	18	55
G1S190	G1	S1	90°	0.5	18	55
G2S100	G2	S1	0°	0.5	18	55
G2S115	G2	S1	15°	0.5	18	55
G2S130	G2	S1	30°	0.5	18	55
G2S145	G2	S1	45°	0.5	18	55
G2S160	G2	S1	60°	0.5	18	55
G2S190	G2	S1	90°	0.5	18	55
G2S1135	G2	S1	135°	0.5	18	55
G1S100e	G1	S1	0°	0.3	30	55
G1S190e	G1	S1	90°	0.3	30	55
G2S100e	G2	S1	0°	0.3	30	55
G2S190e	G2	S1	90°	0.3	30	55
G1S100c	G1	S1	0°	0	55	55
G1S145c	G1	S1	45°	0	55	55
G1S190c	G1	S1	90°	0	55	55
G2S100c	G2	S1	0°	0	55	55
G2S190c	G2	S1	90°	0	55	55
G1S200	G1	S2	0°	0.5	18	55
G1S245	G1	S2	45°	0.5	18	55
G1S290	G1	S2	90°	0.5	18	55
G2S200	G2	S2	0°	0.5	18	55
G2S245	G2	S2	45°	0.5	18	55
G2S290	G2	S2	90°	0.5	18	55
G3S200	G3	S2	0°	0.7	20	110
G3S245	G3	S2	45°	0.7	20	110
G3S290	G3	S2	90°	0.7	20	110
G4S200	G4	S2	0°	0.7	20	110
G4S245	G4	S2	45°	0.7	20	110
G4S290	G4	S2	90°	0.7	20	110

Table 7.1: The numerical experiments. The peri- and apo-galactica are r_p and r_a, respectively, and $e = (r_a - r_p)/(r_a + r_p)$ is the orbital eccentricity.

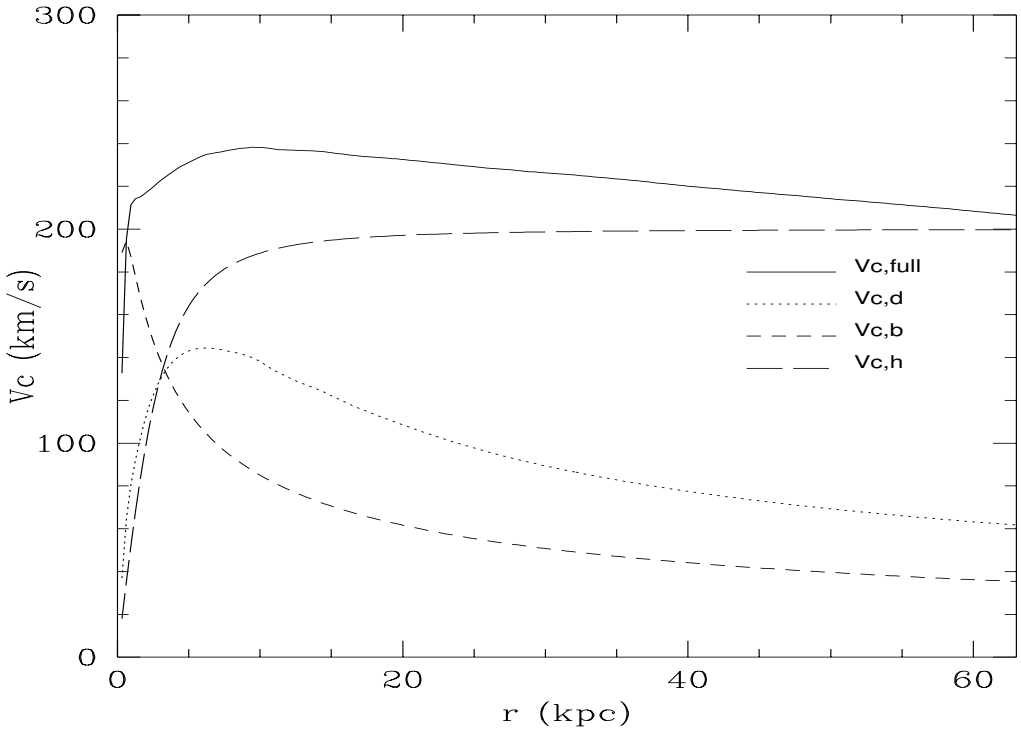

Figure 7.1: Total contribution from the three G1 galaxy components (disc, bulge and halo, see Table 3.1) to the circular velocity (solid line). We also plot the circular velocity for each galaxy component. On very small scales ($r < 1$ kpc) the bulge accounts for the bulk of V_c. Further out, the dynamics is dominated by the halo. The solar radius is at $R_\odot = 8.5$ kpc.

7.3 Satellite Decay

We discuss our results in general terms below before going into detailed consideration of the mass loss and survival of satellites (Section 7.3.2), and the orbital evolution of the inclination angle, eccentricity and precession, respectively (Sections 7.3.3 to 7.3.5).

7.3.1 Introductory comments

We denote by 'G1S145' the compound primary galaxy made, in this case, of a spherical DMH plus embedded disc and bulge, G1, and satellite S1, in an orbital plane initially set at an inclination angle $i = 45°$ with respect to the plane of symmetry of the system. In what follows we take this model as reference, but all models followed a similar evolution.

There are two main physical mechanisms that regulate the satellite's orbital decay: (i) dynamical friction from the disc, bulge and DMH, and (ii) tidal interactions, causing internal heating and mass loss. The evolution of the satellite's orbital radius and mass profile highlight the basic characteristics of these two processes. Dynamical friction causes a steady decrease of the satellite's apo- and peri-centres in time as shown on Fig. 7.2 (dotted line). From $t = 0$ and until $t < 3$ Gyr, both quantities, apo- and peri-centres, decrease monotonically. When $t > 3$ Gyr, the orbital radius $r \approx 5$ or smaller, and the orbital decay is not monotonic anymore. The proximity to the disc means that non-radial forces affect strongly the remaining evolution, along with the structure of the satellite.

To measure changes in the structure of the satellite, we plotted the ten-percentile Lagrange radii centred on the density maximum of the satellite (Fig. 7.2, solid lines). At $t \approx 4$ Gyr, the galactic tidal field has inflated the satellite to the extent that half of its initial mass is spread

throughout the volume circumscribed by its orbit. We note that the inner 10 per cent Lagrange radius is largely unaffected until the very late stages of integration. Our strategy for determining the orbital parameters of the satellite therefore consisted in locating the position of the density maximum of the inner-most Lagrange radius, which then defines a reference coordinate.

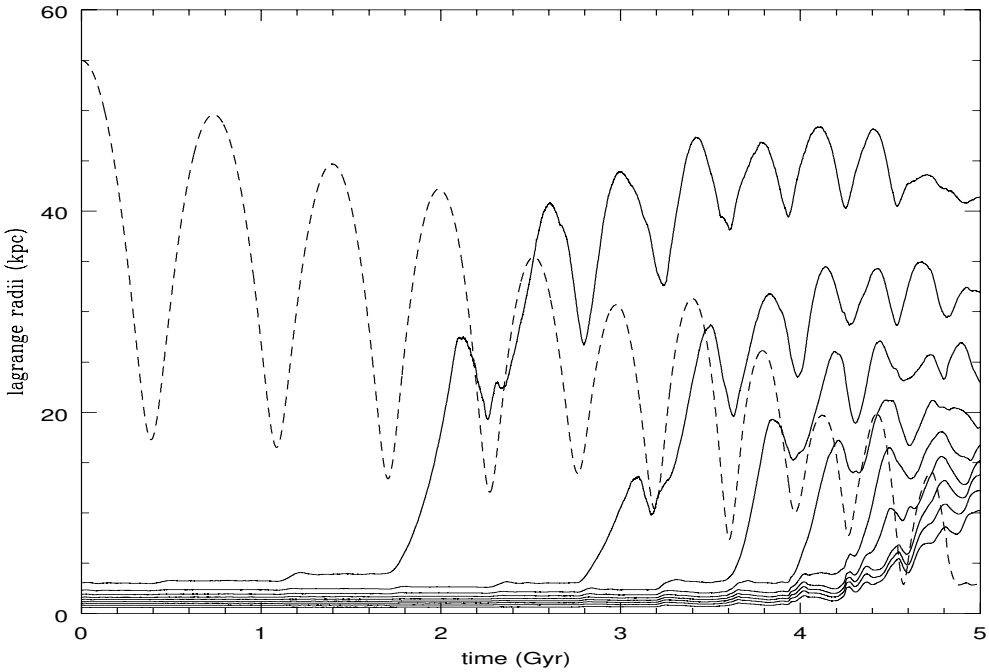

Figure 7.2: Evolution of the satellite's Lagrange radii (solid curves, defined as the radius at which the spherically enclosed mass amounts to 10%, 20%....,90%) for the model G1S145. The dotted line represents the distance of the satellite's centre of density to centre of the primary galaxy. Distances are in kpc. The overall evolution is similar in all other models (Table 7.1).

7.3.2 Mass loss and disruption times

To calculate the mass remaining bound to the satellite, $M_s(t)$, we compute the potential energy $\Phi_i < 0$ of each satellite particle presumed bound to the satellite, and its kinetic energy (T_i) in the satellite frame. Following VW, particles with $E_i = T_i + m_s(\Phi_i + \Phi_{\rm ext}) > 0$ are labelled unbound, where m_s is the mass of one satellite particle. Particles with $E_i > 0$ are removed and the procedure repeated until only negative energy particles are left. $\Phi_{\rm ext} = GM_g(r < r_s)/r_s > 0$ is the external potential from the primary galaxy at the satellite's centre-of-density (r_s). All the particles of the satellite are thus assumed to feel the same external potential, which is a useful and sufficiently accurate approximation, taking into account that most of the bound particles are located very close to this point. For example, in Fig. 7.2 most of the satellite's mass lies at a distance less than 4 kpc from the position of the centre-of-density until the satellite's disruption. This approximation fails whenever the satellite's size is comparable to its distance to the galaxy centre.

Satellites lose mass due to the galaxy's tidal forces. The mass loss happens mostly at peri-galacticon, since the gradient of the galaxy's gravitational force reaches a maximum at that point (see Fig. 7.2). This is seen indirectly in the oscillations of Lagrange radii, always in phase with the orbit of the satellite: the satellite fills its Roche lobe and consequently responds strongly to the changing tidal field. Thus a decrease of the apo-galacticon distance implies an enhanced mass loss. The evolution of satellites exposed to strongly varying tidal fields is discussed at length by Piatek

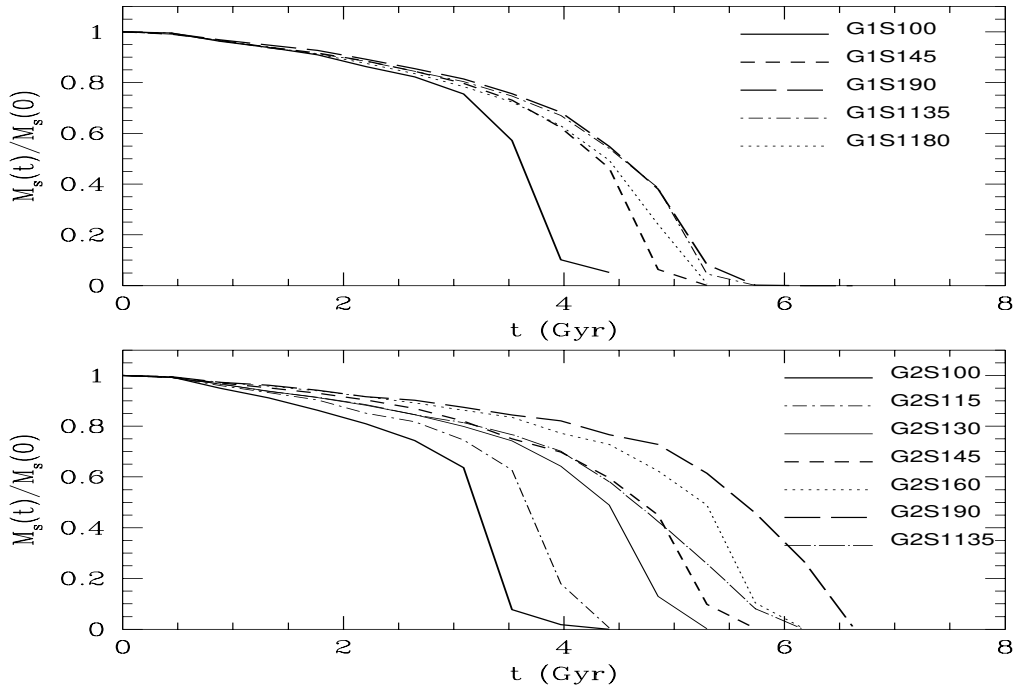

Figure 7.3: Evolution of the satellite mass for $M_s = 0.1 M_d$ and eccentricity $e \simeq 0.5$.

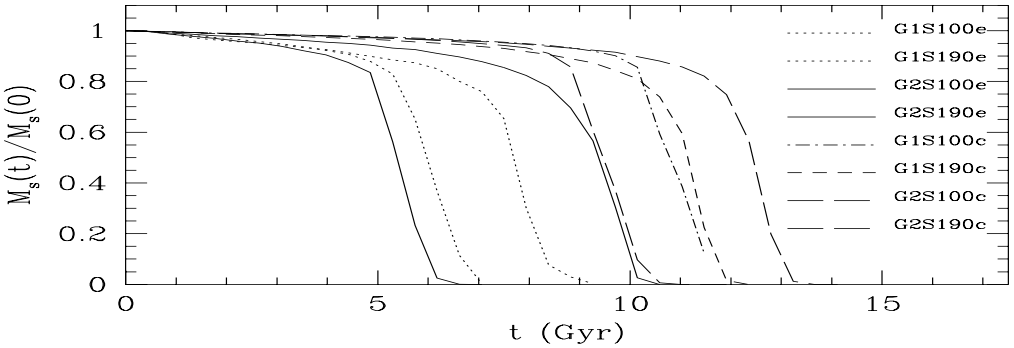

Figure 7.4: As Fig. 7.3 for satellites with $M_s = 0.1\, M_d$ and initial eccentricity $e \simeq 0.3$ and $e = 0$. (Note that the time-axis has changed scale.)

& Pryor (1995) for one peri-galactic passage, whereas long-term satellite harassment is addressed by Kroupa (1997) and Klessen & Kroupa (1998). Consequently, we will not study the internal evolution of the satellites apart from the bound mass fraction.

Satellites with $M_s = 0.1\, M_d$

Fig. 7.3 shows the evolution of the satellite mass for different initial orbital inclinations for satellites with $M_s \equiv M_s(0) = 0.1\, M_d$ and eccentricity $e \simeq 0.5$. From this figure we can assert that: (i) The satellites are disrupted completely at about the same time they reach the galactic disc (Fig. 7.2). (ii) For all the models, the survival time is, at least, 1 Gyr (25%) longer than the equivalent simulations of VW (upper panel of Fig. 7.3). We consider this difference to be indicative of the uncertainty intrinsic to methods that approximate collisionless dynamics. The difference comes about, in part, due to different numbers of particles, but also due to the spatial resolution of the method. Prugniel & Combes (1992) and Whade & Donner (1996) find that dynamical friction is artificially increased due to numerical noise if the particle number is small. Similar differences were

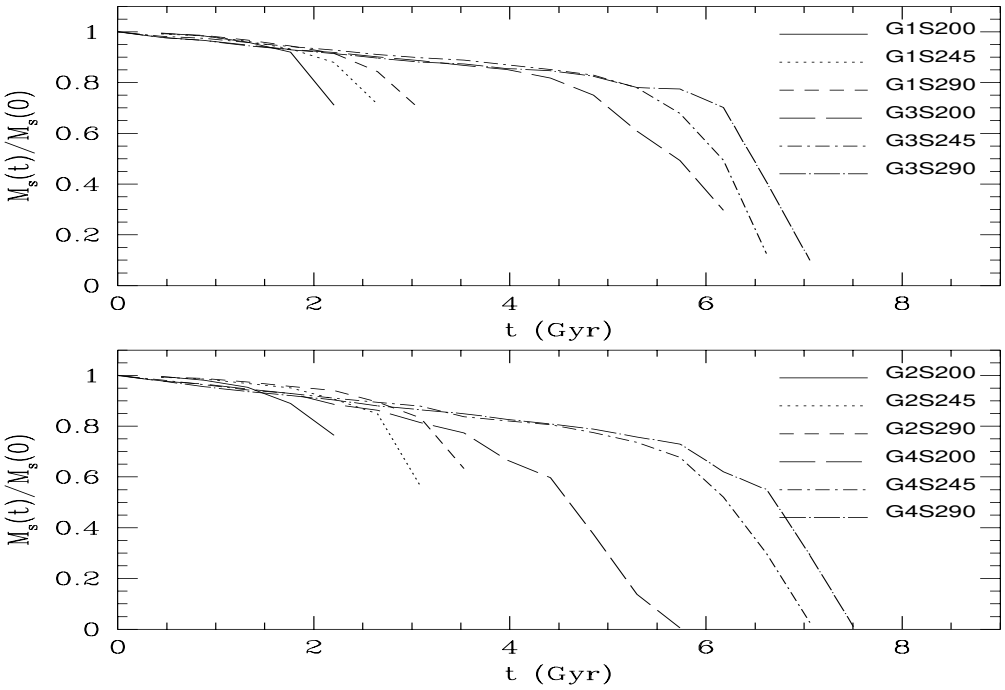

Figure 7.5: As Fig. 7.3 for satellites with $M_s = 0.2M_d$. (Note that the time-axis has changed scale.)

also noted in the computations by Klessen & Kroupa (1998) of satellite harassment using different codes. However, we observe that the range of disruption times for our models G1S1 (as used by VW) is approximately the same, indicating that disc effects are well reproduced by our code and giving confidence to the following results we obtain using flattened DMHs. (iii) Flattened DMHs spread the range of disruption times. In Fig. 7.3 we can see that, for satellites with $M_s = 0.1\,M_d$ embedded within spherical DMHs this range is ~ 1.2 Gyr (upper panel), polar satellites having the longest survival time. For satellites with the same mass but within flattened DMHs the range grows to ~ 2.7 Gyr (lower panel). (iv) Satellites with a high orbital inclination within flattened DMHs have longer survival times than satellites within spherical DMHs with the same initial orbit. For instance, taking the polar satellite as the extreme case, G2S190 survives ~ 1 Gyr longer than G1S190. (v) Satellites with low orbital inclination suffer the contrary effect: those within spherical DMHs survive longer than those within flattened DMHs. Taking the prograde and coplanar orbit as the extreme case, G1S100 survives ~ 0.6 Gyr longer than G2S100.

In Fig. 7.4 we compare polar and coplanar satellites within flattened and spherical DMHs with orbital eccentricity $e \approx 0.3$ and 0 to obtain an indication of the dependency of the life-time on e (orbits with intermediate inclination also have intermediate survival times, Fig. 7.3). As expected, less eccentric orbits lead to longer survival times, since the peri-galactic distance is larger and, moreover, tidal forces are weaker. Furthermore, the survival times show a larger spread. Less eccentric orbits survive longer, so that anisotropic dynamical friction has a longer time to act. We can see that coplanar satellites within a spherical DMH (model G1S100e) decay ~ 0.3 Gyr later than a coplanar satellite within a flattened DMH (model G2S100e), while the decay time of a polar satellite within a spherical DMH (model G1S190e) is ≈ 0.5 Gyr shorter than the corresponding satellite in the flattened DMH (model G2S190e). Thus, the range of survival times increases from about 2.1 Gyr to 4.2 Gyr. This range becomes even larger for circular orbits.

This state of affairs is summarised in Fig. 7.6 for all satellite models, whereas Table 7.2 compares the decay times for S1 satellites in dependence of the orbital eccentricity and inclination. The table nicely shows that the survival time increases significantly with decreasing eccentricity. It also shows that oblate DMHs lead to consistently larger differences, $\Delta\tau$, between the decay times

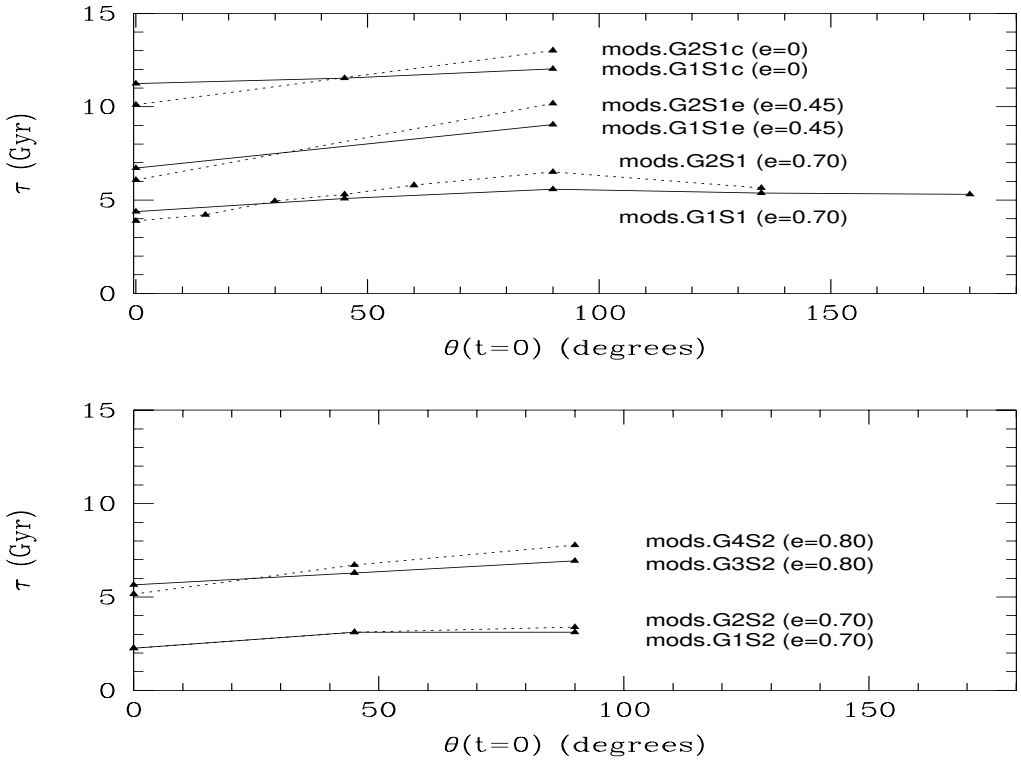

Figure 7.6: The time τ when the satellite mass reaches 10 per cent of its initial value, $M_s(\tau) = 0.1\,M_s$, or the satellite has sinked to the galaxy centre is plotted vs the initial orbital inclination. Upper panel is for satellite models S1 in primary galaxies G1 and G2, whereas the lower panel shows the results for satellites S2. Note that in all cases τ increases with increasing $i < 90^{\rm o}$ for galaxies embedded in a spherical and a flattened DMH, due to dynamical friction on the disc. The effect of this is particularly nicely seen from the different slopes, $d\tau/di$, for prograde ($i = 0 - 90^{\circ}$) and retrograde ($i = 90 - 180^{\circ}$) orbits. The increase is significantly larger for satellites orbiting in flattened DMHs, and becomes larger for decreasing orbital eccentricity (Table 7.2) and decreasing satellite mass, which allows longer coupling of the satellite to the anisotropic velocity field in the DMH.

for polar and coplanar orbits, $\Delta\tau$ consistently being approximately 100 per cent larger in flattened DMHs than in spherical DMHs ($\Delta\tau_{\rm obl} \approx 2\,\Delta\tau_{\rm sph}$). This is the key result of this study.

Satellites with $M_s = 0.2\,M_d$

The temporal evolution of satellite masses with $M_s = 0.2\,M_d$ is shown in Fig. 7.5. There are no significant differences in survival times for satellites in spherical and flattened DMHs if $r_a = 55$ kpc. At the same time, the dependency on the inclination decreases, causing the range to be narrower in both cases. The cause is the fast decay of the satellites, so that the anisotropy of the DMH's velocity dispersion does not have enough time to act. To better assess this, we introduce a set of computations selecting larger initial apo-galactic distances (models G3 and G4). The cut-off radius of the Galaxy is increased, which changes the rotational curve (see Fig. 7.1). The results are also plotted in Fig. 7.5. A similar spread of survival times as for models with $M_s = 0.1\,M_d$ and 'G2' flattened DMHs becomes evident; the range of disruption times for spherical (G3) and flattened DMHs (G4) are, respectively, ~ 1 and ~ 2 Gyr.

The results concerning the disruption times seen on Fig. 4c between small and large DMHs

model	$e(t=0)$	$\tau_0 \equiv$ $\tau(i=0)$ [Gyr]	$\tau_{90} \equiv$ $\tau(i=90)$ [Gyr]	$\Delta\tau \equiv$ $\tau_{90}-\tau_0$ [Gyr]
G2S1c(obl)	0	10.1	12.9	2.8
G1S1c(sph)	0	11.3	12.0	0.7
G2S1e(obl)	0.3	6.1	10.3	4.2
G1S1e(sph)	0.3	6.8	9.2	2.4
G2S1(obl)	0.5	3.8	6.5	2.7
G1S1(sph)	0.5	4.4	5.6	1.2

Table 7.2: Summary of decay times for satellite models S1 ($M_s = 0.1\,M_d$) in oblate (obl) and spherical (sph) DMHs with different initial orbital eccentricity e and orbital inclination i. τ_0 is the decay time when the satellite that is initially on an orbit with inclination $i = 0^o$ has lost 90 per cent of its mass or has sinked to the galaxy centre, whereas τ_{90} is the decay time for polar orbits ($i = 90^o$).

(G1/G3 and G2/G4 pairs displayed on Fig.4c, bottom panel) are related to one another as follows. DMHs G3 and G4 have the same mass as G1 and G2, but are more extended by a factor $\eta = 133\,\mathrm{kpc}/84\,\mathrm{kpc} = 1.58$ (Table 3.1). This implies that the dynamical time-scale ($\propto 1/\sqrt{G\rho}$), i.e. the periods of satellites on equivalent orbits, are longer in haloes G3 and G4 by a factor $\sqrt{\rho(G2)/\rho(G1)} = 1.58^{3/2} = 2$. Orbits in G3 and G4 equivalent to those in G1 and G2, respectively, are orbits with semi-major axes extended by η in a homologous mapping of the systems. Our satellite orbits, however, have apo-galactic distances in G3 and G4 twice as large as in DMHs G1 and G2. The orbital times of models G3S2nn and G4S2nn are in total $1.58^{3/2} \times 2/1.58 = 2 \times 2/1.58 \approx 2.5$ times longer than models of satellites in DMHs G1 and G2. This is approximately what we observe from comparing the curves on Fig. 4c with DMHs G1/G3 or G2/G4.

On the top panel of Fig. 7.5, the time when $M(t)/M(0) \approx 0.10$ is $t \approx 2.5$ Gyr for all G1 models. If the homologous transformation applied strictly, the curves for the G2 halo models should approach 7 Gyr when $M(t)/M(0) = 1/10$. The fact that they are spread between 6 and 7 Gyr, and thus deviate from the homologous map, indicates that the disc and bulge, which were left unchanged, play an important role in the mass decay rate of the satellites. Furthermore, this estimation suggests that the time-scales for orbital decay are controlled by the DMH, while the combined tidal field of the disc and bulge contributes mainly to mass stripping. Similar conclusions would apply for the G2/G4 models shown on the bottom panel of the figure.

Prograde versus retrograde orbits

Results for models with spherical DMHs may be divided into two according to whether the orbit of the satellite is aligned with the disc's angular momentum vector (prograde) or anti-aligned (retrograde). Keeping the initial satellite velocity vector unchanged, a prograde orbit is found for an initial orbital inclination angle $0^\circ < i < 90^\circ$, and retrograde orbits in the cone $90^\circ < i < 180^\circ$.

Table 3 lists four models with spherical G1 DMHs and eccentricity $e = 0.5$ (top segment in the Table). Models G1S100 and G1S1180 are respectively prograde and retrograde with respect to the disc, but are otherwise identical. From Fig. 7.3 (top panel) we find for these two simulations a 90% mass-loss after ≈ 4 Gyr and 5.3 Gyr, respectively, an increase of nearly 25% ; a similar conclusion applies for models G1S145 and G1S1135. These findings are qualitatively similar with those of VW: (i) Satellites on prograde orbits lose angular momentum faster than their retrograde counterparts, leading to more rapid decay. (ii) Polar orbits have a similar decay rate as retrograde orbits, as found from comparing model G1S190 and G1S1135, Fig 7.3. This implies that our treatment of the live disc captures the essential physics relevant for this work.

Figure 7.6 summaries the findings for decay rates for the simulations performed. Point (i) above also applies to flattened DMHs. However, Fig. 7.6 suggests in this case that the difference in decay rates between prograde and retrograde orbits is reduced by about 80 % for flattened DMHs.

For spherical DMHs the above results can be understood partially by considering Chandrasekhar's expression (Chandrasekhar 1960) for dynamical friction,

$$\mathbf{F}_{\rm df} = -\frac{4\pi G^2 M_s^2(t)\rho(<v_s)\ln\Lambda}{\Delta v^3}\mathbf{v}_s, \tag{7.1}$$

$\Delta v = |\vec{v_s} - \vec{v_m}|$ being the relative velocity between the satellite and the disc particle background, v_m is the disc particle velocity and $\rho(<v_s)$ the density calculated only for those particles with velocity less than the satellite's velocity v_s, and $\ln\Lambda$ the Coulomb logarithm, can be estimated as $\Lambda = p_{\rm max}/p_{\rm min}$. In this expression, $p_{\rm max}$ is the maximum impact parameter, and $p_{\rm min}$ the minimum impact parameter (conventionally taken as the half-mass radius of the system). Since these quantities are not well defined, the Coulomb logarithm remains, to a certain degree, an adjustable parameter. The fittings carried out in Chapter 6 show that $\ln\Lambda \simeq 2$.

The different decay rate between prograde orbits and their retrograde counterparts is caused, in part, by the disc's dynamical friction when the satellite is near perigalacticon. Retrograde orbits have a much higher relative velocity Δv due to the disc's rotation and, therefore, they suffer a smaller drag force. The bulge or the DMH's dynamical friction make no differences since both are non-rotational and spherical, which also explains the small differences of decay rates between the polar and the retrograde case (in both cases dynamical friction through the disc can be neglected compared to the DMH's dynamical friction). In addition to dynamical friction, resonances between the satellite and the disc influence the orbital decay, but a detailed analysis goes beyond the aim of this work. As for the different decay rates depending on the satellite's mass, the specific dynamical friction force varies with M_s, so that satellites with $M_s = 0.2\,M_d$ suffer a two times larger friction than those with $M_s = 0.1\,M_d$.

7.3.3 Orbital inclination i

Binney (1977) extended the dynamical friction force (eq. 7.1) to non-isotropic velocity fields. He showed how anisotropic friction leads to orbit alignment with the velocity ellipsoid plane of symmetry of the host galaxy. Here disc and DMH spheroids define a unique $z = 0$ plane of symmetry, common to both mass distribution and velocity ellipsoid. We may, therefore, anticipate enhanced satellite orbit alignment relatively to Binney's analysis, due to the non-uniform, aspherical mass profile.

In Fig. 7.7 we graph the time-evolution of the direction angle i for a set of simulations with oblate G2 DMHs ($q_h = 0.6$) and S1 satellites (solid lines on the figure) as well as two reference runs with spherical G1 DMHs (dotted lines on the figure).

The average of the orbital inclination $i(t)$ decreases monotonically in time for satellites orbiting in flattened DMHs which have initially $i \neq 0°$ or 90°. The decrease in $i(t)$ is more appreciable for smaller values of $i(0)$. This is seen for instance by comparing the curves with $i(0) = 15°$ and 30° to the solutions with $i(0) = 60°$ and 90°. For the latter, polar orbit, no decay of $i(t)$ is observed for the duration of the integration, whereas for the $i(0) = 15°$ case the orbit aligns fully with the plane of symmetry of the system (coincident with the disc of the host galaxy).

By contrast, satellites orbiting in spherical DMHs show little or no decay of $i(t)$, for all initial values of i (dotted lines, Fig. 7.7). This clearly indicates that the anisotropic DMH, and not the disc, drives most of the orbital evolution and alignment, since in all cases a galactic disc is present.

The figure also reveals periodic oscillations of $i(t)$ for satellites on inclined orbits, of frequency approximately in tune with the satellites' orbital motion. Inspection of the figure shows this to be the case for systems with either spherical or flattened DMHs. Note that no such oscillations in $i(t)$ is observed for polar or co-planar orbits. These oscillations correspond to the so-called *nutation* effect, which is present in the motion of bodies in anisotropic potential (see Appendix A).

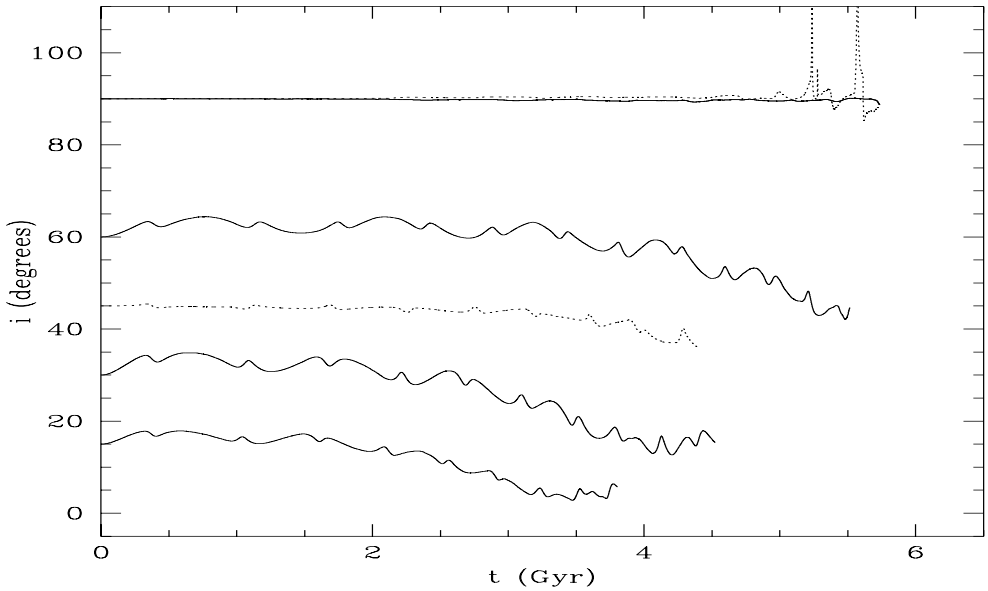

Figure 7.7: Evolution of the orbital inclination for models G2S100, G2S115, G2S130, G2S190 (full lines, satellites within the flattened DMH) and G1S145, G1S190 (dotted lines, satellites within the spherical DMH), until they retain 10% of their initial mass.

Nutation can examined in two phases, (i) when the satellite orbit is motion is dominated by the halo potential and (ii) where the disc potential dominates.

For $0 < t < 3$ Gyr the satellites orbital radius $r_s \gg R_d$. Over this interval of time, the orbits are such that those obtained for flattened DMHs lead to much larger oscillations in $i(t)$ compared with the solutions with spherical DMHs. We therefore attribute these oscillations to torques from the DMH acting on the satellites

$$\mathbf{\Gamma} = \mathbf{r} \times \nabla\Phi = R\left(\frac{\partial\Phi}{\partial z} - z\frac{\partial\Phi}{\partial R}\right)\mathbf{e}_\phi$$

which by symmetry arguments must lie in the plane of the axi-symmetric galaxy. The torque Γ is positive or negative according to the phase of the orbit. This corresponds to the nutation formulation.

For $t > 3$ Gyr the situation is similar for all calculations, independently of the morphology of the DMH. Thus the oscillations we observe clearly for flattened-DMH orbits are now noticeable for the solutions with spherical DMHs, too. In this phase of evolution, $r_s \sim R_d$ or less so that the disc potential contributes most of the force felt by the satellite and hence the torque Γ acting on it. At this stage, a coupling between the disc response and the satellite motion is expected: we observed that these oscillations are highly softened in calculations with a static disc and bulge. Since the orbital angular momentum $L \approx r_s v_s m_s$ and $\Delta L = \Gamma dt \approx r_s G\Sigma(r_s/v_s)$, where Σ is the disc's surface density, both L and the angular momentum accrued ΔL over one revolution will be of comparable magnitude if $v_s^2 \sim GM_d/r_s$, i.e. when the disc potential is the predominant contributor to the force acting on the satellite. The direction angle $i(t)$ varies therefore wildly towards the end of the simulations in all cases save the coplanar $i(0) = 0°$ one, for which $\Gamma = 0$ at all times.

The oscillations or periodic fluctuations we have discussed are subject to enhancements owing to our choice of a grid numerical method of integration. The Cartesian grid code limits the vertical resolution of a thin disc. Consequently the response of the disc to heating by the satellite

is not correctly quantified. Furthermore, once the remnant satellite has merged with the disk, the position of it's centre of density becomes ill-defined by virtue of the satellite ceasing to exist as a bound entity; $i(t)$ will reflect this uncertainty for $t > 3$ Gyr. With 32 mesh points spread over a length of $3R_d$, the position of the centre-of-density and the disc structure are resolved to $l \simeq 3R_d/32 \sim r_s/10$ when $r_s \approx R_d$. Hence the error on the angle i may be estimated to be $\sin i \approx i = l/r_s \sim 1/10$ or 5° approximately. This puts into perspective the magnitude of the oscillations seen on Fig. 6 for $t > 3$ Gyr, though without accounting for them fully. This leads us to conclude that the physical effect of the torque Γ by the disc on the satellite is qualitatively correct, although the quantities somewhat uncertain.

7.3.4 Orbital eccentricity

In Fig. 7.8 we plot the eccentricity evolution for satellites with mass $M_s = 0.1\, M_d$. The eccentricity is calculated from the value of $r_a(t)$ and $r_p(t)$ until the satellite has 10 % of its initial mass.

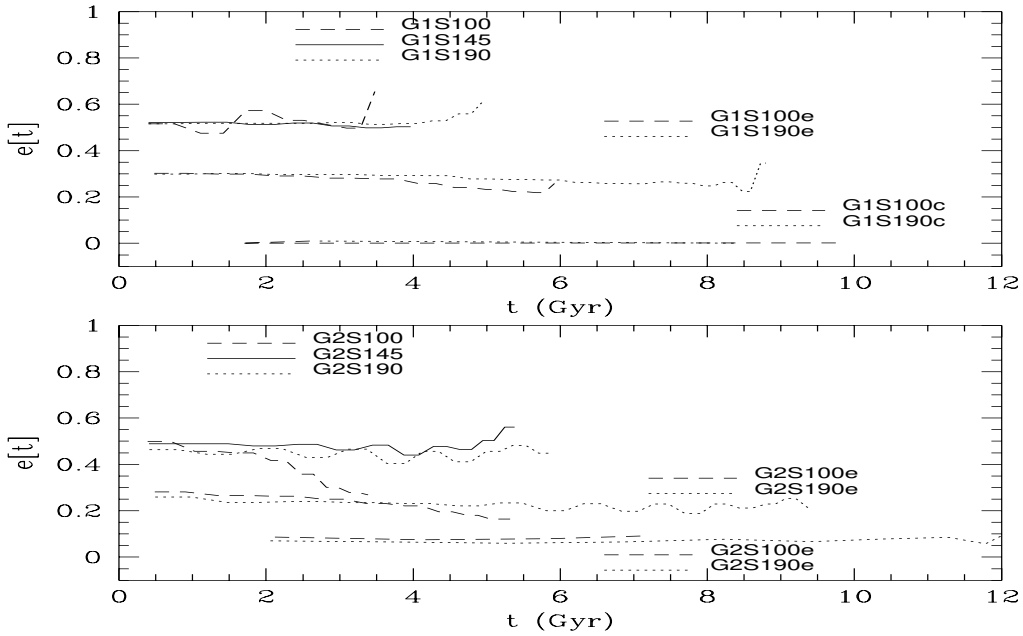

Figure 7.8: The eccentricity evolution for some of the models.

The orbital eccentricity does not remain constant as dynamical friction shrinks the orbit. The evolution of $e(t)$ depends on $e(t = 0)$ and $i(t = 0)$, but from Fig. 7.8 we observe that the general behaviour is for the orbits to remain nearly constant. The only clearly evident exception is prograde model G2S100 ($e(0) = 0.5$), which shows a pronounced decrease of $e(t)$. In this case, dynamical friction from the flattened DMH plus disc is so large that the apo-galactic distance decreases much faster than the peri-galactic distance. Close inspection shows that this is merely the extreme of a general trend. Comparing the co-planar prograde orbits ($i = 0^o$: GnS100, GnS100e, GnS100c; n= 1, 2) with the polar orbits ($i = 90^o$: GnS190, GnS190e, GnS190c), it is evident that the former show a stronger sensitivity on initial eccentricity than the latter. The effect is such that circular co-planar prograde orbits circularise. Disc–satellite coupling via dynamical friction and induction of spiral modes in the disc and associated transfer of angular momentum between satellite and disc are the likely reason, but we do not dwell longer on this, as disc-satellite coupling is not the main topic of this work, which in any case does not resolve the disc vertical structure. We merely state here that the data in Fig. 7.8 suggest that orbits tend to remain with nearly constant eccentricity, occurring that $e(t)$ decreases when dynamical friction is strong

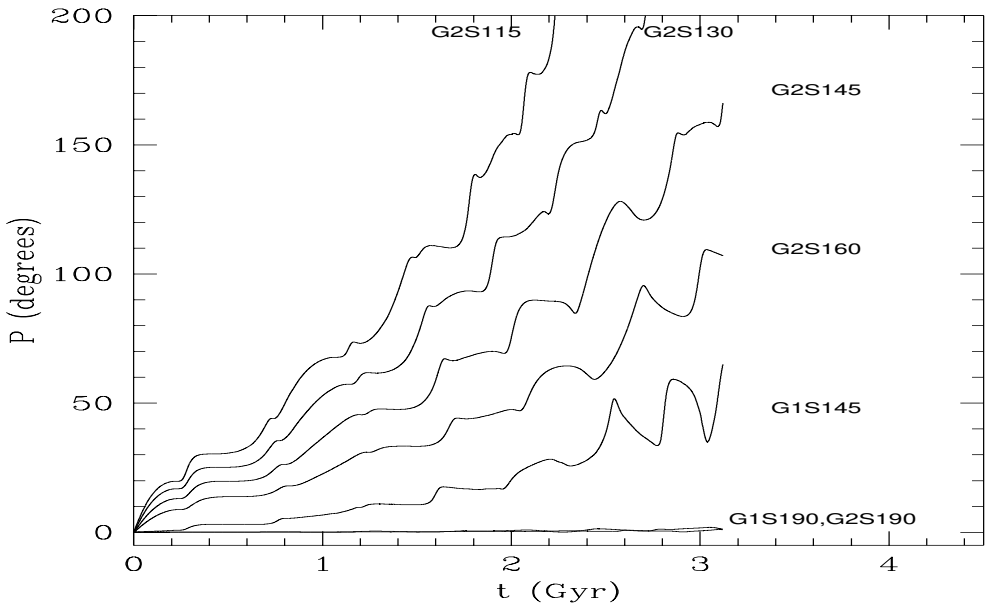

Figure 7.9: The precession angle P for some of our models.

This behaviour agrees with that found by van den Bosch et al. (1999). They perform numerical calculations using a galaxy models similar to G1, with satellite masses on the order of that of our models S1. They observe that the eccentricity remains remarkably constant. Unfortunately, they do not include calculations with $e(0) < 0.6$. We note in passing that our results disagree with those found by Prugniel & Combes (1992), who observe that initially circular orbits rapidly acquire eccentricity.

7.3.5 Orbital precession

The orbital plane of a satellite and its unbound particles precesses in a flattened potential which smears out the tidal debris stream. The precession angle, $P(t)$, is calculated by projecting the orbital angular momentum vector onto the galactic xy plane and measuring its change with time. In Fig. 7.9 we plot P for some of our models. The precession, dP/dt, increases at later times due to the anisotropy of the disc's potential, the satellite having decayed to its vicinity.

As expected, flattened DMHs lead to larger precession. Comparing models G1S145 (satellite within a spherical DMH) and G2S145 (satellite within a flattened DMH), we observe that the change of P is, respectively, $\simeq 50^\circ$ and $\simeq 150^\circ$, i.e, approximately three times larger at $t = 3$ Gyr. Since the DMH is spherical for models with G1 the precession of the orbital plane is due to the disc gravitational quadrupole moment. The orbital plane precesses faster the smaller its inclination is, orbits with $i \leq 45^o$ precessing by 180^o in 3 Gyr. Polar orbits do not precess at all.

7.3.6 Tidal streams

The accretion history of the Milky Way and other major galaxies leaves signatures in the form of old tidal streams in the DMHs of these galaxies as found in observational surveys such as that of Dohm-Palmer et al. (2001), or Martínez-Delgado et al. (2001). The detection of the Sagittarius dwarf tails (Iabata et al. 1994) therefore likely is a generic features of large galaxies.

Theoretical models of this process have shown good agreement with observations (Helmi & White 1999; Zhao et al. 1999; Helmi & de Zeeuw 2000). The changes in orbital inclination i and

the orbital precession in flattened systems imply that the tidal debris emanating from a disrupting satellite will significantly spread out in i, which will make reconstruction of the accretion history of a major galaxy difficult if its DMH is flattened.

In Fig. 7.10 we plot the deviation angle of the satellite's particles from the initial orbital plane in three time snaps. This is done for models G1S145 and G2S145 (Fig. 7.10, $i(0) = 45°$), and for G1S190 and G2S190 (Fig. 7.11, $i(0) = 90°$). The first time-snap shows satellite particles after first passage through perigalacticon at $t = 0.62$ Gyr, the second one is at an intermediate time ($t = 1.52$ Gyr) while the last frame is at a late stage of the satellite orbit. The debris does not remain in the initial orbital plane. This effect becomes more pronounced the closer the satellite is to the galaxy's centre, when the mass loss (Fig. 7.3) and the oscillations of the orbital inclination (Fig. 7.7) primarily occur, and the larger the number of perigalacticon passages is. From Fig. 7.10 we also observe that the deviations from the orbital plane are enhanced when the DMH is flattened since satellite orbits within oblate DMHs align with the symmetry plane (i.e. $i(t) \to 0$). Fig. 7.11 shows that the spread of satellite debris is much smaller for satellites in polar orbits than for those with intermediate inclinations, since inclination decay and oscillations vanish for polar orbits.

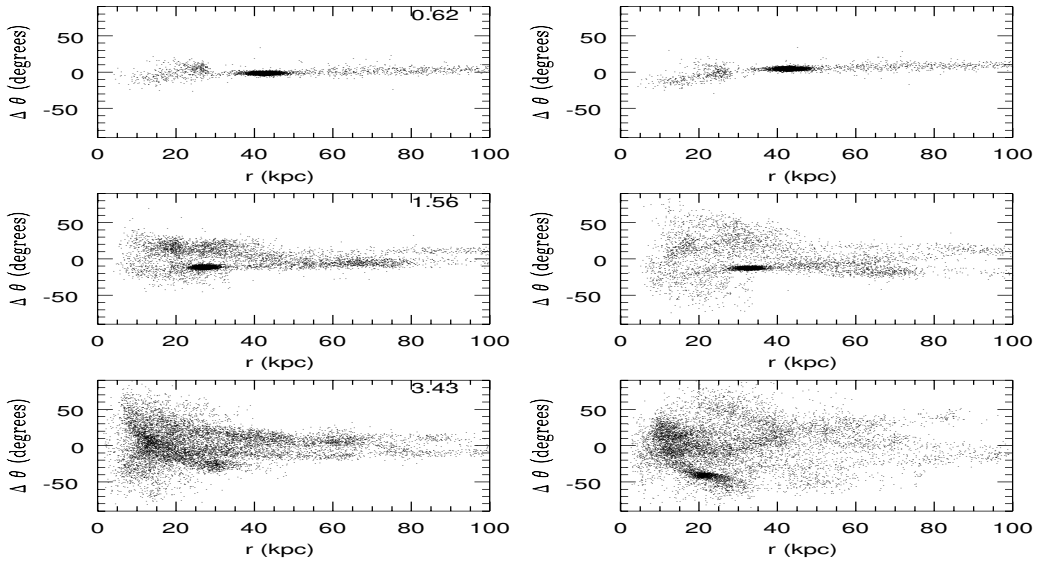

Figure 7.10: **a:** Deviation angles for all satellite particles from the initial orbital plane ($i = 45°$). The left column depicts model G1S145 (spherical DMH), and the right column shows G2S145 (flattened DMH). Rows show three time snaps (given in Gyr). In the last one, the satellite has been fully destroyed.

7.4 Conclusions

In order to assess the importance of dynamical friction in extended oblate DMHs on the distribution of satellite galaxies around their primary, we perform self-consistent N-body computations of satellite galaxies with masses amounting from 10 to 20 per cent of the primary's disc. The satellites are placed on different orbits in spherical and flattened DMHs that have embedded galactic discs and bulges.

The calculations with spherical DMHs lead to results in good agreement with those obtained by VW. Modest differences in quantities are attibuted to the increased mass resolution of our calculations compared with theirs, as well as different linear resolution (grid size versus smoothing length of their TREE algorithm).

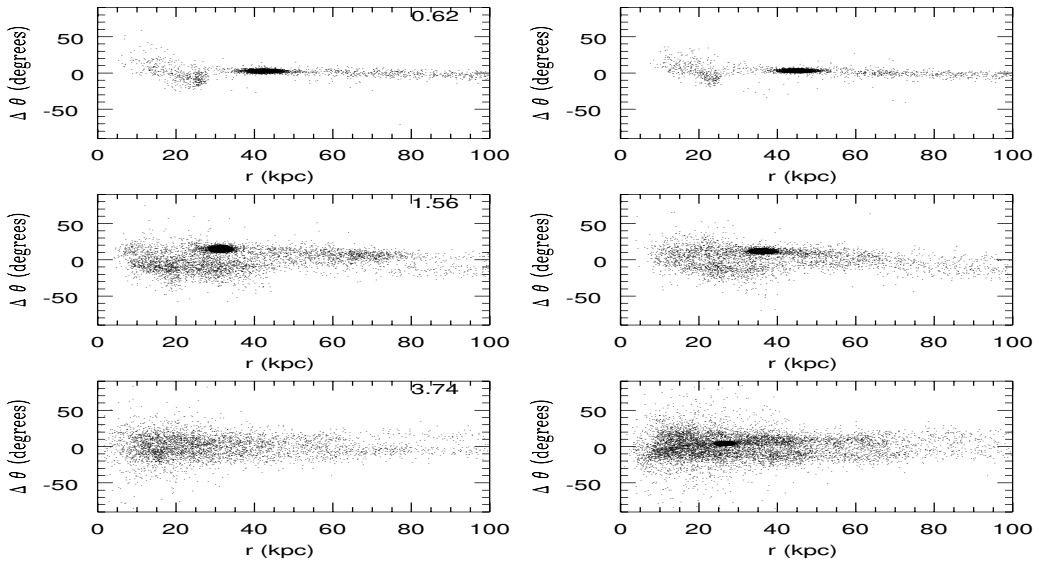

Figure 7.11: **b:** As Fig. 7.10 but for models G1S190 (spherical DMH) and G2S190 (flattened DMH), with initial inclination $i = 90°$.

Satellites evolving in spherical DMHs on prograde orbits relatively to the primary galaxy's disc rotation decay faster than satellites on retrograde orbits or on polar orbits. This results from orbital resonances between the disc and the satellites.

Of particular interest, however, is that our results demonstrate that non-isotropic dynamical friction in flattened DMHs works as a removal mechanism of satellites with low-inclination orbits, whereas it enhances the survival time of satellites on near polar orbits. Thus, satellites on polar orbits survive about 70 per cent longer than satellites on orbits that have a small inclination relative to the primary galaxy's disc (Table 7.2), irrespective of the relative orbital sense (Fig. 7.6) in an oblate DMH with axis ratio $q_h = 0.6$. This is the key result of this investigation.

This result helps understand the distribution of dwarfs galaxies in the Milky Way. Since they are mainly distributed near the galactic pole (Carney et al. 1987) we may infer a selection of survivor dwarfs from a primordial population. The accelerated orbital decay and alignment with the disc of dwarfs within a flattened halo would go some way towards accounting for the data. However if the masses deduced for these satellites (10^8 solar, compared with 10^9 for our models) is a good measure of their mass at the formation time, our computations indicate times as long as a Hubble time for effective mergers. Discrepancies in timescale may well be accounted for if we substitute for the isothermal halo the more concentrated NFW (Navarro, Frenk & White 1995) models or haloes with a steeper cusp (Moore et al. 1998): when each halo model is scaled to the same integrated mass inside the solar radius, the particle velocity dispersion in these models drops faster with radius than for isothermal spheres. Because of the strong dependence of friction on velocity dispersion, this would reduce the timescale for orbital decay very much and offset the effect of reduced satellite masses. We have not, however, performed calculations with different halo mass profiles.

Our computations further show that satellites on orbits with eccentricity $e \geq 0.5$ and with masses larger than 10 per cent of their primary galaxy's disc merge within only a few Gyr with the primary galaxy. The time it takes to merge increases with decreasing orbital eccentricity (Fig. 7.6). We therefore deduce that massive satellites around distant galaxies, such as typically enter the samples that show the Holmberg effect, may be preferentially on near-circular polar orbits or on orbits with apo-galactica further away from their primary galaxy than about 130 kpc.

The calculations also suggest that the orbital eccentricity remains nearly constant for most of the orbits. Only co-planar satellites within a flattened halo suffer an evident circularisation due to the strong dynamical friction.

We also note that the high precession rates of satellite orbits in flattened DMHs and the decrease in orbital inclination leads to tidal debris streams being completely smeared apart for initially inclined orbits.

We want to comment that, despite our use of only two values for the satellite mass in our calculations, this range seems to be representative to reproduce the typical mass of the satellite that Holmberg (1969) and Zaritsky & González (1999) find in their observations when the initial apo-galactic distances is selected properly (Ibata et.al 2001). As Tormen (1997) finds in his numerical calculations of hierarchical galaxy clusters history, more massive satellites ($\sim 10^{11}$) are unlikely to survive due to the large drag force they suffer. On the other hand, though less massive satellites ($\sim 10^8$ solar) feel a negligible drag force, they are quickly disrupted after some peri-galacticon passages due to their low binding energy.

This paper has sought to quantify the effect of aspherical DMHs on the orbits of galactic satellites. The analysis suggests enhanced Holmberg decay, yet what can we say of a population of satellites as a whole? Our model satellites require a few orbits around the host galaxy if dynamical friction is to be effective. Thus within one Hubble time a satellite would require = 5 revolutions (say) or $t = 2$ Gyr for a single revolution at most. In the Milky Way the orbital time $t = 200$ Myr at $r = 10$kpc; assuming an isothermal halo with $\rho \propto r^{-2}$, the critical orbital time $t = 2$ Gyr would be found at $r = 50$ kpc or so. In other words, satellites that are too far from the host galaxy will not have time to experience dynamical friction and hence will not have suffered Holmberg decay. On the other hand, satellites closer to their host galaxy will merge quickly through the process described here. Zaritsky et al. (1999) have noted that satellite populations tend to remain isotropically distributed for satellites with $r > 50$ Kpc.

A more elaborate study is under way, and ultimately we aim at making a statistical study of a modelled observational sample to infer if the Holmberg effect can indeed be produced by flattened DMHs.

Chapter 8

Dynamical friction in flattened systems

8.1 Introduction

The most accepted galaxy formation theory assumes that large-scales structures grew from small amplitude Gaussian fluctuations at the early-stages of the Universe. In hierarchical models, these fluctuations decrease with increasing scales, resulting in the formation of low-mass objects that may merge, building up even more massive structures. The shape and morphology of these objects are strongly dependent on the cosmological models, as one can conclude from the N-body computations, although none of them predict spherical structures. The most successful hierarchical theory is the so-called Cold Dark Matter model (CDM). In this framework, aspherical bound Dark Matter (DMHs) form as a result of gravitational clustering. Dubinsky (1994) finds in his computer simulations a Gaussian distribution of DMH aspect ratios, $q_h \equiv c/a > 0$, where c and a are the minor and major axes of an oblate spheroid, of mean $< q_h >= 1/2$ and dispersion equal to 0.15. Other theories are the Hot Dark Matter model, that predicts haloes as round as $q_h = 0.8$ (Peebles 1993), or Dark Matter candidates such as cold molecular gas (Pfenniger, Combes & Martinet 1994) and massive decaying neutrinos (Sciama 1990), that produce structures as flattened as $q_h = 0.2$.

Observationally, measures of the galaxy axis-ratio becomes a hard subject open to speculation due to the large spread of values that result from different models. The most used techniques are usually: (i) Stellar kinematics. Olling & Merrifield 2000 obtain an axis-ratio of $q_h \approx 0.8$ for our Galaxy. This method has the disadvantage of having access to information of our Galaxy only at small scales. (ii) The flying gas layer method (Olling 1996, Becquaert, Combes & Viallefond 1997) assumes that the HI emission of the Milky Way comes from gas in hydrostatic equilibrium in the Galactic potential, it produces axis-ratios as low as $q_h \approx 0.3$ for the galaxies NGC 891 and 4244, (iii) Warping gas layer. Hofner & Sparke 1994 obtain axis-ratios of approximately 0.7 for NGC 2903 and of $q_h \approx 0.9$ for NGC 2841, 3198, 4565 and 4013, (iv) X-ray isophotes. Boute & Canizares 1998 measure values of $q_h \approx 0.5$ for NGC 3923, 1332 and 720, (v) Polar ring galaxies (Arnaboldi et al. 1993, Sackett et al. 1994) find an axis-ratio of $q_h \approx 0.3$ for NGC 4650A, 0.5 for the galaxy A0136-0801 and 0.7 for AM2020-504, (vi) Precessing dusty discs (Steinman-Cameron, Kormendy & Durisen 1992), measure an axis-ratio of 0.9 for the galaxy NGC 4753.

The last method, which we focus on, is the analysis of satellite dynamics. There are two different approaches to infer the halo shape from satellites.
First, one may attempt to reproduce the observed tidal streams of the Milky Way satellites as done, for instance, by Ibata et al. 2000 who use measures of velocity, position and structure of the Sagittarius dwarf galaxy to constrain the initial parameter space and, subsequently, they calculate in detail the satellite mass loss. They find that the Milky Way cannot be more flattened than $q_h \approx 0.9$, otherwise tidal streams would be too spread and thick compared to the observations.
The second approach is a statistical study of satellite distribution around spiral galaxies. Holm-

berg (1969) and Zaritsky & González (1999) point out that satellites around disc galaxies are found more often aligned with the poles of the host galaxy, the so-called 'Holmberg effect' whereas Quinn & Goodmann (1986) find in their N-body study that the disc alone cannot account for the original statistical distribution of Holmberg's data. A remedy may be sought in the form of an extended non-spherical DMH. An anisotropic velocity (and mass) distribution will cause a satellite's orbit to align with the axes of the velocity ellipsoid of the host galaxy (Binney 1977, hereinafter B77).
For both schemes, a large number of numerical calculations is needed. In the first case, one should integrate several "possible" initial orbital parameters to find the best fit to the observed satellite characteristics, whereas in the second case the satellite initial parameters should statistically reproduce the distributions expected from the cosmological models. So far this is prohibitively time-expensive using any of the present N-body algorithms. The aim of this Chapter is to implement a simple analytic scheme for tracking the dynamical evolution of substructure within flattened as well as spherical DMH's.

The N-body computations of Peñarrubia, Kroupa & Boily 2001, (hereinafter PKB), where it is analysed in detail the effects of the halo asphericity on the satellite decay and disruption, show that the isotropic Chandrasekhar's dynamical friction is not able to explain the results obtained (see Chapter 7 for a summary). For that reason, we implement Binney's expression for dynamical friction in systems with anisotropic velocity dispersions (B77) in our code, which also reproduces Chandrasekhar's for null anisotropy.

In Chapter 6 we carry out a detailed study of the effects that the dependence of the Coulomb logarithm $\ln\Lambda$ on the relative velocity of the two-body encounters and the galacto-centre distance induce on the satellite dynamics. The results indicate that the assumption $\Lambda = \Lambda(r_s)$ leads to the best fit for the first satellite orbits, in agreement with Hashimoto, Funato & Makino (2002). However, this dependence produces orbits that systematically overestimate the satellite decay times (defined as the time the satellite needs to sink into the galaxy central region, which we assume equivalent to the condition $r_s < 3$ kpc). If $\ln\Lambda$=const. the orbit is reproduced less accurately but the decay times are more precise. This quantity is fundamental for the later study on the satellite distribution around spiral galaxies, thus we decide to analyse in detail only Binney's expressions for aspherical systems.
We have also shown that the effects of the system inhomogeneity on the satellite orbit (through the first order term of dynamical friction) are negligible. We decide, therefore, not to implement $F^{(1)}$ in our calculations.

Our goal is to check whether, as Chandrasekhar's expression for spherical haloes, it is reasonably accurate to use the results of B77 to reproduce dynamical friction in aspherical systems. We also compare the results of using Chandrasekhar's formula in axi-symmetric systems to determine the effects of the velocity anisotropy on the satellite decay.

The method followed is essentially that presented in Chapter 6.

8.2 Galaxy and satellite parameters

The galaxy and satellite parameters can be found in Chapter 3. We limit our study to the set of halo parameters enclosed in the model H2, whereas the satellite model corresponds to S1. The galaxy model H2 corresponds to the one of G2, where the disc and bulge have been removed, so that the output data can be used to analyse the disc and bulge effects on the satellite motion.

The values of the galaxy parameters can be found in Table 3.1. We carry a single simulation with the model H5 in order to infer the dependence of our numerical experiments with the galaxy particle number.

Name	Gal. model	Sat. model	i	e	r_p [kpc]	r_a [kpc]
H2S100	H2	S1	0°	0.5	18	55
H2S130	H2	S1	30°	0.5	18	55
H2S145	H2	S1	45°	0.5	18	55
H2S160	H2	S1	60°	0.5	18	55
H2S190	H2	S1	90°	0.5	18	55
H2S100c	H2	S1	0°	0.3	30	55
H2S130c	H2	S1	30°	0.3	30	55
H2S145c	H2	S1	45°	0.3	30	55
H2S160c	H2	S1	60°	0.3	30	55
H2S190c	H2	S1	90°	0.3	30	55
H2S100e	H2	S1	0°	0.7	10	55
H2S130e	H2	S1	30°	0.7	10	55
H2S145e	H2	S1	45°	0.7	10	55
H2S160e	H2	S1	60°	0.7	10	55
H2S190c	H2	S1	90°	0.7	10	55
H5S145	H5	S1	45°	0.5	18	55

Table 8.1: The numerical experiments. The peri- and apo-galactica are r_p and r_a, respectively, and $e = (r_a - r_p)/(r_a + r_p)$ is the orbital ellipticity .

8.3 Numerical calculations

8.3.1 Code parameters

The numerical simulations were carried out by using the mesh-code SUPERBOX (see Chapter 2) to evolve the galaxy-satellite system.

The system used was exactly that of PKB, with the difference that we remove the disc and bulge components. In this paper a detailed description of the system and the grid structure is presented, whereas here we merely give a brief description of the most important orbital parameters.

The grid-structure of the halo and satellite corresponds to that outlined in Chapter 6 and PKB . The time-step is also fixed to the same value to make possible a inter-comparison of the velocity anisotropy effects, not only by employing the semi-analytic code, but also through the numerical data.

8.3.2 Orbital parameters

We carry out a set of calculations varying the parameters of the satellite that remark the differences between the expressions (4.1) and (4.3), i.e Binney's and Chandrasekhar's formulæ, when applying both of them to the decay of a satellite within a flattened halo. These parameters are:
(i) the initial orbital inclination (i), defined as the angle between the initial angular momentum vector of the satellite and the initial angular momentum of the disc. We expect the inclination to decrease in time as predicted by Binney, which shall not occur by using Chandrasekhar's formula. We note that all the calculations proceed with the same orbital sense, which is irrelevant since the halo is non-rotating.
(ii) The satellite's initial orbital eccentricity, defined as $e = (r_a - r_p)/(r_a + r_p)$, where r_a, r_p are the apo and perigalacticon, respectively.

A wider study of the parameter-space (as the satellite mass, initial apo-galacticon distance...etc), is carried out by PKB. Since they do not introduce differences between the two equations of dynamical friction, we fix these values along the set of computations.

The system galaxy-satellite is constructed as outlined in Section 6.2.

The parameters of the numerical experiments are listed in Table 8.1.

8.4 Halo Dynamical Friction

As commented above, Chandrasekhar's expression cannot explain some effects observed in N-body calculations of satellite decay within flatten haloes (PKB). Our aim is to check Binney's approximation (B77) for systems with anisotropic velocity dispersion (for a detailed study of the friction force see Chapter 5).

For simplicity, we reproduce here the analytic formulæ employed along this study. If the distribution function in the velocity space is axi-symmetric, the specific zeroth order friction force is (B77)

$$F_i = -\frac{\sqrt{2\pi}\rho_h(R,z)G^2M_s\sqrt{1-e_v^2}\ln\Lambda_h}{\sigma_R^2\sigma_z}B_R v_i \tag{8.1}$$
$$F_z = -\frac{\sqrt{2\pi}\rho_h(R,z)G^2M_s\sqrt{1-e_v^2}\ln\Lambda_h}{\sigma_R^2\sigma_z}B_z v_z,$$

where $i = x, y$ and (σ_R, σ_z) is the velocity dispersion ellipsoid in cylindrical coordinates with constant eccentricity $e_v^2 = 1 - (\sigma_z/\sigma_R)^2$. We denote $\ln\Lambda_h$ as the Coulomb logarithm of the halo and

$$B_R = \int_0^\infty dq \frac{\exp(-\frac{v_R^2/2\sigma_R^2}{1+q} - \frac{v_z^2/2\sigma_R^2}{1-e_v^2+q})}{(1+q)^2(1-e_v^2+q)^{1/2}}$$

$$B_z = \int_0^\infty dq \frac{\exp(-\frac{v_R^2/2\sigma_R^2}{1+q} - \frac{v_z^2/2\sigma_R^2}{1-e_v^2+q})}{(1+q)(1-e_v^2+q)^{3/2}}$$

As Binney shows, a body with mass M_s will suffer a decrease of its orbital plane inclination whenever $B_z > B_R$ (oblate halo). If the orbit is either coplanar or polar, the inclination remains constant since, respectively, either the perpendicular or the planar component of v is zero. One can easily probe that this expression reproduces Chadrasekhar's when $e_v = 0$, i.e,

$$\mathbf{F}_{\rm ch} = -4\pi G M_s^2 \rho_h(R,z)\ln\Lambda_d\big[\mathrm{erf}(X) - \frac{2X}{\sqrt{\pi}}e^{-X^2}\big]\frac{\mathbf{v}_s}{v_s^3}, \tag{8.2}$$

where $X = |\mathbf{v}_s|/\sqrt{2}\sigma$.

One important aspect to note is that both expressions of dynamical friction have an anisotropic halo density in base of the local approximation (which is denoted by $\rho_h = \rho_h[r,\theta]$, where θ is the azimuthal angle defined by the angular momentum vector). In practice, this implies that the only difference between both expression is that made by the anisotropy of the velocity distribution.

8.5 Fixing the Coulomb logarithm

Making use of the fitting procedure detailed in Chapter 6, we proceed to fix the Coulomb logarithm by requiring the best fit of the semi-analytic to the numerical data during the first 3 and 4 orbits assuming, therefore, that the mass loss effects can be neglected along the early time of the evolution. In Fig. 8.1 we plot the fits of some of the experiments, concretely, those with inclinations 30°, 45° and 60° (columns), with eccentricities 0.3, 0.5 and 0.7 (raws). For each model, the semi-analytic code is employed to generate the satellite orbit using Chandrasekhar's (gree lines) and Binney's (black lines) formula to reproduce dynamical friction. The fitting parameter χ, defined as the discrepancy of the satellite position between numerical and semi-analytic data (eq. 6.2) is calculated for the first 3 and 4 orbits, denoted with solid and dotted lines respectively. This figure clearly shows that Chandrasekhar's formula poorly describes the dependence of the satellite orbit with the initial inclination, leading to a wider dispersion of the Coulomb logarithm values (for this range of inclinations, between 30° and 60°, $\ln\Lambda \in [0.9, 2.8]$). If Binney's expression is used, the variation of $\ln\Lambda$ is highly reduced ($\ln\Lambda \in [2.3, 2.5]$), which proves that this scheme successfully

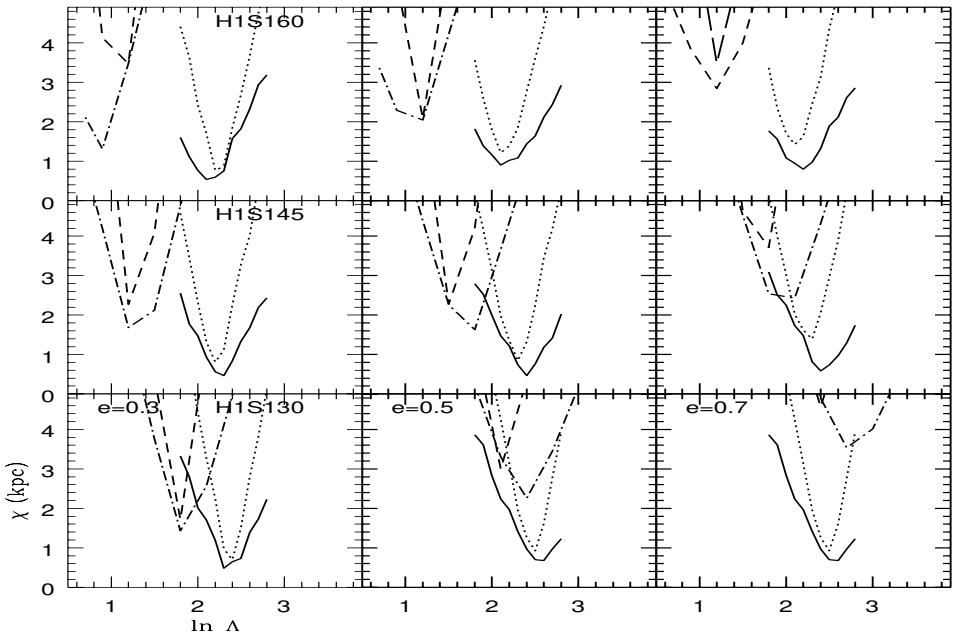

Figure 8.1: Fitting parameter for diverse orbital eccentricities and inclinations. Dotted lines denote fittings of the first 4 orbits, whereas solid lines of the first 3 orbits. We use dashed and dotted-dashed lines to represent the results from Chandrasekhar's expression for $k = 4$ and 3 orbits, respectively.

Friction	k	lnΛ	$\chi_{\rm min}$(kpc)
Binney	3	2.4	1.3
	4	2.4	2.0
Chandrasekhar	3	2.1-2.2	8.1
	4	2.1-2.2	10.6

Table 8.2: Results of the fitting procedure applied to the numerical calculation of Table 8.1 for both formulæ of dynamical friction.

describes the effects of the anisotropic velocity dispersion on the satellite decay, independently of the orbital inclination. These differences become much larger if the range of inclinations is wider.

We must note that Binney's formula also presents barely dependence on the satellite eccentricity, contrary to Chandrasekhar's expression.
Even if the eccentricity and inclination are fixed, i.e the fit is over a given model, Binney's friction improves the accuracy of the fit from 50-150% with respect to Chandrasekhar's result.

If Chandrasekhar friction is used, the Coulomb logarithm that produces the best fit becomes lower as the inclination increases. As we will see below, since dynamical friction is proportional to $\ln\Lambda$, the use of the averaged value implies an overestimation of the force for high inclinations and *viceversa*.

The final averaged over the numerical experiments of Table 8.1 is plotted in Fig. 8.2. This figure shows the high discrepancies produced by Chandrasekhar's expression if the fit is for a large range of orbital inclinations and eccentricities, as expected. The minimum of the curves determines the value of $\ln\Lambda$ that leads to the best fit for both formulæof dynamical friction, which we summarised in Table 8.2. The values of $\chi_{\rm min}$ denote the error per unit curve associated with the fit.

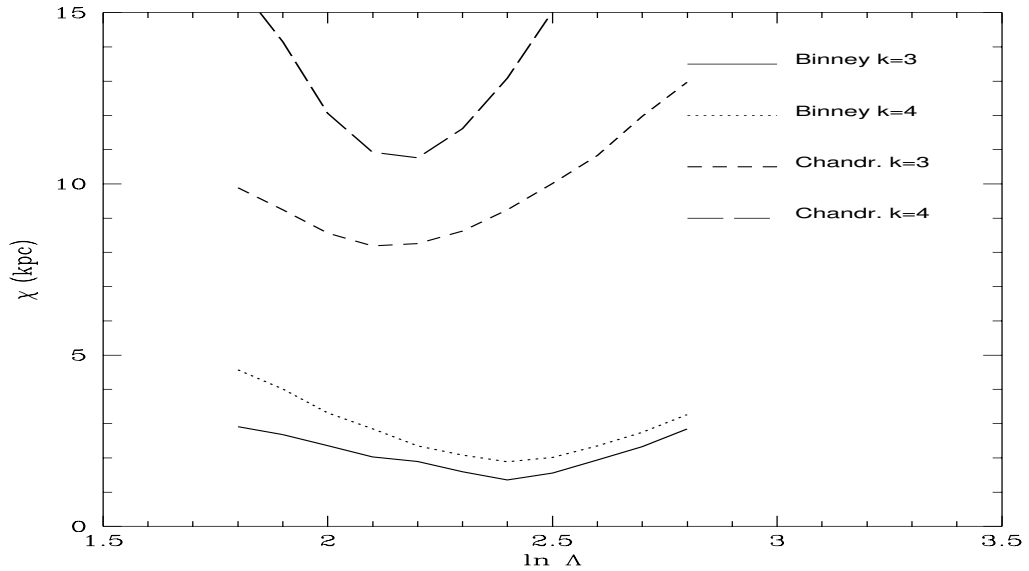

Figure 8.2: Average of the fitting parameters over the calculations of Table 8.1.

8.6 The velocity anisotropy effects

In this Section, we make a comparison of the different effects that the velocity anisotropy induces on the evolution of the satellite orbit.

8.6.1 Satellite decay and mass loss

One of the most important effects of dynamical friction is the monotonic reduction of the orbital angular momentum and energy along the satellite evolution that leads to a progressive decrease of the averaged galacto-centre distance. The numerical calculations carried out by PKB show a strong dependence of the decay time on the initial inclination that must be compared to analytic estimations.

In Fig. 8.3 we plot the radius evolution (left column) and mass evolution (right column) for those models with $e = 0.5$. The value $M_s(t)$ being numerically calculated as explained in Section 4.3. From this figure, we conclude that Binney's expression clearly produces more accurate results than Chandrasekhar's one for the whole range of orbital inclinations. This result is not surprising due to the small dependence of the Coulomb logarithm on the inclination and eccentricity as it is shown in Fig. 8.1.
Additionally, the value of $\ln\Lambda$ that produces $\chi_{\min}$ fits not only the first two and three orbits, but also success in reproducing the decay time of the satellite.

PKB observe that coplanar satellites suffer higher friction than those following polar orbits, leading to survival times over 70% longer. Due to the presence of disc in their galaxy model, it is unclear the contribution of the disc anisotropy on the decay differentiation as a function of the inclination. Our numerical calculations where the disc and bulge are removed show a range of survival times that goes from 3.7 Gyr up to 6 Gyr, using the same orbital parameters and halo flattening as PKB. This implies a decay time differentiation of around 60% between polar and coplanar satellites, which indicates that the disc contribution might be of the order of 10%. The effects of the disc on the satellite orbit are studied in more detail in Chapter 9.

Depending on the symmetry of the halo distribution, one can observe the following effects:

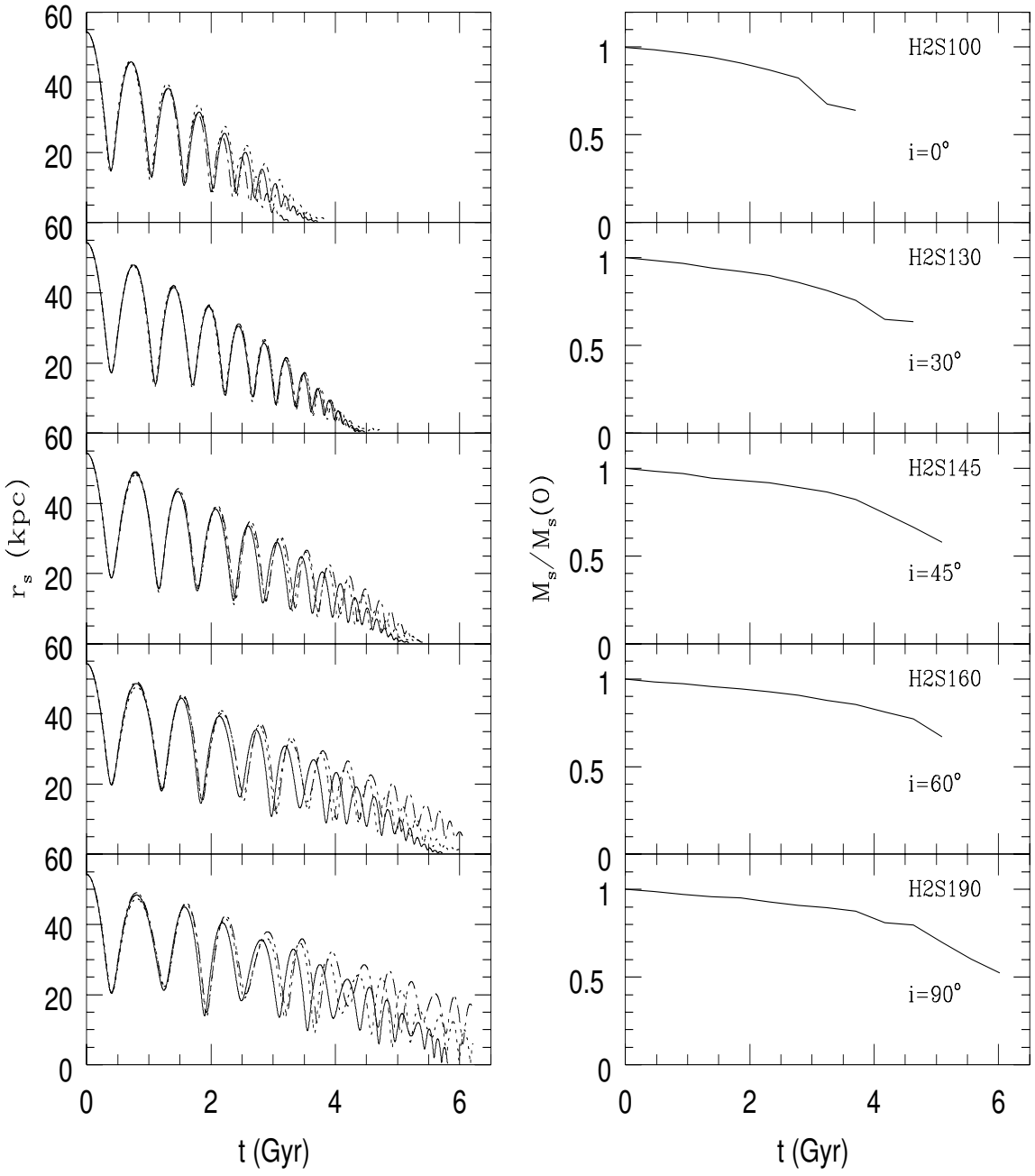

Figure 8.3: Radius and mass evolution for the models of Table 8.1 with $e = 0.5$. Dotted lines represent the numerical evolution, whereas full and dashed lines the data obtained from the semi-analytic code using Binney's and Chandrasekhar's expressions to describe the dynamical friction process.

- **Spherical mass distribution. Isotropic velocity distribution** Satellites orbiting systems with spherical distribution function move along orbits that do not depend on their orientation with respect to the symmetry axis (see Chapter 6).

- **Flattened mass distribution. Isotropic velocity distribution** The spatial asphericity provokes a strong differentiation of the satellite decay as a function of the orbital inclination. Assuming the local approximation as valid, dynamical friction in such a system can be reproduced by Chandrasekhar 's formula. Although this distribution cannot be found in the Nature, it is interesting as an exercise.

- **Flattened mass distribution. Anisotropic velocity distribution** The main influence of the velocity anisotropy on the satellite orbit is the attenuation of the spatial anisotropy effects, which is equivalent to $B_R < B_z$ in Binney's formula (eq. 8.1, oblate systems). As Fig. 8.3 shows, if one assumes an isotropic distribution in velocity space ($B_R = B_z$) or, equivalently, we use Chandrasekhar's formula to reproduce dynamical friction, this leads to an overestimation of dynamical friction for low inclinations and a underestimation for those satellites following high inclined orbits.

For simplicity, we do not plot the radial evolution for $e = 0.3, 0.7$ since these results have been proved to be independent of the initial eccentricity.

Along the orbit, the satellite loses mass due to the action of tidal forces on the satellite particles. The absence of disc and bulge makes the time-scale of the tidal force to be shorter than the motion of the satellite particles around the centre-of-mass. In this regime, the mass stripped by the tidal force can be properly reproduced by the calculus of the Lagrange points, i.e those where the external galaxy potential is equal to the satellite self-potential (see Section 4.3).

The mass evolution represented in Fig. 8.3 is different to that found PKB. They observe in their numerical experiments that all satellites with $M_s = 0.1 M_d$ and $r_0 = 55$ kpc are destroyed before the remaining bound part of the satellite reaches the central region of the galaxy, independently on the orbital eccentricity and inclination (see Chapter 7). However, if the disc and bulge are removed (implementing the same satellite models and initial orbital parameters), the mass evolution shows a nearly monotonic decrease which leads to the incoming of bound satellites in the inner most part of the galaxy. Due to the importance of the disc and bulge effects on the satellite dynamics and mass evolution, we carry out a detailed study in Chapter 9.

8.6.2 Evolution of the orbital inclination and eccentricity

Orbits around non-spherical systems have inclinations (i) that do not remain constant but suffer periodical oscillations due to *nutation* (see Appendix A). Once fixed the initial conditions, the amplitude and frequency of the nutation remain constant if the friction force is removed from the equations of motion whereas, if it is implemented, processes such the nutation and precession vary accordingly to the angular momentum and radial distance evolution. Our interest focus now on the effects induced by the velocity anisotropy on the satellite inclination along the orbit.

In his work, Binney (B77) predicts the progressive reduction of i due to dynamical friction if the velocity dispersion ellipsoid is axi-symmetric (σ_R, σ_z) and $\sigma_R > \sigma_z$. By symmetry, the inclination decrease will not occur if the orbits are either coplanar ($i = 0°$) or polar ($i = 90°$).
The inclination evolution of models with $e = 0.5$ is plotted in Fig. 8.4 (left column), where dotted lines denote the numerical data and solid and dashed lines the semi-analytic evolution if dynamical friction is reproduced by Binney's and Chandrasekhar's formulæ, respectively.
This Figure shows the reduction of the averaged i predicted by Binney and observed by PKB in their numerical calculations. After the satellite has sinked to the most inner region of the halo, the inclinations are as low as 10° barely dependent on their initial value. This large decrease of i is well reproduced by Binney's expression, although the nutation process shows discrepancies with the numerical result, which is connected with the poor fit of the orbit, despite the accurate description of the overall decay process (this is also observed when applying Chandrasekhar's expression for

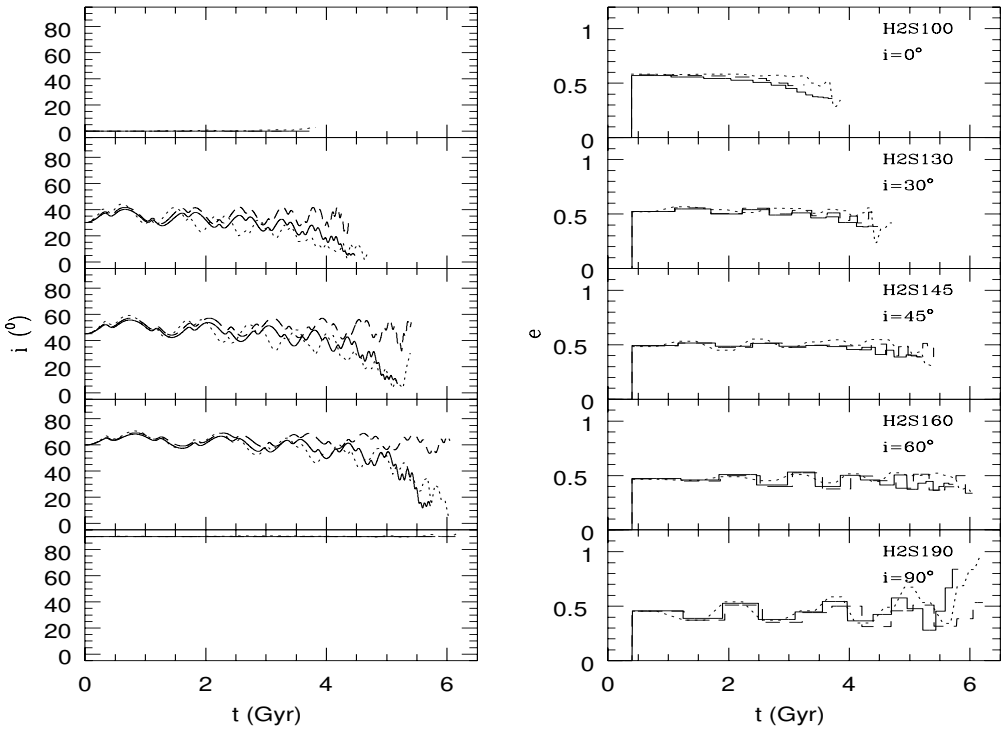

Figure 8.4: Inclination and eccentricity evolution for the models of Table 8.1 with $e = 0.5$. Dotted lines represent the numerical evolution, whereas full and dashed lines the data obtained from the semi-analytic code using Binney's and Chandrasekhar's expressions to describe the dynamical friction process.

dynamical friction in spherical systems, see Chapter 6).
As expected, the orbital inclination of coplanar and polar satellites remains constant.

If dynamical friction is reproduced by Chandrasekhar's formula, i.e the velocity distribution is assumed isotropic, the averaged value of i does not change along the orbit, which clearly comes into contradiction with the numerical results.

In Fig. 8.5 and 8.6 (left columns) we plot the comparison for models with $e = 0.7, 0.3$, respectively. The results show barely dependence on the eccentricity. It is interesting to note that, independently of e, orbits that are neither coplanar nor polar present high drops of the mean value of i. After the satellite sinks to the centre, the final orbital inclination lies for all the models in between 10-20°.

We must remark the importance of the accuracy of the Binney's formula in order to describe correctly the process of inclination decrease that satellites suffer in axi-symmetric systems. This result is crucial to simulate properly the satellite motion and to investigate the satellite distribution around spiral galaxies.

Like the orbital inclination, the eccentricity is one of the orbital parameters that can be indirectly measured from observations to determine the satellite motion around a galaxy. The right column of Fig. 8.4 shows the comparison of the numerical eccentricity evolution with both semi-analytic approaches. As it was observed in Chapter 6, if the Coulomb logarithm is assumed constant, the analytic formulæ of dynamical friction leads to an overestimation of the eccentricity decrease, which occurs mostly at the late-times of the orbit evolution, the so-called *orbital circularisation*, and becomes stronger for low inclined orbits, those that suffer higher dynamical

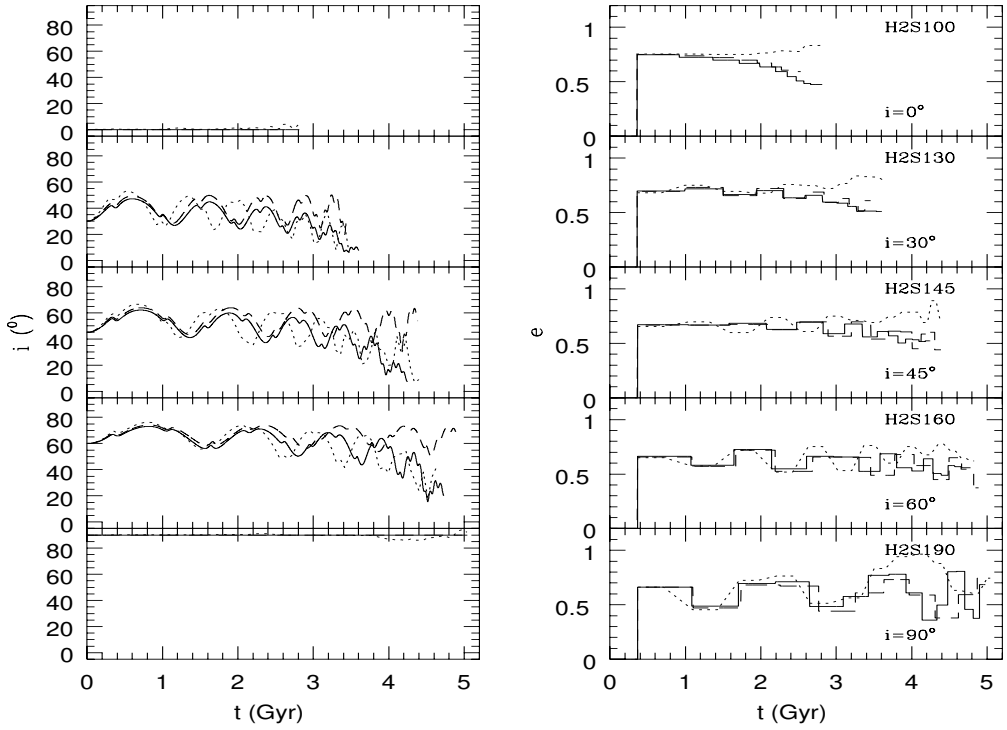

Figure 8.5: As Fig. 8.4 for models with $e = 0.7$. Note that the time-scale has a different value.

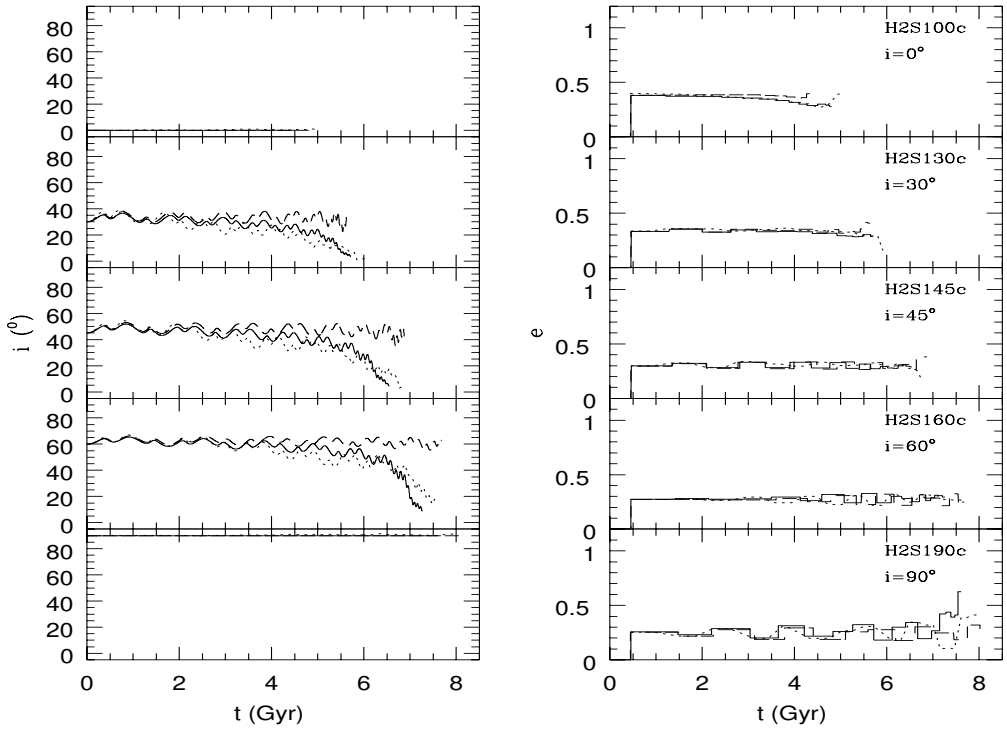

Figure 8.6: As Fig. 8.4 for models with initially $e = 0.3$. Note that the time-scale has a different value.

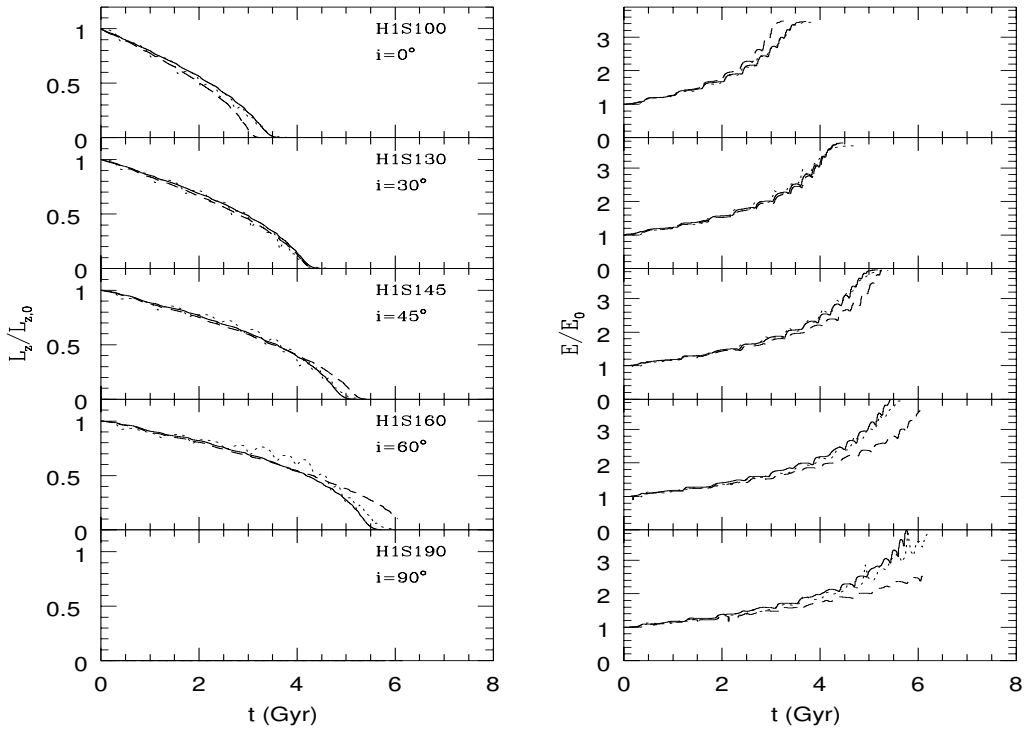

Figure 8.7: Energy and angular momentum evolution along the orbits with $e = 0.5$. The numerical evolution is denoted by dotted lines, whereas the semi-analytic data is represented by solid and dashed lines if dynamical friction is reproduced by Binney's and Chandrasekhar's formulæ, respectively. The quantities E and L_z are normalised to the initial value.

friction. Fig. 8.5 and Fig. 8.6 indicate that the circularisation increases if the initial orbital eccentricity is higher and decreases for more circular orbits. Both dynamical friction expressions reproduce accurately the eccentricity evolution for the first orbital periods, however at late-times the eccentricity exhibits a reduction not present in the numerical calculations that can be as high as 30% for low inclined satellites following high eccentric orbits.

8.6.3 Energy and angular momentum evolution

A flattened system possesses two analytic constants of motion, the energy and the component of the angular momentum perpendicular to the axi-symmetry plane (that we denote as L_z). The total angular momentum $L^2 = L_R^2 + L_z^2$ is, however, not constant along the satellite orbit (see e.g BT), but has periodic variations that correspond to a precession of the orbital plane around the z-axis.

Since the dynamical friction force has an opposite sense with respect to the satellite velocity, it acts decreasing the angular momentum and energy which induces a monotonic sink into the inner regions of the halo potential. The reduction of angular momentum, therefore, implies an increase of the energy (in absolute value), since the potential enhances for decreasing radius. Due to the low magnitude of dynamical friction if compared to the mean field force, we expect an easier comparison between numerical and semi-analytic data by the slow variation of L_z and E along the orbit. In Fig. 8.7 we plot the changes over E and L_z due to dynamical friction for the models with $e = 0.5$. The results are equivalent to those of the radial evolution. The Chandrasekhar's

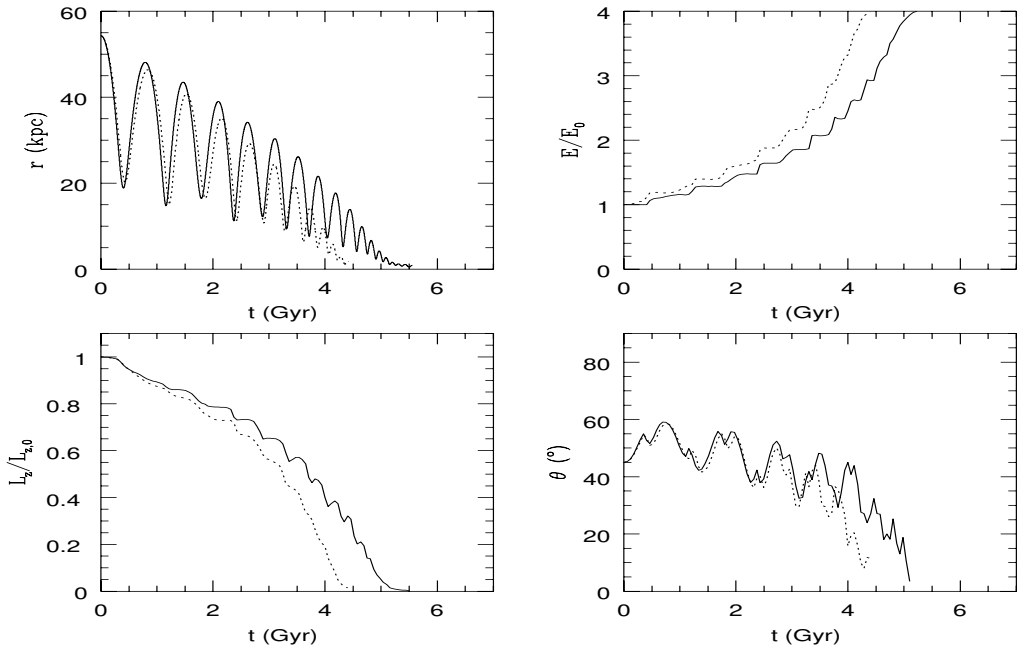

Figure 8.8: Comparison between the model H2S145 (full line) and H5S145 (dotted lines).

formula overestimates dynamical friction for low inclined orbits and underestimate it for high inclined orbits. For orbits with $i < 45°$, this appears as a stronger reduction of the z-component of angular momentum and, equivalently, a large increase of the energy. The effect is contrary for satellites with $i > 45°$.
This figure illustrates how the kinetic energy of the satellite is lost via friction, being observed by the halo particles. At the end of the simulation the angular momentum has a null value, i.e the satellite remains in the inner most part of the galaxy.

It is interesting to note that the energy and angular momentum evolution present small oscillations along their evolution. This behaviour is due to the self-response of the halo to the satellite motion. Since SUPERBOX preserves the total energy and angular momentum, the halo also moves around the centre-of-mass of the system. Due to the complexity of the feedback, it cannot be reproduced analytically, so that we decide to fix the halo centre-of-mass as the coordinate origin in the semi-analytic code (see Chapter 4).

8.6.4 Increasing the number of particles

The selection of the Coulomb logarithm has been shown to be sensitive to numerical parameters like the number of N-body particles and the resolution of the code (e.g Klessen & Kroupa 1998, Fellhauer et al. 2000), through the dependence of the satellite-galaxy particles encounters on these factors.

In a very recent paper Spinnato et al (2003) show that the value of the Coulomb factor Λ is inversely proportional to the system size, which can be interpreted as the cell size for a collisionless particle-mesh code such as SUPERBOX. They show that, if the number of particles is large enough, the value of $\ln\Lambda$ approaches asymptotically to some quantitative value. In order to infer whether the Coulomb logarithm that we find is sensitive to the particle number (N), we carry out a calculation where N is eight times larger (halo model H5). The comparison between the satellite decay is plotted in Fig. 8.8. We observe a decrease of the decay time of around 15% (i.e increase of the friction force) for increasing N which also causes a faster reduction of the z-component of the angular momentum and the orbital inclination (note that the final value of i is for both cases

the same). Fitting the Coulomb logarithm yields to the new value $\ln\Lambda$=2.6, i.e 8% larger than for the model H2.
We think that this relatively small variation of the Coulomb logarithm indicates that the asymptotic value as a function of N might be close to $N \sim 10^7$. Though the variation of $\ln\Lambda$ is relatively small, one can appreciate in Fig. 8.8 that the satellite orbit is significatively altered.

8.7 Conclusions

To asses the accuracy of Binney's equations (B77) in order to reproduce the satellite decay in flattened Dark Matter haloes, we perform a set of numerical calculations varying the orbital inclination as well as the eccentricity of the satellite.

The results of the comparison are contrasted to the widely used Chandrasekhar's formula. By means of the local approximation, both equations include the spatial flattening through the aspherical density profile. This means that the differences on the satellite motion induced by each treatment of dynamical friction come from the anisotropy in velocity space, which is implemented in the calculus of B77.

The accuracy of Binney's and Chandrasekhar's formulæ in fitting the numerical orbits is determined by the calculus of the parameter $\chi^2 = \sum(\mathbf{r}_{\rm num} - \mathbf{r})^2 + \sigma^2\Delta t^2$ at the peri and apo-centres for a given number of orbits. If dynamical friction is reproduced by Binney's equation, this quantity shows discrepancies of approximately $\chi_{\rm min} = 2$ kpc per unit orbit after averaging over the set of experiments and for the first three orbits, meanwhile Chandrasekhar's formula produces values of around $\chi = 10$ kpc.
We conclude that Binney's expression faithfully reproduces the process of dynamical friction in anisotropic systems. The fit is as accurate as that employing Chandrasekhar's formula in isotropic systems (see Chapter 6).

The comparison of the orbits resulting from Chandrasekhar's and Binney's expression of dynamical friction give us the possibility of asses the effects of the velocity anisotropy on the satellite dynamics. We have proved that,
(i) if the density profile is in both equations $\rho = \rho(r, \theta)$, where $\theta = \pi/2 - i$ is the azimuthal angle, the orbits generated by Chandrasekhar's formula overestimate the satellite decay time for polar orbits and underestimate it for coplanar ones. One effect of the velocity anisotropy is then to reduce the interval of decay times as a function of the orbital inclination. The Binney's expression has proved to reproduce accurately the numerical results independently of the initial eccentricity. Comparing the interval obtained by PKB to that where disc and the spherical bulge are removed, we can assert that the disc anisotropy makes it about 10% wider for a disc with mass $M_d = 0.1M_h$.
(ii) Dynamical friction in systems with anisotropic velocity distribution leads to a marked decrease of the orbital inclination (i) which is well reproduced by Binney's expression. After the satellite sinks to the most inner region of the galaxy, i lies within 10-20°, independently of the initial value.
(iii) The study of the energy and angular momentum evolution as a function of the orbital inclination confirm the results of (i) and (ii).

The semi-analytic eccentricity evolution, either employing Chandrasekhar's formula or Binney's one, shows the so-called *circularisation* process, defined as the progressive reduction of e along the orbit. This variation is stronger for increasing friction (like along coplanar orbits or during the late-times of the evolution) and barely takes place in the numerical calculations. A possible solution my be sought in the galacto-distance dependence of the Coulomb logarithm, as proposed by Hashimoto, Funato & Makino (2002). Despite we find that it improves the description of the orbit at early-times, this scheme also overestimates the satellite decay time for all the experiments (see Chapter 6 for more details). The small circularisation along the orbit agrees with the results of van den Bosch et al. (1999).

Our experiments show the effects that the presence of disc and bulge introduce on the satellite mass loss by comparing them to those of PKB. This is analysed in detail in Chapter 9 , though we can advance that their absence leads to the survival of a bound remanent after the satellites comes to the inner most region of the halo, contrary to the results of PKB. This results confirms

the importance of the disc and bulge presence in order to reproduce realistically the satellite distribution around spiral galaxies.

The dependence of our results on the number of N-body particles is small. Increasing N by a factor eight yields to differences of 8% in the value of the Coulomb logarithm.

This study has proved that Binney's expression of dynamical friction is accurate in order to describe the satellite decay in flattened haloes, independently of the initial orbital inclination and eccentricity. The results, therefore, allow the implementation of the semi-analytic code of Binney's equation to carry out a statistical analysis of the satellite evolution around flattened systems, which would be time prohibitive if one utilises a N-body code.

Chapter 9

Disc and bulge effects on the satellite

9.1 Introduction

The currently favoured cold Dark Matter theory of galaxy formation postulates that the formation of a massive spiral galaxy like our own is a consequence of the hierarchical assembly of sub-galactic dark haloes, and the subsequent accretion of cooled baryonic gas in a virialized, galaxy-scale dark halo (e.g Peacock 1999). Numerical calculations based on this picture are able to, at least qualitatively, reproduce the characteristics of a disc galaxy (e.g Navarro & Steinmez 2000), though some difficulties still remain, like the overestimation of the disc vertical width and the number of satellite galaxies.

The study of the repeated close encounters and merges of the galaxy substructures seems to be meaningful to investigate the properties and evolution of galaxies affected by such processes. Several N-body calculations were performed during the last decade in order to analyse the influence of minor mergers on galactic discs in greater detail (e.g Quinn et al. 1993, VW). One of the main conclusions was that merging satellite within the range of mass ratios $M_s/M_d \simeq 0.05, 0.2$ can cause a vertical thickening of the baryonic disc of a factor between 2 and four, depending on the galacto-centre distance, due to the response of the "stars" to the satellite perturbation. However, the huge parameter space of such studies complicates the overall inference of the effects induced by the merging process on the disc evolution. The quantitate results also depend crucially on parameters like the gas content and behaviour in the disc, induced by star formation or by the satellite orbit.

Here in this Chapter, we attempt to study the problem from the opposite point of view, formulating the following question: how does the disc (and bulge) presence affect the dynamics, the merging rate and the mass evolution of satellites? This subject of investigation has been widely analysed by carrying out numerical experiments (e.g Quinn & Goodman 1983 and VW) and with semi-analytic modelling (Tóth & Ostriker 1992, Taylor & Babul 2001, hereinafter TB) in order to determine the merging rate as a function of the orbital and galaxy parameters. These treatments agree, that the main mechanism that successfully describes the satellite orbital evolution is dynamical friction (see Chapter 5 for a detailed theoretical description . Depending on the parameters of the orbit, galaxy and satellite, this process may lead either to the final merge of the satellite into the galaxy or to its previous destruction.

Despite of the small mass ratio of the disc and bulge if compared to that of the halo, the baryonic component [1] may play an important role in order to accelerate the mass loss of the

[1] Hereinafter, we take the liberty of denoting the disc and bulge particles as the "baryonic component of the galaxy", regarding that in SUPERBOX these particles are identical to those of the Dark Matter halo, interacting to each other only through gravity. Our definition, therefore, goes beyond the N-body scheme and it is thought to give insights in a cosmological background.

satellite via tidal shocks (e.g Sptizer 1987, Kundić & Ostriker 1995, Gnedin & Ostriker 1997, Gnedin & Ostriker 1999) and the enhancement of the decay rate when the satellite comes some scale-lengths close to these galaxy components, as concluded from the study of TB. Thus, the mass loss also controls through dynamical friction (regarding that the specific friction force accomplishes $F_{\rm df} \propto M_s[t]$) the decay process.

In Section 9.3 we investigate the effects that the disc and bulge presence induce on the satellite orbit and evolution by comparing the numerical calculations of Chapters 6 and 8 , where the galaxy is formed by a pure Dark Matter halo with axis-ratio 1 (spherical) and 0.6 (oblate axi-symmetric), respectively, to those where the disc and bulge substructures are included in the modelling of the galaxy (Chapter 7, corresponding to the numerical experiments of PKB). In both cases, we use spherical and axi-symmetric haloes, attempting to determine the influence of the halo shape on the disc and bulge contributions.

In the second part of this Chapter, Section 9.4, we want to determine the accuracy of the self-consistent semi-analytic code (Chapter 4) in order to describe the satellite evolution. Whereas in previous Chapters the satellite mass is implemented as an external output obtained from the N-body data, so that effects induced by mass loss can be distinguished from those induced by dynamical friction, in this Chapter we make use of the mass loss scheme outlined in Section 4.3. The results can be compared with those obtained by TB using a similar semi-analytic code. One must, however, bear in mind that TB uses the numerical experiments carried out by VW in order to select the free parameters (disc and halo Coulomb logarithms plus the "energy factor", which multiplies eq. 4.5 and 4.7), whereas we use those of PKB. In both cases, galaxy and satellite models are the same.
We expect differences in the final value of the Coulomb logarithms since: (i) the models of PKB are composed by nine times more N-body particles for the halo and double the disc particles and (ii) PKB and VW make use of different N-body methods, (mesh and tree codes, respectively).

If the semi-analytic treatment proves to produce an accurate description of the numerical data, we shall use this code to carry out a statistical survey of the satellite distribution around spiral galaxies in a following Chapter.

9.2 Numerical experiments

In this Section the numerical experiments carried out along our study are outlined. We attempt to analyse of the disc and bulge effects on the satellite dynamics and mass evolution. With that purpose in mind, we collect the calculations carried out in previous Chapters, which possess the same orbital, satellite and SUPERBOX parameters, the only difference being the presence of disc and bulge. These parameters are summarised in Table 8.1.

To analyse of the disc and bulge effects we employ four different galaxy models, denoted as H1, H2, G1 and G2, where "H" means the galaxy formed by a pure halo, "G" if bulge and disc are included, "1" if the halo is spherical and "2" if it is flattened with axi-ratio $q_h = 0.6$. The characters "a,e" denote different orbital eccentricities.

For more information, we give explicitely the list of tables in which the properties of the galaxy components and the satellite can be found,
(i) Galaxy model H1, H2, G1 and G2: Table 3.1
(ii) Satellite models: S1 and S2: Table 3.2.

9.3 Numerical analysis

In this Section we examine the satellite decay and mass loss of the models presented in Table 9.1 in order to determine the contribution of the baryonic substructure on the satellite evolution.

Halo shape	Name	Gal. model	Sat. model	i_i	e	r_p [kpc]	r_a [kpc]
Spher.	H1S1a	H1	S1	–	0.5	18	55
$q_h = 1$	G1S100	G1	S1	0°	0.5	18	55
	G1S1180	G1	S1	180°	0.5	18	55
	G1S145	G1	S1	45°	0.5	18	55
	G1S1135	G1	S1	135°	0.5	18	55
	G1S190	G1	S1	90°	0.5	18	55
	H1S1e	H1	S1	–	0.3	30	55
	G1S100e	G1	S1	0°	0.3	30	55
	G1S190e	G1	S1	90°	0.3	30	55
Oblate	H2S100	H2	S1	0°	0.5	18	55
$q_h = 0.6$	G2S100	G2	S1	0°	0.5	18	55
	H2S130	H2	S1	30°	0.5	18	55
	G2S130	G2	S1	30°	0.5	18	55
	H2S145	H2	S1	45°	0.5	18	55
	G2S145	G2	S1	45°	0.5	18	55
	G2S1135	G2	S1	135°	0.5	18	55
	H2S160	H2	S1	60°	0.5	18	55
	G2S160	G2	S1	60°	0.5	18	55
	H2S190	H2	S1	90°	0.5	18	55
	G2S190	G2	S1	90°	0.5	18	55
	H2S100e	H2	S1	0°	0.3	30	55
	G2S100e	G2	S1	0°	0.3	30	55
	H2S190e	H2	S1	90°	0.3	30	55
	G2S190e	G2	S1	90°	0.3	30	55

Table 9.1: Numerical experiments. The peri- and apo-galactica are r_p and r_a, respectively, and $e = (r_a - r_p)/(r_a + r_p)$ is the orbital ellipticity. Galaxy models "G" include disc and bulge, whereas in the models "H" the galaxy is only formed by the halo of the models "G". The numbers "1,2" denotes sphericity and oblateness, respectively. Note that the galaxy models H1 are spherical, so that the orbit is invariant with respect to the inclination. q_h denotes the minor to major axis-ratio of the halo.

9.3.1 Spherical halo

The progressive loss of angular momentum and energy through the action of dynamical friction leads to the monotonic decrease of the satellite galacto-centre distance. The contribution of each galaxy subsystem to the drag force cannot be, in principle, decoupled. However, the comparison between different orbital parameters may help to estimate the contribution of each component to the satellite decay.

In the left column of Fig. 9.1 we plot the comparison of the radius evolution between the models H1 and G1 for different inclinations and eccentricities. Since the halo of the galaxies H1 and G1 is spherical, the only anisotropy of this last model is induced by the disc flattening and rotation (see Chapter 7 for a detailed discussion of the dependence of the survival time on the orbital inclination).
This figure shows that, for non-rotating haloes, the presence of the disc in the inner region of the galaxy introduces a dependence of the decay time on the orbital sense of motion through dynamical friction, so that prograde satellites (those with orbits aligned with the disc angular momentum vector) decay about 1 Gyr faster than the retrograde (anti-aligned) ones if $i = 0°$ and around 0.5 Gyr for orbits with $i = 45°$. The numerical calculations also demonstrate that polar orbits survive longer than those coplanar. This dependence of the decay times on the orbital inclinations come through the $1/\Delta v^2$ in dynamical friction, where Δv is the relative velocity between the satellite

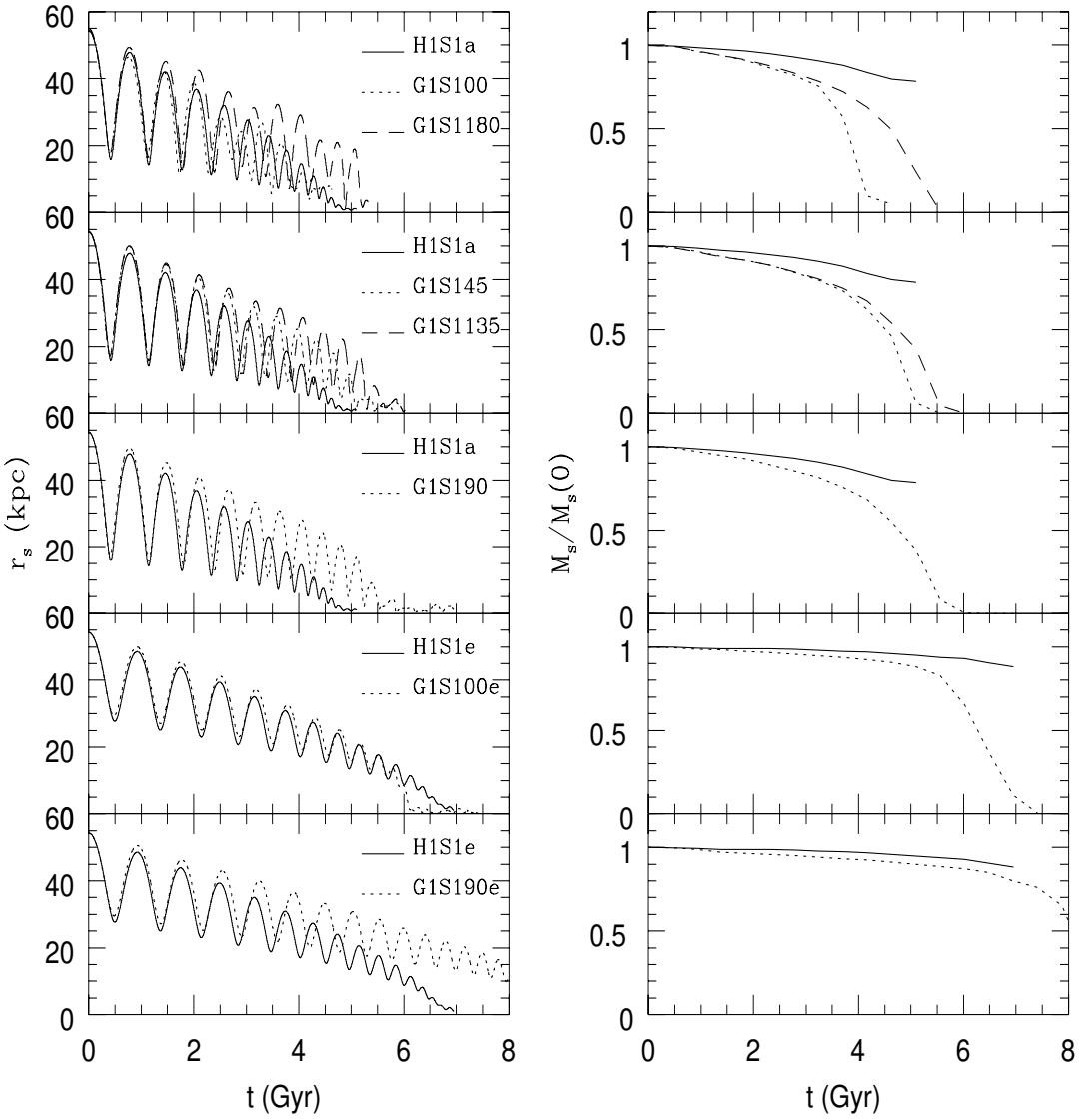

Figure 9.1: Radius and mass evolution for the satellite models within H1 (spherical halo) and G1 (H1 plus disc and bulge) of Table 9.1.

and the disc particles. These results are also found by VW.

Comparing the decay of satellites within H1 (full lines) and G1 (dotted and dashed lines) galaxies we observe that, independently of the orbital eccentricity, the decay times of satellites within the galaxy model H1 are very similar to those within G1 moving on coplanar prograde orbits. Apparently, one should expect longer decay times for models without disc and bulge, due to the absence of dynamical friction from these components. Since the friction force goes as $1/\Delta v^2$, intuitively, satellites within H1 galaxies should have similar or larger decay times than those following orbits with $i > 90°$, where the relative velocity is larger and the disc friction can be neglected if compared with the halo one [2], so that one would expect the model H1S1a to sink into the galaxy centre in a time close to the models G1S1n, where $n \geq 90$. This is, however, not the case due to the strong mass loss induced by disc via tidal forces and shocks along the orbit.

The right column of Fig. 9.1 shows the mass evolution of the satellite. Satellites within H1

[2] The halo is non-rotational, which implies that the differences on the satellite motion as a function of the orbital sense are induced by the disc rotational velocity. It is evident that prograde orbits, where the satellite moves with the rotational sense of the disc, suffer more friction than the retrograde ones

galaxies lose their angular momentum before they are destroyed by the action of tidal forces, which in practice means that these satellites reach the inner most region of the galaxy like a compact body with some per cent of their original mass. This behaviour contrasts with the mass evolution of the satellites within G1 galaxies, which suffer a strong mass loss at late-times (when the disc and bulge start to dominate the galaxy potential) that leads to their final destruction (the satellite is considered destroyed if $M_s < 0.1 M_s[0]$). The larger bound mass of satellites orbiting in the H1 galaxy leads to an enhancement of dynamical friction that gives rise to shorter merge times.

This results show that the disc presence introduce two opposite effects:
(i) It enhances dynamical friction mainly for prograde satellites following low inclined orbits, which have a minimum relative velocity with respect to the disc particles. The larger value of dynamical friction leads to shorter decay times.
(ii) It decreases the satellite mass through tidal heating and tidal forces (see Section 4.3 for more details). Satellites do not suffer from disc and bulge shocks if their orbits are coplanar. In this case, the disc tidal force increases as the satellite sinks to inner regions, being responsible for the progressive mass loss. The disc and bulge dominates the galaxy potential for $r_s < 7$ kpc, which approximately is equivalent to the last Gyr of the satellite evolution, when most of the mass loss occurs (see Fig. 7.1). If the orbit is inclined with respect to the disc plane, rapid potential changes occur when satellites cross the disc which lead to a perturbative response of the satellite particles. As a result, their binding energy decreases. This process is called *tidal heating* or also *tidal shock*. Tidal heating has been shown to be nearly independent of the orbital sense (Gnedin & Ostriker 1999). However, it depends on the orbital inclination, so that polar orbits suffer smaller heating than low inclined ones due to the shorter duration of the shock.
The smaller value of M_s due to the disc effects provokes an overall reduction of dynamical friction and, therefore, larger decay times.

Since satellites within H1 galaxies have decay times shorter or comparable to those within G1 galaxies, we conclude that the overall reduction of dynamical friction due to the enhanced mass loss dominates over the additional disc friction.

9.3.2 Flattened halo

In Fig. 9.2 we repeat the comparison for the galaxy models G2-H2. As we find for the models G1-H1, the presence of the disc and bulge leads to a steep decrease of the satellite mass at the late-times, which does not occur if the baryonic galaxy components are removed. As a result, the satellite decay times in both galaxies are comparable.

It is interesting to point out the differences that the halo flattening induce on the disc effects:
(i) Comparing prograde and retrograde orbits within G1 and G2 galaxies, we find that the satellite decay times are very similar, as we observe for the models G2S145 and G2S1135 (prograde and retrograde orbits, respectively).
(ii) The dependence of the decay time on the orbital inclination is mainly produced by the halo, as the comparison between polar and coplanar orbits within the galaxy models G2 and H2 shows.
(iii) For most part of the orbit, the mass evolution of satellites within G2 galaxies is very close to that of satellites within H2 galaxies (like for the models G1S1, a rapid mass loss occurs at late-times due to tidal stripping). The differences in the mass evolution are remarkably smaller than for satellites within galaxies with spherical haloes. This may indicate a strong reduction of the resonance frequencies of the satellite particles, although this goes further our topic of study.

Points (i) and (ii) indicate that the satellite decay within galaxies with haloes as flattened as $q_h = 0.6$ may be largely dominated by the halo friction. The point (iii) also points out that the disc contribution to the mass loss via shocks is partly reduced if the satellite moves in galaxies with flattened haloes. Like for the models G1S1, tidal forces made by the disc and bulge potentials lead to the final satellite disruption at late-times of the evolution.

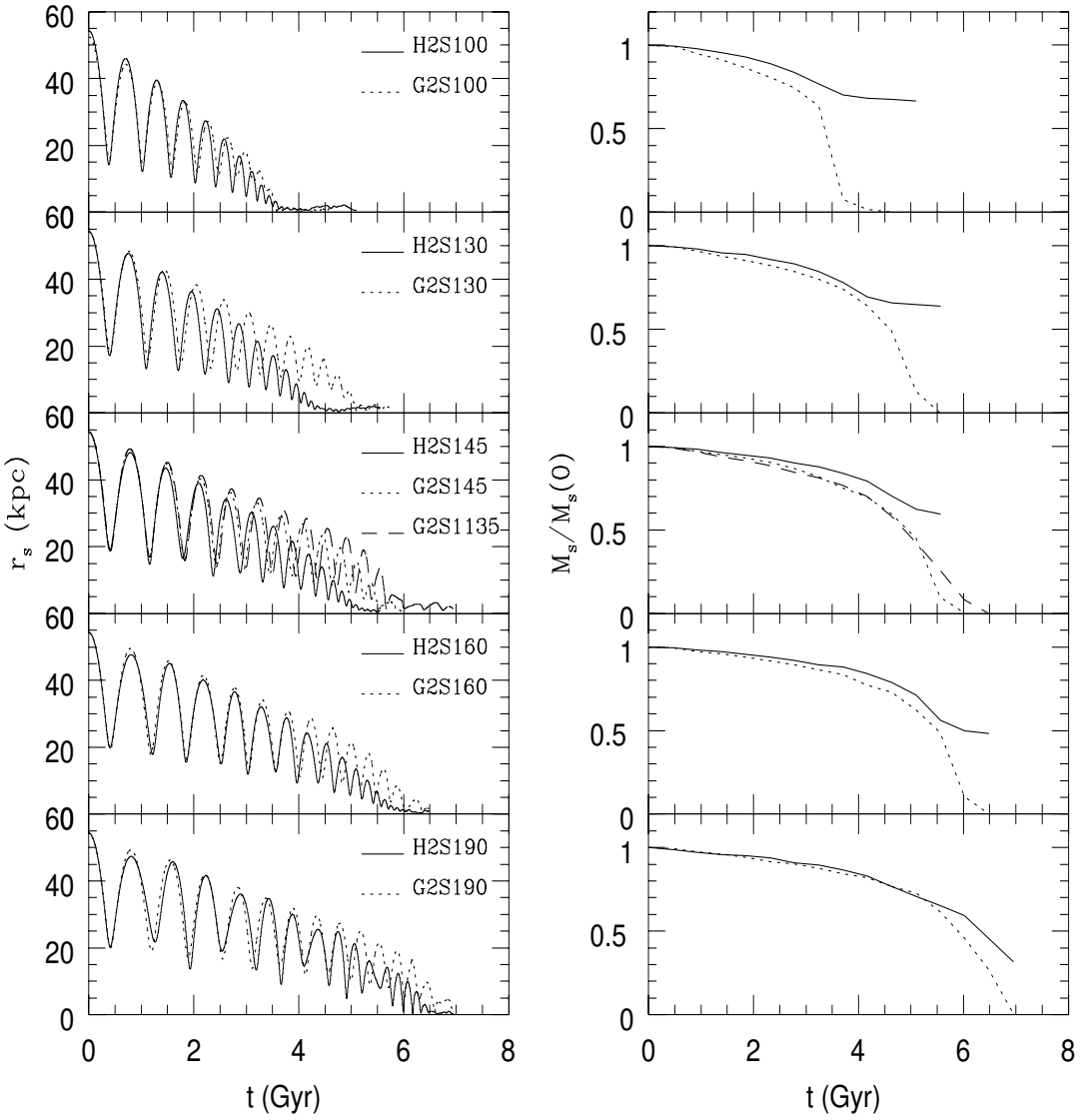

Figure 9.2: Radius and mass evolution for the satellite models within H2 (oblate halo, $q_h = 0.6$) and G2 (H2 plus disc and bulge) of Table 9.1 with initial eccentricity $e \simeq 0.5$.

9.4 Semi-analytic analysis

We attempt to reproduce the results of the previous section employing the semi-analytic code developed in Chapter 4.

This code successfully describes the satellite decay if the mass loss is calculated from the numerical data (see Chapters 6 and 8). One crucial point, therefore, is the theoretical description of the mass evolution for the set of orbital and satellite parameters employed along the numerical study.

In order to check the semi-analytic scheme, we attempt to reproduce the numerical data of PKB, which present a set of orbital eccentricities and satellite masses wide enough to cover the most important range of parameter space used in the subsequent study of the satellite distribution around spiral galaxies. Observational data mainly provides the number of satellites as a function of the galacto-centre distance and inclination, so that we put special attention on the evolution of these parameters.

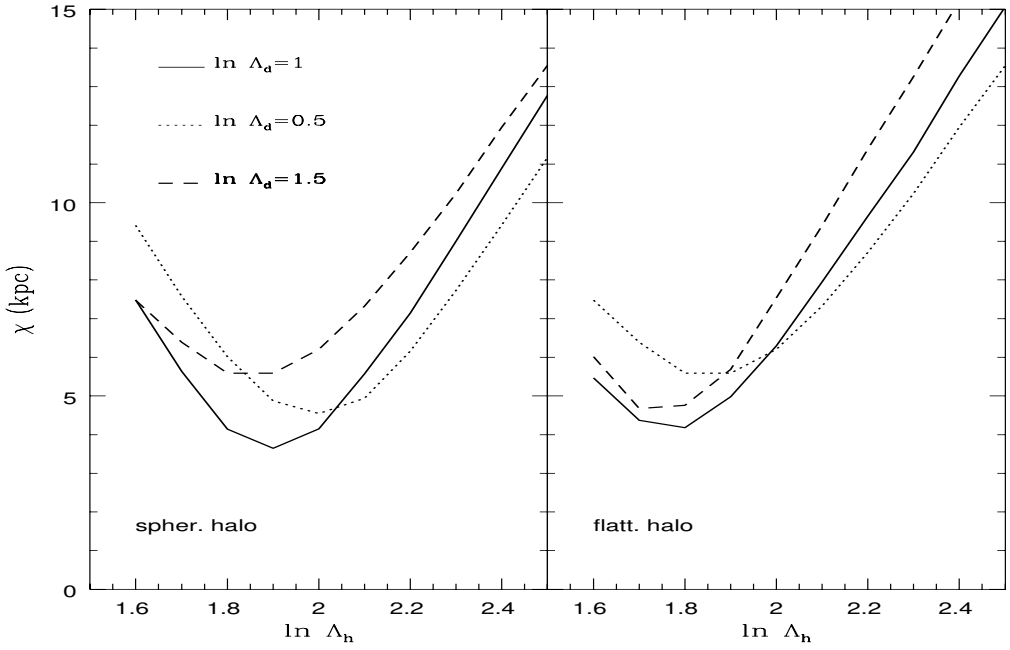

Figure 9.3: Averaged fitting parameters as a function of the halo Coulomb logarithm for models of Table 9.1 with spherical and flattened halo. Each curve is obtained fixing the $\ln\Lambda_d$ to a given value. The calculus of χ results from the average over the first four orbits ($k = 4$).

9.4.1 Fitting the Coulomb logarithms

The free parameters of the semi-analytic code are the Coulomb logarithm of the disc and halo. Due to the spherical symmetry of the bulge, the friction introduces no differentiation on the decay time as a function of the orbital inclination. If one also has into account the small extension of the bulge system, we expect negligible effects on the satellite motion until it reaches the inner region of the galaxy where Chandrasekhar's and Binney's expressions of dynamical friction lose accuracy. We decide, therefore, to neglect the bulge contribution to the total friction force of the galaxy.

We select the free parameters to the set of simulations presented in Table 9.1 using the fitting procedure of Section 6.3. Reproducing the numerical calculations will provide a wide range of satellite and orbital parameters necessary to describe the satellite merging in spiral galaxies depending on the halo axis-ratio.

It is of special interest to check whether the code can give accurately the decay time and orbital inclination if a statistical study of the satellite distribution shall be carried out in following Chapters. For that reason, the calculus of the fitting parameter χ is done for $k = 4$, covering as much time of the orbital evolution as possible. Larger values of k correspond to epochs where the mass loss may alter strongly the satellite motion, leading to effects that can be confused with those from dynamical friction.

In Fig. 9.3 we plot the results of the fitting procedure. The panels shows the χ parameters averaged over the models of Table 9.1 as a function of the halo Coulomb logarithm for three different values of $\ln\Lambda_d$. The calculations of the left panel account for G1 models, whereas those of the right one for the G2 models. The values of the respective Coulomb logarithms that produce the best fit to the numerical data are summarised in Table 8.2. The values obtained in Chapter 6 and 8 ($\ln\Lambda_h = 2, 2.4$, respectively) indicate that the disc presence slightly decreases the overall contribution of the halo friction, the halo Coulomb logarithm being reduced over 10% (spherical halo) and 25% (flattened halo). If compared to the value of TB ($\ln\Lambda_h = 2.4$), who calibrate the semi-analytic code using the numerical experiments of VW), the reduction is about 25%, despite

Friction	k	$\ln\Lambda_h$	$\ln\Lambda_d$	$\chi_{\min}$(kpc)
G1 models	4	1.9	1.0	3.4
G2 models	4	1.8	1.0	4.1

Table 9.2: Results of the fitting procedure applied to the numerical calculation of Table 9.1 for G1 models (left panel) and G2 models (right panel).

the larger number of N-body particles N leads to the increase of the Coulomb logarithm (N_h of the VW's halo model is 9 times smaller in PKB's work, whereas N_d is twice larger). This result suggests that, whereas the effects induced by the galaxy subsystems are reproduced equivalently in both numerical codes, the semi-analytic calibration of the Coulomb logarithm is sensitive to the numerical scheme.
Contrary to the halo Coulomb logarithm, the disc friction shows values of $\ln\Lambda_d$ that double that of TB. Again, it is unclear the reason for such an increase, (i) one possibility can be the low resolution of SUPERBOX in order to resolve the vertical structure of the disc, which may lead to an overestimation of dynamical friction (see Chapter 4), (ii) the second possibility can be found in the estimation of the disc parameters (such the vertical length and central velocity dispersion). TB fit them to the *final* values once the satellite has been destroyed, however, we decide to use the initial values, i.e without evolution, so that the code can be use in a full consistent way, independently of the numerical results. Due to the disc heating both, the disc vertical length and the velocity dispersions, become larger after the satellite sink. This increase likely produces an enhancement of dynamical friction due to the smaller values of the satellite velocity with respect to the disc particles.
Of course, our treatment also suffers from the "time dependence" of $\ln\Lambda_d$ due to the variation of the galaxy parameters along the satellite orbit. These "feedback" effects partially reduce the accuracy of the semi-analytic code. Unfortunately, they cannot be removed at this level of approximation.

The comparison of the fit between G1 and G2 models also provides information. The degree of accuracy $\chi_{\min}$ shows a slightly better reproduction of the numerical data if the halo is spherical. The lower dependence of $\ln\Lambda_h$ of the disc value agrees with the numerical results, which shows that the effects due to the anisotropy of the halo distribution function dominate over those of the disc within this range of orbital and satellite parameters. As a result, the selection of $\ln\Lambda_h$ becomes less sensitive to the magnitude of the disc friction.

It is interesting to remark the small dependence of $\ln\Lambda_h$ on the halo anisotropy, which makes possible the use of the semi-analytic code in a wide range of q_h.

9.4.2 Satellite decay and mass loss

In Section 4.3 we present the scheme implemented in the semi-analytic code in order to treat the satellite mass loss process. Mass stripping is induced by the tidal field of the parent galaxy, which removes those particles that become unbound along the satellite evolution. As it is shown above, this process is highly enhanced through bulge and disc tidal shocks. Our semi-analytic code implements the Gnedin & Ostriker (1999) expressions of tidal heating, which permits the analysis of the satellite's mass evolution for a wide range of orbits[3].

Satellites with medium eccentricity $e \simeq 0.5$

Fig. 9.4 shows the satellite evolution on five orbits with different inclinations within the galaxy model G1. The angle i is that between the angular momentum vector and the disc rotation, so

[3] The main advantage of this semi-analytic treatment is that it provides the expressions of satellite heating in two regimes, "rapid" and "slow", which accounts for a wide range of orbital eccentricities. The distinction comes from the comparison of the shock time-scale and the dynamical time of the stars moving around the centre-of-mass of the satellite. Denoting τ as the shock time-scale and t_h the dynamical time at the half-mass radius, the "rapid" shock regime accomplishes $\tau \ll t_h$ (highly eccentric orbits) and *viceversa* in the case of "slow" shocks (nearly circular orbits).

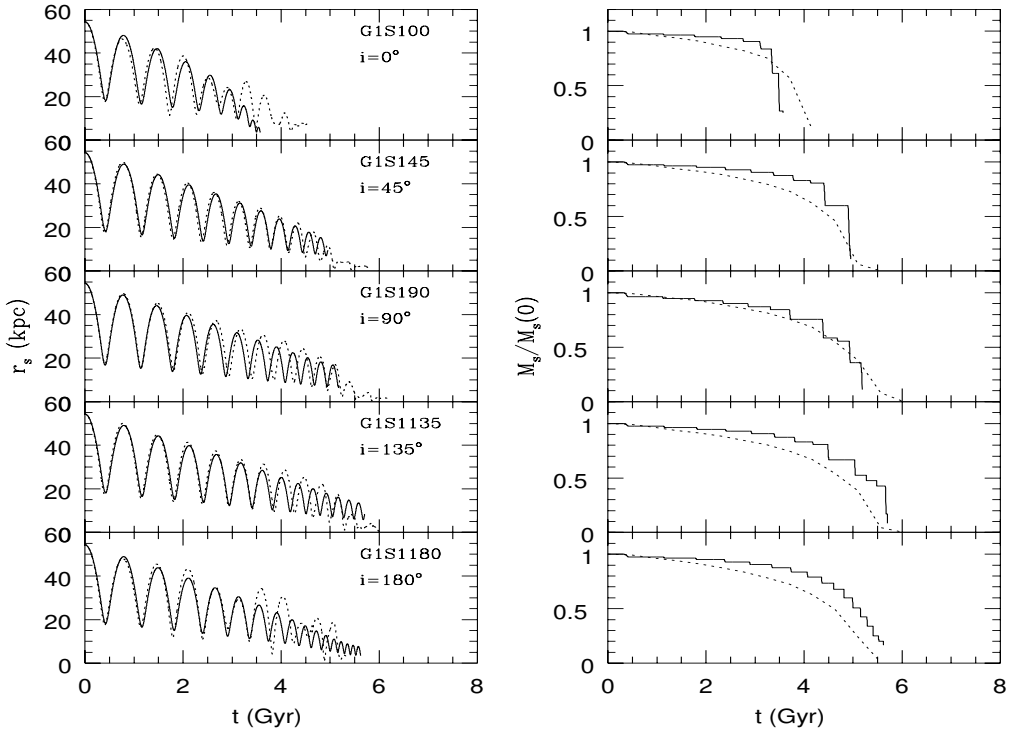

Figure 9.4: Satellite decay and mass evolution as a function of the inclination for the models G1S1 (spherical halo). The dotted lines represent the numerical results whereas the solid ones the semi-analytic evolution. The disc and halo Coulomb logarithms are those given in Table 9.2.

that $i < 90°$ and $i > 90°$ denote prograde and retrograde orbits, respectively, meanwhile $i = 0°$ and $i = 90°$ are coplanar and polar orbits.
The semi-analytic scheme successfully describes the satellite decay (left column) independently of the orbital inclination. The mass evolution (right column) also shows that the analytic approximations successfully provide the bound mass for different inclinations, the discrepancy being less than 20% until the satellite has less than ten per cent of its initial mass. The label of accuracy is very similar to that achieved by TB using a semi-analytic approach to the tidal shock process instead of the analytic expressions that are employed in our scheme. We note that: (i) Chandrasekhar's expression is used in order to reproduce the disc friction and (ii) meanwhile the satellite mass is calculated from the N-body each 0.312 Gyr, the semi-analytic codes provides $M_s(t)$ each time-step (0.0013 Gyr), which explains the smooth mass evolution present in the numerical curves and the high resolution of the semi-analytic ones.

Fig. 9.5 shows similar results for satellites within the galaxy G2 (flattened halo). The bound mass curves of inclined satellites (those with $i \neq 0°, 90°$) present strong "jumps" due to the eccentricity variation along the orbit which enhances the energy gain from tidal shocks. The overall evolution, however, clearly traces accurately the mass loss and the final destruction of the satellites.

Our semi-analytic scheme also reproduces the disc effects on the decay time-scales of the satellite observed in the numerical calculations of VW and PKB. In spherical haloes, prograde orbits decay faster than the retrograde ones due to the disc dynamical friction so that, for example, the coplanar (prograde) satellite G1S100 decays within a time 30% shorter than the G1S1180 (retrograde). This discrepancy is in 0.5 Gyr enhanced by the semi-analytic code, which may indicate an overestimation of disc dynamical friction. The orbital distinction depending on the rotation sense is reduced in non-rotating flattened haloes due to the enhanced density, which increases dynamical friction. One can observe that, meanwhile the difference in the decay time

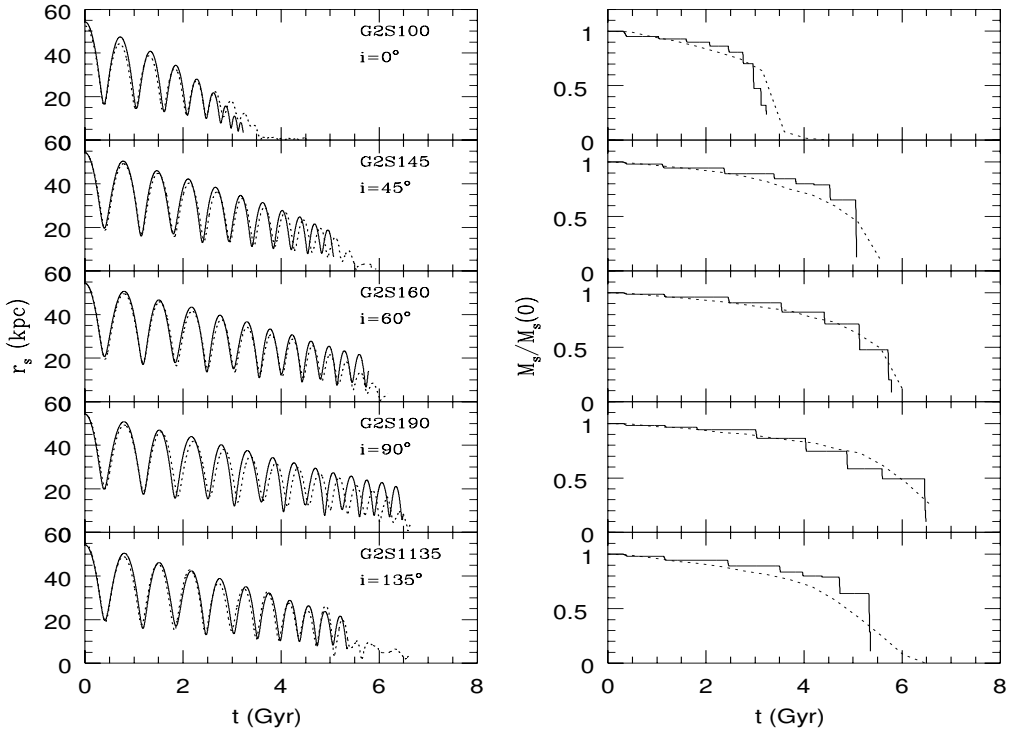

Figure 9.5: As Fig. 9.4 with the galaxy model being G2 (flattened halo).

between the orbits G1S145 and G1S1135 is around a 10%, in flattened haloes it comes down to 4% approximately, which is accurately reproduced by the semi-analytic code. In this case, the satellite decay time is dominated by the Dark Matter component.

As expected, the minimum and maximum decay times occur for the coplanar and polar orbits, independently of the halo axis-ratio, which define the "decay time range" $\Delta t = \tau_{90} - \tau_0$, where τ_{90} is the decay time of a polar orbit following PKB's notation. As PKB observe, the comparison with flattened haloes shows that $\Delta\tau(q_h = 1) = 0.3\Delta\tau(q_h = 0.6)$, so that the halo flattening enhances the dependence of the decay time on the orbital inclination.

Satellites with $e \simeq 0.3$ and $e = 0$

In Fig. 9.6 we plot the comparison between the semi-analytic and numerical galacto-centre distance and mass evolution for models with $e \simeq 0.3$. The lower mean density along the orbits induces a longer decay time due to to the decrease of dynamical friction. The semi-analytic data reproduces the effects made by the halo anisotropy as well as the decay time ranges, with discrepancies less than 25%. The orbit is remarkably well traced in all the calculations.

The mass evolution shows a negligible mass loss process until the late times of the orbit, when it suffers a dramatic loss. Due to the low eccentricity, the tidal radius accomplishes along most of the orbit $R_t \gg r_t$, even taking into account the heating expansion from the shocks. However, the energy gain is cumulative process that leads to a strong expansion of the mass shells due to the large number of disc(bulge)-satellite encounters, taking into account that the satellite starts crossing the disc for $r_s < 15$ kpc (if compared to the $e = 0.5$ orbits). At some point of the orbit, as a result of the tidal heating, even the inner most shells of the satellite have extensions comparable to the tidal radius, which leads to the rapid mass loss. The Fig. 5 of TB shows that, if the adiabatic correction is assumed independent of the radius r (measured in the satellite frame), the semi-analytic scheme overestimates the mass loss for orbit less eccentric than $e \simeq 0.5$. Our proposal, based on the semi-analytic work of Gnedin & Ostriker (1999) solves this problem by

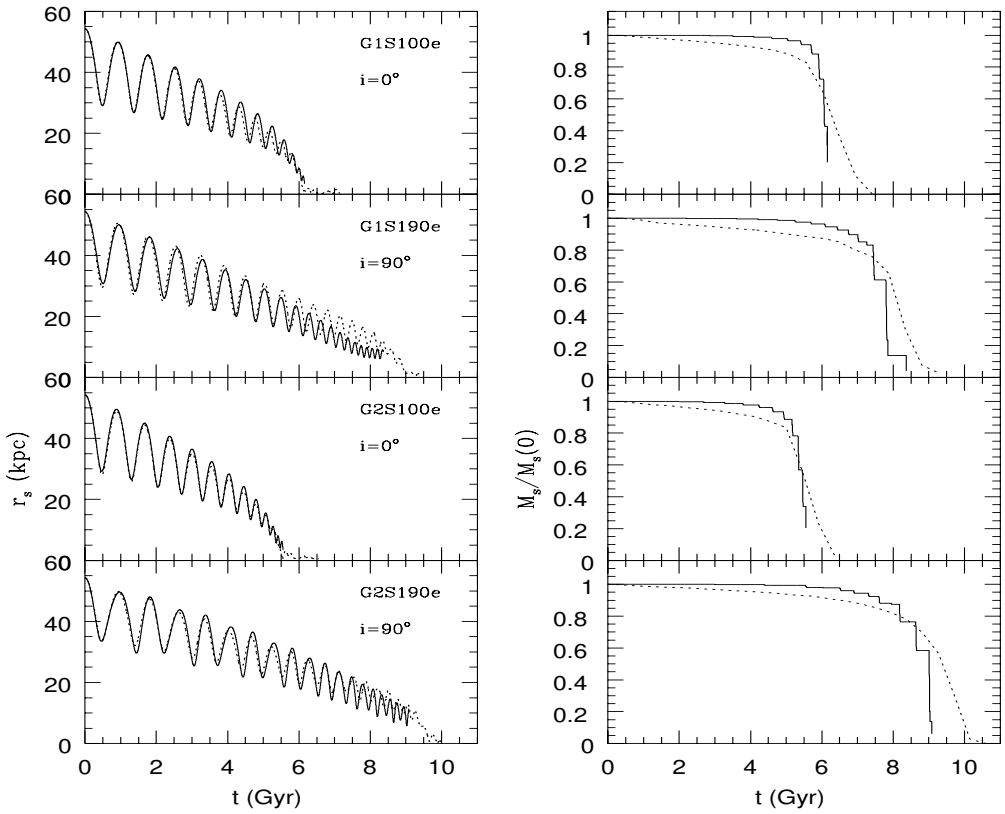

Figure 9.6: Satellite decay and mass evolution as a function of the inclination for the models with $e \simeq 0.3$.

re-distributing the energy gain after the shock as a function of the satellite star radius, so that the adiabatic correction accomplishes $A(r \sim r_t) \simeq 1$ and $A(r \ll r_t) \simeq 0$, which strongly reduces the heating expansion in the inner most shells of the satellite (see for more details Chapter 4).

Fig. 9.7 shows than our scheme also reproduces the mass and radius evolution in the threshold case of quasi-circular orbits (note that circular orbits $e = 0$ are solely available in spherical systems) for both halo shapes. The small oscillations present in the numerical calculations are likely produced by the galaxy response to the satellite gravity, which makes the centre-of-mass of this last not to be fixed (we recall that r_s is measured from this point). However, the galaxy does not behave as a rigid body, so that the less massive sub-components, such as the disc and bulge, will strongly react to the satellite gravity and *viceversa*. For instance, if one assumes that the halo remains at a fixed position, the disc-satellite pair will suffer changes in their distance with respect to the galaxy centre-of-mass of around $\Delta r \simeq r_s M_s/M_d = 6$ kpc as we see in this plot. If the galaxy potential is axi-symmetric, only satellites in the symmetry plane can move along orbits with $e = 0$.

It is interesting to underline that these satellites barely suffer from tidal shocks, neither from the disc nor from the bulge, so that the mass loss is purely induced by the galaxy tides (note that for disc shocks $\langle \Delta E \rangle_{t_{\rm sh}=0} \propto g_m^2$, where g_m is the vertical acceleration, see eq. 4.5, therefore going as $g_m^2 \sim 1/r_s^4$).

In the semi-analytic calculations, the absence of disc and bulge leads to the final survival of a bound remanent after the satellite has sinked into the inner most part of the galaxy. However, this contrasts with the numerical results. The reason may be found in a lack of resolution in order to calculate $R_t \sim r_c$ kpc. We comment this below. An insight in this direction is that the

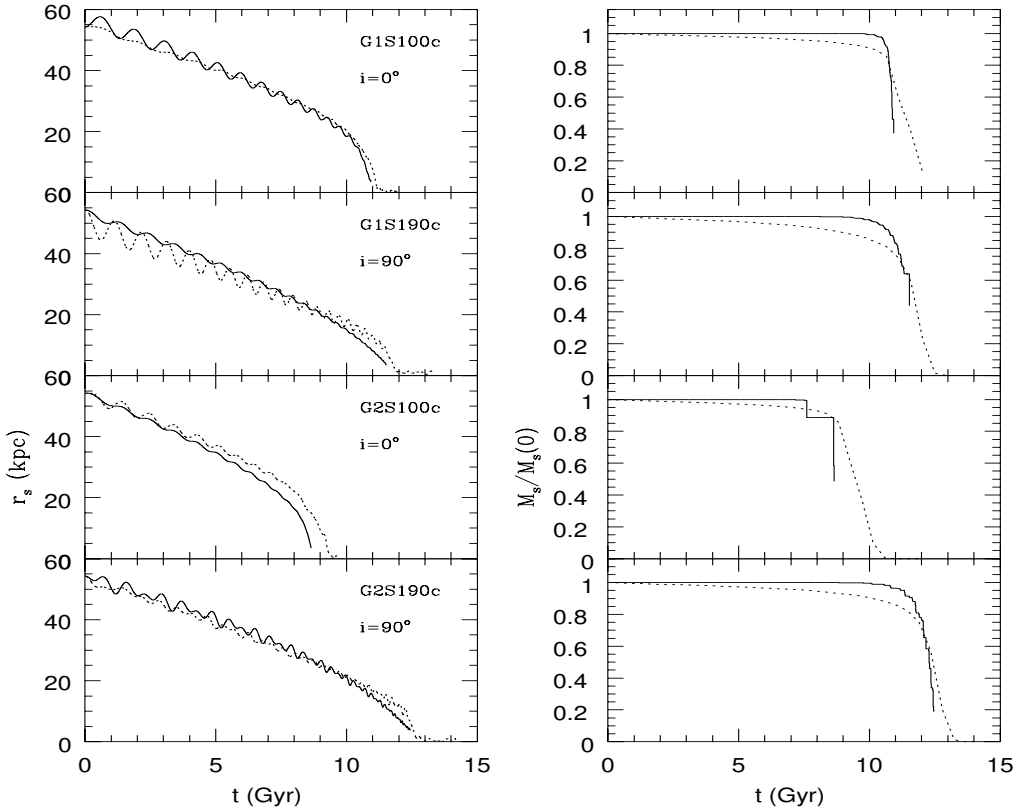

Figure 9.7: As Fig. 9.6 for circular orbits in G1 and G2 galaxy models.

semi-analytic code accurately reproduces the disruption of eccentric satellites with $e = 0.3$, see Fig. 9.6, since for these orbits the tidal heating is stronger and the satellite is more expanded.

Satellites with mass $M_s = 0.2M_d$

We test the efficiency of the semi-analytic code in order to describe the satellite decay and mass loss of more massive satellites. We make use of the numerical experiments G1S2 and G2S2 (with different inclinations) of PKB. They also present calculations with the galaxy models G3 and G4. However, we shall not carry out comparisons with these simulations since the grid resolution is twice poorer than in the models G1 and G2, which is expected to change the Coulomb logarithm than better fits to the numerical data.

In Fig. 9.8 we plot the mass and distance evolution for the models with $M_s = 0.2M_d$. The figure shows a good agreement between the semi-analytic and numerical satellite evolution. The decay times are around twice reduced if we double the satellite mass, as expected from the linear dependence of dynamical friction on M_s. As PKB find, the range of decay times show little dependence on the satellite mass. Whereas for $M_s = 0.1M_d$ we have that $\Delta\tau(q_h = 1)/\tau_{90} \simeq 0.2$ and $\Delta\tau(q_h = 0.6)/\tau_{90} \simeq 0.4$, for $M_s = 0.2M_d$ we find $\Delta\tau(q_h = 1)/\tau_{90} \simeq 0.3$ and $\Delta\tau(q_h = 0.6)/\tau_{90} \simeq 0.4$.

The small reduction of the decay range when increasing M_s may be found in the fast decay of the satellites if compared to the same orbits and $M_s = 0.1M_d$, so that the effects induced by the anisotropy velocity distribution do not have time enough to act before the satellite loses its angular momentum.

As a result of the high binding energy of the satellite particles, a bound remanent reaches the inner most region of the galaxy, independently of the orbital inclination and halo flattening. The

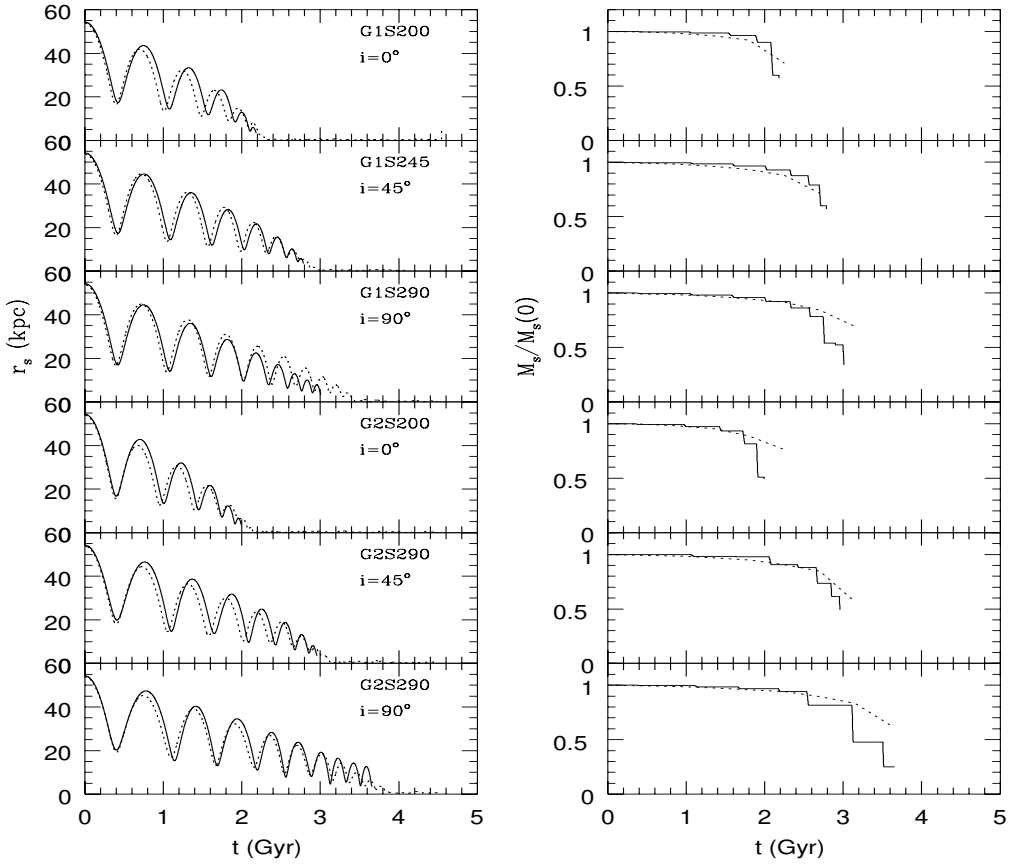

Figure 9.8: Mass and galacto-centre evolution for models with $M_s = 0.2M_d$ and initial orbital eccentricity $e \simeq 0.5$. The galaxy models are G1 and G2.

polar satellites show a stronger mass loss rates in the late-times of the orbit evolution if compared to the numerical data which, however, lead to small discrepancies in the distance evolution.

9.4.3 Orbital inclination

One of the main effects of the velocity anisotropy on the orbit evolution is the decrease of the orbital inclination through the dynamical friction action. The Binney's expressions have been proved to be accurate in order to reproduce such a reduction (see Chapter 8).

PKB propose the halo flattening as a removal mechanism of satellites following low inclined orbits, whereas it enhances the survival times of satellites on near polar orbits. This result may help to understand the anisotropic satellite distribution observed by Holmberg (1969), Zaritsky & González (1999) and Carney et al. (1987), who find in their observational samples that most of satellite galaxies are located on near polar orbits.

Bearing in mind the statistical study of the satellite evolution, we attempt to test the semi-analytic code in order to describe the inclination decrease in flattened Dark Matter haloes.

Satellites moving within axi-symmetric systems experience periodic variations of the angular momentum vector known as "precession" and "nutation". For a better understanding of the inclination evolution we put special emphasis on the nutation process.
The amplitude of the nutation $\Delta\cos\theta = \cos\theta_1 - \cos\theta_0$, where $\theta = \pi/2 - i$ and θ_1, θ_0 are the maximum and minimum value of the azimuthal angle, can be approximated in the regime of low asphericity as (see Appendix A)

$$\Delta \cos\theta = (I_z - I_R)\frac{3GM(r)}{2a^2\langle r\rangle}\sin^2\theta_0\cos^2\theta_0, \tag{9.1}$$

with a period of

$$T = 2\pi\frac{\langle r\rangle^2\cos^2\theta_0}{a}, \tag{9.2}$$

I_i being the inertia tensors of the galaxy per unit mass with respect to the axi-symmetry plane and a the z-component of the angular momentum vector, which is a constant of motion. The quantity $\langle r\rangle$ denotes the averaged galacto-centre distance. Even if our system can not be considered nearly spherical, these expressions reproduce the general evolution of the inclination and its dependence on the orbital parameters. From these equations we expect that, (i) the angle θ remains constant if the galaxy is spherical ($I_z = I_R$), (ii) coplanar and polar orbits ($\theta = 0$ and $\theta = \pi/2$, respectively) do not suffer from nutation, (iii) the nutation period decreases due to the satellite decay and (iv) the amplitude is nearly constant along most part of the orbit, before the disc potential dominates (the halo mass profile can be approximated as $M(r) \propto r$ for $r > 15$ kpc, see Fig. 7.1).

Fig. 9.9 shows the orbital evolution of satellites following inclined orbits, regarding that the inclination of polar as well as coplanar satellites remains constant along their evolution. The periodic oscillations of the inclination represent the nutation of the angular momentum, which is produced by the asphericity of the mass distribution, whereas the progressive decay of the averaged inclination is caused by the anisotropic velocity distribution.

The semi-analytic code reproduces the inclination reduction for different initial values and satellite masses, although with a slight underestimation at late-times of the orbit (the discrepancy is between 5 and 30 per cent depending on the initial inclination).
The numerical calculations also show inclination reduction for satellites moving within the galaxy model G1 (spherical halo), which is likely produced by the anisotropic velocity distribution of the disc. The semi-analytic results also show a small decrease of i. The reason is unclear, since the disc dynamical friction is treated by Chandrasekhar's expression (in Chapter we prove that this theoretical approximation to dynamical friction does not produce such an effect, even if the mass distribution is axi-symmetric), and might be caused by the poor resolution at small distances (the variation of i occurs at $r_s \sim 2$ kpc, where the approximation we use in our scheme may be not valid). As expected, massive satellites and those on low inclined orbits suffer stronger inclination decrease, due to the larger value of dynamical friction along the evolution.

The results can be likely improved if a more accurate theoretical treatment of the disc dynamical friction is included which, so far, goes beyond our purpose.

9.5 Conclusions

We confirm the differentiation of the decay time depending on the orbital sense of motion, which agrees with the numerical calculations of PKB and VW. As PKB, we also observe in the semi-analytic data that this dependence is reduced if the galaxy halo is aspherical.

Our results agree with those of TB in order to asses the importance of the disc presence in order to reduce the satellite mass by means of tidal shocks at the peri-galacticon passages. The semi-analytic scheme developed by Gnedin & Ostriker (1999) has been proved to reproduce the satellite heating after the encounters with the disc and bulge if the energy gain adds up after each shock, which leads to a progressive expansion of the satellite mass shells. As a result of the tidal heating, satellites are destroyed before they reach the most inner region of the galaxy. Numerical calculations where the disc and bulge were removed and those with more massive satellites show that bound remanents of the satellite can survive and reach distances comparable to the bulge scale-length.

We have developed an analytic treatment of the satellite decay in spiral galaxies that reproduces in a self-consistent way the numerical calculations after the Coulomb logarithms of the different galaxy components are fixed.

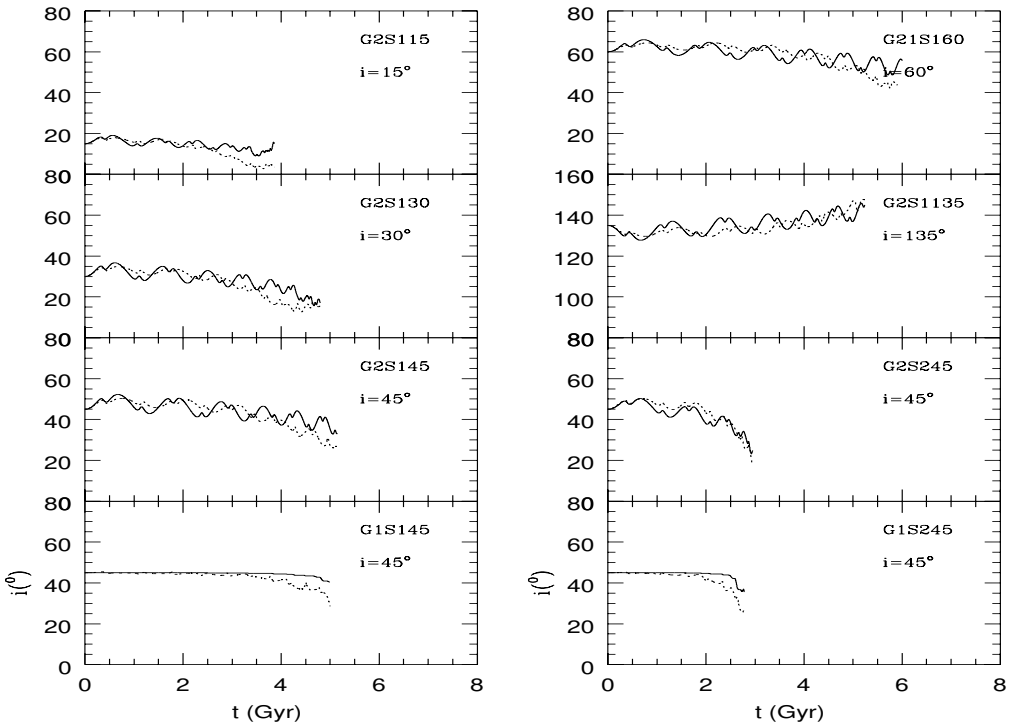

Figure 9.9: Inclination evolution for satellites following inclined orbits.

This code also reproduces the effects that aspherical Dark Matter haloes induce on the satellite evolution, specially the decay time range and inclination decrease, thanks to the use of Binney's formulæ. The results indicate that a better approximation to the disc friction might be necessary to describe more precisely the satellite dynamics at late-times of the orbit, where the disc potential dominates. At this range of distances, the mass evolution scheme implemented in the semi-analytic code can suffer from resolution limitations for satellites with a concentrated mass distribution or for those with small shell expansion as a result of tidal heating, like for example, satellites following circular or coplanar orbits, these last independently of the eccentricity. The improvement of the semi-analytic code in the inner region of the galaxy is, however, difficult to carry out. Taking into account that $R_t \simeq [M_s/M_g(r_s)]^{1/3} r_s$, one needs resolutions of the order of $r_s \simeq [M_g(r_s)/M_s]^{1/3} r_c \sim 2$ kpc to account for the total destruction of satellite on orbits with negligible tidal heating. The analytic approaches, however, are only valid in the distance range $r_s \gg r_c = 1$ kpc. We note that, despite the mismatch at late-times, the influence on the satellite decay is minimum due to the small galacto-centre distance.

The remarkable accuracy of the semi-analytic scheme in order to reproduce the numerical data for a wide range of orbital eccentricities, inclinations and satellite masses gives us confidence to carry out a statistical survey of the satellite distribution around spiral galaxies in a following Chapter.

Chapter 10

Satellite distribution in flattened haloes

10.1 Introduction

[1]In this Chapter we analyse the possible connection between satellite dynamics in flattened Dark Matter haloes and the anisotropic satellite distribution around spiral galaxies.

Peñarrubia, Kroupa & Boily (2001), hereinafter PKB, find in their numerical calculations that satellites initially located at 55 kpc suffer decays that are strongly dependent on the orbital inclination, so that polar satellites survive around 70% longer that coplanar ones. These results suggest dynamical friction as the mechanism that removes low inclined satellites, yet can this effect be extrapolated to a population of satellites as a whole? To answer this question, a statistical survey of satellite orbits and masses is carried out and compared with the observational data available nowadays.

We must note that this is a preliminary study, which will be analysed in depth in a following project. Here, the problem is presented, together with the main effects of the halo morphology on the satellite distribution.

10.2 Observations

So far, there are two samples of satellite distributions around spiral galaxies which are large enough to be statistically treated.

The first was collected by Holmberg (1969) and accounts for satellites within a projected radius of 50 kpc from the disc, counting optical companions on the Palomar Sky Survey plates. In order to determine the orbital inclination with respect to the axi-symmetry plane, the selection criterion discards galaxies with disc inclinations larger than 30 degrees with respect to the line-of-sight. The total number of primaries was 58, with 218 satellites. From these satellites, Holmberg found 45 companions (optical and physical) within 30° of the major axis and 173 between 30° and 90°. Had these companions been observed in a statistical isotropic distribution (i.e, where the number of satellites is independent of the inclination), the expected number in the first bin would be $218/3 \simeq 73$ instead of the observed 45.

Following the reasoning of Quinn & Goodman (1987), a possible solution for such a remarkable absence of satellites in low inclinations might be the extinction by the dust in the orbital plane. However, since the radial density profile of the disc is exponential with a typical scale-length of 3.5 kpc (Bahcall, Smith & Soneira 1982), satellites at distances as large as 50 kpc must suffer

[1]This Chapter presents the preliminary results of the future paper Peñarrubia, Kroupa & Just, to be submitted to MNRAS. Although the study is not yet complete, we want to show that the available observational data of the satellite distribution around spiral galaxies presents a morphology not yet understood.

from negligible light absorption. Quinn & Goodmann attempted to verify this data by scanning the Fisher-Tully catalogue (1981) and the UGC (Nilson 1973), which provides the magnitudes, position angles, axis-ratios, red-shifts and the HI lines. After discarding those satellites with velocities that differ by no more than the HI line width and those that may not be bound to the parent galaxies, they obtained only 7 satellites within 50 kpc.
Contrary to Holmberg's result, the studies on satellite distribution carried out by Busch (1983) and MacGillivray et al. (1982) present no evidence for polar alignment. At the present, there is no confirmation of the so-called Holmberg effect in the literature.

A new sample of galaxies was presented by Zaritsky et al. (1997), including 69 parent galaxies with luminosities similar to that of the Milky Way and with distances not larger than 100 Mpc (for $H_0 = 75 \mathrm{kms}^{-1}\mathrm{Mpc}^{-1}$). Around these spiral galaxies 115 satellites were identified as physical companions with, unfortunately, only 9 of them lying within 50 kpc. The main result of this survey is the presence of the Holmberg effect at distances *larger* than 250 kpc, whereas for smaller distances the satellite distribution appears to be nearly isotropic. The apparent anisotropy at large projected radii is similar to that found by Holmberg for $R < 50$ kpc.
The observations of Zaritsky et al. (1993) and Zaritsky & González (1999) give a range of apparent magnitude within $\Delta m_v \in [2, 7]$ compared to the parent galaxies (we note that from the 115 satellites of the sample, 61 have $\Delta m_v \leq 5$ and approximately 35 $\Delta m_v \leq 3$, so that the observations are mostly fulfilled by massive satellites). The conversion of the apparent magnitude into mass can be estimated as

$$\frac{M_s}{M_d} = \frac{\Upsilon_s}{\Upsilon_d} 10^{-\Delta m/5}, \tag{10.1}$$

where Υ is the mass-to-light ratio (using the notation of BT). The range of masses is therefore $M_s/M_d \in \Upsilon_s/\Upsilon_d[0.06, 0.4]$. Since most of the satellites sample are irregular, one expects $\Upsilon_s/\Upsilon_d < 1$. However, the type indicates that most of them are strongly altered by the action of tidal fields of the parent galaxy. This means that they have lost a large fraction of the initial mass, this effect being stronger for the low massive satellites due to their smaller binding energy.

10.3 The galaxy and satellite parameters

In this Section we present the galaxy and satellite models employed in order to reproduce the observed satellite galaxy distribution around spiral galaxies with properties similar to the Milky Way. The models are illustrated in more detail in Chapter 3, whereas here we merely comment some parameters changed to account for the larger distance scales used for this study.

10.3.1 The parent galaxy

The galaxy model is composed by disc, bulge and halo. The halo cut-off radius is expanded out to $r_{\mathrm{cut}} = 504$ kpc in order to investigate the satellite distribution at distances as large as those presented by Zaritsky et al. (1997). The core-radius of the halo is $\gamma = 3.5$ kpc. Since the halo is nearly isothermal ($r_{\mathrm{cut}} \gg \gamma$), the mass has been linearly enhanced so that the velocity curve reproduces that determined by Bahcall, Smith and Soneira (1982). The halo mass corresponds to $M_h(r_{\mathrm{cut}}) = 84 M_d \simeq 4.7 \times 10^{12} M_\odot$. The halo axis-ratio q_h is treated as a free parameter that can be varied in order to discern the possible connection between halo shape and the observed anisotropic satellite distribution.

10.3.2 The satellite

The satellite is a King model with concentration $c = \log_{10}(r_t/r_c) = 0.8$, where r_c and r_t are the core and "tidal" radii, respectively. These models fit early-type dwarf galaxies (Binggeli et al. 1984).

Since the satellite is treated as point-mass, the influence on the satellite model is through mass loss, which is negligible for distances larger than 200 kpc. Taking into account that the halo

distance distribution has a constant surface density and that, for the range of masses presented below, satellites with initially $R < 60$ kpc and $M_s = 0.1 M_d$ merge into the parent galaxy (independently of the initial orbital eccentricity), one has that the fraction of satellites sensitive to a possible concentration distribution is of the order of 30 per cent, which is reduced for more massive satellites. This rough estimate is supported by the small changes over the mass distribution after the sample is evolved (see below).

10.4 Projection effects

The final distribution of satellites with respect to the axi-symmetry plane will be different after projecting the positions on the sky. To estimate the effects that the random projection introduces, we make use of the analytical treatment of Quinn & Goodman (1986).

Consider first a coordinate system aligned to the velocity distribution ellipsoid where the satellite position is given by the radius R and the inclination i with respect the axi-symmetry plane. Defining now a Cartesian coordinate system on the sky (x, z), z being the axis perpendicular to the disc, the coordinate change is equivalent to the Euler transformation (see Goldstein 1980)

$$\begin{aligned} x &= R(\cos\Omega\cos\psi - \sin\Omega\sin\psi\cos i) \\ y &= R(\sin\Omega\cos\psi + \cos\Omega\sin\psi\cos i) \\ z &= R\sin\psi\sin i, \end{aligned} \tag{10.2}$$

where Ω and ψ, are the ascending node and mean anomaly, respectively.

The distribution function that one observes on the sky $\sigma(x, z)$ results from the average over the function $\sigma(R, i)$ in the galaxy frame. Assuming a uniform distribution of circular obits R =const, the average over Ω, ψ is straightforward, leading to the solution

$$\sigma_s(r,\phi) = \pi^{-2}\frac{H(R^2 - r^2)H(R^2\sin^2 i - r^2\sin^2\phi)}{\sqrt{R^2 - r^2}\sqrt{R^2\sin^2 i - r^2\sin^2\phi}}, \tag{10.3}$$

where the suffix s denotes that the average is done for a given satellite with coordinates in the galaxy frame (R, i) and the Heavy-side function is defined as $H(x) = 1$ if $x > 0$ and $H(x) = 0$ if $x \leq 0$. If we have a sample of circular orbits distributed as $\sigma(R, i)$, the resulting projected surface density is

$$\begin{aligned} \sigma(r,\phi) = \pi^{-2}\int_0^\infty dR\int_{-1}^1 d(\cos i)\sigma(R,i) \\ \times\frac{H(R^2 - r^2)H(R^2\sin^2 i - r^2\sin^2\phi)}{\sqrt{R^2 - r^2}\sqrt{R^2\sin^2 i - r^2\sin^2\phi}}, \end{aligned} \tag{10.4}$$

the coordinates (r, ϕ) being the projected galacto-centre distance and the projected inclination with respect to the disc plane, respectively.

Observational values of $\sigma(R, \phi)$ predict a larger number of satellites in high inclined orbits, i.e $\phi \sim \pi/2$. Since the projection average reduces this anisotropy, one may expect distributions in the galaxy coordinates that might as extreme as

$$\sigma(R, i) = \sigma_0 R^{2-\beta} H(\sin i - \sin i_0), \tag{10.5}$$

corresponding to a spatial density distribution going as $R^{-\beta}$ ($\beta = 2$ would account for a homogeneous surface density) and to the complete absence of satellites with inclinations less than i_0 (or larger than $\pi - i_0$ in the case of retrograde satellites). The radial and angular dependence of the resulting distribution function can be expressed as,

$$\sigma(r,\phi) \propto r^{1-\beta}\sigma'(\phi)$$

The function $\sigma(r, \phi)$ normalised to the value at 90° is shown in Fig. 10.1 for a given distance. As expected, the projection effects strongly reduce the anisotropy observed in the galaxy frame. The

shallower the spatial distribution is ($\beta \to 1$) for a fixed i_0, the weaker is the excess of satellites in high inclined orbits. The anisotropy can be enhanced by choosing i_0 sufficiently close to zero, however, even if all orbits are polar, $i_0 = 90°$, the number of satellites with $\phi = 0°$ is not zero.

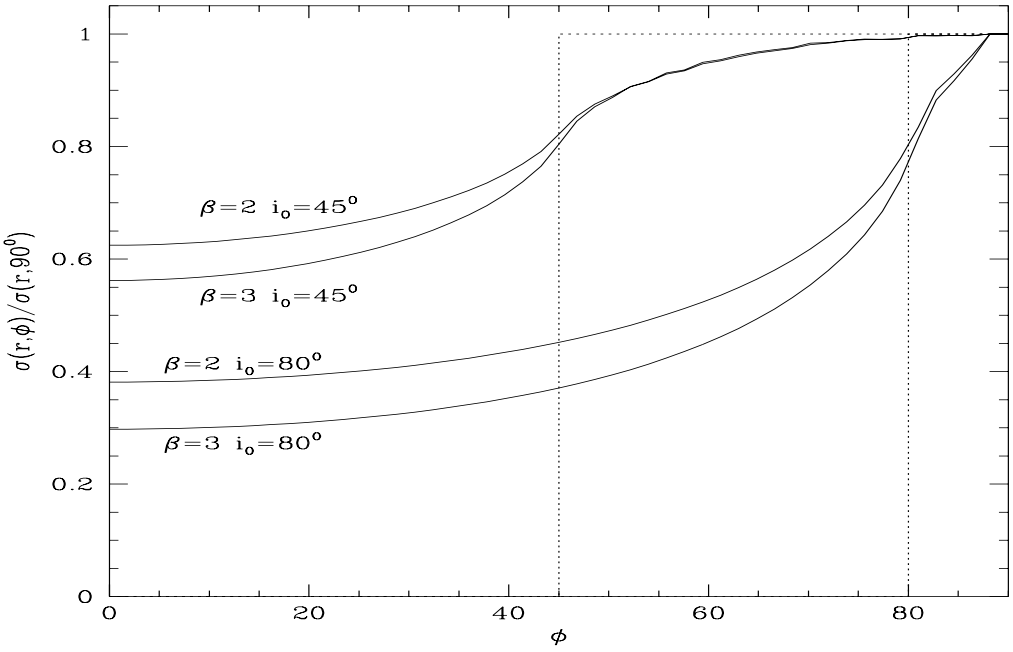

Figure 10.1: Projected surface density as a function of the inclination with respect to the disc plane for several values of the minimum inclination (i_0) and the power-law slope of the spatial density profile (β). Dotted lines represent the corresponding distribution functions before projection (normalised to the 90° value).

One can expect the curves presented in Fig. 10.1 to be barely dependent on the orbital eccentricity. Non closed eccentric orbits result in a similar projected distribution, since (i) the satellite spends most time at the apo-galacticon and (ii) the apsides of the orbit form an annuli in the orbital plane (assuming the dynamical time to be short compared to the Hubble time). The resulting time average is, therefore, similar to a circular orbit with $R \leq R_a$, where R_a is the apo-galacticon.

Holmberg (1969) and Zaritsky et al. (1997) observe anisotropies after averaging over a given distance range of the order of $\sigma(0°)/\sigma(90°) \simeq 0.52$, which would indicate a very significant absence of low inclined satellites in the galaxy frame together with a steep spatial distribution.

10.5 Experiments

The strong constraints that observations produce indicate that there must be a mechanism that removes those satellites within some minimum inclination, which might be as high as 45°. In order to assert whether dynamical friction in flattened haloes can be responsible of such an anisotropy, we carry out an statistical survey of satellite evolution to compare with the observational data. We must note that one of the main incognita is the initial distribution of orbits and masses.

However, due to the complexity that the initial satellite distribution may present, it is useful first to carry out a separate study of the different effects that the different orbital parameters and satellite masses induce on the final distribution, in order to obtain a feeling for the evolution.

10.5.1 Inclination evolution

The inclination i of satellites moving within and around flattened systems does not remain constant along the orbit. There are two driving mechanisms that determine the evolution of i: (i) the nutation effect and (ii) dynamical friction.

Nutation

Nutation arises due to the potential quadrupole (Q) of the galaxy. Due to the small disc extension (around 95 per cent of its mass lies within 3.5 kpc) and taking into account that $Q \sim 1/r^3$ (whereas the zeroth order of the potential expansion goes as $1/r$) the galaxy quadrupole acting on satellites is mainly produced by the anisotropic mass distribution of the halo.
For low halo asphericity, nutation can be estimated as a function of the orbital and galaxy parameters (see Appendix A),

$$\cos i_1 - \cos i = (I_z - I_R)\frac{3GM}{2a^2 r}\sin^2 i_1 \cos^2 i_1 \times \left[1 - \cos\left(\frac{a}{r^2\cos^2 i_1}t\right)\right], \tag{10.6}$$

where I_x is an eigen-component of the inertia tensor per unit mass (accomplishing that $I_z > I_R$ in oblate systems). We denote as M the mass inside the radius r, a the initial z-component of the angular momentum vector and i_1 the initial inclination. It is interesting to note that orbits with $i_1 = 0°, 90°$ remain with constant inclination, whereas the maximum variation occurs for those with $i_1 = 45°$. Since a is maximum for circular orbits, we expect a stronger nutation the more eccentric the orbits are.

Due to the nutation effect, orbits initially at the apo-centre evolve to inclinations that are equal or larger than the initial one, since $\cos i_1 - \cos i \geq 0$. Assuming an orbital period much shorter than the Hubble time, the averaged time dependence of nutation is simply 1/2. The number of satellites per unit inclination is $N(i) = \sigma_0 \sin i$, where σ_0 independent of i indicates that the distribution is isotropic. The change over the inclination distribution is therefore

$$\sigma(R,i) = R^{2-\beta}\left|\frac{dN}{d\cos i}\right| = R^{2-\beta}\left|\frac{dN}{d\cos i_1}\right|\left|\frac{d\cos i_1}{d\cos i}\right| \equiv R^{2-\beta}\sigma_0\left[1 - K\sin^2 i_1 \cos i_1 + K\cos i_1\right]^{-1}, \tag{10.7}$$

where

$$K = (I_z - I_R)\frac{3GM}{2a^2 r}.$$

To check this estimate, we carry out an experiment where dynamical friction is switched off and compare the resulting curve with the initial one, Fig. 10.2. We use a sample of 1000 satellites homogeneously distributed within [39, 66] kpc, (in order to obtain a phase-mixing we do not employ a single value of the initial distance) and with orbital eccentricity $e = (R_a - R_p)/(R_a + R_p) = 0.3$, where R_a, R_p are the apo and peri-galactica, respectively. The points represent the expectation from eq. (10.7), which shows a remarkable agreement with the semi-analytic result if fitting K.

Stronger halo flattening as well as more radial orbits will lead to a stronger anisotropy in the inclination distribution *only* due to nutation.

Dynamical friction

Satellites moving through a background of less massive particles with an anisotropic velocity distribution suffer a monotonic decrease of the averaged inclination via dynamical friction (see Chapter 7). This reduction is larger the stronger the friction force becomes and affects neither polar nor coplanar satellites. The effect on the final distribution is, therefore, opposite to that induced by nutation. However, whereas nutation is nearly independent of r in isothermal haloes,

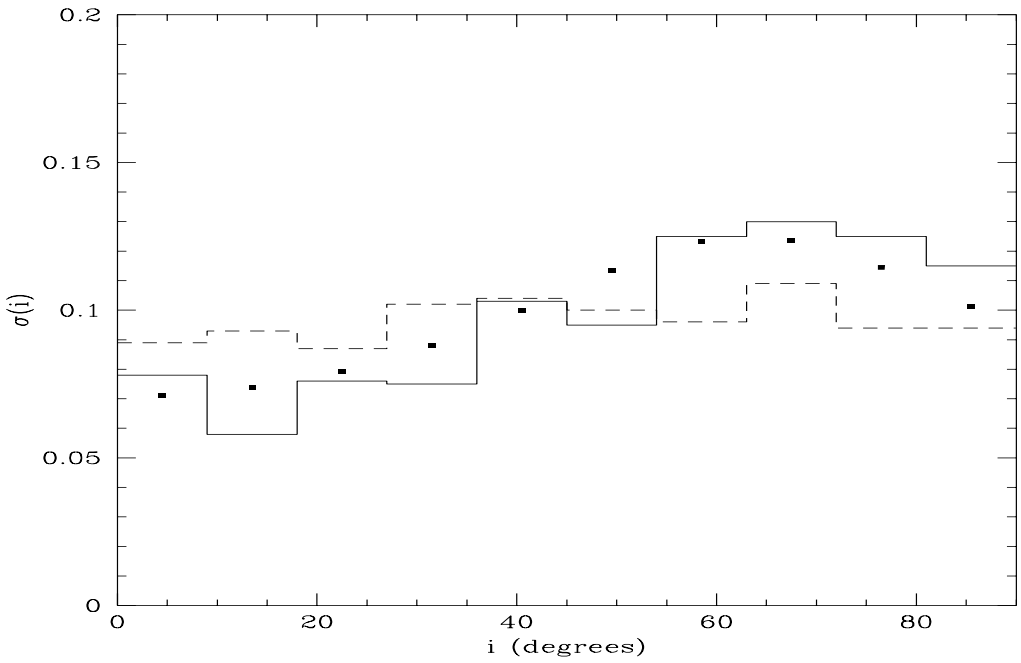

Figure 10.2: Distribution in inclination after the sample is evolved one Hubble time *without* dynamical friction (solid line) compared with the initial one (dashed line). Points represent the analytical estimate from eq. (10.7) arbitrarily normalised with $K = 0.8$. The bin is 10°. The set of 1000 satellites are initially homogeneously distributed within $[39, 66]$ kpc with initial eccentricity $e = 0.3$. The halo axis-ratio is $q_h = 0.5$.

dynamical friction scales as $\rho_h \propto 1/r^2$, so that we expect the inclination decrease at large distances to become negligible.

10.5.2 Single orbital parameters and mass values

By means of dynamical friction, the satellite suffers angular momentum loss that leads to the progressive sink to the galaxy centre. The satellite decay time (which as a matter of fact we consider equivalent to the survival time, even if satellites reach the inner most region of the galaxy) is a function of the initial orbital parameters and mass

$$t_{\rm df} = t_{\rm df}(i, R_0, e, M_s),$$

where R_0 is the initial distance, i the inclination and e the orbital eccentricity.

In a spherical isothermal sphere, the decay time of circular orbits goes as (e.g BT)

$$t_{\rm df} \propto \frac{R_0^2}{M_s}. \tag{10.8}$$

If the satellite moves in an eccentric orbit ($e > 0$) with apo-galacticon $R_a = R_0$, one expects a shorter decay time than the same orbit with $e = 0$ since (i) the initial angular momentum is lower and (ii) dynamical friction at the peri-galacticon is roughly of the order of $\rho(R_p)/\rho(R_a) = (R_a/R_p)^2$ larger than at apo-galacticon (note that the larger satellite velocity reduces the friction force at $R = R_p$, so that this value overestimates the fraction).

The flattening of the halo and the disc implies the decay time to be dependent on the satellite inclination. PKB find that polar and coplanar orbits posses the maximum and minimum decay time, respectively, which agrees with the theoretical description of dynamical friction seen in Chapter 5. Polar satellites, therefore, survive longer than those in low inclination orbits.

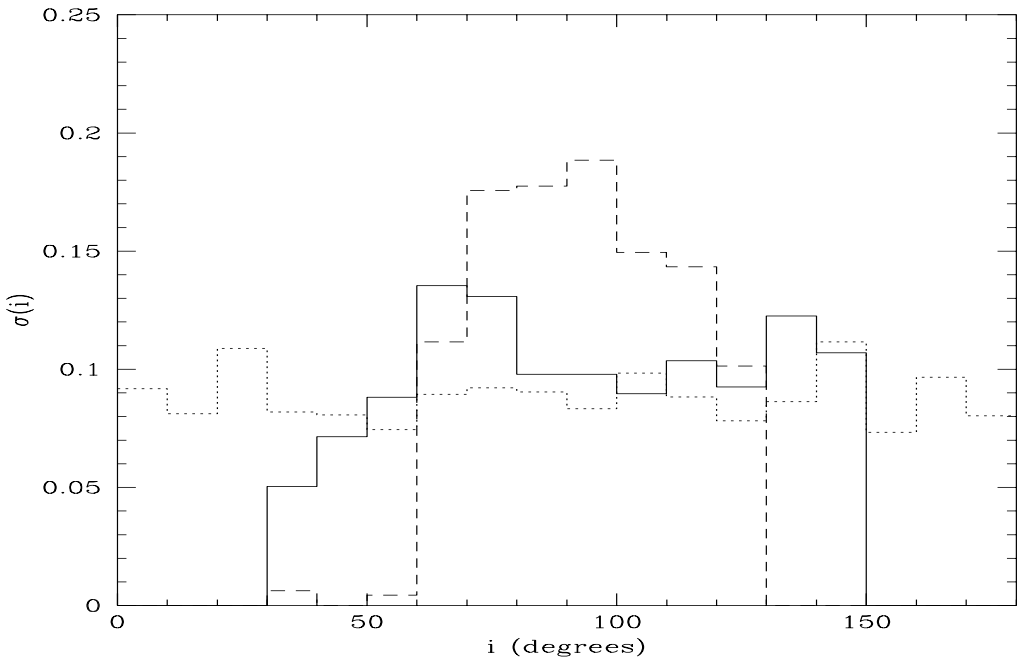

Figure 10.3: Distribution of satellites with initial $(R_0, e, M_s) = (45 \text{ kpc}, 0, 0.1M_d)$ as a function of the inclination. Dotted and solid lines represent the initial ($t = 0$) and evolved ($t = t_H$) distributions. The dashed line accounts for the initial inclination distribution of surviving satellites. The sample contains 1000 satellites, from which 277 survive. The bin is 10° wide and the halo axis-ratio $q_h = 0.5$. Note: curves are normalised to the number of satellites in the set.

Consider first a set of satellites with fixed parameters (R_0, e, M_s) and different inclinations, $i \in [0°, 180°]$, where $i > 90°$ denotes that the orbital sense is retrograde to the disc rotation. We assume that orbits survive when $t_{\rm df} > t_H$ the Hubble time ($t_H = 12$ Gyr) and $M_s(t_H) > 0.01M_d$ (lower mass satellites would be missed by the observational magnitude limit). One has three possible cases,

- $t_{\rm df}(i = 90°) < t_H$, which implies that no satellites can be observed after one Hubble time, independently of the initial inclination.
- $t_{\rm df}(i = 0°) \leq t_H \leq t_{\rm df}(i = 90°)$, therefore, only those satellites with some $i \geq i_0$ (or equivalently $i \leq \pi - i_0$ for the retrograde ones) can survive after one Hubble time and be observed. We define i_0 as the *minimum inclination*, which is dependent on the parameters (R_0, e, M_s).
- $t_{\rm df}(i = 0°) \geq t_H$, all the satellites of the sample will survive.

It is evident, that neither the first case nor the last one can cause the observational anisotropy present in the inclination distribution. To show that only a distribution of satellites with initial parameters corresponding to the second case will result to a anisotropic inclination distribution, we carry out a simple experiment. We create a sample of 1000 galaxies isotropically distributed within a halo of axis-ratio $q_h = 0.5$, with $(R_0, e, M_s) = (45 \text{ kpc}, 0, 0.1M_d)$, i.e., we locate all satellites at the apo-galacticon with eccentricity $e \simeq 0$ (regarding that orbits in flattened haloes do not exist since L_R, the planar component of the angular momentum, is not a constant of motion).
After evolving the system we obtain the distribution plotted in Fig. 10.3, where the minimum inclination is $i_0 \simeq 30°$. The dashed line shows the initial inclination distribution of the surviving satellites. As a result of the inclination decrease along the orbit through dynamical friction, the final distribution covers the range $[30°, 150°]$. Had the orbital inclination remained constant, the

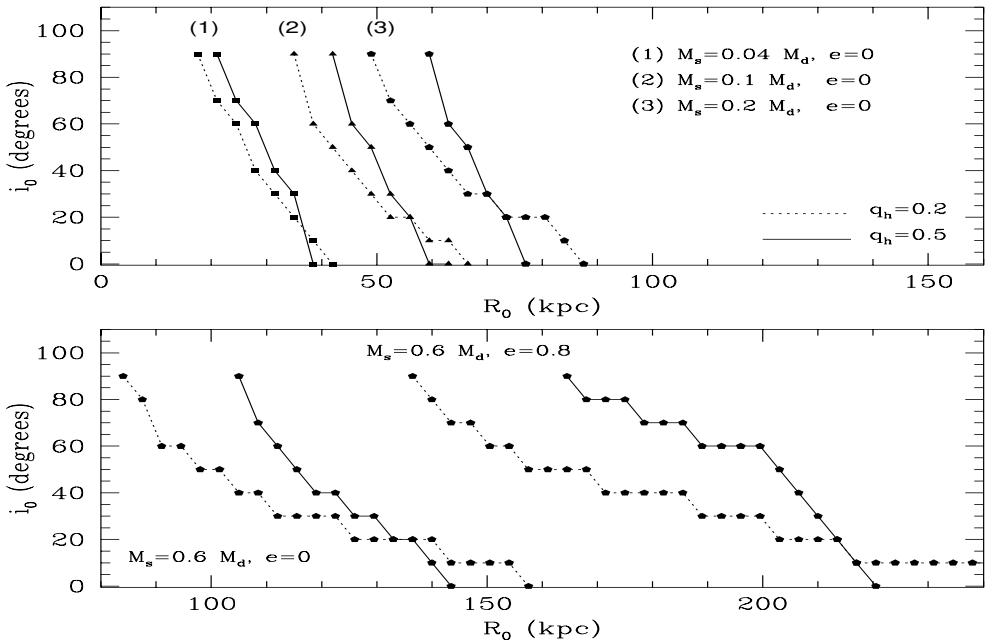

Figure 10.4: Minimum inclination as a function of the galacto-centre distance for four satellite masses. Satellites follow circular ($e = 0$) and highly eccentric orbits ($e = 0.8$) within a flattened halo of axis-ratio $q_h = 0.5$ (solid lines) and $q_h = 0.2$ (dotted lines). Notation: $i_0 = 90°$ indicates that no satellite survives, whereas $i_0 = 0°$ denotes the survival of all satellites. For a given mass, satellites with initial R_0, i_0 to the left of the curves do not survive independently of the initial orbital eccentricity. The resolution in inclination is 10°. Note that two panels are plotted for a better distinction of the curves.

resulting distribution curve would present a nearly Heaviside function within the range $[60°, 120°]$. Applying eq. (10.5) to the resulting inclination distribution, we obtain a projected anisotropy of 0.73 for $\beta = 2$ and 0.69 for $\beta = 3$ which do not reproduce the observational value (0.52).

In Fig. 10.4 we plot the minimum inclination as a function of the galacto-centre distance for four satellite masses and two halo axis-ratios $q_h = 0.2, 0.5$. The eccentricity is fixed to $e = 0$ (circular orbits) and $e = 0.8$ (highly eccentric orbit) to determine the function $i_0 = i_0(R_0, M_s)$. This Figure shows that satellites with $M_s = 0.1 M_d$ and initial distance $R_0 = 45$ kpc, the minimum inclination is $i_0 \simeq 60°$ for $q_h = 0.5$, which means that satellites with initial $i < i_0$ are all destroyed after one Hubble time whereas those with $i > i_0$ survive. Looking at the $M_s = 0.2 M_s$ curve one sees that for this initial distance (and eccentricity) no satellite can be observed whereas if $M_s = 0.04 M_d$ again all survive independently of the initial inclination. The calculus for $M_s = 0.6 M_d$ represents the extreme case, for which the satellite must be located large initial distances in order to observe it at $t = t_H$. If satellites move along high eccentric orbits $e = 0.8$ the decay time is strongly reduced, so that minimum distance for survival is approximately 50% larger compared with the case $e = 0$. This plot shows that satellites with $M_s \leq 0.6 M_d$ and R_0 of the order or larger than 250 kpc will survive independently of the initial inclination and orbital eccentricity.

It is also interesting to note that the expected minimum inclination of the example shown in Fig. 10.3 is $i_0 \simeq 60°$, which agrees with the resulting distribution represented by the dashed line (no inclination evolution).

We must remark that the anisotropy of Fig. 10.3 can be increased by selecting properly a combination of (R_0, e, M_s). For instance, samples of satellites in haloes $q_h = 0.5$ with an initial isotropic distribution and $(R_0, e, M_s) = (24\,\text{kpc}, 0, 0.04\,M_d), (40\,\text{kpc}, 0, 0.1\,M_d), (60\,\text{kpc}, 0, 0.2\,M_d)$ would result after one Hubble time to a Heavy-side distribution with $i_0 \sim 80°$ without inclination

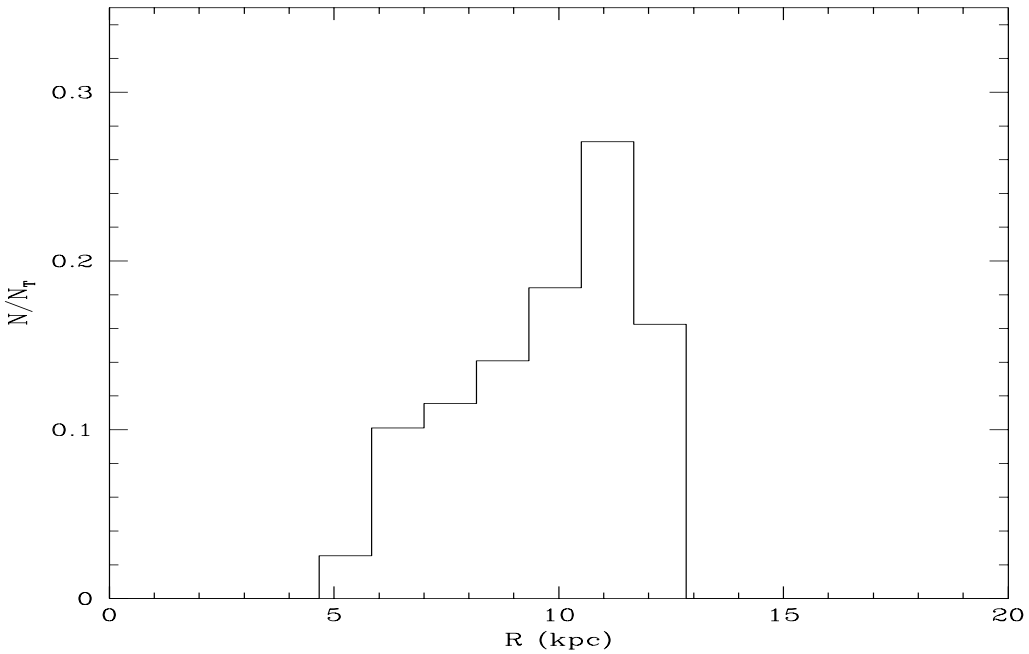

Figure 10.5: Distance distribution of the sample of Fig. 10.5 evolved one Hubble time. Solely those satellites that survive are included in the calculus, $N_T = 277$.

evolution.

If the halo is more flattened, the range of initial distances in which one expects a resulting anisotropic distribution becomes wider. The maximum effect occurs for massive satellites ($M_s = 0.2M_d$) for which $\Delta r \equiv r(i = 0°) - r(i = 90°)$ becomes $\Delta r(q_h = 0.5) \simeq 0.25\Delta r(q_h = 0.2)$, whereas if $M_s = 0.04$ one has $\Delta r(q_h = 0.5) \simeq 0.7\Delta r(q_h = 0.2)$.

The next question is how the distance distribution appears after the system is evolved. If the decay rate was independent of the galacto-centric distance, one would expect a Heaviside distribution. However, the numerical calculations of PKB, as well as those of Chapter 8, show that the rate is accelerated at distances close to the galaxy centre, so that the range of distances within the satellite might be found after one Hubble time will be smaller. In Fig. 10.5 we plot the resulting distance distribution of Fig. 10.3. The histogram is not a Heaviside function though, it presents a cut-off at large distances corresponding to satellites with initial inclination $i_1 = 90°$. Due to the non-linear decay rate, the final distance is very sensitive to the initial inclination, so that small variations of i_1 lead to strong differences on the final distance, which explains the larger number of satellite at $R(t = t_H) \sim 10$ kpc. We conclude that, if originally all satellites are located at a given distance, the final distribution will be strongly peaked at $R(t = t_H, i_1 \simeq 90°)$.

10.5.3 Distribution of orbital parameters and masses

To assume that satellites formed with a single set of (R_0, e, M_s) is strongly unphysical since all cosmological theories of galaxy formation predict values that follow distribution functions. The question is, how does a continuous distribution of orbital parameters and satellite masses alter the final distribution?.

To answer it, we build up a sample of 1000 satellite galaxies with $(e, M_s) = (0, 0.1M_d)$ homogeneously distributed, $\beta(t = 0) = 2$, within the range $R_0 \in [20, 80]$ kpc, which includes the three cases discussed above: (i) satellites with $R < 40$ kpc will decay before one Hubble time, (ii) those with $R > 60$ kpc are observed after one Hubble time independently of the initial inclination and (iii)the survival of satellites with intermediate initial distances depends on the initial orbital

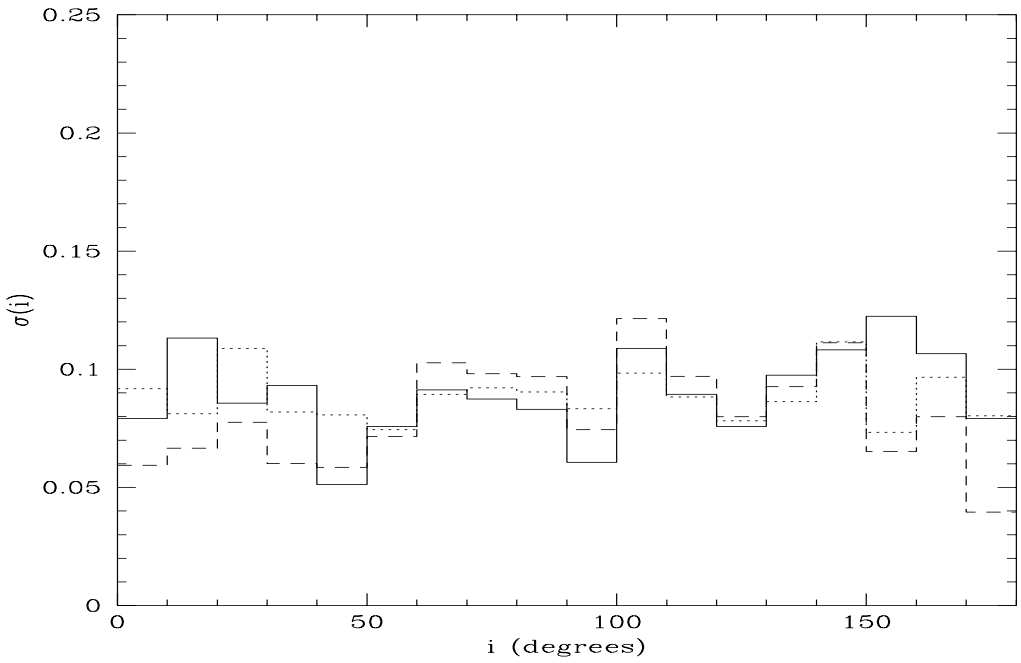

Figure 10.6: As Fig. 10.3 with the sample covering a range of initial distances $R_0 \in [20, 80]$ kpc.

inclination. The resulting distribution is plotted in Fig. 10.6. The number of satellites after one Hubble time is 580, approximately half of them lie within the range $0° < i_0 < 90°$. The dashed line (initial inclination distribution of the surviving satellites) shows still some anisotropy which, however, is strongly smoothed if compared to that of Fig. 10.3. The distribution becomes nearly isotropic due to the inclination decrease along the evolution (solid line).

This exercise has been repeated changing the orbital eccentricity and satellite mass, leading to the same conclusion: only a given fraction of satellite masses and orbits, those for which the combination of (R_0, e, M_s) makes $0° < i_0 < 90°$, can produce the observed anisotropic inclination distribution.

We want to emphasise the small dependence of the final distribution on the orbital sense. This result agrees with the numerical calculations of PKB, who find that the differentiation in the decay time between prograde and retrograde orbits (via dynamical friction) is strongly smoothed as a result of the halo flattening.

10.6 The initial satellite distribution

In this Section we outline the initial set of satellite masses and orbits that outcome from the Monte-Carlo scheme once some initial distribution is assumed.

10.6.1 The satellite masses

The appearance of large substructures in the Universe is usually described by small fluctuations in the initial background density that lead to the present mass distribution through the so-called *merger tree* process. In this scenario, dark matter haloes form hierarchically through the accretion and merging of smaller substructures that condensed from the fluctuations of the initial density field.

Since the collapse and viralization of dark matter haloes is thought to be non-linear, authors usually resort to N-body calculations in order to follow the formation and evolution of these

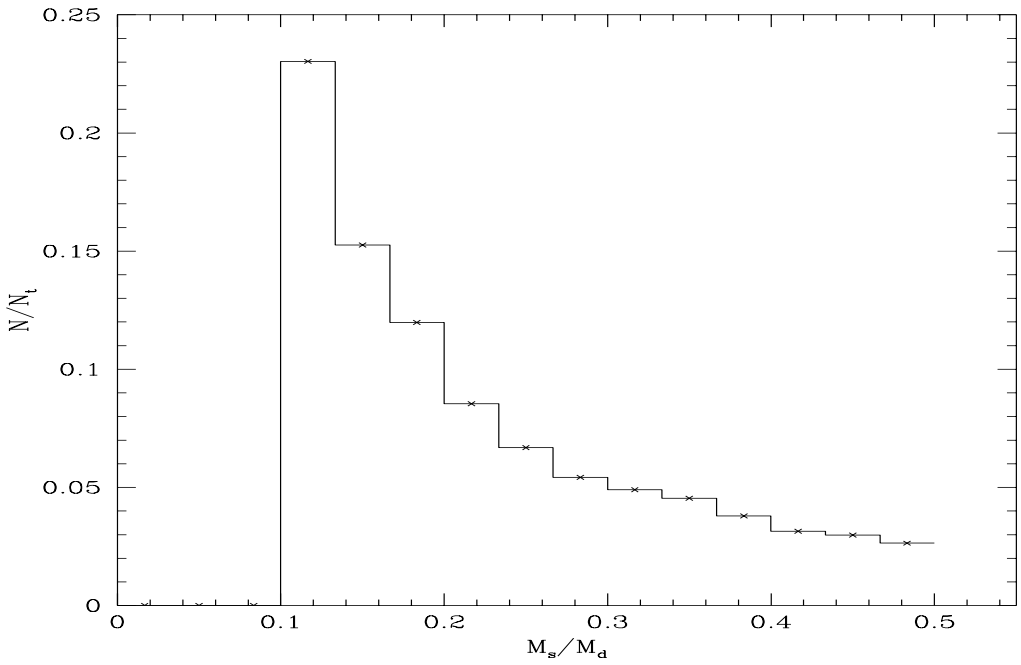

Figure 10.7: Initial mass distribution for a sample of $N_t = 10000$ satellites.

systems. Unfortunately, this scheme suffers from strong limitations, like expensive computational times and low resolution.

The alternative can be found in the Press-Schechter formalism (Press & Schechter 1974). This scheme has been found to be in remarkable agreement with the N-body computations, providing the initial mass distribution from the linear analysis of the fluctuation spectrum, and the corresponding evolution through a hierarchical clustering (e.g, Efstathiou et al. 1988, Lacey & Cole 1994 and references therein). This theory has also been extended (Bond et al. 1991, Lacey & Cole 1993) to follow the history of individual particles in order to produce the merger-trees of individual haloes.

In our study of the satellite distribution in spiral galaxies, we simply employ the Press-Schechter scheme to reproduce the initial mass spectrum of satellites within a given halo. This theory predicts that the cumulative total mass $\mathcal{M}(M)$ below the mass M as

$$\mathcal{M}(M) \propto M^{1-\alpha}, \tag{10.9}$$

where α has been found to have a value of $1/2$ in order produce the best fit to numerical calculations (Press & Schechter 1974, Lacey & Cole 1993, Tormen 1997). We note that, though this distribution diverges for $M \to 0$, the cumulative mass is integrable.

Taking into dynamical constraints, we limit our analysis to a range of masses $M_s \in [0.1, 0.6]\, M_d$ which recovers most part of the observational data after the set of satellites has been evolved.

In Fig. 10.7 we plot the initial mass distribution obtained from the Press-Schechter formalism within the range commented above. The figure is done for a set of 10000 satellites, 90 per cent of them having $0.1 M_d \leq M_s \leq 0.5 M_d$.

10.6.2 Spatial distribution

Theoretical studies of hierarchical galaxy formation in the CDM frame, where the density peaks that are site of galaxy collapse in the Gaussian random field, predict triaxial systems (Bardeen et al. 1986). Using the CDM spectrum, cosmological N-body calculations (Frenk et al. 1988, Dubinsky & Calberg 1991) result to highly flattened haloes with prolate triaxial shapes (if $c \leq b \leq a$ then

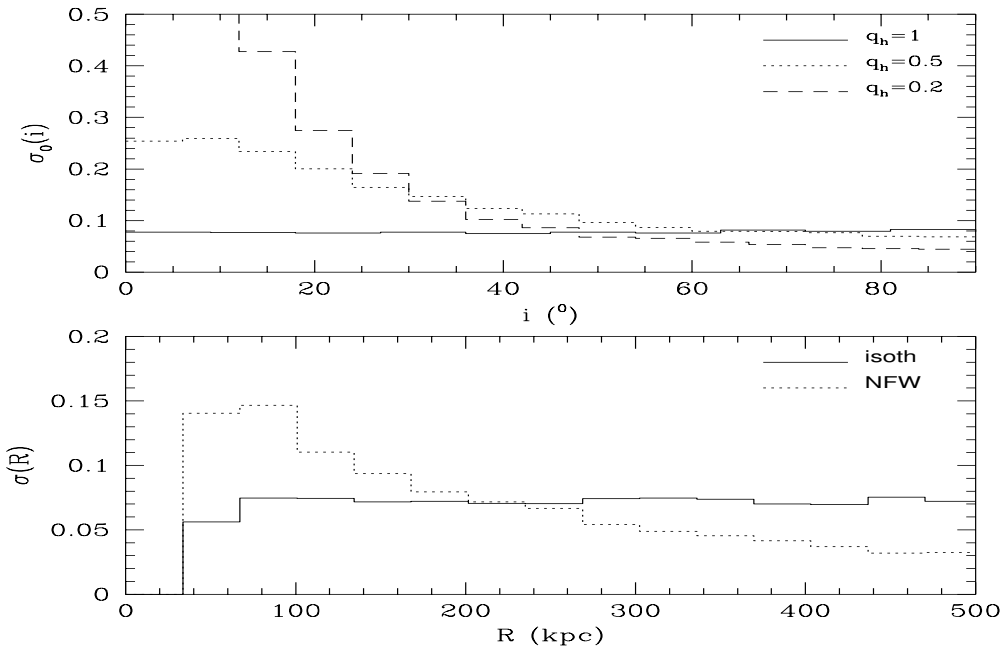

Figure 10.8: **Upper panel**: Initial inclination distribution for three values of q_h. The sample of satellites contains $N_t = 10000$. **Lower panel**: Spatial distribution of satellites when using a singular isothermal profile and that propose by NFW.

$c/b > b/a \simeq 0.5$ and $c/a \simeq 0.5$). The dissipative infall of gas during the formation of a galaxy modifies the halo shape, so that the axial ratio b/a grows to $0.7 - 0.8$ whereas c/a barely changes (Dubinsky 1994).

CDM cosmology predicts the formation within haloes of substructures with nearly scale free density profile, that one can identify as satellite galaxies. Whereas it is not obvious that the initial spatial distribution of such objects should account for the halo mass distribution, in this preliminary study we assume that satellites follow the density profile of the parent galaxy. For comparison, we also include samples with isotropic inclination distributions at $t = 0$.

Isothermal model

Consider first a flattened halo with a singular isothermal profile, then

$$\rho_{\rm isoth}(R,i) = \frac{\rho_0}{R^2}\left[\cos^2(i) + \sin^2(i)/q_h^2\right]^{-1}, \tag{10.10}$$

where ρ_0 is a constant.

The first hypothesis in our work is that the satellite distribution follows the mass distribution of the parent galaxy. We generate a sample of satellites using the Monte Carlo scheme by calculating the probability of each satellite to move along a orbit with initial inclination i. The normalised cumulative probability as a function of the inclination is from eq. (10.10)

$$\hat{\mathcal{P}}(<i) = \frac{1}{2}\left\{1 + \frac{\mathrm{atanh}[\sqrt{1-q_h^2}\cos(i)]}{\mathrm{atanh}\sqrt{1-q_h^2}}\right\}. \tag{10.11}$$

The resulting initial inclination distribution (number of satellites per unit angle, σ_0), is plotted in the upper panel Fig. 10.8 for three values of q_h. We note that smaller halo axis-ratios give rise to larger number of satellites at small orbital inclinations.

We also generate samples where the initial inclination distribution is isotropic, since the results are more straightforward to interpret.

NFW model

Navarro, Frenk & White (1996), hereinafter NFW, use high-resolution N-body calculations in order to investigate the structure of galactic haloes and galaxy cluster haloes. They find an "universal" density profile that matches halo masses ranging from dwarf satellites to those of rich galaxy clusters

$$\rho_{\rm nfw} = \frac{\rho_1}{R(1+R/R_{sc})^2}, \tag{10.12}$$

where R_{sc} is the scale-radius. This profile is nearly isothermal for small radii, producing a "core" for $R \ll R_{sc}$, i.e the central part show a nearly constant density profile, which fits better to observations than models with a singular density curve for $R \to 0$. The outer region presents a steeper profile, $1/R^3$, that results to a decrease of the surface density for $R > R_{sc}$. Although this modelling of halo mass distribution solves problems like the un-correlation between luminosity and dynamics in bright galaxies (see NFW for more details) and match observations of intra-cluster structures, some uncertainties still remain, since (i) the abundance of galaxies from the N-body simulations is largely overestimated and (ii) the density profile is too steep at small radii to fit to observations of dwarf galaxies.

The analysis of the satellite abundance as a function of the galacto-centre distance may give insights on the halo profile. With this aim in mind, we also employ the density profile of eq. 10.12 in order to reproduce the satellite distribution. The normalised cumulative probability as a function of R is

$$\begin{aligned}\hat{\mathcal{P}}(<R) = \frac{R_{\rm cut}+R_{sc}}{R+R_{sc}}\left[\ln\left(\frac{R+R_{sc}}{R_{sc}}\right)(R+R_{sc})-R\right] \\ \times\left[\ln\left(\frac{R_{\rm cut}+R_{sc}}{R_{sc}}\right)(R_{\rm cut}+R_{sc})-R_{\rm cut}\right]^{-1},\end{aligned} \tag{10.13}$$

where $R_{\rm cut}$ is the halo cut-off radius.

The comparison of the initial inclination distribution between the isothermal model and that proposed by NFW is plotted in the lower panel Fig. 10.8 for a sample of $N_t = 10000$ satellites. This Figure shows that, compared to isothermal distributions, NFW haloes provide a larger number of satellites for $R < R_{sc} = 250$ kpc whereas in the outer region this number decreases.

The range of distances where we initially locate satellites accounts for the observational data of Zaritsky et al. (1993), so that $R \in [40, 500]$ kpc, approximately. Satellites with $R < 40$ kpc decay to the centre independently of the initial orbital eccentricity (for the range of masses given above). We expect that satellites with $R > 300$ kpc suffer small friction due to the low density at such large distances.

10.6.3 Eccentricity distribution

The number of satellites as a function of the orbital eccentricity that we use is that found by van den Bosch et al. (1999). Defining the initial orbital circularity as $\eta = L/L_c(E)$ where $L_c(E) = R_c(E)V_c$ is the initial angular momentum of a circular orbit with radius $R_c(E) = \exp[(E - 1/2V_c^2)/V_c^2]$ and the same energy (note that $0 \geq \eta \geq 1$, so that orbits with null circularity are radial and with $\eta = 1$ circular). For an isothermal sphere one has that

$$\frac{1}{x^2} + \frac{2}{\eta^2}\ln(x) - \frac{1}{\eta^2} = 0, \tag{10.14}$$

where the peri (R_p) and apo-centre (R_a) are given by the roots of the equality, the eccentricity being $e(\eta) = (R_a - R_p)/(R_a + R_p)$ and $x = R/R_c$.

Assuming that (i) orbits have an isotropic eccentricity distribution and (ii) the energy of the orbit is independent of the cicularicity, van den Bosch et al. proves that if the galaxy potential

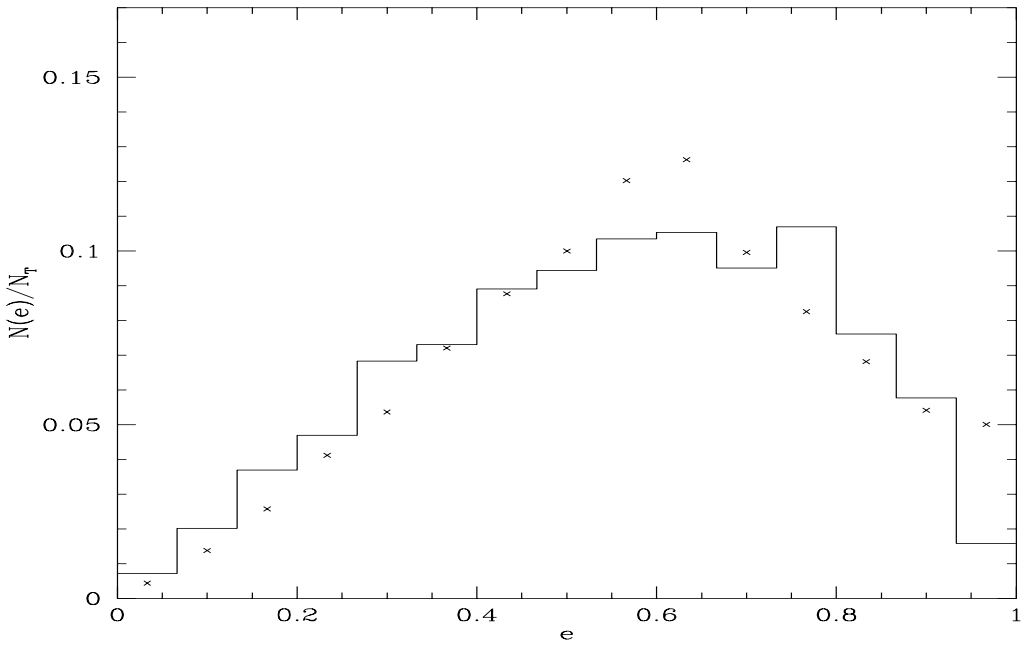

Figure 10.9: Initial eccentricity distribution for a sample of $N_t = 10000$ satellites (solid line). Points represent the initial distribution of $\xi = v/V_c$.

can be written as $\Phi = V_c^2 \log(R)$, the distributions of cicularicity and energy are

$$\mathcal{P}(E) = \frac{R}{u_H V_c^2} \exp\left[-\frac{E}{V_c^2}\right] \qquad (10.15)$$
$$\mathcal{P}(\eta) = \frac{\eta}{\sqrt{\eta_{\rm max}^2 - \eta^2}},$$

where

$$u_H = \int_0^\infty du \exp(-u) \int_0^{\eta_{\rm max}} \frac{\eta d\eta}{\sqrt{\eta_{\rm max}^2 - \eta^2}}$$
$$\eta_{\rm max} = \sqrt{2u} \exp(-u + 1/2),$$

denoting $u = 2E/V_c^2$. The Monte-Carlo scheme employed to produce the distribution function $N = N(e)$ from this last equation is explained in detail in this paper.

In Fig. 10.9 we plot the eccentricity distribution if the initial satellite energy is assumed independent of e. For technical reasons, it is useful to define the quantity $\xi \equiv v/V_c = R_c(E)/R_0\eta$, which gives the initial velocity that leads to a given value of e. The distribution of ξ is represented by dotted points. This figure shows that most of the satellite move along orbits with intermediate eccentricities, avoiding circular as well as radial orbits. The averaged eccentricity is $\bar{e} = 0.55$.

If the system is not an isothermal sphere, but it has the density profile presents a cut-off radius , van den Bosch et al. (1999) find for $r_{\rm cut}/\gamma = 24$ differences in the distribution shape around 10% for $e > 0.7$ and negligible for smaller eccentricities (see their Fig. 5).

10.6.4 Set of calculations

In Table 10.1 we present the samples employed for our study. The initial spatial distributions of the satellite samples are those of eq. (10.10), isothermal, and (10.12) which follows the NFW profile. The initial inclination distributions are either isotropic or matching the axis-ratio of the halo ($q = 0.2, 0.5$). In all samples, the initial eccentricity distribution is that outlined in Section 10.6.3.

Set	Spatial distrib.	Inclin. Distrib.	q_h	N_t	N_e
1	Isoth.	Isotropic	0.5	10^4	8442
2	Isoth.	Isotropic	0.2	10^4	7398
3	Isoth.	Flat. $q = 0.5$	0.5	10^4	7420
4	NFW	Isotropic	0.5	10^4	7180
5	NFW	Isotropic	0.2	10^4	7133
6	NFW	Flat. $q = 0.5$	0.5	10^4	7369

Table 10.1: Set of calculations. N_t denotes the initial number of satellites in the sample, whereas N_e after evolving it one Hubble time. q_h is the halo axis-ratio of the parent galaxy. The spatial as well as the inclination distributions are either isotropic or flattened at $t = 0$.

We must comment that our initial sample of satellites is not in equilibrium, since all orbit are located initially at the apo-centre. We expect, for instance, the final distribution to present averaged distances smaller than the initial one due to non-zero eccentricity (besides the decrease induced by dynamical processes such dynamical friction) or the overall increase of the orbital inclination due to nutation.

10.7 Results

We present the evolved satellite samples presented above, together with the comparison with the observational data of Zaritsky et al. (1997) and Holmberg (1969). The halo axis-ratio is a free parameter to fit to the observed distributions, regarding that the most favoured cosmological model predicts a Gaussian asphericity function centred at $q_h = 0.5$.

10.7.1 Evolution of distance, mass and inclination

The final distributions of our samples are determined by complex processes such as dynamical friction and mass loss, which highly depend on the initial orbital parameters of the satellites.

In order to illustrate how dynamical friction in systems with anisotropic velocity dispersions alters the initial distributions, we plot in Fig. 10.10 the averaged radius and orbital inclination of the evolved samples 1 and 2 as a function of the initial galacto-centre distance (R_0). The upper panel shows that the final satellite radii are of the order of 20 to 80 % of their initial values by means of dynamical friction. The decrease of the mean galacto-centre distance is clearly dependent on the radius where the satellites are initially located. So that, for orbits lying at $R_0 > 200$ kpc, dynamical friction is much more inefficient that for orbits with $R_0 < 200$ kpc. The *plateau* visible at large radii indicates that a mean decrease of 15-20 per cent can be expected even for $R_0 \sim 500$ kpc. The reduction of the mean R is in this case not caused by dynamical friction but by the eccentricity distribution (we recall that $N(e)$ does not depend on R_0). We conclude that dynamical friction is negligible for R_0 larger than approximately 250 kpc, independently of the halo shape, which agrees with the results of Fig. 10.4.
Dynamical friction strongly reduces the galacto-centre distance for $R_0 < 200$ kpc, thus, a large fraction of satellites initially located within this interval merge with the parent galaxy after one Hubble time. Haloes with axis-ratio $q_h = 0.2$ are less efficient than those with $q_h = 0.5$ in order to remove satellites due to the stronger dependence of the satellite decay time on the orbital inclination. This corresponds to the results plotted in Fig. 10.4, where it is shown that more flattened haloes increase the survival times for those satellites with approximately $i_0 > 20°$, independently of the initial mass and orbital eccentricity.

The mass loss fraction is plotted in the middle panel. We observe that only those satellites at $R_0 < 150$ kpc suffer mass loss. The satellite mass is stripped away by the combined action of tidal forces and shocks. Both mechanisms produce non-negligible effects near the disc, $R < 50$ kpc, which explains the nearly flat curve for distances larger than 200 kpc. Satellites with larger radii

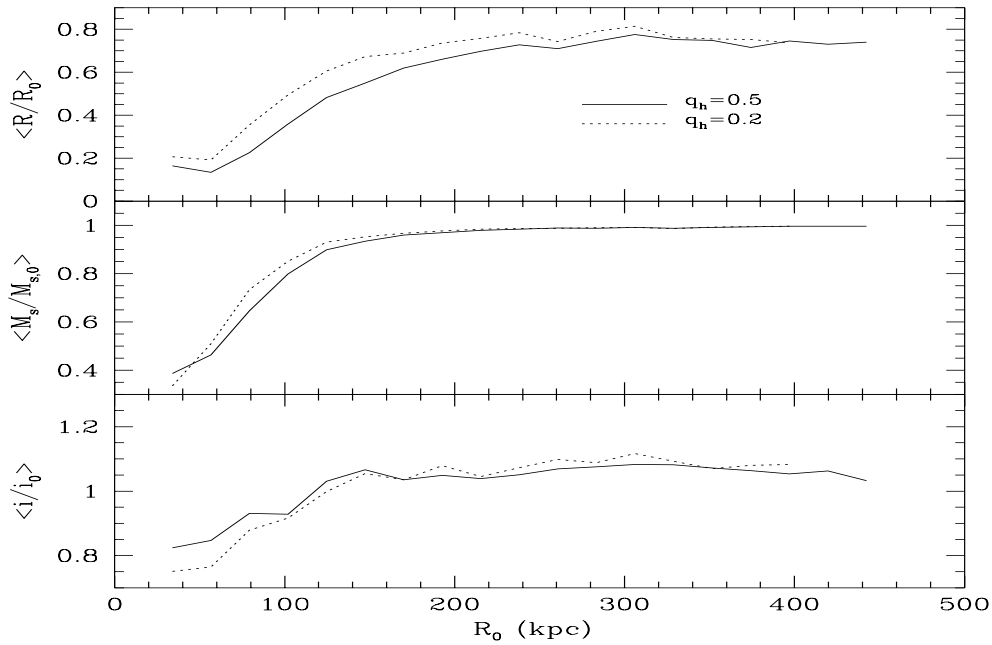

Figure 10.10: **Upper panel**: Average of the evolved to initial distance ratio after the evolution of the samples 1 (solid lines) and 2 (dotted lines) as a function of the initial radius R_0. **Middle panel**: Average of the mass variation after the evolution. **Lower panel**: Average of the inclination variation.

have approximately the same mass after one Hubble time. it is interesting to note that satellites embedded in highly flattened haloes suffer, in average, lower mass loss. This is connected to the slower decay shown in the upper panel, since larger average distances imply weaker tidal interactions.

The inclination evolution also shows a clear dependence on the initial galacto-centre distance. Orbits initially at radii larger than 200 kpc show enhanced inclinations after one Hubble time, which is probably due to nutation. Three aspects point to this explanation: (i) the average value of i/i_0 is larger if the galaxy halo is more flattened, (ii) dynamical friction is inefficient for $R_0 > 250$, the only force acting on the satellite at those radii is, therefore, that induced by the aspherical potential of the halo and (iii) in isothermal haloes, the satellite nutation is nearly independent of the distance, which would result to a roughly constant increase of the averaged inclination for radii where the other forces acting on the satellite are negligible.
If satellites are close to the disc, $R_0 < 100$ kpc, dynamical friction dominates over nutation in order to alter the orbital inclination. As PKB show, a strong reduction of this quantity is expected if satellites move within haloes with anisotropic velocity distributions. The inclination decrease is around 5-10% larger if the halo has an axis-ratio $q_h = 0.2$. The maximum reduction of the orbital inclination is around 20-25% of its initial value.

10.7.2 Inclination distribution

In Fig. 10.11 we plot the inclination distribution after evolution ($t = t_H = 12 \times 10^9$ yr). Panels in the upper row shows the number of satellites per unit inclination for those satellites located with $R \in [9, 500]$ kpc and $R \in [200, 500]$ kpc (in the galaxy frame, i.e, radii are not projected). Comparing both panels we observe that the anisotropy of the distribution is stronger for satellites at large radii if the initial distribution is isotropic (sets 1 and 2). However, if the initial distribution follows that of the halo particles, the final inclination of the satellites is roughly independent of

the distance range. In this case, the number of satellites in low inclinations is remarkably large, obtaining a final distribution similar to that of the halo (oblate).

The comparison of the resulting histograms of the samples 1 and 2 (where the halo axis-ratio is $q_h = 0.5, 0.2$, respectively) show that (i) for highly flattened haloes ($q_h = 0.2$), the value of σ_0 in the whole range of distances is larger for $i < 15°$, $i > 75°$ than in haloes with $q_h = 0.5$, whereas for intermediate inclinations ($i \sim 45°$) we have that $\sigma_0(q_h = 0.2) < \sigma_0(q_h = 0.5)$. (ii) If the calculus is carried out for satellites located at large radii (upper-right panel), both distributions show small differences. The anisotropy is, independently of q_h, $\sigma_0(0°) \simeq 0.6\sigma_0(90°)$.

The strong differentiation between the inner and the outer distributions is induced by the dependence of the decay time on the galacto-centre distance. In all of our samples, most of the satellites orbiting at radii larger than 200 kpc survive after one Hubble time evolution (see Fig. 10.4). As Fig. 10.10 indicates, satellites initially located at $R_0 < 150$ kpc, suffer strong decays, together with a marked decrease of the orbital inclination that increases the final number of satellites moving along low inclined orbits. Dynamical friction also reduces the main radii of those satellites within $150 \leq R_0 \leq 250$, though with barely inclination decrease (PKB show that the reduction of i mainly occurs at late times of the satellite evolution, when satellites are close to the galaxy centre. Within this range of initial distances one has that, in average, $R \in [70, 175]$ kpc after evolution expecting, therefore, low decrease of the orbital inclination). This satellites smooth the inclination distribution at $R < 200$ kpc.
In the outer regions ($R_0 > 250$ kpc) the effect is the opposite. Dynamical friction is negligible and the dominant effect on the inclination evolution is nutation, which affects the final distribution as shown in Fig. 10.2. In the range $150 \leq R_0 \leq 250$, however, the decay of satellites to $R < 150$ kpc occurs mainly for those with low i, since dynamical friction is stronger than for those following near polar orbits (see PKB). This enhances the anisotropy of the inclination distribution shown in the upper-right panel of Fig. 10.11.

The upper-left panel shows that, whereas $\sigma_0(90°)$ is barely independent on the distance scale, the number of satellites with $i < 45°$ enhances for $R < 200$ kpc due to the flow of satellites from outer regions, which is stronger the more flattened the halo is.

In the lower raw panels we plot the distributions after projecting them into the sky. The main effect of the projection is the strong reduction of the anisotropy, so that, if for $r > 200$ kpc one has that $\sigma_0(i = 0°) \simeq 0.6\ \sigma_0(i = 90°)$, after projection $\sigma_0(\phi = 0°) \simeq 0.8\ \sigma_0(\phi = 90°)$, which means that the projected number of satellites on polar orbits compared to that in coplanar is 25% smaller [2].

In both intervals, the resulting distributions differ strongly to that observed by Zaritsky & González (1999) (long-dashed lines) independently of the halo shape and initial inclination configuration, especially at large radii. The observational data show very large anisotropies which indicate that, in the galaxy frame, a large fraction of satellites must move in nearly polar orbits. Comparing these curves with those of Fig. 10.1 (where we assume that all satellite follow circular orbits) one finds that, in order to observe $\sigma_{\rm obs}(\phi = 0°)/\sigma_{\rm obs}(\phi = 90°) \sim 0.04/0.12 \simeq 0.33$ at $r > 200$ kpc, the distribution in the galaxy frame requires the total absence of satellites within $[0°, 80°]$ and spatial distributions scaling as $\sigma(R) \propto R^{-1}$.

We must note, however, that the observational surface density is zero for $\phi = 0°$. This indicates that the data available are not complete, since even if all satellite move in (non-radial) polar orbits, $\sigma_0(0°) \neq 0$ due to the projection effects (see Section 10.4).

A similar calculus was carried out for the samples 4, 5 and 6, corresponding to an initial spatial distribution that follows the NFW profile. The results are very similar to those plotted in Fig. 10.11, indicating that the final distribution of orbital inclinations is barely correlated to the initial satellite distribution in space.

[2] note that (i) ϕ denotes the projected satellite inclination with respect to the disc plane and (ii) we use projected distances to differentiate the satellites that belong to the inner and outer distance ranges

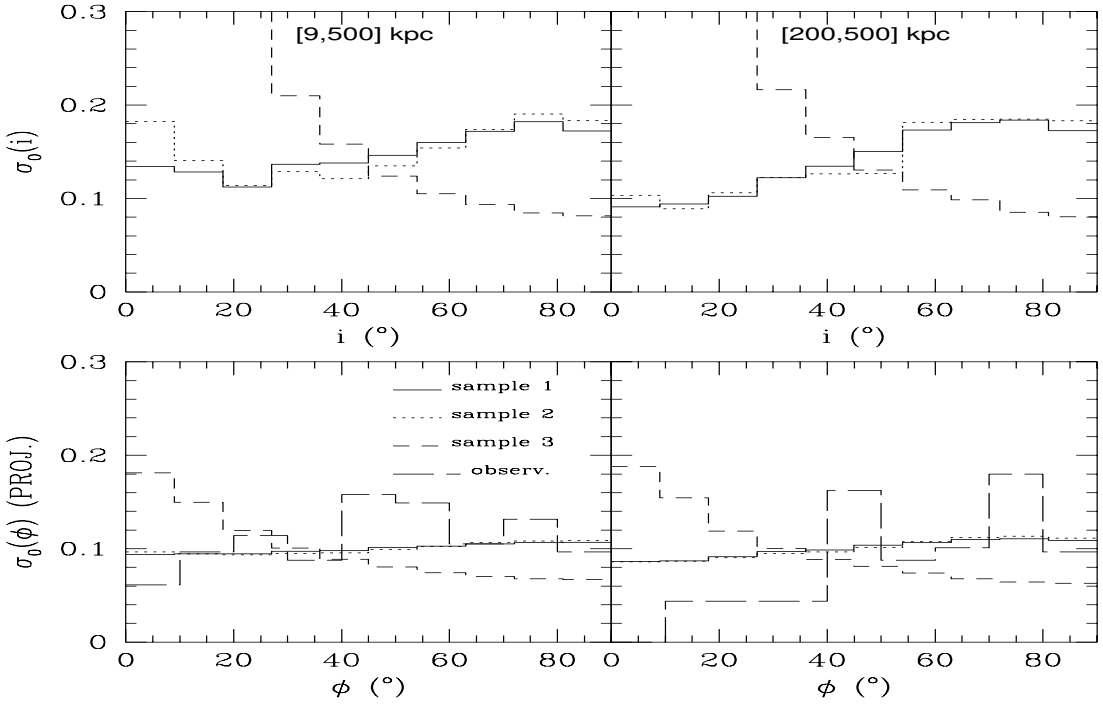

Figure 10.11: Inclination distribution at $t = t_H$. **Upper raw**: Inclination histograms for two distance ranges (Samples 1, 2 and 3 of Table 10.1). **Lower raw**: Projected distribution compared to the observational data of Zaritsky & González (1999).

10.7.3 Distance and mass distributions

In Fig. 10.12 we plot the final distribution of the projected distances and masses for the samples 1 and 4.

The distance distribution of the initially isothermal sample shows a linear decrease for $r > 100$ kpc, i.e $\sigma(r) \propto r^{-1}$. Since the apparent satellite-parent galaxy separation is reduced by the projection, so that $R^{2-\beta} \rightarrow r^{1-\beta}$ (Section 10.4, $\beta = 2$ for an isothermal profile), the linear behaviour of $\sigma(r)$ indicates that, at large radii, the distance distribution suffers barely changes after the system has been evolved, which also occurs when the satellite sample follows initially the NFW profile. As we conclude in Section 10.7.1, these results suggest that dynamical friction effects can be neglected for $R_0 > 250$ kpc.

For $r < 100$ kpc we observe a strong decrease of the satellite number. At this distance scale, dynamical friction proves to be an efficient mechanism in order to remove satellites, which leads to steep decrease of $\sigma(r)$ for $r \rightarrow 0$ (see also the upper-panel Fig. 10.10).

In this panel, we also compare the evolve distributions to the curve obtained from the observations of Zaritsky et al. (1993). Unfortunately, the number of satellites belonging to the observational sample is to low to produce accurate statistics in order to determine the initial profile that best fit to observations.

The projected samples show a lack of satellites for $r > 300$ kpc. To solve this problem one should initially locate more satellites at radii $R_0 > 500$ kpc. However, it is not clear whether these bodies are not affected by the background structures present in the Dark Matter dominated Universe, even if galaxies in the observational sample appear as isolated.

In the lower panel we represent the evolved mass distributions. The resulting mass spectra do not differ strongly to the initial mass since mass removal mechanisms, like tidal forces and shocks, are solely effective near the disc ($R < 50$ kpc). Satellites with initial distances larger than 150 kpc (around 75% of satellites at $t = 0$) suffer a negligible mass loss along their evolution. As a

result, the final distribution show small differences depending on the initial density profile. These are only visible for those satellites with initial masses between 0.1 and 0.2 disc masses, since more massive satellites own larger binding energies which reduce the mass stripping.
The best fit to the observational mass spectrum occurs for $\Upsilon_s/\Upsilon_d = 0.5$. Satellites that originally follow the NFW profile show stronger mass evolution than those with an isothermal spatial distribution. The reason is that this sample presents a larger number of satellites at $r < 50$ kpc, which indicates a higher interaction with the disc (via shocks) and the inner galaxy potential (via tidal mass stripping).
The evolved samples show a reasonable agreement for $M_s < 0.2M_d$. However, more massive satellites are so far not observed, which represent approximately the 40% of the total number of satellites in our sample. It is not clear whether this can significatively alter the inclination and distance distributions commented above.

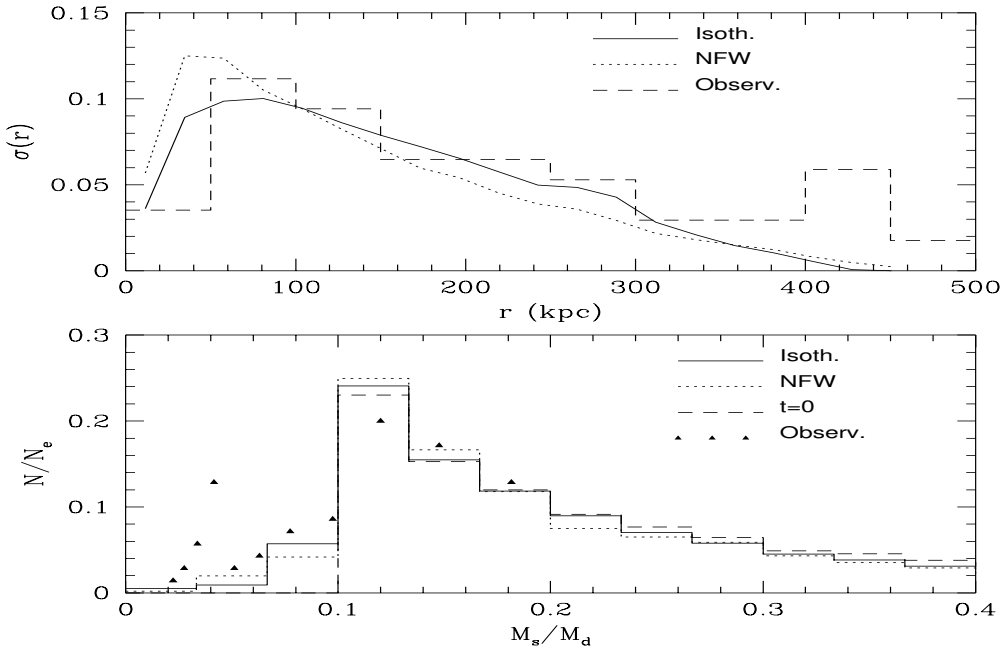

Figure 10.12: **Upper panel**: Projected distance distribution after evolution compared to observations of Zaritsky et al. (1993). **Lower panel**: Evolved mass distribution compared to the observational data of Zaritsky & González (1999). We use eq. (10.1), to convert apparent magnitudes into satellite masses, where the best fit is found for $\Upsilon_s/\Upsilon_d = 0.5$. We denote N/N_e as the number of satellites per mass interval normalised to the number of surviving satellites after one Hubble time.

10.8 Discussion

We have performed a statistical study of the satellite evolution in spiral galaxies based on the hierarchical scenario assumed by the CDM cosmology. This investigation may put light on the, so far, non-understood highly anisotropic distribution of satellites. The idea beyond this analysis is the possible connection between the halo asphericity, predicted by CDM, with the location of satellites in spiral galaxies.

Observational data show projected distributions that in the galaxy frame would imply the total absence of satellites for orbital inclinations lower that 80°. If we assume that these samples are complete, there must be a strong mechanism that remove those satellites in low inclined orbits.

Dynamical friction in spiral galaxies with flattened haloes cannot explain such observations with the initial satellite distributions employed in this exercise. The resulting inclination distributions that we obtain are by far more isotropic than those observed by Zaritsky et al. (1993), independently whether the initial spatial distribution follows an isothermal profile or that proposed by NFW. Even haloes as flattened as $q_h = 0.2$ are not able to increase the preference of satellite to be located on high inclined orbits.

It is usually assumed that satellites formed in a spatial distribution that follows the Dark Matter halo's one. However, the samples matching the oblateness of halo at $t = 0$, remain oblate after their evolution, i.e $\sigma(90^\circ) < \sigma(0^\circ)$ which, therefore, goes against the observational data.

A possible reason for such a mismatch with observations might be that the initial distributions that we use do not correspond to those in the Universe at early times. However, (i) the resulting galacto-centre distance distributions show a remarkable agreement with the observations for $r <$ 300 kpc, (ii) different eccentricity distributions to that proposed by van den Bosch et al. (1999) would result to a change of the slope of the distance distribution (for instance, if all satellite follow nearly radial orbits, the projected spatial distribution would appear steeper), but it is unlikely that the final inclination distribution became more anisotropic, since it appears as barely dependent of the spatial gradient. (iii) The satellite mass spectrum is not known. However, decreasing the mass range seems not a remedy since this would lead to a decrease of the friction force and, therefore, a decrease of the effects of the halo flattening on the orbital inclination evolution.

We have analysed the evolutionary solution to the also known as "Holmberg problem" without success. A solution might be found in the initial distribution of inclinations. For instance, had satellites formed initially in a prolate distribution, they would be observed today preferentially in polar orbits if Dark Matter haloes are flattened.

Another open question is whether the initial distribution is in equilibrium or, on the contrary, it follows the Dark Matter evolution on the galaxy scale at early times. This will be analysed in Peñarrubia, Kroupa & Just (2003) in more detail.

Bibliography

- Arnaboldi M., Capaccioli M., Cappellaro E., Held E.V., Sparke L.S., 1993, A&A, 267, 21
- Bahcall J.N., Schmidt M., Soneira R.M., 1982, ApJ, 258, L23
- Bahcall N., Ostriker J.P., Pelmutter S., Steinhardt P.J., Science, 284, 1481
- Bardeen J.M., Bond J.R., Kaiser N., Szalay A.S., 1986, ApJ, 304, 15
- Barnes, J.E, 1988, ApJ, 331, 699
- Becquaert J.F., Combes F., Viallefond F., 1997, A&A, 325, 41
- Begeman K.G., Broeils A.H., Sanders R.H., 1991, MRAS, 249, 532
- Binggeli B., Sandage A., Tarenghi M., 1984, AJ, 89, 64
- Binney J., 1977, MNRAS, 181, 735
- Binney J., 1992, ARA&A, 30, 51
- Binney J., Merrifield M., 1998, Galactic Astronomy. Princeton University Press, Princeton, New Jersey
- Binney J., Tremaine S., 1987, Galactic Dynamics. Princeton University Press, Princeton, New Jersey (BT)
- Boily C.M., Kroupa P., Peñarrubia J., 2001, NewA, 6, 27 (BKP)
- Bond J. R., Cole S., Efstathiou G., Keiser N., Szalay A., 1986, ApJ, 304, 15
- Boute D.A., Canizares C.R., 1998, ApJ, 468, 184
- Buote D.A., Jeltema T.E., Canizares C.R., Garmire G.P., 2002, ApJ, 577, 183
- Busch A. E., 1983, M.Sc. thesis, University of Toronto
- Carney B., Lathman D.W., 1987, in Kormendy J., Knapp G.R., eds, Proc. IAU Symp 117, Dark Matter in the Universe. Reidel, Dordrecht, p.39
- Carr B., 1994, ARA&A, 32, 531
- Chandrasekhar S., 1943, ApJ, 97, 255
- Chandrasekhar S., 1960, Principles of Stellar Dynamics. Dover, New York
- Colin P. Avila-Reese V., Valenzuela O., 2000, ApJ, 542,622
- Colpi M., Mayer L., Governato F., 1999, ApJ, 525, 720
- Cora S.A., Muzzio J.C., Vergne M.M., 1997, MNRAS, 289, 253

- Dohm-Palmer R. C., Helmi A., Morrison H., Mateo M., Olszewski E. W., Harding P., Freeman K. C., Norris J., Shectman S. A., ApJ, 555, 37
- Dubinsky J., 1994, ApJ, 431, 617
- Dubinsky J., Calberg R., 1991, ApJ, 378, 496
- Efstathiou G., Frenk C. S., White S. D. M., Davis M., 1988, MNRAS, 235, 715
- Einasto J., Kaasik A., Saar E., 1974, Nature, 250, 309
- Fellhauer M., Kroupa P., Baumgardt H., Bien R., Boily C. M., Spurzem R., Wassmer N., 2000, NewA, 5, 305
- Fich M., Tremaine S., 1999, ARA&A, 29, 409
- Firmani C., D'Onghia E., Chincarini G., Hernández X., Avila-Reese V., 2000b, MNRAS, 321, 713
- Fisher J. R., Tully R. B., 1981, ApJ Suppl, 47, 139
- Freeman K.C., 1970, ApJ, 160, 811
- Frenk C.S., White S.D.M., Davis M., Efstathiou G., 1988, ApJ, 327, 507
- Fukugita M., Hogan C.J., Peebles P.J.E., ApJ, 503, 518
- Ghigna S., Moore B., Governato F., Lake G., Quinn T., Stadel J., 1999, ApJ, 554, 616
- Goodman J., 2000, NewA, 5, 103
- Gnedin O.Y., Hernquist L., Ostriker J.P., 1999, ApJ, 514, 109
- Gnedin O.Y.,Ostriker J.P., 1997, ApJ, 474, 223G
- Gnedin O.Y.,Ostriker J.P., 1999, ApJ, 513, 626 (GO)
- Goldstein, H, 1980, Classical Mechanics, Singapore. Addison-Weasley
- González A.H., Williams K.A., Bullock J.S., Kolatt T.S., Primack J.R., 1999, ApJ, 528, 145
- Hashimoto Y., Funato Y., Makino J., 2002, astro-ph/0208452
- Helmi A., White S.D.M., 1999, MNRAS, 307, 495
- Helmi A., de Zeeuw P.T., 2000, MNRAS, 319, 657
- Hernquist L., 1990, ApJ, 356, 359
- Hernquist L., 1993, ApJS, 86, 389
- Hofner P., Sparke L., 1994, ApJ, 428, 466
- Hohl F., 1970, NASA Technical Report R-343
- Holmberg E., 1969, Arkiv. Astr, 5, 305
- Ibata R., Lewis G.F., Irwin M., Totten E., Quinn T., 2001, ApJ, in press
- Ibata, R. A., Gilmore, G. & Irwin, M. J. 1994, Nature 370, 194
- Johnston K., Sigurdsson S., Hernquist L., 1999, MNRAS, 302, 771
- Keeton C.R., Kochanek C.S., 1998, ApJ, 495, 157

- King I.R., 1962, AJ, 67, 471
- King I.R., 1966, AJ, 71, 65
- Klessen R.S., Kroupa P., 1998, ApJ, 498, 143
- Klypin A., Kravtsov A.V., Bullock J.S., Primack J.R., 2001, ApJ, 554,903
- Kroupa P., 1997, NewA, 2, 139
- Kundić T., Ostriker J.P., 1995, ApJ, 438, 702
- Lacey C., Cole S., 1993, MNRAS, 262, 627
- Lacey C., Cole S., 1994, MNRAS, 271, 676
- Landau l.D., Lifschitz E.M., The classical Theory of Fields, Pergamon, Oxford, pp. 358-368
- Lewis J.R., Freeman K.C., 1989, AJ, 97, 139
- Lin, D.N.C., Tremaine S., 1983, ApJ, 264, 364
- MacGillivray H. T., Dodd R. J., MacNally B. V., Corwin H. G. Jr., 1982, MNRAS, 198, 605
- Maller A.H., Flores R.A., Primack J.R., 1997, ApJ, 486, 681
- Maller A.H., Simard L., Guhathakurta P., Hjorth J., Jaunsen A.O., Flores R., Primack J.R., 2000, ApJ, 533, 194
- Martínez-Delgado D., Aparicio, A., Gómez-Flechoso, M. A., Carrera R., 2001, ApJ, 547, 133
- Mckay T.A. et al, ApJ, 2002, 571, L85
- Milgrom M., 1983, AJ, 270, 365
- Moore B., Quinn T., Governato F., Stadel J., Lake G., 1999b, MNRAS, 310, 1147
- Moore B., Ghigna S., Governato F., Lake G., Quinn T., Stadel J., Tozzi P., 1999a, ApJ, 524, L19
- Navarro J.F., Frenk C.S., White S.D.M., 1996, ApJ, 462, 563 (NFW)
- Navarro J.F., Frenk C.S., White S.D.M., 1997, ApJ, 490, 493
- Navarro J.F., Steinmez M., 2000, ApJ,538, 477
- Nelson R.W., Tremaine S., 1999, MNRAS, 306, 1
- Nilson P., 1973, Uppsala General Catalogue of Galaxies, Uppsala, Sweden. Upsala Offset Centre AB.
- Olling R.P., 1996, AJ, 112, 481
- Olling R.P., Merrifield M.R., 2000, MNRAS, 311, 361
- Ostriker J.P., Peebles P.J.E., Yahil A., 1974 ApJ, 193L, 10
- Ostriker J.P., 1993, ARA&A, 31, 689
- Peacock J.A., 1999, Cosmological Physics. Cambridge, Cambridge University Press
- Peñarrubia J., Kroupa P., Just A., in preparation
- Peñarrubia J., Kroupa P., Boily C.M., 2001, MNRAS, 333, 779 (PKB)

- Peebles P.J.E., 1993, 'Principes of Physical Cosmology', Princeton University Press, Priceton
- Peebles P.J.E., 2000, ApJ, 534, L127
- Percival W.J., and 25 co-authors, MNRAS, 337, 1068
- Persic M., Salucci P., Stel F., 1996, MNRAS, 281, 27
- Pfenniger D., Combes F., Martinet L., 1994, A&A, 285, 79
- Piatek S., Pryor C., 1995, AJ, 109, 1071
- Popolo A., Gambera M., 1999, A&A, 342, 34
- Prada F., Vitvitska M., Klypin A., Holtzman J.A., Schlegel D.J., Grevel E., Rix H.W., brinkmann J., Mckay T.A., 2003, astro-ph/0301360
- Press W., Schechter P., 1974, ApJ, 187, 425
- Press W.P., Flannery B.P., Teukolsky S.A., Vetterling W.T., 1986, Numerical Recipes. Cambridge University Press, New York
- Prugniel Ph., Combes F., 1992, A&A, 259, 25
- Quinn P.J., Goodmann J., 1986, ApJ, 306, 472
- Quinn P.J., Hernquist L., Fullagar D.P., 1993, ApJ, 403, 74
- Sánchez-Salcedo F.J., Brandenburg A., 1999, ApJ, 522,35
- Sánchez-Salcedo F.J., Brandenburg A., 2001, MNRAS, 322,67
- Sackett P.D., Rix H.W., Jarvis B.J., Freeman K.C., 1994, ApJ, 436, 629
- Sanders R.H., 1990, A&A Rev., 2, 1
- Sciama D., 1990, MNRAS, 244, 1
- Smith D.R., Bernstein G.M., Fischer P., Jarvis M., 2001, apJ, 551, 643
- Sofue Y., Rubin V., 2001, ARA&A, 39, 107
- Spergel D.N., Steinhardt P.J., 2000, Phys.Rev.Lett., 84,3760
- Spinnato P.F., Fellhauer M., Portegies Zwart S.F., astro-ph/0212494
- Spitzer L. Jr., 1987, Dynamical Evolution of Globular Clusters, Princeton University Press, Princeton
- Spitzer L., 1942, ApJ, 95, 329
- Steinman-Cameron T.Y., Kormendy J., Durisen R.H., 1992, AJ, 104, 1339
- Stenmetz M., White D.M., 1997, 288, 545
- Tóth G., Ostriker J.P, 1992, ApJ, 389, 5
- Taylor J.E., Babul A., 2001, ApJ, 559, 716 (TB)
- Tormen G., 1997, MNRAS, 290, 411
- van den Bosch F. C., Lewis G. F., Lake G., Stadel J., 1999. ApJ, 515, 50
- de Vaucouleurs G., 1948, Annales d'Astrophysique, 11, 247

- Velázquez H., White S.D.M., 1999, MNRAS, 304, 254 (VW)
- Weinberg M. D., 1994, AJ, 108, 1398
- Weinberg M.D., 2000, ApJ, 532, 922
- Whade M., Donner K.J., 1996, A&A, 312, 431
- Zaritsky D., González A., 1999, PASP, 111, 1508
- Zaritsky D., Olszewski E. W., Schommer R. A., Peterson R. C., Aaronson M., 1989, ApJ, 345, 759
- Zaritsky D., Smith R., Frenk C, White S. D. M., 1993, ApJ, 405, 464
- Zaritsky D., Smith R., Frenk C, White S. D. M., 1997, ApJ, 478, 39
- Zaritsky D., White S.D.M., 1994, ApJ, 435, 599
- Zhao H., Johnston K.V., Hernquist L., Spergel D.N., 1999, A&A, 348, L49
- Zwicky F., 1933, Helvetica Physica Acta, 6, 10

Chapter 11

Summary

The results presented in this Thesis can be summarised as,

- **Theoretical study of dynamical friction**
  In Chapter 5 we have presented a detailed develop of the method and the different approximations that lead to the final expressions of dynamical friction in inhomogeneous systems. The main results are:
  (i) For completeness with the local and the straight line approximations, the Coulomb logarithm must include a galacto-centre distance dependence so that the maximum impact parameter can be estimated as,

$$b_1^2 = b_0^2 + Q^2 + \left(\frac{\rho}{||\nabla rho||}\right)^2 \frac{V_0^2}{4v_M^2 + V_0^2},$$

  where b_0 is the minimum impact parameter, ρ is the system density profile, V_0 is the relative velocity (in the straight line approximation) of the satellite-background particle encounter, the satellite moving with a velocity v_M and Q is a free parameter to fit to the N-body data. The Coulomb logarithm in our scheme, therefore, provides the explicit dependence on V_0, v_M and ρ.
  (ii) We also calculate the first order term of specific dynamical friction that results from the local approximation, which scales as $F^{[1]} \propto M_s^2||\nabla\rho||$, whereas $F^{[0]} \propto M_s\rho$, which implies that the ratio $F^{[1]}/F^{[0]}$ increases for decreasing galacto-centre distance and satellite mass.
  We have also developed the expression of dynamical friction in flattened systems, where $\rho = \rho(r, \theta)$, θ being the azimuthal angle. The velocity dispersion ellipsoid of axi-symmetric systems owns two components (σ_R, σ_z), which accomplish $\sigma_R \geq \sigma_z$.

- **Semi-analytic study of dynamical friction**
  In Chapter 4 we outline a semi-analytic code that can reproduce the satellite dynamics and evolution once the galaxy and satellite profiles are provided. This code implements the analytic formulæ of dynamical friction presented in Chapter 5 in order to test these expressions as against the N-body data.
  First, in Chapter 6 we check dynamical friction in a spherical systems. The results indicate that (i) the velocity dependence of the Coulomb logarithm can be neglected and (ii) for satellites with initially $M_s = 0.1M_d$, where M_d is the disc mass, the contribution of $F^{[1]}$ to dynamical friction is approximately $10 - 30\%$ at the peri and apo-galactica, respectively. Moreover, since $F^{[1]}$ is parallel to $\hat{\mathbf{e}}_\perp = [\hat{\mathbf{n}} - (\hat{\mathbf{n}} \cdot \hat{\mathbf{v}}_M) \cdot \hat{\mathbf{v}}_M]/||\hat{\mathbf{n}} - (\hat{\mathbf{n}} \cdot \hat{\mathbf{v}}_M) \cdot \hat{\mathbf{v}}_M||$, the component of $\hat{\mathbf{e}}_\perp$ parallel to $\mathbf{v}_M$ nearly vanishes after the average over one orbital period. The resulting curves of the satellite's galacto-centre distance evolution where $\mathbf{F}_{\rm df} = \mathbf{F}^{[0]} + \mathbf{F}^{[1]}$ and $\mathbf{F}_{\rm df} = \mathbf{F}^{[0]}$ show discrepancies of solely 0.5 kpc after 5 Gyr.
  Once it has been shown that neither the velocity dependence of the Coulomb logarithm nor the addition of the first order term $\mathbf{F}^{[1]}$ introduce significant effects on the satellite dynamics,

in Chapter 8 we test the expressions of dynamical friction in axi-symmetric systems assuming that $\ln\Lambda$ =const and $\mathbf{F}_{\rm df} = \mathbf{F}^{[0]}$. We observe that (i) polar satellites survive longest, whereas coplanar orbit present the fastest decay, (ii) for $\sigma_z/\sigma_R = 0.6$, the decay time of polar satellites τ_{90} if compared with that of coplanar ones τ_0 accomplishes $(\tau_{90}-\tau_0)/(\tau_{90}+\tau_0) \simeq 0.26$ (orbital eccentricity $e = 0.5$), (iii) the orbital inclination (i) suffers a strong decrease not observed in spherical systems. Satellites, therefore, tend to align with the symmetry plane along their evolution. For orbits not aligned with the symmetry axes, the final inclination after the merge is $i \sim 10 - 20°$, independently of $i(t = 0)$. The analytic expressions of Chapter 4 reproduce remarkably well these effects. We show that the anisotropy in velocity space is responsible for the inclination reduction, whereas the dependence of the decay time on the initial inclination is due to (i) the density flattening, which increases $\Delta\tau = \tau_{90} - \tau_0$ and (ii) the velocity anisotropy, which reduces $\Delta\tau$. Since $(\tau_{90} - \tau_0)/(\tau_{90} + \tau_0) \simeq 0.26$ we conclude that the flattened density dominates the spread of decay times as a function of the orbital inclination.

- **Disc and bulge effects**
  An important aspect for cosmological studies is to determine the contribution of the galactic baryonic components (namely, disc and bulge) to the satellite evolution. In Chapter 9 we compare the N-body evolution of several orbits in galaxies with and without bulge and disc for two halo axis-ratios $q_h = 0.6$ and $q_h = 1$. The results can be summarised as follows:
  (i) The disc and bulge presence enhances the satellite mass loss through the action of tidal forces and tidal heating which, as a result, slows down the satellite decay. On the another hand, these components induce additional dynamical friction that reduces the decay time. Both effects are of the same magnitude, so that satellites in galaxies with and without a baryonic mass fraction present similar decay times. The disc rotation also differentiates the satellite orbit with respect to its orbital sense (i.e., prograde and retrograde orbits), so orbits anti-aligned with the disc rotation survive longer than those aligned (for example, orbits with orbital inclinations $i = 45°$ (prograde) and $i = 135°$ in galaxies with $q_h = 1$ show $(\tau_{135} - \tau_{45})/(\tau_{135} + \tau_{45}) \simeq 0.06$. However, this effect is negligible if the halo is flattened $q_h = 0.6$.
  (ii) In the second part of Chapter 9 we check the accuracy of the self-consistent semi-analytic code in order to describe the satellite evolution in spiral galaxies (i.e., galaxies formed by disc, bulge and Dark Matter halo). For that purpose, we implement a analytic scheme of mass loss. The comparison is carried out for a large set of orbital parameters, satellite masses and the two values of halo flattening. We find that the semi-analytic algorithm reproduces remarkably well the satellite dynamics as well as its mass evolution.

- **Satellite distribution**
  In Chapter 10 we outline the present observational data of the satellite distribution in spiral galaxies. This distribution is highly anisotropic, in the sense that the major part of satellite galaxies is located with $\phi > 45°$ with respect to the disc plane. After the subtraction of the projection effects, this anisotropy suggests the total absence of satellites with orbital inclinations lower than approximately 80°.
  The main goal of Chapter 10 is the analysis of the possible connection between the preference of satellites to move on high inclined orbits and the Dark Matter halo flattening. The state of affairs is still preliminary. We evolve satellite samples with different initial distributions: (i) the initial spatial distribution is selected either to be isothermal or to follow a Navarro, Frenk & White (1997) profile, (ii) the initial inclination distribution is either isotropic or it matches the halo mass distribution. The galaxy parameters are assumed constant and independent of the satellite sample.
  The evolved distributions show that, (i) the resulting anisotropy is roughly independent of the initial spatial distribution, (ii) those samples that mimic the mass flattening at $t = 0$, present inclination distribution where the number of satellites moving on low inclined orbits is much larger than those on nearly polar orbits ("oblate" shape) which, therefore,

goes against observations, (iii) those samples initially isotropic become "prolate" as a consequence of the halo flattening. However, after projecting the sample onto the sky, the final value $\sigma(0°)/\sigma(90°) \simeq 0.8$ (for $q_h = 0.5$), where σ is the surface density as a function of the inclination ($\sigma = 1$ denotes isotropy), is by far lower than the observational one $\sigma_{\rm obs}(0°)/\sigma_{\rm obs}(90°) \simeq 0.33$.

We want to continue with this investigation in a following project, which must include a more realistic description of the galaxy evolution. Satellite dynamics may give insights on the halo shape and the initial satellite distribution, which are directly connected with Dark Matter models. Since satellites are observed as far as 500 kpc from the parent galaxy, this study may also constrain the halo density profile at large radii. These investigations will provide a hint on the Dark Matter nature.

Appendix A

Precession and nutation

Due to the complexity of the motion of a particle within a axi-symmetric system, it is more straight forward to analyse the evolution of the planes defined by the angular momentum (**L**) to describe the orbit of the satellite. In doing this, we shall apply the Euler angles for the satellite coordinates (see Fig. A.1), defined as

$$\begin{aligned} \omega_x &= \dot{\phi}\sin\theta\sin\psi + \dot{\theta}\cos\psi \\ \omega_y &= \dot{\phi}\sin\theta\cos\psi - \dot{\theta}\sin\psi \\ \omega_z &= \dot{\phi}\cos\theta + \dot{\psi}, \end{aligned} \tag{A.1}$$

where ω is (Goldstein 1980)

$$\mathbf{v} = \dot{R}\mathbf{e}_R + \dot{z}\mathbf{e}_z + \omega \times \mathbf{r}. \tag{A.2}$$

The position of the satellite in the orbital plane is determined by $(R, z, \psi, \dot{R}, \dot{z}, \dot{\psi})$, whereas the plane itself by the angular momentum vector, with coordinates (θ, ϕ). Note that eq. A.2 recovers eq. 1B-23 of Binney & Tremaine (1987), hereinafter BT, if $\dot{\theta} = \dot{\phi} = 0\ \forall t$.

Using this angles and spherical coordinates, the kinetic and total energy of the satellite are

$$\begin{aligned} T &= \frac{1}{2}(\dot{R}^2 + \dot{z}^2) + \frac{1}{2}R^2\omega_z^2 + \frac{1}{2}z^2\omega_R^2 \\ E &= T + \Phi(r, \theta), \end{aligned} \tag{A.3}$$

the potential supposed axi-symmetric. Using the Euler coordinates, the orbit of the satellite in the orbital plane is defined by the potential and can be parametrised as $(R[\psi], z[\psi])$.

Therefore, the Langrange function is

$$\begin{aligned} \mathcal{L} &= \frac{1}{2}(\dot{R}^2 + \dot{z}^2) + \frac{1}{2}z^2\omega_R^2 + \frac{1}{2}R^2\omega_z^2 - \Phi(r, \theta) = \\ &= \frac{1}{2}(\dot{R}^2 + \dot{z}^2) + \frac{1}{2}z^2(\dot{\theta}^2 + \dot{\phi}^2\sin^2\theta) + \frac{1}{2}R^2(\dot{\psi} + \dot{\phi}\cos\theta)^2 - \Phi(r, \theta). \end{aligned} \tag{A.4}$$

Since in the Lagrangian ϕ and ψ do not appear explicitely we have two constant of motion

$$\begin{aligned} p_\psi &= r^2\sin^2\theta(\dot{\psi} + \dot{\phi}\cos\theta) = R^2\omega_z \equiv a \\ p_\phi &= (R^2\cos^2\theta + z^2\sin^2\theta)\dot{\phi} + R^2\cos\theta\dot{\psi} \equiv b, \end{aligned} \tag{A.5}$$

the constant a being simply the z-component of the angular momentum. After some algebra, one could easily check that last equations are equivalent to

$$\begin{aligned} \dot{\phi} &= \frac{b - a\cos\theta}{z^2\sin^2\theta} \\ \dot{\psi} &= \frac{a}{R^2} - \cos\theta\frac{b - a\cos\theta}{z^2\sin^2\theta}. \end{aligned} \tag{A.6}$$

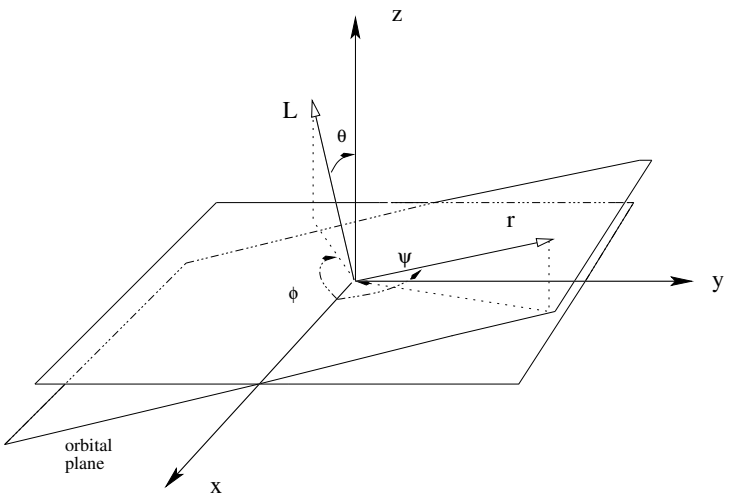

Figure A.1: Euler coordinates of the satellite's position vector (**r**) and the angular momentum vector (**L**).

It is straight forward to check that if there is no variation of the angular momentum vector, i.e, $\dot{\phi} = 0\ \forall t$ (which, as we see later, is equivalent to have a spherical potential), then these last equations reduce to the condition:

$$b = a\cos\theta, \tag{A.7}$$

and therefore the angular momentum of the satellite is just

$$\dot{\psi}R^2 = a = \text{const.}$$

Substituting the constant of motion in the equation of the energy (A.4) and using the definition of the angular velocities (A.2) one finds

$$\begin{aligned} E &= \frac{1}{2}(\dot{R}^2 + \dot{z}^2) + \frac{1}{2}z^2(\dot{\theta}^2 + \dot{\phi}^2\sin^2\theta) + \frac{1}{2}R^2\omega_z^2 + \Phi(r,\theta) \\ &\equiv \frac{1}{2}(\dot{R}^2 + \dot{z}^2) + \frac{1}{2}z^2(\dot{\theta}^2 + \dot{\phi}^2\sin^2\theta) + \Phi_{\text{eff}}, \end{aligned} \tag{A.8}$$

where $\Phi_{\text{eff}} = \Phi + a^2/(2R^2)$ is the effective potential typically defined in axi-symmetric systems. Note that $E = E(a,b)$ is also a constant of motion. From this last equation one could solve the evolution of θ by quadratures if $R[\psi(t)], z[\psi(t)]$ were known

$$\dot{\theta}^2\sin^2\theta = \left[E - \frac{1}{2}(\dot{R}^2 + \dot{z}^2) - \Phi_{\text{eff}}\right]\frac{2(1-u^2)}{z^2} - \frac{(b - a\cos\theta)^2}{z^4}, \tag{A.9}$$

where we substitute the value of $\dot{\phi}$ from the eq. (A.7).
Defining the variable:

$$u = \cos\theta,$$

it becomes

$$\dot{u}^2 = \left[E - \frac{1}{2}(\dot{R}^2 + \dot{z}^2) - \Phi_{\text{eff}}\right]\frac{2(1-u^2)}{z^2} - \frac{(b - au)^2}{z^4}. \tag{A.10}$$

As expected, the function $f(u)$ is not determined for $z \to 0$ ($f(u) = 0/0$), corresponding to the case in which the angular momentum is parallel to the z-axis, i.e, coplanar orbits.

It is immediate to find that the condition of $\dot{\theta} = \dot{\phi} = 0\ \forall t$ is therefore equivalent to

$$E = \frac{1}{2}(\dot{R}^2 + \dot{z}^2) + \Phi_{\rm eff},$$

which recovers eq. 3.53 of BT.

Until here, the development of these expressions has been done without loss of generality and it holds for any particle moving within an axi-symmetric system. However, to carry on our study on of the evolution Euler planes, we should use a determined potential and a given orbital eccentricity.

We define now:

$$\alpha(u) = E - \frac{1}{2}(\dot{R}^2 + \dot{z}^2) - \Phi_{\rm eff} = E - \frac{1}{2}(\dot{R}^2 + \dot{z}^2) - \frac{a^2}{2R^2} - \Phi(u), \tag{A.11}$$

which accomplishes $\alpha(u) \geq 0$ (the equality being for spherical systems).

Giving the initial conditions

$$\dot{\phi}(t=0) = \dot{\theta}(t=0) = 0$$

$$u(t=0) = u_0,$$

it is straight forward to show that $b = au_0$ and $\alpha(u_0) = 0$ at $t = 0$. Since the value of $(R[\psi], z[\psi])$ does not depend explicitely on θ, the equation of the nutation becomes

$$\dot{u}^2 \equiv f(u) = [\Phi(u_0) - \Phi(u)]\frac{2(1-u^2)}{z^2} - \frac{a^2}{z^4}(u_0 - u)^2. \tag{A.12}$$

The function $f(u)$ is limited to the interval (-1,1) corresponding to $\theta \in (-\pi/2, \pi/2)$, thus any value of u which makes $f(u) < 0$ or locates out of this range has no physical meaning.

The solution of this last equation is in general not analytical, and should be calculated numerically. However, it is interesting to estimate the behaviour of $f(u)$. By definition $f(u_0) = 0$, so that the initial condition is a root. For u tending to ± 1 the function is $\propto -(u_0 \mp 1)^2 < 0$, so that the function is negative at $\theta = \mp\pi/2$. This implies that, at least, to roots must be present within the interval $u \in (-1, 1)$

Although this expression appears to be complicate, one can actually analyse qualitatively the evolution of θ by calculating the points in which $\dot{\theta}$ changes of sign, i.e, $f(u) = 0$.
Let's concentrate the our calculus in the interval $0 < u_0 < 1$. Since the initial condition must by definition be a root and since $f(u) < 0$ for $u \to 0$, we can assert that within (0,1) there are two roots, i.e, two values of θ for which $\dot{\theta}$ is zero, that we call u_0, u_1 . Out of this range, we have that $\dot{\theta}^2 < 0$ with, therefore, no physical meaning. The evolution of θ limited within two fixed values is called **nutation**. At the same time, the variation of θ implies a variation of ϕ defined as the **precession** of the orbit. (see Goldstein 1980).

One can actually calculate the magnitude of the nutation $u_1 - u_0$ by imposing $f(u_1) = 0$. However, this equality has no analytical solution for our system, and the root must be found numerically.

In Fig. (A.2) we plot the function $f(u)$ with initial conditions as in our model H2S145 (substituting the initial v_s by the circular velocity). To determine the value of $\alpha(u)$ we calculate numerically the potential for different θ, whereas the constant a is simply the z-component of the angular momentum at $t = 0$ and $E = \Phi_{\rm eff}(u_0)$. As we see, there are two roots, $u_0 = \cos(\pi/4) \sim 0.71$ and $u_1 \sim 0.5$, i.e, $\theta_1 \sim 60°$. The amplitude of the nutation is therefore $\Delta\theta \sim 15°$ which is slightly lower than what we find in the numerical calculations.

The eq. (A.12) is a non-linear differential equation with no analytical solution. Even though, it is interesting to obtain the dependence of the nutation on the orbital parameters. For that purpose we attempt to solve it in the regime of low asphericity, for which it is accomplished that

$$\frac{z^2|\Delta\Phi|}{a^2} << 1. \tag{A.13}$$

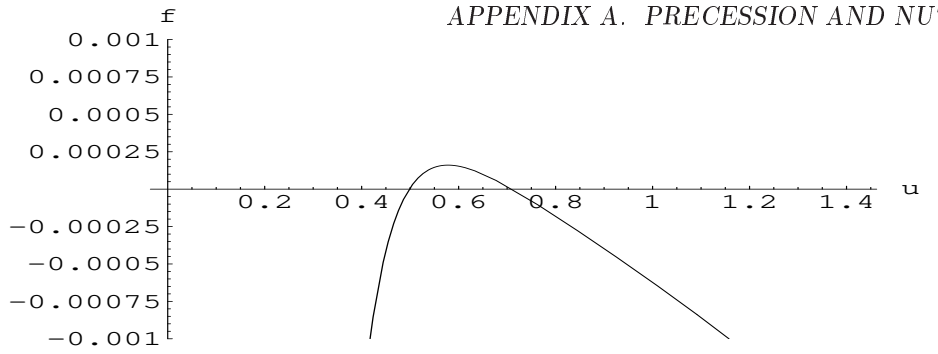

Figure A.2: Behaviour of $f(u)$ using the initial conditions of the model H1S145 to determine the constants.

The potential of an oblate halo with peaked density profile can be expanded in Harmonic series

$$\Phi(u) = -\frac{GM}{r} + \frac{GM}{2r^3}(I_z - I_R)P_2(u) + \mathcal{O}\left(\frac{a_1}{r}\right)^4, \tag{A.14}$$

where $P_n(u)$ is a Legendre polynomial and I_x an eigen-component of the inertia tensor per unit mass (accomplishing that $I_z > I_R$ in oblate systems). We denote as M the mass inside the radius r and a_1 the semi-major axis of the oblate. The equations of motion integration for such a potential leads to the solution

$$x_i(t) = x_{0,i}\cos\left[w_1(t-t_0)\right]\left\{1 + \frac{w_2^2}{w_1^2}\frac{x_{0,i}^2}{8r^2}\cos^2\left[w_1(t-t_0)\right]\right\}, \tag{A.15}$$

where

$$w_2^2 = \frac{9}{2}\frac{I_z - I_R}{r^2}; \quad w_1^2 = G\bar{\rho} + w_1^2; \quad \bar{\rho} = \frac{M}{4\pi r^3/3},$$

and x_i the components of the position vector in Cartesian coordinates. The average over one orbit of period $T = 2\pi/w_1$ of the particle motion leads to the equation

$$< x_i >^2 = \frac{w_1}{2\pi}\int_{t_0}^{2\pi/w_1} x_i^2 dt = x_{0,i}^2\left[1 + \frac{5}{16}\left(\frac{w_2}{w_1}\right)^4\left(\frac{x_{0,i}^2}{8r^2}\right)^2\right]. \tag{A.16}$$

Since our aim is to give a general quantitative description of the satellite evolution, in the regime of low asphericy, we shall approximate $< x_i >^2 \simeq x_{0,i}^2$ and therefore, for a satellite following a circular orbit the averaged vertical component is $< z^2 > = r^2u_0^2 = \text{const}$.

Defining the variable $x = u - u_0$, the condition of low asphericity also implies $x_1 = u_0 - u_1 << 1$, where u_1 denotes the second root of $f(u)$. Since the value of $|\Delta\Phi|$ is small we shall approximate $u_0^2 - u^2 = (u_0 - u)(u_0 + u) \simeq 2u_0x$, and $1 - u^2 \simeq 1 - u_0^2$, then

$$\dot{x}^2 \simeq x\left[(I_z - I_R)\frac{3GM}{r^5}\frac{(1-u_0^2)}{u_0^2} + \frac{a^2}{r^4u_0^4}x\right], \tag{A.17}$$

the solution is analytical and using our initial conditions it can be expressed as

$$x(t) = (I_z - I_R)\frac{3GM}{2a^2r}(1-u_0^2)u_0^2\left[1 - \cos\left(\frac{a}{r^2u_0^2}t\right)\right]. \tag{A.18}$$

The solution gives an amplitude of

$$x_1 = (I_z - I_R)\frac{3GM}{a^2r}(1-u_0^2)u_0^2, \tag{A.19}$$

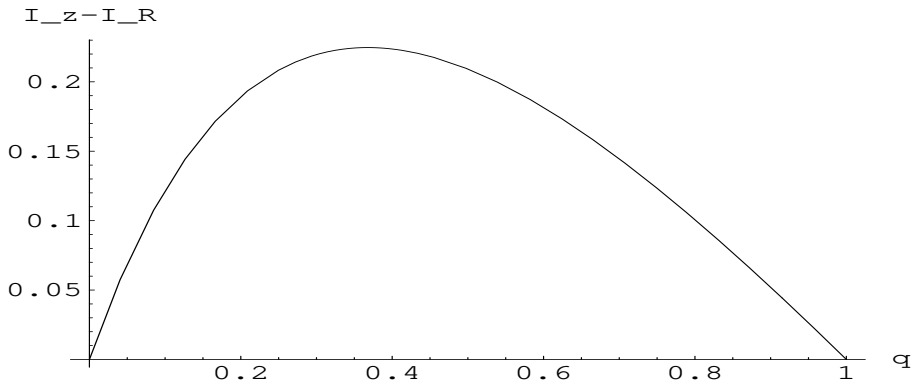

Figure A.3: Value of $(I_z - I_R)$ normailised to $3G/(2\sigma^2 r)$ as a function of q_h.

and a period of

$$T = 2\pi \frac{r^2 u_0^2}{a}. \tag{A.20}$$

From the eq. (A.7), the precession in this regime is

$$\dot{\phi} = \frac{a(u_0 - u)}{< z^2 > (1 - u_0^2)} \simeq \frac{ax}{r^2 u_0^2 (1 - u_0^2)} = \tag{A.21}$$
$$(I_z - I_R) \frac{3GM}{2ar^3} \left[1 - \cos\left(\frac{a}{r^2 u_0^2} t \right) \right].$$

As it is deduced from the last equations,
(i) Precession and nutation vanish in spherical systems (for which $I_z = I_R$).
(ii) Satellites following coplanar orbits do not present either precession or nutation. In the case of a satellite in a polar orbit, the nutation vanishes, suffering however precession.
(iii) The nutation and precession periods are the same, both being proportional to r^2/a.
(iv) The precession accomplishes that $\dot{\phi} \geq 0$ thus there is no change of the precession sense. Equivalently, the nutation makes that $u_0 - u \geq 0$ (oblate systems).

Consider that the Dark Matter halo employed in our numerical and semi-analytic calculations has a density profile that can be approached as

$$\rho = \frac{\sigma^2}{2\pi G r^2} \frac{1}{\sin^2\theta + \cos^2\theta / q_h^2}, \tag{A.22}$$

then the moments of intertia difference can be written as

$$I_z - I_R = \frac{2\sigma^2 r}{3G} \frac{q_h}{(1 - q_h^2)^{3/2}} \left[3q_h (1 - q_h^2)^{1/2} - (2 + q_h^2) \, \mathrm{atan}\left(\frac{\sqrt{1 - q_h^2}}{q_h} \right) \right]. \tag{A.23}$$

In Fig. A.3 we plot the value of $3G(I_z - I_R)/(2\sigma^2 r)$ as a function of q_h. We can observe that the maximum lies at $q_h \simeq 0.4$, whereas for the numerical calculations of Chapter 9 $q_h = 0.6$, thus

$$I_z - I_R \simeq 0.34 \frac{\sigma^2 r}{3G},$$

the amplitude of nutation being

$$\Delta \cos\theta \simeq 0.34 \sigma^2 M(r) \sin^2\theta_0 \cos^2\theta_0.$$

For a circular orbit with initially $\theta = 45^\circ$ and $r = 55$ kpc, one has that from Fig. 3.1 and Fig. 3.2 $M_h(< 55\mathrm{kpc}) \simeq 0.65 M_h(r_{\mathrm{cut}})$, whereas $\sigma \simeq 0.32 \times 262 \mathrm{kms}^{-1}$, respectively. The amplitude estimate is $\Delta \cos\theta \sim 0.025$, so that $\Delta\theta \sim 10^\circ$. This is roughly the amplitude that we observe in Fig. 8.6.

Appendix B

Integration over velocity space

We carry explicitely out the integrals of eq. (5.26) and (5.30) which correspond to the integration in velocity space of the zeroth and first order dynamical friction, respectively.

The integral over θ

Since v^2 of the Dark Matter particles is a function of θ, we must specify the distribution function before going on. The distribution function in velocity space is a Gaussian for the explicite integration, although the general results do not depend strongly on the special shape of $f(v^2)$.

$$f(v^2) = \frac{1}{(\sqrt{2\pi}\sigma)^3}\exp(-\frac{v^2}{2\sigma^2})\frac{1}{(\sqrt{2\pi}\sigma)^3}\exp(-X^2-W^2)\exp(-u\mu) \qquad \text{with} \quad u = 2WX, \tag{B.1}$$

where where we define $\mu \equiv \cos\theta$ for simplicity.

For the zeroth order term (eq. 5.26) one must solve

$$\begin{aligned}\int_{-1}^{1} 2\pi\mu\exp(-u\mu)d\mu &= -4\pi\left[\frac{\cosh(u)}{u} - \frac{\sinh(u)}{u^2}\right] \\ &\approx \frac{-4\pi u}{3}\left[1+\frac{u^2}{10}\right] \quad \text{for} \quad u << 1,\end{aligned} \tag{B.2}$$

and for the first order components (eqs. 5.30)

$$\begin{aligned}\int_{-1}^{1} \pi[1+\mu^2]\exp(-u\mu)d\mu &= -4\pi\left[\frac{\cosh(u)}{u^2} - \frac{1+u^2}{u^3}\sinh(u)\right] \\ &\approx \frac{8\pi}{3}\left[1+\frac{u^2}{5}\right] \quad \text{for} \quad u << 1\end{aligned} \tag{B.3}$$

$$\begin{aligned}\int_{-1}^{1} 2\pi[1-\mu^2]\exp(-u\mu)d\mu &= 8\pi\left[\frac{\cosh(u)}{u^2} - \frac{\sinh(u)}{u^3}\right] \\ &\approx \frac{8\pi}{3}\left[1+\frac{u^2}{10}\right] \quad \text{for} \quad u << 1,\end{aligned} \tag{B.4}$$

where for completeness the Taylor expansions for small velocities are also given.

Inserting the results of the angle integration into the equations of both dynamical friction terms

we find

$$\mathbf{F}^{(0)} = -\frac{4\pi G^2 m(M+m)^2 n_0}{\sqrt{\pi}\sigma^2}\frac{\mathbf{v}_M}{v_M} \tag{B.5}$$
$$\times \int_0^\infty \ln\Lambda \exp(-W^2-X^2)\left[\frac{\cosh(2WX)}{WX} - \frac{\sinh(2WX)}{2W^2X^2}\right] dW$$
$$= -K_{\rm ch}\hat{\mathbf{e}}_{v_M}\int_0^\infty \ln(\Lambda) g(X,W) dW.$$

Here we used $K_{\rm ch}$, explicitely given in eq. 5.28 and the function

$$g(X,W) = \frac{2}{\sqrt{\pi}}\exp(-W^2-X^2)\left[\frac{\cosh(2WX)}{WX} - \frac{\sinh(2WX)}{2W^2X^2}\right], \tag{B.6}$$

recalling that $\Lambda = \Lambda(X,W)$, eq. (5.16) and (5.18).

For the inhomogeneous terms we get from eq. (5.30) the parallel component

$$\mathbf{F}^{(1)}_{\parallel} = \frac{-G^3 m(M+m)^2\sqrt{\pi}n_r}{\sigma^4 X^2}\cos(\Psi)\hat{\mathbf{e}}_{v_M} \times \tag{B.7}$$
$$\int_0^\infty \ln(\Lambda)\exp(-W^2-X^2)\left[\cosh(2WX) - \frac{\sinh(2WX)}{2WX}\right]\frac{dW}{W^4}$$
$$= -K_{\rm ch}\cos(\Psi)\hat{\mathbf{e}}_{v_M}\int_0^\infty \ln(\Lambda) g_{\rm par}(X,W) dW, \tag{B.8}$$

and the orthogonal component

$$\mathbf{F}^{(1)}_{\perp} = \frac{-G^3 m(M+m)^2\sqrt{\pi}n_r}{2\sigma^4 X^2}\sin(\Psi)\hat{\mathbf{e}}_{\perp} \times$$
$$\int_0^\infty \ln(\Lambda)\exp(-W^2-X^2) \times \left[\frac{4W^2X^2+1}{2WX}\sinh(2WX) - \cosh(2WX)\right]\frac{dW}{W^4}$$
$$= -K_{\rm ch}\sin(\Psi)\hat{\mathbf{e}}_{\perp}\int_0^\infty \ln(\Lambda) g_{\rm ort}(X,W) dW, \tag{B.9}$$

where we used analogous functions

$$g_{\rm par}(X,W) = \frac{\pi G(M+m)}{4\sigma^2 l}\frac{g(X,W)}{W^3X} \tag{B.10}$$
$$g_{\rm ort}(X,W) = \frac{\pi G(M+m)}{4\sigma^2 l}\frac{2h(X,W)-g(X,W)}{2W^3X} \quad \text{with} \tag{B.11}$$
$$h(X,W) = \frac{2}{\sqrt{\pi}}\exp(-W^2-X^2)\sinh(2WX).$$

Chandrasekhar's friction formula

With the approximation of a Coulomb logarithm $\ln\Lambda_0$ independent of W we find the standard Chandrasekhar friction formula by solving the integral present in eq. (B.5) by parts

$$\int_0^\infty g(X,W)dW = \frac{2}{\sqrt{\pi}}\int_0^\infty \exp(-W^2-X^2)\left[\frac{\cosh(2WX)}{WX} - \frac{\sinh(2WX)}{2W^2X^2}\right]dW$$
$$= \frac{2}{\sqrt{\pi}X}\left[\exp(-W^2-X^2)\frac{\sinh(2WX)}{2WX}\bigg|_0^\infty + \frac{1}{X}\int_0^\infty \exp(-W^2-X^2)\sinh(2WX)dW\right]$$
$$= \frac{2}{\sqrt{\pi}X}\left[-\exp(-X^2) + \frac{1}{2X}\int_{-X}^{X}\exp(-Y^2)dY\right]$$
$$= \frac{1}{X^2}\left[erf(X) - \frac{2X}{\sqrt{\pi}}\exp(-X^2)\right]. \tag{B.12}$$

Inserting this into eq. (B.5) we find the result

$$\mathbf{F}^{(0)} \approx -K_{\rm ch} \ln \Lambda_0 \frac{\hat{\mathbf{e}}_{v_M}}{X^2} \left[erf(X) - \frac{2X}{\sqrt{\pi}} \exp(-X^2) \right] . \tag{B.13}$$

Since the maximum impact parameter depends on the local scale length, it also depends on the position of the satellite. The use of the global value $\langle \ln \Lambda \rangle$ neglects as well the position dependence of the Coulomb logarithm.

Acknowledgments

Being close to finish my PhD (unbelievable!), I realize that it wouldn't have been possible without the help of many people.

I want to thank Andreas Just and Rainer Spurzem for their support and help. The quality of this Thesis would have surely been much lower without their useful comments.

I appreciate much the collaboration with Pavel Kroupa and Chris Boily, both have shown me (in a very different way, I must say) how to deal with Astrophysics. I'm very grateful to Mike Fellhauer for his help with SUPERBOX.

I would also thank Pr. Wielen, for his financial support during the last and a half year as well as the SFB439 for travel trips and the first two years of my stay in Germany.

No tengo más remedio que dedicar unas palabras a todos los impresentables que he conocido por aquí, veáse Gerardo "gañán", "Polito", el "Toifel", David, Angel, Antonio, Kike, Julio, Gustavo, Mauricio...etc, menuda "Armada" de pacotilla, pero que bien nos lo hemos pasado, viva Dios.

Gracias Pau, lo nuestro en el instituto ha sido como la peli de "Solos ante el peligro", a ver si llegamos a ver el final donde siempre ganan los buenos.

En especial quisiera darles las gracias a mis padres. Papá, mamá, sin vosotros no sería nada, todo me lo habeis dado. Gracias de todo corazón por vuestro apoyo y, sobre todo, por vuestro cariño.

Sabine, mi pequeño bicho, cuantas cosas he descubierto contigo, cuantas cosas me has enseñado, cuanto te quiero. No hubiese podido vivir en Heidelberg sin tí. Gracias por tu amor, tu paciencia y tu fidelidad. Sabine, a ti te dedico esta tesis, aunque te merezcas muchísimo más.